



THESE

pour l'obtention du grade de Docteur, délivré par
l'ECOLE NORMALE SUPERIEURE DE LYON

Ecole Doctorale N°52
PHAST - Physique et Astrophysique

Discipline : SCIENCES DE L'UNIVERS (Sciences de l'Univers)

Soutenue publiquement le 13 octobre 2025, par :

Armand LECLERC

Topologie des ondes pour l'astérosismologie
Wave topology for asteroseismology

Après avis de :

Michel RIEUTORD, Professeur des universités, Université de Toulouse	Rapporteur
Kévin BELKACEM, Chargé de recherche - HDR, Observatoire de Paris / CNRS	Rapporteur

Devant le jury composé de :

Michel RIEUTORD, Professeur des universités, Université de Toulouse	Rapporteur
Kévin BELKACEM, Chargé de recherche - HDR, Observatoire de Paris / CNRS	Rapporteur
Isabelle BARAFFE, Directrice de recherche, ENS de Lyon / CNRS	Examinateuse
Jacqueline BLOCH, Directrice de recherche, Université Paris-Saclay / CNRS	Examinateuse
Lisa BUGNET, Professeure, Institut des Sciences et Technologies d'Autriche	Examinateuse
Guillaume LAIBE, Professeur des universités, ENS de Lyon	Directeur de thèse

Contents

Avant-propos	5
PART I INTRODUCTION	8
I Waves in planets and stars	9
I.1 Waves on Earth	9
i Atmosphere and ocean	9
ii Seismology	11
I.2 Asteroseismology	13
i Waves as stellar probes	14
ii Waves as stellar active processes	15
iii Observations	17
I.3 How to study waves?	19
i Analytical approaches	21
ii Numerical approaches	25
II Wave topology	27
II.1 Eigenvalues, eigenvectors and Berry	27
II.2 Polarization relations influence on ray-tracing	32
II.3 The Chern number and concept of spectral flow	35
i Topology	35
ii Bulk-boundary correspondence	37
II.4 Topological waves	41
i The Kelvin and Yanai waves	41
ii The Lamb wave	42
iii Topological modes elsewhere in physics	44
<i>Aims of the thesis</i>	47
PART II GEOPHYSICAL AND ASTROPHYSICAL INERTIAL WAVES	48
III Inertial waves in convective zones	49
IV Shallow water waves on a sphere	60
PART III A TOPOLOGICAL WAVE IN STELLAR OSCILLATIONS	83
V The nature of <i>f</i>-modes	84
V.1 A practical set of variables	85
VI Topological mixed <i>f/g</i> modes in the Sun	96
VII Berry phase importance of solar <i>p</i>-modes	119

Contents

PART IV \mathcal{PT} SYMMETRY AND INSTABILITIES	133
VIII \mathcal{PT} symmetry in waves and instabilities	134
IX Exceptional modes of convective instability	144
<i>General conclusion</i>	152
Appendices	157
A Solving for normal modes with DEDALUS	157
B Berry curvature expression for asteroseismology	160
Bibliography	162

Sommaire

Avant-propos	5
PARTIE I : INTRODUCTION	7
I Ondes dans les planètes et les étoiles	8
II Topologie des ondes	26
PARTIE II : ONDES INERTIELLES GÉOPHYSIQUES ET ASTROPHYSIQUES	47
III Ondes inertielles en zone convective	48
IV Ondes d'eau peu profonde sur une sphère	55
PARTIE III : UNE ONDE TOPOLOGIQUE DANS LES OSCILLATIONS STELLAIRES	63
V La nature du mode f	64
VI Mode mixte f/g topologique dans le Soleil	71
VII Importance de la phase de Berry dans les modes acoustiques solaires	76
PARTIE IV : SYMÉTRIE \mathcal{PT} ET INSTABILITÉS	81
VIII Symétrie \mathcal{PT} des ondes astrophysiques	82
IX Modes exceptionnels de l'instabilité convective	93
Conclusion	99
Appendices	104
Bibliographie	113

Avant-propos

Remerciements

Ma thèse se termine, et maintenant que la partie scientifique de ce manuscrit est écrite, je peux prendre le temps ici d'exprimer ma gratitude à tous ceux et toutes celles qui ont fait que ces trois années passées au CRAL ont été si belles. Il faut que je commence par Guillaume, un directeur de thèse dont l'enthousiasme et l'énergie sont aussi constants qu'infaillibles. Tu as su trouver le bon sujet pour moi, tu m'as donné confiance dans ce qu'on faisait, et tu sais dire quand les slides sont moches ou quand les brouillons d'articles sont mauvais. J'ai vraiment beaucoup appris avec toi, et je n'aurais pas pu espérer tomber mieux. Toujours emballé, toujours positif et motivé, on aurait pu étudier n'importe quoi que ça aurait été passionnant. Guillaume, ma meilleure idée pendant cette thèse a été de la faire sous ta direction. Même si officiellement, je n'ai qu'un directeur de thèse, je dois absolument remercier Pierre et Antoine d'être tellement intervenus dans les projets que nous avions. Antoine, ton instinct lors des discussions pendant des projets interdisciplinaires a toujours été impressionnant, et source de remarques qui nous ont souvent beaucoup fait avancer. Pierre, outre la topologie que tu m'as patiemment apprise au tableau, je retiens de toi une certaine approche de la recherche, où le but premier est d'abord la clarté de compréhension. Ensuite, comment pourrais-je remercier Pierre et Antoine sans aussi exprimer ma gratitude à leur fils spirituel, le Dr Perez. Nicolas, Guillaume a été très inspiré de te mettre le grappin dessus après ta soutenance, car cette thèse aurait été significativement moins aboutie sans tes contributions. Faudrait-il une preuve par les chiffres, il suffirait de compter les articles signés en commun. Je suis ravi – et fier – que mon Chapitre II ait passé ton contrôle technique. Je remercie maintenant le dernier à avoir directement contribué à mes travaux de thèse, qui est Arthur Le Saux. Je suis particulièrement fier du projet que nous avons mené ensemble, qui a changé beaucoup de choses à la fois dans mes propres compréhensions et dans l'impact de cette thèse, en l'amenant au sein même de la physique stellaire. Arthur, Nicolas, Antoine, Pierre et Guillaume, j'espère continuer à travailler avec chacun d'entre vous.

Je voudrais avoir un mot aussi pour ceux qui ont toujours été prêts à discuter de science. Je pense notamment à Gilles, Thomas, Quentin, Elliot et Hamed, avec qui j'ai eu un nombre de discussions particulièrement enrichissantes. Isabelle, il faut que j'en profite pour te remercier de m'avoir invité à Exeter juste avant cette thèse. Car même si ce n'était qu'un stage, j'en ai gardé beaucoup de la physique stellaire et de la physique des simulations.

Merci à mes co-thésards pour les souvenirs, Tim, Pascal et Romain. J'espère qu'on se reverra tous les quatre un jour ! Merci aussi à Pierre, arrivé plus tard mais toujours prêt à défendre les théoriciens face aux numériciens. Léo, Yona, Antonin et Adnan, même si vous êtes de ce camp-là, j'ai beaucoup aimé qu'on soit collègues au CRAL.

Merci à lamifa d'être toujours là, je vous aime tous, Méli, Alexandre, Marine et Elizabeth. Merci papa d'avoir consciencieusement relu mon anglais, dans les parties fraîchement écrites de ce manuscrit qui en avaient besoin. I hope ze engliche teacheur was plized. Merci maman d'avoir joué, à l'époque, le rôle particulièrement important de réussir à m'inscrire en prépa alors que j'avais manqué la date limite... Je ne suis pas sûr que je serais ici aujourd'hui, et pour ça merci maman ! Enfin je termine avec la plus importante, ma femme Tessa à qui je dois mille mercis. Car il faut l'avouer, si j'ai passé de si belles années pendant ma thèse, c'est quand même surtout grâce à toi.

Motivations et buts initiaux

Contexte

En 2017, Pierre Delplace, Brad Marston et Antoine Venaille publient un article dans *Science* intitulé *Topological origin of equatorial waves*, dans lequel ils dévoilent un lien entre les isolants topologiques, ces matériaux conducteurs d'électricité qui n'auraient pas dû l'être, et les ondes océaniques piégées à l'équateur. Ce pont conceptuel entre physique quantique et physique des ondes dans les fluides a révélé une structure abstraite commune des équations régissant ces problèmes très différents. Cette structure commune est caractérisée par la topologie, qui a été employée dans les années 80 pour expliquer ce problème de conductivité anormale de certains matériaux, une prouesse récompensée par le prix Nobel de physique en 2016. Etonnamment, un emploi semblable est tout aussi possible sur le problème des ondes équatoriales, et révèle l'origine topologique d'ondes particulières de cette région du globe.

Cette étude pionnière a ouvert un champ disciplinaire, car beaucoup de questions surviennent alors : qu'apprend-t-on des ondes de leurs propriétés topologiques ? Quels sont les ingrédients nécessaires pour qu'un problème d'ondes dans un fluide exhibe de telles propriétés, et dans quelles situations va-t-on les trouver ? Un nombre d'études s'en est suivi, s'attaquant à ces questions.

Amener la topologie en astrophysique

Le but général de cette thèse a été de pointer la lumière de la topologie vers un nombre de problèmes d'ondes dans des fluides astrophysiques, une direction qui n'avait pas encore été explorée jusqu'alors, et deux questions se posaient. La première a été d'identifier si effectivement, certaines ondes dans certaines situations astrophysiques sont soumises à des contraintes topologiques sous-jacentes. On dira alors que ces ondes sont topologiquement non-triviales, dans un sens défini et détaillé en Chapitre II. Les travaux de cette thèse sont particulièrement orientés vers les ondes dans les intérieurs planétaires et stellaires, dans lesquels la richesse des structures, des processus dynamiques et thermodynamiques est connue pour générer des problèmes d'ondes aux propriétés très variées, potentiellement propices aux propriétés topologiques. La seconde question générale de cette thèse a été d'établir ce qui pouvait être appris des ondes et des objets dans lesquels elles se propagent grâce à leurs propriétés topologiques. Autrement dit, qu'apprend-on quand on conclut que certaines ondes sont topologiquement non-triviales ? De plus, est-ce que ces propriétés sont détectables ou mesurables avec les outils d'observation actuels ? Les outils de la topologie permettent de conclure sur la localisation spatiale, la robustesse aux perturbations, et souvent l'unidirectionnalité de certains modes appelés *modes topologiques* des ondes. S'ils sont identifiés, les propriétés uniques de ces modes peuvent aider à comprendre une phénoménologie particulière des objets où ils sont trouvés. Par exemple, les modes topologiques identifiés par Delplace, Marston et Venaille, sont connus pour se propager dans l'océan, à l'équateur, uniquement vers l'Est. Ils ne peuvent pas se propager vers l'Ouest, et cette propriété est à la base du phénomène El Niño, cette vague de chaleur générée en Asie qui se déplace vers les Amériques. La topologie des ondes est un moyen générique d'étudier si des ondes peuvent générer ce genre de phénomènes.

Les ondes dans les fluides astrophysiques sont étudiées depuis longtemps, car elles sont un excellent moyen de sonder les objets stellaires comme les étoiles et les planètes, mais aussi car elles jouent des rôles dynamiques cruciaux. Les instabilités linéaires, le transport d'énergie et de moment cinétique sont autant de processus qui participent à l'évolution et à la forme des étoiles, des disques d'accrétion et protoplanétaires, des galaxies, des planètes et des atmosphères. Toutes les communautés scientifiques qui étudient tous ces objets étudient les ondes qui s'y propagent. Puisque la topologie des ondes est une technique d'analyse complémentaire encore non-exploitée, qui peut révéler des propriétés uniques de certains modes, développer cette analyse contribuera à l'avancement de notre compréhension d'un nombre de phénomènes dans tous ces objets.

*Nature is not a mean human being. Nature is a very gentle,
sometimes austere, but really a straightforward creature.*
Tadashi Tokieda

List of publications

- Leclerc, A., Laibe, G., Delplace, P., Venaille, A., & Perez, N. (2022). Topological modes in stellar oscillations. *The Astrophysical Journal*, 940(1), 84.
- Venaille, A., Onuki, Y., Perez, N., & Leclerc, A. (2023). From ray tracing to waves of topological origin in continuous media. *SciPost Physics*, 14(4), 062.
- Leclerc, A., Jezequel, L., Perez, N., Bhandare, A., Laibe, G., & Delplace, P. (2024). Exceptional ring of the buoyancy instability in stars. *Physical Review Research*, 6(1), L012055.
- Leclerc, A., Laibe, G., & Perez, N. (2024). PT and anti-PT symmetries for astrophysical waves. *Astronomy & Astrophysics*, 689, A237.
- Leclerc, A., Laibe, G., & Perez, N. (2024). Wave topology of stellar inertial waves. *Physical Review Research*, 6(4), 043299.
- Perez N., Leclerc A., Laibe G. & Delplace, P. (2025). Topology of shallow-water waves on a rotating sphere. *Journal of Fluid Mechanics*. 2025;1003:A35.
- Leclerc, A. & Laibe, G. (2025). The importance of Berry phase in solar acoustic modes. *The Astrophysical Journal Letters*, 983(1), L17.
- Le Saux, A., Leclerc, A., Laibe, G., Delplace, P., Venaille, A. (2025). *The Astrophysical Journal Letters*, 987(1), L12.

Part I

Introduction

Waves in planets and stars

Résumé

Ce premier chapitre introduit dans un premier temps l'étude des ondes se propageant dans les planètes et les étoiles. Sur Terre, l'atmosphère et l'océan sont parcourus par des ondes acoustiques, des ondes de gravité et des ondes inertielles, qui sont impliquées dans un nombre de processus géophysiques et climatiques. L'intérieur de la Terre a été révélé par des ondes similaires, grâce au développement de la sismologie. Dans une seconde partie, le domaine de la sismologie des étoiles, l'*astéroismologie*, est présenté. Il est montré avec plus de détails comment ces ondes servent de sondes pour osculter l'intérieur des étoiles, qui serait autrement inaccessible. Elles donnent accès aux profils de densité, pression, température, taux de rotation d'un grand nombre d'étoiles, et notamment du Soleil, et depuis peu à des estimations de l'amplitude du champ magnétique dans certains cœurs. Les techniques d'observation sont résumées, avant qu'il soit montré comment les études théoriques sont habituellement menées. Le chapitre se termine sur une discussion des études numériques des ondes dans les intérieurs stellaires.

This thesis is a contribution to the theory of wave propagation in geophysical and astrophysical fluids. The study of waves in fluids started in the 18th century, with some key steps found in the works of D'Alembert [1], Lagrange [2], Laplace [3], Kelvin [4], Boussinesq [5], Rayleigh [6], Stokes [7], then Lamb [8] and Lighthill [9]. Waves constitute many phenomena that humans have seen, heard and felt propagating in their environment, should it be in the air, water or ground. This chapter starts by discussing these phenomena on Earth, in the atmosphere, in the oceans and in seismology. It then introduces the fascinating field of asteroseismology, the study of waves in the interiors of stars which are a source of periodic variability of their luminosity. The chapter ends by presenting the various ways waves are usually studied and described in stellar physics. It aims at providing the global picture in which this thesis fits, and bring the motivation of the work presented in this manuscript.

I.1 Waves on Earth

The epitome of a wave in everyone's mind is the ocean wave. The disturbances of the surface of water when the wind blows on the sea, or when a rock is thrown in a lake, form these vertical periodic displacements of the surface moving away from their source. Those are *surface gravity waves*, as they exist because the surface of the water is being pulled down by gravity. Many other types of waves are found propagating through parts of the Earth, each type having its own restoring force, opposed to the disturbance and making it vibrate.

I.1.i Atmosphere and ocean

The atmosphere and the oceans of the Earth have many properties in common as they are both the large fluid parts of the surface of the Earth. They are both relatively compressible, stratified and follow the daily rotation of the planet. These three properties impose three different forces with various relative strengths acting on the flows happening inside them, in addition to gravity: buoyancy, pressure forces and the Coriolis force.

These forces govern most geophysical fluid dynamics. From large-scale flows like the Jet Stream

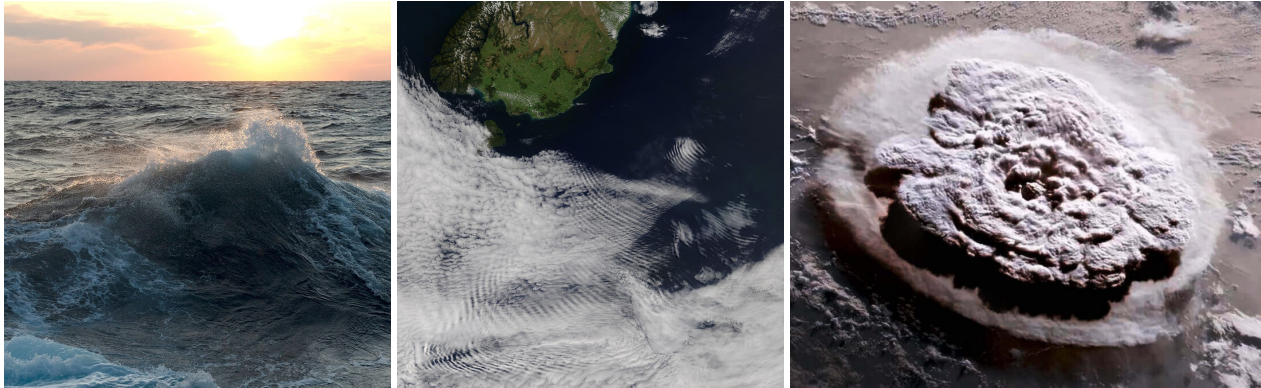


Figure I.1: Waves occur naturally in Earth’s fluids. **Left:** Ocean waves in the Gulf of Mexico¹. **Middle:** Gravity waves seen in the clouds near Auckland Islands². **Right:** Shock wave emitted by the eruption of Hunga Tonga³. It was heard 9000 km away.

¹Credits: Chris Linder, Woods Hole Oceanographic Institution. ²Credits: Jeff Schmaltz, LANCE/EOSDIS Rapid Response. ³Credits: NOAA/NESDIS.

and the Gulf Stream to the weather difference between two neighboring cities, all atmospheric and oceanic motions obey the balance of these forces [10]. In particular, each of these three forces allows for the propagation of one type of wave. If compressibility dominates, the wave is an *acoustic wave*. If buoyancy is the main restoring force, a *gravity wave* is found, either an *internal gravity wave* if it propagates in the bulk of the fluid or a *surface gravity wave* if it’s only propagating at its surface. They have no relation with *gravitational waves*, which are disturbances of the metric of spacetime in extremely violent astrophysical events and will not be studied in this thesis. The third force is the Coriolis force and is entirely due to Earth’s rotation. This force acts as a deviation to the right in the northern hemisphere and to the left in the southern hemisphere, making clockwise or anticlockwise vortices. The associated waves due to this force are *inertial waves*, as they are restored by a non-inertial force in the rotating frame.

If a fluid is both buoyant and rotating, the two kinds of waves it should support are internal gravity waves and inertial waves, and they mix into one kind known as *gravito-inertial* or *internal* waves. Such waves are found in the atmosphere, for example in pictures from satellites as on Figure I.1. These internal waves are easily visible as they make the air go up and down, changing its temperature. The colder air makes water vapor condensate in small droplets and forms clouds, making apparent long white ridges along the crests of the wave.

Acoustic waves are just as familiar as they are our primitive source of communication. Natural phenomena also produce sounds on terrestrial scales, albeit not very often. It does happen for punctual, violent events like volcanic eruptions or meteors crashing. A volcano eruption is the liberation of high-pressure material into the atmosphere. This huge pressure difference causes a shock wave, which is a blast of high amplitude acoustic waves. They travel much faster than internal waves, at a speed of 1200 km/h. The loudest sound ever recorded in human history is actually a blast wave from the eruption of the Krakatoa volcano, in Indonesia in 1883. The shock wave traveled seven times across the globe, and it is estimated that it was emitted with an intensity 310 dB [11]. In January 2022, the Hunga Tonga volcano erupted in the Pacific ocean, and satellites have been able to observe it. Figure I.1 shows a picture where one can see the blast wave as a white disc centered on the volcano.

This special type of large-scale horizontal acoustic waves emitted by eruptions have a special name: they are Lamb waves [12, 13, 14]. They are propagating close to the ground, in the first 10 km of altitude, and are detected after these violent atmospheric events. For instance, a Lamb wave was conclusively detected after the Hunga Tonga eruption [15]. We will come back to these particular wave modes in Chapter II.

For the violent events presented above, acoustic waves are active processes of the physical system, as they transport a significant amount of energy, acting like a pressure relief valve. But when they have small amplitudes, acoustic waves have another use in geophysics, specifically in oceanography

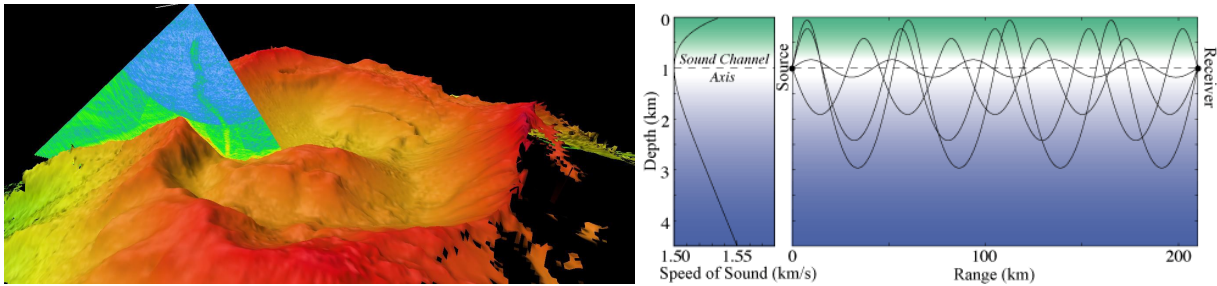


Figure I.2: Acoustic waves can be used to probe the ocean. **Left:** A sonar mapping the seafloor¹.

Right: Acoustic rays propagate in the SOFAR waveguide between emitter and receiver, probing the profile of speed of sound². The spatial inhomogeneity of sound speed causes mirages-like effects of acoustic waves.

¹Credits: NOAA Ocean Exploration. ²Credits: Discovery of Sounds in the Sea, dosits.org.

where they are used only as probes. A sonar can be used to determine the topography of the seabed using the reflection of the sound on it, as illustrated on Figure I.2 (left). The technique of *acoustic tomography* amounts to sending pulses through the ocean and measuring the time delay between emitter and receiver. The propagation equations can then be used to infer the profile of the sound speed in the ocean [16]. This technique is used for instance to probe a particular region of the ocean called SOFAR, where there exists of minimum of sound speed at about 1 km below the surface. It acts as a waveguide as can be seen on Figure I.2 (right), a phenomenon which has been used to communicate without having messages reaching the surface where boats could intercept them during WWII.

A second important event due to waves on Earth is El Niño [17, 18]. It is a recurrent phenomenon involving a heat wave emerging in southern Asia, traveling eastward along the equator and reaching the Americas. It lasts for a few months overall, and happens every few years in a non-periodic pattern. This eastward propagation is supported by Kelvin waves, which are gravito-inertial waves trapped at the equator and propagating only eastward. We will come back to these special waves in Chapter II.

I.1.ii Seismology

Tapping on a wall tells you right away if it is hollow from the sound it makes. That is the essence of seismology: the vibrations caused by earthquakes travel through the inner regions of the Earth, and reach back the surface. With a theoretical understanding of this propagation one can deduce a great deal of the structure of these regions [19, 20, 21].

Being an elastic medium, the interior of the planet is able to support the propagation of waves which are different from those found in the atmosphere and the ocean. P-waves are supported by the compression of the medium, and as such are analogous to acoustic waves. They deform the material in the same direction as they propagate. S-waves have their name as they deform the material in the orthogonal direction of their propagation, in a motion of shear. These two classes of waves are fundamentally different, and for example have two different velocities of propagation. P-waves propagate faster and reach the detectors first.

Earthquakes regularly cause shocks in the crust of the Earth and launch these waves in all directions, as drawn on Figure I.3 (left). P-waves propagate fast and follow certain trajectories, S-waves are slightly slower and follow other trajectories. Upon entering a new layer with a change in the medium of the interior of the planet, the waves are partially or totally reflected and transmitted, leading to a spray of perturbations across the globe from only one source. All these paths arrive at certain destinations and take a certain time to arrive, and seismologists use this data to deduce the position and nature of the layers which caused these paths.

Modern seismology started in the 19th century when Scotland was hit by a series of earthquakes which caused European scientists to study prediction methods and build sensitive seismometers [22]. The first long-distance detection was in 1889 when a seismometer in Germany recorded an

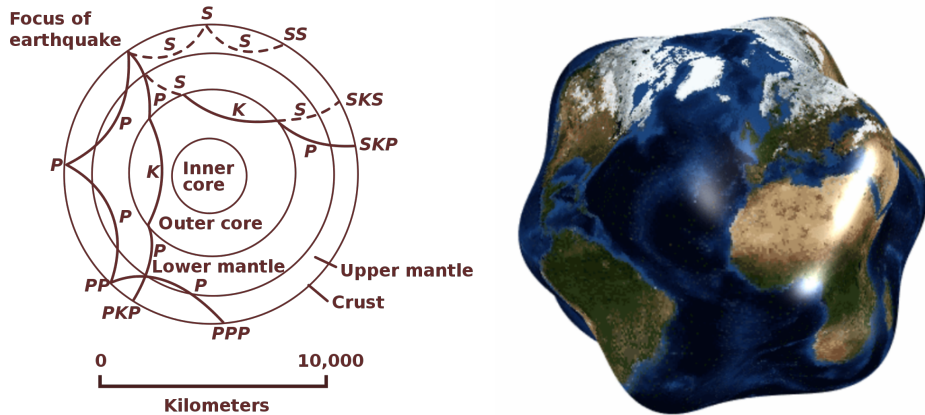


Figure I.3: Seismic activity reveals the internal structure of the Earth. **Left:** The time delay and position at the reception of waves emitted from an earthquake highly depend on the internal layers¹. **Right:** The Earth may oscillate coherently as one or several of its normal modes, here obviously exaggerated².

¹Credits: Seismology page of Wikipedia. ²Credits: Harvard seismology department.

earthquake in Japan. From then on, the increasing quality of seismometers lead to a rapid development of seismology and a series of inferences on the interior of the planet. In 1906, separate arrivals of waves were interpreted from the presence of an iron inner core. In 1909, Mohorovičić discovered a discontinuity in the velocity of the waves and deduced that it is the interface between crust and mantle [23]. In 1926, it is understood that the region under the mantle dubbed "outer core" must be liquid [24]. The great advances of seismology laid the groundwork for the theory of plate tectonics. These advances were achieved with the support of theoretical studies of elasticity waves developed at the same time, built on the foundational works of Navier who in 1822 defined the notion of stress tensor [25] and Poisson who found the two types of polarizations of elastic waves in 1838 [26]. At the end of the 19th century, Rayleigh [27] and Love [28] provided the first theoretical descriptions of seismic waves, with the important additions of two surface waves named after them. In 1904, Lamb gave the first theoretical seismogram [29]. After that, the theoretical studies were joined by the data from seismometers.

Today, the two major motivations for seismology studies are societal and economical. Indeed, there are some attempts at designing methods to predict earthquakes (like the VAN method [30]) or at least estimate seismic hazard, in order to prevent the thousands of deaths they cause every year [20]. The economical interest in seismology is in engineering, either in the sense of earthquake-resistant buildings construction, or in the sense of prospection for oil or natural gas. There is a third application of seismology, which is military monitoring. This aims at detecting nuclear bomb tests, as the associated explosions can be detected with seismometers anywhere around the globe.

This strategy of studying the trajectories of the waves through the planet is the natural way of working with these perturbations. The excitation mechanism is a point source at the focus of the earthquake, which is very small compared to the size of the Earth. Therefore the emissions of perturbations are well localized in space, and trajectories are well defined and can be followed precisely. However, a complementary description can be used, in the form of standing waves, otherwise known as normal modes which are global harmonic oscillations of the planet as shown on Figure I.3 (right) (chapter 8 of [20]). This mathematically equivalent formulation of linear perturbations characterizes the problem in a different way, looking for the resonance frequencies of the Earth as a body, just like a bell has its own frequencies. The excitation mechanism does not matter much in this problem, it will simply input power in some modes and not in others. The first normal modes of oscillation of the Earth were detected after the Great Chilean earthquake, on 22 May 1960. With its magnitude of 9.5, it is the most powerful earthquake ever recorded and it has excited large-scale oscillations of the globe [31]. The data here is the exact value of the resonance frequencies. One can then adapt a model of the inner regions of the planet to match these frequencies. It is a second way of inferring

the internal structure of the Earth by using seismic activity.

Seismology has provided an immense amount of information on the structure of our planet. It seemed only natural than one could exploit wave activity in other bodies of the sky to probe their interior as well, leading to several fields of extraterrestrial seismology [32].

In 1969, among other instruments the Apollo 11 mission installed a seismometer on the Moon [33]. NASA still has an interest in future lunar seismology missions, for instance as a part of their Development and Advancement of Lunar Instrumentation (DALI) program.

Seismic studies of other planets started fifty years ago, when the Viking mission (NASA) put the first seismometer on Mars in 1978 [34] and the Venera mission (Soviet Union) put one on Venus in 1982 [35]. Today, the InSight mission (NASA) measures the seismic activity of Mars since 2018 [36]. We only have seismic data on one of our non-neighbors planets: Saturn. Thanks to its rings in resonance with its oscillation modes, the Cassini mission has been able to provide astronomers with the frequencies of a few modes of Saturn [37, 38]. Regarding Jupiter, the light we see reflected by its surface does show oscillation modes [39], but the uncertainties are too great to be used in practice to infer the Jovian inner structure.

I.2 Asteroseismology

The Sun, our closest star, serves as a unique reference in the quest to understanding stellar evolution. Its measured parameters such as radius, mass, luminosity or the surface abundance of each element have become reference units for astronomers. Its proximity allows us to get high precision observations and use it as a laboratory to test physical processes and build a coherent description of stellar structure and evolution. Its study not only provides crucial data and insights on the life cycle of stars, but also offers broader insights for astrophysics as stars are the building blocks of galaxies and hosts of exoplanets. In 1962, a five-minute oscillation was seen perturbing the surface of the Sun [40]. This perturbation was explained a few years later as being a standing acoustic wave [41] leading to the start of *helioseismology*, and *asteroseismology*, the study of waves in stars [42, 43, 44].

But interestingly, the Sun was not the first star we noticed that had a variable luminosity. In fact, hundreds of thousands of stars were classified as *variable stars* at the time of the detection of the 5-minute solar oscillation. Letting the events of novae aside, the first recording of a star with changing luminosity was in 1596. Fabricius saw the brightness of *Mira Ceti* decline over a few months, and decades later it was established that the brightness was periodically changing every 11 months. In the 18th century, it was discovered that the luminosity of δ *Cephei* was also oscillating. After that, with the increasing quality of telescopes and number of astronomers came a systematic classification of variable stars, which demanded explanations. Naturally, among the possible causes standing waves were discussed, and their study finds its roots in the seminal paper of Cowling in 1941¹ [45, 46, 47]. The first textbook on stellar oscillation modes was written by Ledoux and Walraven in 1958 [42], who provided more details on the history of variable stars.

At the time, variability was not yet used for seismology purposes. The main application of the study of variable stars is the discovery of a relation between luminosity and oscillation period of Cepheids, the stars with close similarities with δ *Cephei*. This law was discovered in 1912 by Leavitt [48] and provided a crucially important tool to measure galactic distances. Indeed, it is easy to measure the oscillation period and the brightness received on Earth from the light emitted by a Cepheid. From the luminosity-period law, one deduces how much the brightness decreases when the light travels to the Earth and obtains the distance traveled. Cepheids are thus standard candles, allowing for precise distance measures. They were used by Hubble for two major discoveries: in 1924 he found that the stars in Andromeda are much farther than the ones of the Milky Way, which implies that Andromeda is a second galaxy and not a part of the Milky Way [49]. In 1929, Hubble measured the distances of a set of galaxies and combined the measures with the data of their velocities to obtain the famous Hubble law which shows that the Universe expands [50].

¹Even though investigations of nonradial perturbations were started by Rosseland and Pekeris in previous years.

1.2.i Waves as stellar probes

Since the 70s, stellar oscillations have been studied for seismic purposes, i.e to access the insides of stars. Helioseismology has revolutionized our understanding of the Sun. The detection of standing acoustic waves, or *p*-modes, granted access to the solar interior. These oscillation modes reveal the Sun's internal structure and dynamics, enabling us to infer what they are from seismic data. These methods, known as seismic inversions, allow one to obtain a precise model of the star's interior based on observed oscillation frequencies. For instance, we now know for sure that the Sun is mainly made of two layers, the radiative zone in the inner 70% of the radius, and a convective zone in the outer 30%, and rotates around itself. Inversions have been particularly effective at probing the location of the interface between the radiative and convective zones, the rotation profile throughout the solar interior [51], the helium abundance in the convective envelope and the efficiency of chemical diffusion [52]. All of this was possible because the exact frequencies of acoustic modes depend on all these features of the solar structure and dynamics.

Thanks to the high precision data from space telescopes and ground based networks, the development of inversion methods has revealed most of the Sun's internal structure (outer 90 % of the total radius) and rotation profile (outer 80 %) (see the detailed review by [53]). Many of the aspects of the interior of the Sun are thus constrained, and consensual models like *model S* [54] or any other Standard Solar Model [53] can be compared to the results of these inversion methods to reveal its shortcomings.

Recently, inertial and Rossby waves, driven by solar rotation, have provided new insights into superadiabaticity and turbulent viscosity in the deep convection zone [55] and on the Sun's latitudinal differential rotation [56]. Nevertheless, these modes are confined to the convective envelope, leaving the core inaccessible to current helioseismology.

To date, constraints on the solar core solely come from neutrinos, which have recently revealed the Carbon-Nitrogen-Oxygen cycle and provided insights into stellar metallicity and energy production [57]. The key target of helioseismologists has then been the detection of solar internal gravity waves, or *g*-modes, which are buoyancy-driven waves in the Sun's interior. Despite decades of study [58, 59], *g*-modes remain undetected in the Sun. While some claims of detection exist [60, 61], none are confirmed [62, 63]. Their detection is difficult due to their small surface evanescent amplitude and overlap with solar granulation noise [64], and seems out of reach of current instruments and techniques.

Helioseismology has been incredibly successful at shedding light on the Sun's interior, which triggered the systematic search of waves in other stars. Today, variable stars are classified according to their pulsations characteristics [65]. A star can be a Slowly Pulsating B star (SPB), a ZZ Ceti, a delta Scuti (δ Sct), a Cepheid (β or δ Cep), an RR Lyrae (RR Lyr), or a gamma Doradus (γ Dor). It can be solar-like, a Red Giant or a White Dwarf. All these classes gather similar stars with similar pulsations characteristics, determined mainly by the mass and the age of the star, as shown on Figure I.4. These classes differ by the types of modes appearing: we can see *p*-modes, *g*-modes or *r*-modes depending on whether compressibility, buoyancy or rotation dominates in the uppermost layer of the star. The pulsation class also characterizes the main excitation mechanism of the waves, be it stochastically driven by a convective motion [58, 66] or by a mechanism involving the opacity [67, 68]. These are the two main driving mechanisms of waves in stars. The former is a by-product of turbulent convective motion, stochastically compressing the stellar fluid and imposing shear against the stably stratified zone next to it, thus generating acoustic waves and buoyancy waves. The latter is known as the κ -mechanism as κ is the notation for the opacity of the fluid, and the process is the following: at the particular region where the temperature is close to the temperature of ionization, a small compression will adiabatically heat the fluid, which will further ionize. This will significantly increase its opacity, blocking some of the radiative flow which will further heat the fluid. Therefore, a compression releases heat: it is a heat engine. The perturbations are thus able to draw energy from the medium through this mechanism, which drives waves who take the energy away.

Through this extensive classification and study of the pulsations of our neighbors, asteroseismology has been able to measure with unparalleled precision masses, radii, ages, and rotation rates of

hundreds of stars around us in the Milky Way. To this day, no other approach is able to match its precision. This is a leap forward in the understanding of formation and life cycle of stars. But the work is not over, even on the single case of the Sun. A global understanding of angular momentum transport and mixing of elements is yet to be achieved, as it requires observational constraints for the innermost 10-20% of the Sun's radial layers [69, 70]. Unfortunately, the core of the Sun remains beyond reach. The main reason for that is that the non-radial acoustic modes used for inversion are refracted before reaching the core, where their horizontal wavelength becomes infinitesimally small, keeping them out of the innermost core region.

For similar reasons, the evolution, structure and amplitude of the solar magnetic field is almost totally unconstrained, even though we know it must exist and reach approximately 1 G in its intermediate layers [71]. It may be a lot larger in the core. This value seems low, as a recent survey shows that stars are born with magnetic fields of around 10^4 G [72]. They should thus dissipate it, and it's unclear how and where the magnetic energy goes. In the later stages of the lifetime of a low mass star, it becomes a Red Giant. Recently, asteroseismology has been able to measure magnetic fields of 10^4 - 10^5 G in their cores by using perturbations of dipoles modes [73]. Complementarily, it has been suggested that the surprising absence of these dipole modes in other Red Giants could be explained by even stronger core magnetic fields, of about 10^5 - 10^7 G [74, 75]. This seismic technique was also applied to a main-sequence SPB star which suggests a similarly strong core magnetic field of 5×10^5 G [76]. Therefore, it seems that stellar magnetic fields are very diverse and change a lot during the lifetime of the stars. A precise characterization of the magnetic field of the Sun would provide a crucial reference point for the advancement towards a theory of stellar magnetic fields.

Questions are also still open regarding the solar cycle, its circulation currents, and the properties of its convective zone, and their possible interactions. These phenomena determine the repartition of energy in the star, causing the turbulent motion on the solar surface and solar storms which directly affect life on Earth and determine the possibility of life on other planets. Therefore, a comprehensive picture of solar weather is needed to predict stellar storms in other stellar systems, an especially relevant parameter for the search of life on exoplanets. Convection, and its efficiency at penetrating the radiative zone [77], may also explain a mixing and a burning of certain elements [78] and the excitation of bursts of gravity waves [79]. All these unknown features of the Sun will be probed in the future by seismology.

The study of normal modes is also pursued in neutron stars and black holes, as they can provide data on physics which cannot be accessed in laboratories. Indeed, the oscillations of a neutron star highly depend on the equation of state of the fluid it is made of. Establishing the equation of state of a neutron star would provide important insight in the phase transitions occurring at extreme densities of matter where general relativity, quantum chromodynamics, superconductivity and superfluidity all come into play [80, 81, 82]. Oscillations of neutron stars are thus a gold mine of data for fundamental physics, as their exact frequencies will be signatures of these phenomena. Similarly, the frequencies of normal modes of black holes are now data measured by gravitational waves detectors. These modes are excited by merger and compose the gravitational waves signal. They are investigated today as they could bear information on quantum gravity physics, should their frequencies deviate from the predictions of pure general relativity [83, 84, 85, 86].

I.2.ii Waves as stellar active processes

Asteroseismology is the use of waves for probing purposes. In this case, these propagative perturbations in the fluid are seen as such: probes, motions which are small and only capable of obeying the large-scale structure and flows. While there is indeed an immense difference in the amount of energy put in the waves compared to the total energy of the large-scale structure of the star², this does not mean that the behavior of waves does not affect the star. And in that sense, waves are not just probes but *active dynamical processes of the star's evolution*.

Research on such processes of feedback of the waves is not asteroseismology in the proper sense. The

²The variations of light curves show oscillations of a few 10^1 mmag in magnitude, yielding the rough estimate $E_{\text{waves}}/E_{\text{star}} \sim \Delta I/I_{\text{star}} \sim 10^{-2}$.

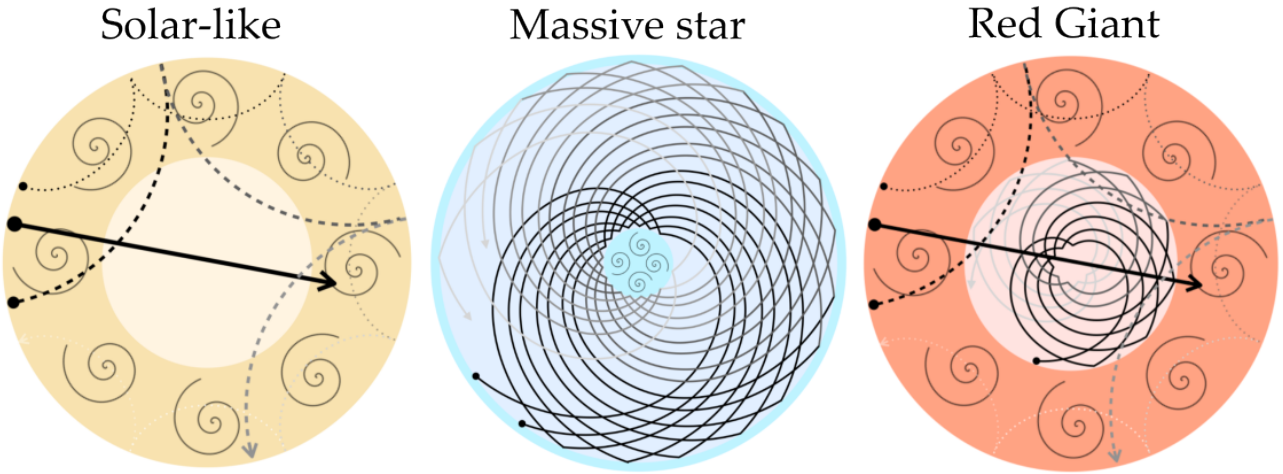


Figure I.4: Internal structures of stars are very diverse, affecting the propagation of waves, especially selecting which waves reach the surface and make its brightness vary (by about 1%)¹. The convective zone (swirls) may be outside or inside, depending on the star's mass. Dashed curves are acoustic waves, solid curves are internal gravity waves.

¹Courtesy of Lisa Bugnet, from [87].

questions tackled are rather along the lines of: where does the energy put in the waves come from? Does it empty a specific energy reservoir? How and where do the waves deposit their energy? As they propagate, do they transport more than just energy? Can they redistribute angular momentum? Can they carry chemical elements and help the mixing in non-convective regions, where stratification prevents vertical mixing? These questions are conceptually very different from those asked by asteroseismology, as the point here is not to observe the wave on the surface anymore, but understand its dynamical role in the star.

The main property of a wave is its ability to propagate, making it a prime candidate for transporting a variety of physical and chemical quantities. As stated in I.2.i, important questions regarding the rotation of stars remain open, and it has been suggested that internal gravity waves may affect their rotations by transporting angular momentum [88, 89]. When excited by turbulent plumes at the top of the radiative zone and propagating downwards, internal gravity waves may deposit their angular momentum and slow the rotation of the core, as it is required to explain the observed rotation rate of the core of subgiant stars [69, 90]. This is one possible mechanism involved in the long-sought global theory of angular momentum transport in stars.

A second important quantity transported by internal gravity waves is thermal energy. This transport by internal waves has been especially studied in massive stars ($M \sim 5M_{\odot}$), where the convective zone is in the core. The waves are then excited from the core to the surface. High-resolution simulations have shown that they dissipate close to the surface, and therefore deposit energy responsible for an additional heating [91, 92], further confirmed by [93]. Should it last, a wave-induced local heating is bound to contribute to the evolution of the star, by possibly shortening its lifespan. For instance in another context, local heating due to damping of internal gravity waves have been shown to generate a local convection zone in Red Giants during helium flashes [94].

Waves in stars are linear, i.e they have sufficiently low amplitudes such that their governing equations are linear in the perturbed fields. And linear waves are not efficient to transport chemicals elements in stars [95]. Transport of elements by waves is much more efficient when they are non-linear, as they may interact or break. The breaking of internal wave have been studied as a possible mechanism for mixing of elements in the ocean [96], and is still an active field of research in oceanography and atmospheric science. The fact is that waves in stars are *very* linear, and require particularly strong excitation mechanisms to reach amplitudes where they may break, and possibly mix elements inside the stably stratified regions in the star [9, 59, 97]. Tidal forces exciting such strong trains of

internal gravity waves which could later break have been investigated for the possibility of distributing angular momentum close to the core [98, 99].

Nonlinearity is famous for making analytical traction more difficult. Another interesting mathematical difficulty arising in physically relevant wave problems is the case of *attractors*, which have been shown to appear in inertial waves propagating in rotating shells [100, 101]. Attractors are singular solutions of the wave problem confined to a razor-thin width, existing due to the hyperbolic character of linear incompressible inviscid inertial wave equations. These solutions are regularized to a non-zero width when introducing viscosity ν , but have the striking property of having a constant dissipation rate when taking the inviscid limit $\nu \rightarrow 0$ [102]. This result suggested a possible very localized deposition of energy by the attractor, even when viscosity is asymptotically low which is the case in stellar interiors and atmospheres, leading to further numerical investigation [103, 104, 105]. However, the importance of this phenomenon compared to other stellar internal processes is still to be determined.

I.2.iii Observations

Long gone are the days of naked-eye observation of variable stars. The synergy of theory and observations of stellar oscillations lead to great advances over the last few decades, and we are now at a state where the open questions concern vibrations undetectable without instruments. The trained eye can discern variations of a star's brightness of 0.1 mag; current instruments have a μ mag precision [106]. The causes of 0.1 mag variations are now common knowledge, and the objects of current research are orders of magnitude fainter. Furthermore, complementary observational data is obtained by spectroscopy, the study of the wavelengths composing the light emitted by the star's surface.

The *photometric* approach measures the intensity of the light coming from the star, with sufficient precision so as to see its variations. The surface of a star changes its luminosity if there are changes of temperature, it is thus a thermodynamic signature of the wave. The data obtained is a light-curve $I(t)$, as the one shown on Figure I.5 (top right). The *spectroscopic* approach decomposes the light coming from the star with a spectrometer to obtain a time-dependent spectrum $I_\lambda(\lambda, t)$. If the surface vibrates with some radial velocity, the Doppler effect makes the position of the peaks in I_λ oscillate. It is thus a kinematic signature of the wave. Because of this fundamental difference between the photometric and the spectroscopic measures, the noise in the data is different. The spectroscopic observations are less noisy, making higher signal-to-noise ratio and leading to detections of more modes [107]. However, as spectroscopy decomposes the light into its components, more light is needed for this technique, i.e. bigger telescopes. This mostly prevents this approach for space-based instruments, which have other advantages. This explains why most space telescopes with asteroseismic purposes have photometric instruments, and most ground-based instruments for asteroseismic purposes are spectrometers.

Most stars have a variability of the order of the minute, or the hour. Theoretically, this means that a few hours of exposition is enough to capture a few oscillations and measure frequencies. However, actually using these frequencies as seismic constraints demands a precise determination which requires months-long datasets³. Several independent observations can be patched together into a long dataset, but the patching introduces defaults into the Fourier transform of the signal, limiting the accuracy of this technique. The only way to obtain useful precise datasets is to have continuous, long observations. Regardless of looking at the Sun or other stars, the day-night cycle is an obstruction, as is the weather, and scheduling. There are two solutions: either a network of ground-based observatories, coordinated to form an uninterrupted observation, or space-based instruments on board of satellites. Both solutions are implemented, for helioseismology and for asteroseismology missions. But a third solution takes advantage of the 6-month-long nights occurring at the poles in winter, providing uninterrupted exposure as well. This is a recent proposal by the SIAMOIS project [108].

Helioseismology observations are mostly made by two ground-based networks of solar observatories, and two satellites. The Birmingham Solar Oscillations Network (BiSON) is made of 6 obser-

³The Sun rotates approx. once every 24 days. Its rotation can only be deduced by observing waves for at least one rotation, i.e one month.

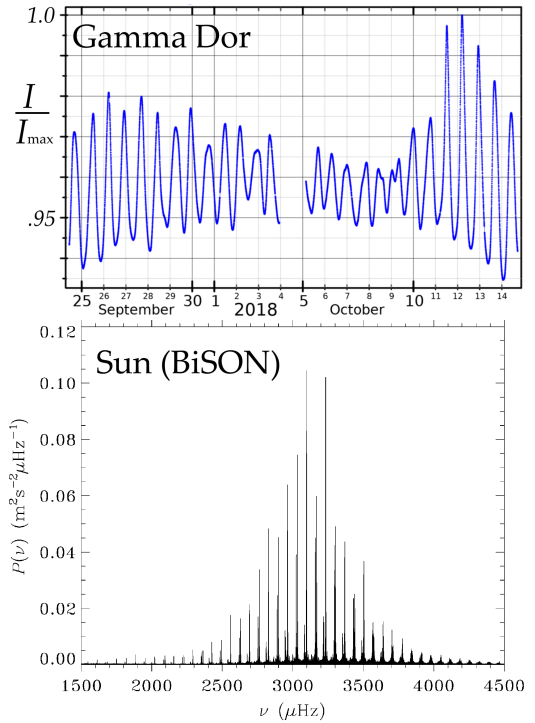
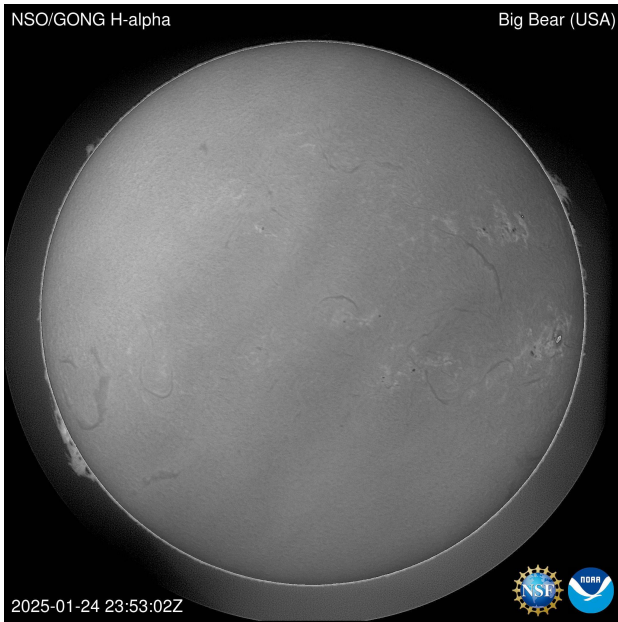


Figure I.5: **Left:** a picture of Sun from the Big Bear Lake Solar Observatory, Jan 2025. Eruptions can be seen, but waves are not visible without data treatment¹. **Top right:** The brightness of Gamma Doradus. This light curve is an observation by the space telescope TESS in 2018². **Bottom right:** power spectrum of the Doppler velocity data over the whole solar disc.³

¹Credits: GONG [109] (<https://gong.nso.edu/>). ²Adapted from the Gamma_Doradus_variable page of Wikipedia.

³Credits: BiSON [110].

vatories across the globe, performing spectroscopic observations and providing acoustic modes data [110]. The Global Oscillation Network Group (GONG) is also made of 6 solar observatories performing spectroscopic measures, providing acoustic modes data and magnetograms of the solar surface [109]. The first satellite was the Solar and Heliospheric Observatory (SoHO) (ESA/NASA), launched in 1995 with three missions: space weather and solar wind, for which it has two instruments; solar chromosphere and corona (6 instruments); and helioseismology with 3 instruments. These instruments are GOLF [111], MDI [112] and VIRGO [113]. The first two are spectrometers, and VIRGO is photometric; this has the immense advantage of comparing the two approaches in identical conditions. The second satellite was the successor of SoHO, named Solar Dynamics Observatory (SDO) (NASA) and was launched in 2010 with the mission of studying the solar magnetic field and solar winds. The only instruments serving for helioseismology purposes is HMI, the more efficient version of MDI (which has since stopped operating). SDO provided stunning images and videos of the activity of the Sun⁴.

Asteroseismology observations are mostly provided by space telescopes onboard satellites. This means that most data is photometric. One project of a ground-based network of 8 observatories is currently under development, the Stellar Oscillation Network Group (SONG) [114]. They will be equipped with photometers for high-precision asteroseismic measures of a few select stars. An additional mission is to detect exoplanets around these stars. Until now, asteroseismic observations have been performed by 6 space telescopes. In chronological order of launch, they are WIRE (NASA, 1999), MOST (Canada, 2003), CoRoT (ESA, 2006), Kepler (NASA, 2009), BRITE (Canada-Austria-Poland, 2013), and TESS (NASA, 2018). Depending on their instruments, some are focused on cool dwarfs and sub-giants, while others observe every kind of stars. A new spacecraft is under development: PLATO, currently in its late stages of development by ESA. It is planned for launch in 2026, with a main mission of exoplanets detection. It will focus on solar-like stars, sub giants and red dwarfs,

⁴https://en.wikipedia.org/wiki/Solar_Dynamics_Observatory

looking for rocky exoplanets in the vicinity of one million stars. Asteroseismology is its secondary mission.

CoRoT [115] and *Kepler* [116] brought asteroseismology to a new level, by providing a catalogue of data on thousands of stars. The amount of data generated by PLATO will be a similar leap.

For any other star than the Sun, the surface is not resolved, meaning that telescopes and instruments cannot distinguish its spatial extension. The light curve $I(t)$ is the total contribution of light emitted by the solar disc, averaged by the reduction into a single point in the sky. Unfortunately for asteroseismology, this means that oscillations modes with a fine horizontal structure will contribute to zero in this averaged light curve. All of the information about modes with more than ~ 2 or 3 node line at the surface will be excluded and cannot reach us, and only the modes with the longest horizontal wavelengths will be detectable. For the Sun however, its proximity lets us see the whole disc, and one can obtain the intensity of the light for every point of the surface. This means that a lot more modes are detectable. These difficulties of mode visibility on distant stars are equally present in spectroscopic measurements.

I.3 How to study waves?

The amount of manpower and investments put in the instruments and networks listed above proves that the study of waves is astronomers' best way into stellar interiors. In order to be able to interpret the data, we need a theoretical understanding of wave propagation, providing definitions, predictions, and signatures of these vibrations. Waves being a fundamental concept in physics and all its domains, textbooks and careers have been devoted to their study. This section provides an overview of the various ways waves in astrophysical and geophysical fluids manifest and are usually studied. Waves in stellar interiors are in the linear regime, due to the huge amount of energy of the equilibrium state. This section and the rest of this thesis is thus restricted to linear waves; no blast wave, shock wave or soliton shall be considered.

Let us start with the prototypal example of waves: the acoustic wave. In an homogeneous compressible fluid in its rest frame, small adiabatic perturbations in velocity, pressure and density satisfy

$$\partial_t \mathbf{v}' = -\frac{1}{\rho_0} \nabla p', \quad (\text{I.1})$$

$$\partial_t \rho' = -\rho_0 \nabla \cdot \mathbf{v}', \quad (\text{I.2})$$

$$p' = c_s^2 \rho', \quad (\text{I.3})$$

where $c_s^2 \equiv \Gamma_1 \left(\frac{\partial P}{\partial \rho} \right)_S$ is given by the equation of state of the fluid. \mathbf{v}' , p' and ρ' are the Eulerian perturbations of velocity, pressure and density, and the equations are the linearized conservation of momentum, mass and entropy. This third equation is thermodynamical and represents the fact that the oscillation do not exchange energy with the medium. It is instantaneous as it involves no time-derivative, and we interpret that p' and ρ' are redundant variables in the dynamical evolution. We use it to remove ρ' from the second equation and obtain the 2×2 system

$$\partial_t \mathbf{v}' = -\frac{1}{\rho_0} \nabla p', \quad (\text{I.4})$$

$$\partial_t p' = -c_s^2 \rho_0 \nabla \cdot \mathbf{v}'. \quad (\text{I.5})$$

This system entirely governs the evolution of acoustic waves. Removing \mathbf{v}' reduces the system to the famous D'Alembert equation

$$(\partial_{tt} - c_s^2 \Delta) p' = 0, \quad (\text{I.6})$$

whose solutions show the propagation of the pressure disturbances. Indeed, the formal solutions of D'Alembert in 1D are $p' = f(x - c_s t) + g(x + c_s t)$: the two patterns $f(x)$ and $g(x)$ propagate through space as time evolves to the right and to the left respectively, with velocity c_s . The velocity of propagation is an interesting quantity, as it depends on the temperature and the composition of

the fluid. Therefore, measuring c_s by analyzing the time needed by waves to travel is a way to infer composition and temperature. This is the essence of *tomography*, particularly used in oceanography to map the temperature and salinity of the oceans [16] (see Fig. I.2). The measure is the time taken by an acoustic wave between an emitter and a receiver. This technique is implemented in oceans where we have access; it is obviously impossible to use it in asteroseismology as we have no way of having local emitters nor local receivers on stars, even the Sun. However, other techniques relying on the propagation of acoustic waves have been developed for the Sun, together they form the field of *local helioseismology* [117, 118].

But the main point about waves in stars is looking for standing waves. Standing waves are particular solutions of the wave equation where the perturbation is separated in its time and space dependencies. For instance, for Equation (I.6), they are the solutions of the form $p'(t, \mathbf{x}) = a(t)b(\mathbf{x})$. For linear waves, $a(t)$ can only be a harmonic function $a(t) = \cos(\omega t + \phi)$, such that standing acoustic waves are the solutions of

$$\Delta b + \frac{\omega^2}{c_s^2} b = 0. \quad (\text{I.7})$$

This equation must be provided with boundary conditions on b . Indeed, standing waves do not propagate: a perturbation $p'(t, \mathbf{x}) = \cos(\omega t)b(\mathbf{x})$ is a global oscillation in every part of the fluid simultaneously, each part simply oscillating as $\cos(\omega t)$. It is global and thus involves the perturbations at the boundaries and depend on what they are. Equation (I.7) is known as a Helmholtz equation. Along with boundary conditions, it provides the set of normal modes of oscillation of the body considered. Normal modes, global oscillations and standing waves are synonyms. This set is discrete, and each of this mode has its own frequency ω called eigenfrequency. The set of eigenfrequencies of a star is the central tool of asteroseismology, as it is highly dependent on its structure. In this simple example above, the eigenfrequencies are only given by c_s and by the geometry of the cavity where the fluid wave is placed. But in a star where every quantity is inhomogeneous, the standing wave equation involves the profile $c_s(r)$, the pressure gradient $\frac{dP_0}{dr}$, the rotation rate $\Omega(r, \theta)$ and any other quantity to which the waves are sensitive. All those quantities have an influence on the solutions $b(\mathbf{x})$ and thus on the frequencies of the normal modes. This is the essence of the approach of asteroseismology.

Looking at waves as propagating perturbations in a body or as normal modes of oscillations of the body is fundamentally different, and leads to very distinct mathematical characterizations, numerical studies and observational techniques. In this thesis, as the majority of the helio and asteroseismic communities, I focused on the study of normal modes.

Before discussing waves in inhomogeneous fluids, I wish to define two fundamental quantities of the waves obtained in a local viewpoint, i.e in a small spatial region of the fluid small enough to approximate that it is homogeneous. Taking Equations (I.4)-(I.5) in 1D and performing Fourier transforms such that $p'(t, x) = p'e^{i(\omega t - kx)}$, the system becomes

$$\omega \begin{pmatrix} v'_x \\ p' \end{pmatrix} = \begin{pmatrix} 0 & \frac{1}{\rho_0} k \\ c_s^2 \rho_0 k & 0 \end{pmatrix} \begin{pmatrix} v'_x \\ p' \end{pmatrix}. \quad (\text{I.8})$$

This form of equation involving a matrix is generic, as the waves are linear. The matrix yields all the essential information of wave propagation, by its eigenvalues and its eigenvectors.

Indeed, the eigenvalues relate ω to k : it is the *dispersion relation* of the waves. In this example, one obtains

$$\omega = \pm c_s |k|. \quad (\text{I.9})$$

There are two solutions because it is a 2×2 matrix, as two fields are involved, velocity and pressure. This is clearly generic: there are as many dispersion relations as there are perturbed fields (after removing the instantaneous equations). In this manuscript, this number will often be called the number of *wavebands* in the system, as it is the number of curves $\omega(k)$ when tracing all the eigenvalues in a $\omega - k$ diagram. This term of *wavebands* comes from condensed matter physics, where an electrically isolating material has a valence band and a conductive band of electrons, determined by the eigenvalues of the Hamiltonian [119, 120]. The Schrödinger equation in condensed matter physics is

the analogue of Equation (I.8), where the unknown is the presence probability density wavefunction. The concepts from condensed matter physics slightly colors the language used in this thesis. Complementary information is found by analyzing the eigenvectors. Each waveband has its eigenvector. The eigenvector of the chosen waveband relates the amplitudes p' and v'_x . For instance, the band $\omega = +c_s k$ is the band of right-propagating waves which has the eigenvector

$$\begin{pmatrix} v'_x \\ p' \end{pmatrix} = A \begin{pmatrix} 1 \\ c_s \rho_0 \end{pmatrix}, \quad (\text{I.10})$$

where A can be any non-zero complex number (with the appropriate dimension). At this point, A has no physical meaning as the waves are linear; they can have any amplitude with no repercussion on the dynamics. The eigenvector provides the information on the *relative* amplitude and phase of p' and v'_x . Indeed, one has

$$p'/v'_x = c_s \rho_0. \quad (\text{I.11})$$

$c_s \rho$ is then the relation between the amplitudes, and the fields $p'(t, x)$ and $v'_x(t, x)$ are always in phase because it is a real number. For right-propagating waves, pressure maxima are positive maxima of the velocity v_x .

This information on the relations between the several perturbed fields is the *polarization* of the wave. This information is given by the eigenvectors of the matrix in the dynamical equation. Many results of this thesis are the consequences of the role of polarizations on the waves in inhomogeneous media.

I.3.i Analytical approaches

Analytical derivations have managed to provide approximate expressions of the frequencies of oscillations of stars [42, 43, 44]. These expressions give a physical understanding of the determination of the positions of the modes in the star and as well as their frequencies, in the form of quantitative relations. These relations allowed for the easy formulation of *inverse problems*: how to quantitatively determine the features of the star, from the set of oscillation frequencies measured by telescopes ? Here is recalled the main analytical approach used in asteroseismology, its approximations and the principal laws it yields. Many steps of calculations and details are skipped, as the aim is rather to highlight the most well-known route in order to clearly put this thesis in perspective with it afterwards. A complete and almost exhaustive course on the theory of asteroseismology is found in the lecture notes of J. Christensen-Dalsgaard [121].

Before studying the linear perturbations of a star, one needs to describe the equilibrium state to be perturbed. For simplicity, consider a non-rotating, non-magnetic star, which is a self-gravitating fluid. It is free of any external influence like accretion or tides, its normal modes are therefore its *free oscillations*. The background state is the solution to

$$\mathbf{0} = -\nabla P_0 - \rho_0 \nabla \Phi_0, \quad (\text{I.12})$$

$$\Delta \Phi_0 = 4\pi G \rho_0, \quad (\text{I.13})$$

$$\nabla \cdot \mathbf{F}_0 = \rho_0 \epsilon_0. \quad (\text{I.14})$$

The first equation is the hydrostatic equilibrium, the second is the gravitational Laplace equation. The third equation is the conservation of energy: \mathbf{F}_0 is the energy flux, and ϵ_0 is a source of energy mostly due to nuclear reactions. These occur in the core so that ϵ_0 is negligible in most layers. One needs to describe the transport of this energy through these layers up to the surface where it is radiated away. In radiative zones, this flux is dominated by radiation where photons have very short free paths, and the *diffusion approximation* is appropriate, where $\mathbf{F}_0 = -\frac{16\sigma T_0^3}{3\kappa\rho_0} \nabla T_0$ (σ is Stefan-Boltzmann constant, κ is the opacity). The system of equations is closed by adding an equation of state $f(P, \rho, T) = 0$ relating P_0, T_0, ρ_0 . In convective regions, the transport is dominated by convective motions; the energy flux is difficult to write down and is usually modeled by Mixing Length Theory (MLT) [122]. The microphysics of the stellar fluid are crucially important as they determine the opacity κ and the EOS $f = 0$, through the mean molecular weight, the ionization fraction, phase transitions, etc.

A simple way of bypassing the difficulties of thermal transport and equation of state is to postulate a simple relation between P_0 and ρ_0 in the form of a power law: $P_0 = K \rho_0^\gamma$. These models are called

polytropic, and the value of γ represents a particular model: $\gamma = 0$ is an incompressible medium, $\gamma = 1$ is an isothermal one, $\gamma = 3$ is a good model of a radiative zone, $\gamma = 4/3$ models an ultra-relativistic White Dwarf. A choice of γ is a choice of structure. It is in no way related to the adiabatic exponent $\Gamma_1 = (\frac{\partial \ln P}{\partial \ln \rho})_S$.

Many good numerical codes solve these equations with tabulated values of κ and EOS to provide accurate models of stellar equilibria. The most well-known is MESA [123], which actually solves the evolution of the equilibrium during the life of the star. From now on, I will consider that the equilibrium state is given, and that it is spherically symmetric as the star is non-rotating and non-magnetic such that nothing can break this symmetry.

Linear perturbations of the resting state of a star follow

$$\partial_t \mathbf{v}' = -\frac{1}{\rho_0} \nabla P' + \frac{\rho'}{\rho_0^2} \nabla P_0 - \nabla \Phi', \quad (\text{I.15})$$

$$\partial_t \rho' + \rho_0 \nabla \cdot \mathbf{v}' + v'_r \frac{d\rho_0}{dr} = 0, \quad (\text{I.16})$$

$$\Delta \Phi' = 4\pi G \rho'. \quad (\text{I.17})$$

The viscosity term is omitted as it is negligible, the main dissipation term for waves in stars being thermal diffusivity and turbulent dissipation. This system needs to be closed by an energy equation representing the energy transfer between the perturbation and the background. These transfers are very small in most regions of the star; indeed, the thermal diffusivity time is $\tau_{KH} = \frac{GM^2}{R}/L \sim 10^7$ years, while the oscillations periods are of the minute or hour (Section I.2). It is thus a very good approximation to assume that the waves keep their energy: the perturbations are adiabatic transforms. A Lagrangian perturbation of pressure δP and density $\delta \rho$ has $\delta P = \Gamma_1 \frac{P_0}{\rho_0} \delta \rho = c_s^2 \delta \rho$, as a fluid Lagrangian particle has constant entropy under adiabatic transforms. In Eulerian form, this equation reads

$$\partial_t P' + v'_r \frac{dP_0}{dr} = c_s^2 (\partial_t \rho' + v'_r \frac{d\rho_0}{dr}). \quad (\text{I.18})$$

Equations (I.15)-(I.18) govern all perturbations of the star. Equation (I.17) is often an obstacle to analytical traction, as it is a non-local interaction. Fortunately, it has been noted that it is often very reasonable to neglect Φ' , i.e assuming that the perturbation is not self-gravitating. This is the *Cowling approximation* [47], which holds true as soon as the mode has a few nodes in the radial or the angular direction [124, 125]. This approximation is used throughout this thesis.

Investigating standing waves amounts to looking for solutions of the form $\rho'(r, \theta, \phi, t) \propto \cos(\omega t)$ and find which values of ω make it possible to have a solution. It is particularly convenient to generalize the solution to its complex form with $\rho' = \text{Re}(e^{i\omega t} \underline{\rho}'(r, \theta, \phi))$. Furthermore, as none of the background quantities depend on the angles, one can always separate the perturbations as $\underline{\rho}'(r, \theta, \phi) = \underline{\rho}' Y_\ell^m(\theta, \phi)$ where Y_ℓ^m is a spherical harmonic. In other words, the radial and horizontal are separable, and the horizontal direction is easily dealt with as there is not background horizontal gradient. The real perturbation is thus of the form $\rho' \propto \text{Re}(\underline{\rho}'(r)) P_\ell^m(\theta) \cos(\omega t - m\phi)$: the radial and co-latitudinal dependencies are given by $\rho'(r)$ and the Legendre polynomial P_ℓ^m , the perturbation pattern being standing in these two directions. The pattern however travels in the ϕ direction. In the following, symbols distinguishing real from complex perturbations are not underlined.

In order to obtain analytical constraints on the frequencies ω , a sensible strategy is to de-couple Equations (I.15),(I.16),(I.18) into a single ODE of high order on a single perturbed field. This technique is motivated by the fact that many ODEs have been studied extensively and for which solutions are well known. For this aim, one removes ρ' , v'_r and v'_ϕ from the equations and obtains

$$\frac{dv'_r}{dr} + \left(\frac{2}{r} - \frac{1}{\Gamma_1 H_P} \right) v'_r = \frac{i\omega}{\rho_0 c_s^2} \left(\frac{L_\ell^2}{\omega^2} - 1 \right) P', \quad (\text{I.19})$$

$$\frac{dP'}{dr} + \frac{1}{\Gamma_1 H_P} P' = \frac{\rho_0}{i\omega} (\omega^2 - N^2) v'_r. \quad (\text{I.20})$$

We defined the pressure scale height $H_P \equiv -1/\frac{d \ln P_0}{dr}$, the Lamb frequency squared $L_\ell^2 \equiv c_s^2 \ell(\ell+1)/r^2$ and the Brunt-Väisälä or buoyancy frequency $N^2 \equiv g(\frac{1}{\Gamma_1} \frac{d \ln P_0}{dr} - \frac{d \ln \rho_0}{dr})$. $g = \frac{d \Phi_0}{dr} > 0$ is the local gravity field. L_ℓ/c_s is the horizontal (angular) wavenumber.

Let us assume that the radial wavelengths are short compared to r and H_P so as to remove the associated terms in the left hand sides. One then obtains the desired single ODE

$$\frac{d^2 v'_r}{dr^2} + \frac{1}{c_s^2 \omega^2} (\omega^2 - L_\ell^2) (\omega^2 - N^2) v'_r = 0. \quad (\text{I.21})$$

The form of this final equation allows for an analysis. Indeed, defining $K^2 \equiv \frac{1}{c_s^2 \omega^2} (\omega^2 - L_\ell^2) (\omega^2 - N^2)$, this equation can be seen as an harmonic oscillator $\frac{d^2 v'_r}{dr^2} + K^2 v'_r = 0$ when $K^2 > 0$, and an evanescence equation when $K^2 < 0$. This tells us about the propagativity of waves of various frequencies in the regions of the star. For instance, a wave of frequency ω can only propagate if $\omega > L_\ell$ and $\omega > N$ or if $\omega < L_\ell$ and $\omega < N$. The former is the region where acoustic waves propagate, the latter is the radiative zone where internal gravity waves propagate. The relation between K and ω can be seen as a dispersion relation.

Furthermore, as K^2 is a function of r , Equation (I.21) may rather be seen as a Schrödinger equation of a particle of energy 0 in a potential well $V_\omega(r) \equiv K^2(r)$. This is the equivalent of the Helmholtz equation (I.7) in an inhomogeneous medium. A famous procedure provides an approximated solution for modes varying rapidly in this medium, i.e. when $K \gg \frac{d \ln K}{dr}$. This is a situation where the well V_ω is deep. This is the Jeffreys-Wentzel-Kramers-Brillouin (JWKB) method, which then provides the solution

$$v'_r \sim e^{i \int^r K dr}. \quad (\text{I.22})$$

This method is particularly useful, as it provides the expression of the eigenfunctions of perturbations. It is then straightforward to impose boundary conditions, which are going to constrain the frequencies ω to take discrete values. For instance, demanding that v'_r is 0 at some radii r_0 and r_1 amounts to have $\sin(i \int_{r_0}^{r_1} K dr) = 0$, i.e. $\int_{r_0}^{r_1} K dr = n\pi$. This is a quantization condition providing the eigenfrequencies ω_n .

Special care must be taken at the turning points of the wave, where $K^2 = 0$, as the condition $K \gg \frac{d \ln K}{dr}$ is obviously violated. One must connect the JWKB solution to the evanescent solution on the other side of the turning point. On this other side, the solution is usually an Airy function, and smoothly connecting the two imposes the addition of a reflection phase named a Maslov index [43]. Furthermore, the approximation of having no term in $1/H_P$ is also violated at the turning points. These two effects correct the quantization law.

In any case, this method is extremely powerful, as it provides both the eigenfunction of perturbations and the eigenfrequencies ω_n . This is the basis for famous laws on p -modes and g -modes frequencies. Duvall's law [126] says that frequencies $\nu = \omega/2\pi$ of p -modes are

$$\nu = \left(n + \frac{\ell}{2} + \alpha\right) \Delta\nu, \quad (\text{I.23})$$

$$\text{where } \Delta\nu = \left(2 \int_0^R dr / c_s\right)^{-1}, \quad (\text{I.24})$$

where α is a correction term accounting for Maslov indexes and the effect of H_P .

Tassoul's law⁵ [127, 128] provides the equivalent relation for g -modes, whose periods $P = 2\pi/\omega$ must follow

$$P = \frac{2\pi^2 (n + \frac{1}{2})}{\sqrt{\ell(\ell+1)}} \left(\int_{r_1}^{r_2} \frac{N}{r} dr \right)^{-1}. \quad (\text{I.25})$$

r_1 and r_2 are the bounds of the radiative zone where $N > 0$. This law is relatively unaffected by H_P corrections, as they are mostly important at the surface.

These two laws state that p -modes are approximately uniformly spaced in frequencies, and g -modes are approximately uniformly spaced in periods. In both laws, the integral is a reminiscence of the

⁵This law was actually found the year before by H. Shibahashi from Tokyo University.

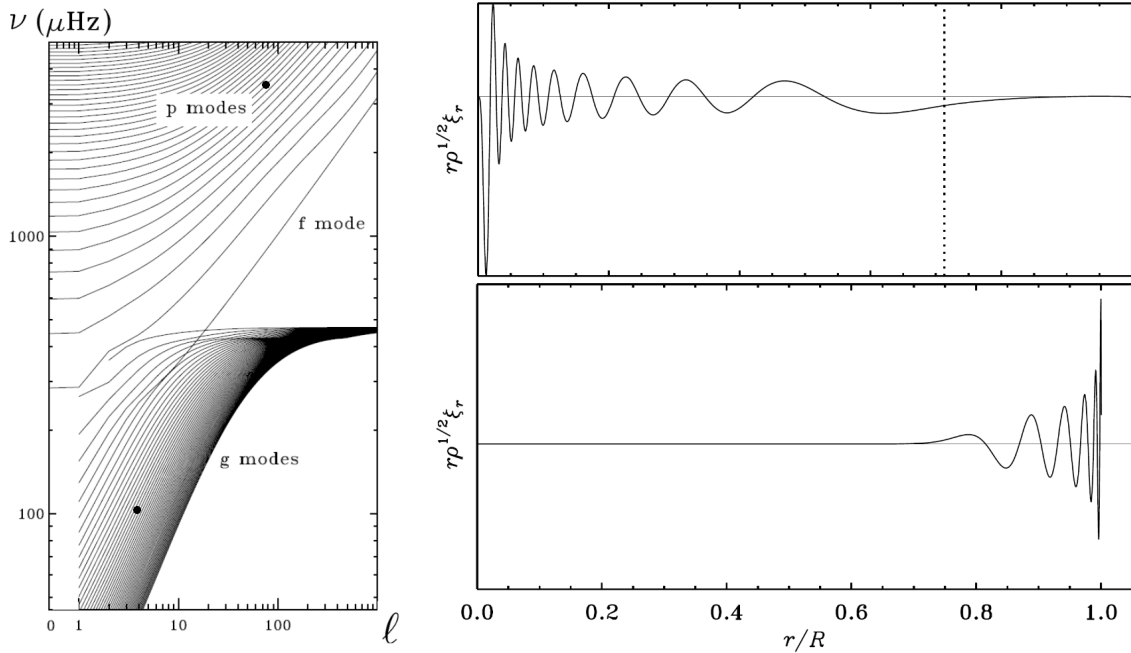


Figure I.6: Numerical calculation of the normal modes of a standard model of the Sun¹. **Left:** Oscillation frequencies of the Sun against harmonic degree, called the dispersion relation of normal modes. **Right:** Perturbations in the star of a *p*-mode and a *g*-mode. Top: *g*-mode of order $n = 19$, degree $\ell = 4$. Bottom: *p*-mode of order $n = 10$, degree $\ell = 60$. $\xi_r = -iv_r/\omega$ is the Lagrangian radial displacement.

¹ Adapted from the textbook [106].

integral of the JWKB solution.

An important limit to this technique is that it intrinsically rests on a high n approximation. Indeed, n being the radial order of the mode, it counts the number of radial nodes of the perturbation, hence short wavelengths are high n modes. It is however applicable to any degree ℓ . In Chapter VII, I will construct an alternative technique which instead provides eigenfrequencies for any n including lowest order modes. This technique rests instead on a high ℓ limit.

It seems however that low order, low degree modes demand a full solution of the oscillation equation. Such solutions can only be reached analytically in idealized models. A classical model is the polytropic atmosphere for which $P_0(z) = K\rho_0(z)^{1+1/m}$, considered to be infinitely deep and under a uniform gravity field g , the top of the atmosphere being at $z = 0$. Solving for the hydrostatic equilibrium yields $\rho_0(z) = \rho(-\frac{z}{H})^m$ and $K = \rho g H / (m + 1)$ where ρ and H are constants. One has $N^2 = (m - \frac{m+1}{\Gamma_1}) \frac{g}{-z}$ and $c_s^2 = \frac{\Gamma_1 g H}{m+1} \frac{-z}{H}$. The background quantities of this model are all power laws, which is why one ends up with a solvable equation for standing waves. Under the Cowling approximation, a wave of the form $v'_r = v'_r(z)e^{i(kx - \omega t)}$ is a solution when

$$\frac{m+1}{\Gamma_1} \left(\frac{\omega^2}{gk} \right)^2 - (2n+m) \left(\frac{\omega^2}{gk} \right) + (m - \frac{m+1}{\Gamma_1}) = 0, \quad (\text{I.26})$$

for n a strictly positive integer [129]. Here, the horizontal wavenumber represents the harmonic degree through $k = \sqrt{\ell(\ell+1)/R}$. There are two solutions: the largest is the frequency of the *p*-mode with radial order n , the smallest is the *g*-mode of order n . This solution was first found by Lamb [29]. A $n = 0$ solution must be added which satisfies $\omega^2 = gk$. This mode is called the *f*-mode for fundamental mode. In this model, all standing waves are found exactly. However, an important ingredient has been removed in this ideal setup: the sphericity of the star. There is also no interface between convective and radiative zones, nor phase transition in the structure.

A second ideal model allows to explore an effect of self-gravity, as it lets one find analytical solutions without using the Cowling approximation. It is the problem of the free oscillations of an incompressible ball of fluid of mass M , at rest under its own gravity. The density is constant for $r < R$ equals to

$\rho_0 = M/\frac{4}{3}\pi R^3$ and zero outside. Solving Poisson's equation yields $g = \frac{GM}{R^3}r$ and the hydrostatic equilibrium gives $P_0(r) = \frac{3GM^2}{8\pi R^4}(1 - (\frac{r}{R})^2)$. Incompressible perturbations (while keeping perturbations of the gravitational potential Φ') are found decomposed on spherical harmonics as $f(r)e^{i\omega t}Y_\ell^m(\theta, \phi)$, and are solutions when

$$\omega^2 = \frac{GM}{R^3} \frac{2\ell(\ell-1)}{2\ell+1}. \quad (\text{I.27})$$

There is only one branch of solutions ($n = 0$) as there is no internal buoyancy which could support g -modes, nor compressibility for p -modes. There is thus only the f -mode which can perturb the incompressible ball. This result was found by Kelvin when he was still Thomson [4]. The interesting difference with the f -mode from the previous model is that here, the frequency is zero for both $\ell = 0$ and $\ell = 1$, while in the polytropic atmosphere it is only $\omega = 0$ for $k = \ell/R = 0$. This means that a dipolar perturbation is not pulled back by any restoring force when accounting for self-gravity. This is the consequence of a symmetry of the problem: the star is isolated in space, and should therefore be able to uniformly travel in any direction through any change of reference frame. This symmetry under a galilean boost imposes that there is no energy difference in having this velocity. Thus, any push of the star will not be pulled back. The dipolar, $n = 0$ mode is exactly this push, which must have $\omega = 0$.

This is the main consequence of the Cowling approximation. This is particularly striking when solving for the normal modes of the Sun with and without this approximation: the $\ell = 1, n = 0$ mode is seen plunging to zero frequency through the whole band of g -modes [130].

The point of analytical methods on the theory of wave is to provide an understanding of their behavior. The goal is to precisely know how the structure of the star and the process in it impact the frequencies and amplitudes of the modes. This understanding is vital to interpret the observational data, as wave identification is sometimes difficult. A recent example occurred 3 years ago when vorticity waves on the surface of the Sun were reported, with an undetermined nature [131].

I.3.ii Numerical approaches

A number of numerical codes can solve the linear problem without the need for idealized models. The harmonic solutions $e^{i\omega t}$ of Equations (I.15)-(I.18) can be computed for any model of stellar interior. At the time of the development of the theory of asteroseismology [43, 44], the low computational performances represented a challenge to obtain accurate codes of linear oscillation modes. Today, the efficiency and accuracy of the available methods make them indispensable. They provide the data shown on Figure I.6, which is the oscillation spectrum and some eigenfunctions of modes of a model of the Sun. Spherically-symmetric models of stars are the numerical data of $P_0(r)$, $\rho_0(r)$, $c_s(r)$, etc, and are called *1D models*. This is what MESA or any 1D stellar evolution code computes. Determining the frequencies of a numerical 1D model is a job for a numerical code, the most widely used being GYRE [132]. It is already interfaced with MESA, such that it is quite easy to produce a model of star and compute its normal modes. This is the starting point to design quantitative inference methods: one can either fit a 1D model until its numerical modes match the frequencies (*seismic inversion*), or simulate different evolutionary histories of the star from its birth until its numerical modes match the frequencies (*forward modeling*). A considerable body of work developing accurate inversion techniques is still being developed [133], notably by investigating the use of deep learning techniques (see for example [134, 135, 136]).

When one has a good understanding of a star and the behavior of the waves in it, numerical codes computing normal modes frequencies are the only way to obtain quantitative estimate and accurate inversions. However, this situation is a late stage of stellar modeling. Indeed, this point is reached when one has a good guess of the internal structure of the star and a good guess of the types of waves detected at its surface.

However, several phenomena are simplified in 1D models, for instance rotation, convection, overshooting, and magnetic fields. The reason is that the first two need a full hydrodynamical simulation, and the third breaks spherical symmetry. Therefore, the interaction with the waves need to be

investigated in the full non-linear problem. With the development of high performance codes and computing clusters, fully compressible hydrodynamical simulations of the interiors of stars have emerged in the last decade. These codes shed a new light on wave-flow interaction and provide experiments on which a global understanding of wave excitation, transport and dissipation can be built. Among these codes are found MUSIC [137, 138, 92], DEDALUS [139, 93] or SLH [140], which can compute the 3D flow with full compressibility and self-gravity, and offer the possibility of stellar MHD simulations.

These simulations allowed in the past for experiments on specific mechanisms first studied theoretically. For instance, a possible explanation for the absence of some dipolar modes in some RGB stars was given by [74] on simple theoretical arguments. The anisotropic structure of a strong magnetic field in the core would disperse any incoming dipole g -mode, and prevent it from going back to the surface and construct a standing wave. A numerical experiment was performed by [75] with DEDALUS which found good agreement of their results with this dispersive mechanism, giving strength to its probable role in RGB stars.

Overall, the numerical approach to the study of waves has two aims: performing quantitative inferences from observational data, and providing controlled realistic experiments to confront theoretical studies. The point of theoretical studies is to give an understanding and intelligible explanations of the behavior of waves. The goal is to provide physical interpretations in order to make educated guesses of stellar interiors. It is these guesses which constitute the starting point of quantitative inversion methods, which can only come later.

The level of precision of current asteroseismic observations is such that the limiting factor in interpretation is the uncertainty on the theory. The theory of waves in stars is the aim of this thesis, whose current frontiers are many. For instance waves in magnetized stars, in highly deformed fast rotating stars, or in relativistic neutron stars are current active fields of research.

Wave topology

Résumé

Les concepts de la topologie des ondes sont introduits dans ce chapitre. Trois objets mathématiques sont définis et présentés, la *phase de Berry*, la *courbure de Berry* et le *nombre de Chern*. Ces objets, utilisés d'abord en matière condensée pour expliquer certains phénomènes de conduction électrique anormale, sont discutés ici dans un contexte d'ondes dans les fluides avec un accent sur les résultats connus en ondes géophysiques. La phase et la courbure de Berry sont des objets géométriques, et le nombre de Chern est un nombre entier de nature topologique. Le principe fondateur de la topologie des ondes est la *correspondance bord-volume*, qui montre que ce nombre topologique oblige l'existence de certaines ondes aux propriétés spéciales dans le fluide étudié. Le chapitre se termine par une revue de ces ondes dites topologiques, qui ont été identifiées et étudiées dans des domaines divers de la physique, historiquement d'abord en matière condensée puis en acoustique, élasticité, physique des plasma, ondes géophysiques, photonique, matière active, chimie et informatique quantique. Cette quantité d'études dans ces domaines d'effets topologiques a eu lieu dans les deux dernières décennies.

The aim of this chapter is to introduce the essential concepts and tools of wave topology. It is presented how the *Berry phase*, the *Berry curvature* and the *Chern number* are quantities naturally arising from the equations governing the evolution of waves in astrophysical and geophysical fluids, even if their role in this context was revealed only recently with the first study in 2017 [141]. It is then shown how these quantities shape the propagation of waves. The cornerstone of wave topology is the *bulk-boundary correspondence*, a principle introduced in the third Section. The fourth and last Section reviews the recent application of wave topology in geophysics, and provides an overview of the fast advances of topology in various disciplines of physics.

The kind of topological physics discussed here was developed in the context of condensed matter physics. The majority of the literature on this topic thus adopts a quantum perspective, with aims directed towards quantized electrical transport. Instead, this Chapter proposes an introduction to topological physics from a fluid dynamicist standpoint.

Some results presented in this chapter have been published in *From ray tracing to waves of topological origin in continuous media*, Venaille, Onuki, Perez, Leclerc, **SciPost Physics** 2023 [142].

II.1 Eigenvalues, eigenvectors and Berry

Let us consider a generic form of time-evolution linear equation

$$i\partial_t \mathbf{X} = \hat{\mathbf{H}}(r, \partial_x) \mathbf{X}, \quad (\text{II.1})$$

where \mathbf{X} is a vector containing real or complex functions. In fluid dynamics, Equation (II.1) would be the system of linearized equations where time derivatives are isolated in the left-hand side, with \mathbf{X} typically containing the values of the fields perturbed by the waves, such as velocity, pressure, density, temperature, ... In quantum physics, Equation (II.1) is the Schrödinger equation, and \mathbf{X} is the wavefunction of the system. In condensed matter, it is the wave function of a particle, which could be a fermion, a boson, a photon. For instance, calculations of the conductivity of a crystal solve

II. Wave topology

for the wavefunction of an electron in a lattice.

Here, r is a parameter which may vary with time t or space x , representing inhomogeneity of the medium in which the wave propagates. It may be a cutoff frequency, a strength of magnetic field, a rotation rate, or any other external quantity relevant for the waves.

Importantly, we shall assume that the operator $\hat{\mathbf{H}}$ governing the dynamics is self-adjoint with respect to a scalar product $\langle \cdot, \cdot \rangle$ for certain boundary conditions, such that $\hat{\mathbf{H}}^\dagger = \hat{\mathbf{H}}$. This important condition restricts the discussion to the realm of Hermitian topology, which concerns the first three Parts of this thesis. Part IV discusses waves in non-Hermitian problems, which behave significantly differently. The form of Equation (II.1) is sufficiently general to describe many different wave problems relevant for astrophysical research. Indeed, it will be shown in the other Chapters that with this equation, one can discuss compressible or incompressible waves, including stratification, rotation, and plane-parallel or spherical geometries in such a form. Non-adiabaticity, diffusion and dissipation do also fit in this form, but break hermiticity of $\hat{\mathbf{H}}$, and shall only be discussed in Part IV.

Let us take as a first approach the simple sub-case of constant r , to try to generalize it to varying r afterwards. As $\hat{\mathbf{H}}$ does not depend explicitly on t and x , one may look for solutions in the form of plane waves $\mathbf{X} \propto e^{i(\omega t - kx)}$. In that case, one has

$$\omega \mathbf{X} = \mathbf{H}(r, k) \mathbf{X}, \quad (\text{II.2})$$

which is simply an eigenvalue equation of a matrix, whose dimensions are given by the number of perturbed fields. Let us label by q this number, which is the dimension of \mathbf{X} and \mathbf{H} is thus a $q \times q$ matrix. This matrix is Hermitian by virtue of the hermiticity of $\hat{\mathbf{H}}$, such that it is diagonalizable with real eigenvalues $\Omega_i(r, k)$ for $i = 1 \dots q$. When choosing a value of i between 1 and q , the label of an eigenvalue which is continuous in the parameter space, we say that we chose a *waveband*. The case of acoustic waves in a 1D homogeneous medium discussed in Section I.3 had $q = 2$, and $\Omega_1 = -c_s |k|$ and $\Omega_2 = +c_s |k|$.

One has then obtained $\omega = \Omega_i(r, k)$, the dispersion relation for each waveband, and may for instance study the influence of r on the frequencies of the waves. Furthermore, each eigenvalue comes with its eigenvector $\mathbf{X}_i(r, k)$. As introduced in Section I.3, $\mathbf{X} = \mathbf{X}_i(r, k)$ are the polarization relations of the waveband i .

From these results, one can calculate $\Omega_i(r, k)$ and $\mathbf{X}_i(r, k)$ for all r and k , and map the parameter space with all the values. Now, what happens to a wave $\mathbf{X}(x, t)$ when r is *not* constant, and varies with time? Specifically when r varies more slowly than the period of the wave?

In the static case, with $r = r(0) = r(t)$, a wave of the waveband i with wavenumber k evolves with time as

$$\mathbf{X}(x, t = 0) = \mathbf{X}_i(r, k) e^{-ikx} \xrightarrow{t} \mathbf{X}(x, t) = \mathbf{X}_i(r, k) e^{-ikx + i\Omega_i(r, k)t}. \quad (\text{II.3})$$

Expectedly, it starts from being polarized as $\mathbf{X}_i(r, k)$, and ends at being polarized as $\mathbf{X}_i(r, k)$, with a total phase given by the time evolution $\Omega_i(r, k)t$, sometimes called the dynamical phase.

Then, if instead r evolves slowly from r_0 to r_1 during the propagation, an intuitive guess would be that the final state of the wave is

$$\mathbf{X}(x, t = 0) = \mathbf{X}_i(r, k) e^{-ikx} \xrightarrow{t} \mathbf{X}(x, t) = \mathbf{X}_i(r_1, k) e^{-ikx + i \int \Omega_i(r(t), k) dt}. \quad (\text{II.4})$$

That would represent that the wave ends at $\mathbf{X}_i(r_1, k)$, with a total phase picked up by the accumulation of the dynamical phase as the integral $\int \Omega_i dt$, as a WKB solution would expect (see Section I.2). Surprisingly, this is not quite right. Upon solving Equation (II.1), one finds that the solution is instead

$$\mathbf{X}_i(r_1, k) e^{-ikx + i \int \Omega_i(r(t), k) dt} e^{i\phi_B}, \quad (\text{II.5})$$

$$\text{with } \phi_B = i \int_{r_0}^{r_1} \mathbf{X}_i^\dagger \cdot \partial_r \mathbf{X}_i dr. \quad (\text{II.6})$$

The total phase picked up is the accumulation of dynamical phase plus a second term ϕ_B , which depends only on the path followed in parameter space, and is independent on the time taken to

II. Wave topology

follow it. It is thus called a *geometric phase*, or *Berry phase*.

Written in a more generic manner, when \mathbf{X} starts from an eigenvector of the waveband i and evolves following slowly a path Γ in a parameter space spanned by \mathbf{a} , it picks up an additional phase

$$\phi_B = i \int_{\Gamma} \mathbf{X}_i^\dagger \cdot \nabla_{\mathbf{a}} \mathbf{X}_i \, d\mathbf{a}. \quad (\text{II.7})$$

It will be shown that the quantity $\mathbf{X}_i^\dagger \cdot \nabla_{\mathbf{a}} \mathbf{X}_i$ is non-zero when the waves propagate in a medium where some symmetry is broken, such as time-reversal or mirror symmetries. It is however zero in simple cases, in nonrotating, nonmagnetic, homogeneous media.

In the example above, $\mathbf{a} = (r, k)^\top$ spans a 2D parameter space. The parameter space contains wavenumbers and external parameters. In all the cases discussed in this thesis, the parameter space will be three-dimensional.

The appearance of this geometrical phase is a subtle phenomenon of a parametrized linear eigenvalue equation. First noticed in 1956 by Pancharatnam who studied interference of light beams in different states of elliptic polarizations [143], it was also identified in molecular physics in 1958 by [144] who studied coupling between electronic and vibrational modes. A unified description of this effect on slow changes of an eigenvector was given by Berry in 1984 [145], who discussed it in quantum physics context. From this point, the geometrical phase or Berry phase attracted a considerable amount of attention in all fields of physics [146], sought after in quantum physics [147, 148], optics [149, 150], molecular physics [151, 152], superconducting circuits [153], condensed matter [154, 155], or rotating fluids [156, 157]. It became a center of interest of studies when the instrumental accuracy was sufficient to isolate its effects.

This quantity can be measured when the system \mathbf{X} comes back to its initial position in parameter space. This observability condition is related to a gauge freedom which is discussed in the next paragraph. It is thus imposed that the path Γ in parameter space must be closed for ϕ_B to be observable and measured.

A simple way to produce such closed paths is for the medium to change periodically. For instance, such a slow periodic change occur in nature in Foucault's pendulum [156, 157]. The pendulum is initiated at mid-latitude on the rotating Earth, initially oscillating in the North-South direction. As the day passes, the inertia of the pendulum makes the plane of oscillation rotate. After a time $T = 24\text{h}$ passed, the Earth came back to its original orientation, but the direction of oscillation did not come back to the North-South direction, by the action of the Coriolis force. The pendulum now oscillates at an angle $\phi_B = 2\pi(1 - \sin \theta)$ with the North-South direction, where θ is the latitude. This is the direct consequence of the ideas presented above, imposing a geometric phase ϕ_B [157].

This suggests that inertial waves in rotating fluids are likely to exhibit effects linked to the Berry phase, because rotation directly imposes a periodic change. It is indeed the case, and is the subject of Section II.2 and both Chapters of Part II. Rotation is however not necessary for the Berry phase to manifest in a wave problem. As stated above, this phase manifests when the medium slowly changes and comes back to its initial configuration. Let us consider a wavepacket propagating in a fluid that is static but inhomogeneous, made up of waves of a certain waveband i (for example acoustic waves). The trajectory of the center of this wavepacket can be described in a phase space (\mathbf{x}, \mathbf{k}) [158]. The position $\mathbf{x}(t)$ and wavenumber $\mathbf{k}(t)$ evolve with time following the wave equation and trace the trajectory of the wavepacket, also called ray. Generically these trajectories are not closed and fill a region confined between the turning points of the wave [159]; but certain solutions are periodic as they follow a close path in the phase space. These solutions are standing waves, coherently oscillating throughout the fluid between their turning points, and they are the key object of study of asteroseismology. Interestingly, the fact that their paths are *closed* implies that they intrinsically perform the slow periodic changes needed for the Berry phase to manifest. In regard with the notations used above, the system would be the polarization vector \mathbf{X} in a parameter space $\mathbf{a} = (x, k_x)^\top$. I will come back to this effect in the next Section II.2 and in Chapter VII.

An important condition for the manifestation of non-zero Berry phase – and topology – is the ne-

II. Wave topology

cessity for a symmetry to be broken [160]. Indeed, such effects have been noted first in systems where time-reversal symmetry $t \mapsto -t$ was broken [161, 162], before being identified in models where other symmetries are broken [163, 164]. In other words, waves in static homogeneous media can exhibit no Berry phase.

But astrophysical fluids are generically neither static nor homogeneous. Rotation and magnetic fields both break time-reversal symmetry and are commonly found in stars and planets. Self-gravity in stellar interiors can only be balanced by a pressure gradient, which breaks the vertical mirror symmetry between up and down. Hence, waves in stars and planets are likely to be subjects to Berry phase related effects.

Before moving on to see what these effects are, the mathematical origin of the Berry phase is discussed here from the viewpoint of a gauge theory. Indeed, Equation (II.2) was presented as a parametric eigenvalue equation. At each point in parameter space \mathbf{a} , the solution is an eigenvalue $\Omega_i(\mathbf{a})$ and its eigenvector $\mathbf{X}_i(\mathbf{a})$. However, as it is a linear equation, the eigenvector is determined up to a complex multiplicative number. Imposing a normalization condition $\mathbf{X}_i^\dagger \cdot \mathbf{X}_i = 1$ leaves that this complex multiplicative number is of norm 1. Therefore, one concludes that there is a degeneracy of solutions, as the same physical solution is given by every vector of

$$\{e^{i\varphi} \mathbf{X}_i(\mathbf{a}) | \varphi \in [0, 2\pi]\}, \quad (\text{II.8})$$

which is a 1D space, represented as a vertical orange line on Figure II.1 (middle). Physically, it must be interpreted by the fact that \mathbf{X}_i only contains *relative* amplitudes and phase differences between the fields of the wave. A global change of phase of all the fields only amounts to re-defining the origin of times $t = 0$ ¹.

This set of physically equivalent solutions must be seen as a *fiber*. For the waveband i , there is one fiber for each point in parameter space \mathbf{a} : the set of solutions of $\mathbf{H}(\mathbf{a})\mathbf{X} = \Omega_i(\mathbf{a})\mathbf{X}$ for this particular value of \mathbf{a} . The fiber is said to be *above* the parameter space. Together, all the fibers for all the points \mathbf{a} form a *fiber bundle*.

Going back to the example of acoustic waves in 1D homogeneous media, for the waveband $\Omega_+ = +c_s|k|$ we selected the eigenvector $\mathbf{X}_i = \begin{pmatrix} 1 \\ c_s\rho_0 \end{pmatrix}$, but we could have chosen $\mathbf{X}_i = \begin{pmatrix} e^{i\pi/7} \\ c_s\rho_0 e^{i\pi/7} \end{pmatrix}$ as a representative of the fiber $\{ \begin{pmatrix} e^{i\varphi} \\ c_s\rho_0 e^{i\varphi} \end{pmatrix} | \varphi \in [0, 2\pi] \}$.

In terms of gauge theory, this freedom of choice of a representative is *gauge* choice, with respect to the $U(1)$ symmetry. $U(1)$ is the group of complex numbers of norm 1, under which the physical solution \mathbf{X}_i is invariant. These considerations reveal that linear eigenvalue equations are embedded in a gauge theory framework. When formally solving for $\mathbf{X}_i(\mathbf{a})$ for all \mathbf{a} and selecting a representative vector, one performs a gauge choice at each point \mathbf{a} . Changing the selected eigenvector as

$$\mathbf{X}_i(\mathbf{a}) \rightarrow \tilde{\mathbf{X}}_i(\mathbf{a}) = e^{i\varphi(\mathbf{a})} \mathbf{X}_i(\mathbf{a}) \quad (\text{II.9})$$

is a gauge transformation. We stress that the gauge choice is mathematical, and one must keep in mind that only gauge-invariant quantities are physical, i.e. quantities that do not depend on the gauge choice. Among those, one finds

- The dispersion relation $\omega = \Omega_i(\mathbf{a})$,
- The energy $\mathbf{X}_i^\dagger \cdot \mathbf{X}_i = \tilde{\mathbf{X}}_i^\dagger \cdot \tilde{\mathbf{X}}_i = 1$,
- Relative amplitude and phase between components. For instance f and g are the first two components, $f/g = \mathbf{X}_{i,1}/\mathbf{X}_{i,2} = \tilde{\mathbf{X}}_{i,1}/\tilde{\mathbf{X}}_{i,2}$,
- The Berry phase ϕ_B on a closed path, as we will show below.

¹ $\mathbf{X}_i e^{-ikx+i\Omega_i t}$ and $\mathbf{X}_i e^{-ikx+i\Omega_i t+i\varphi} = \mathbf{X}_i e^{-ikx+i\Omega_i \tau}$ are the same wave, the second being measured with a time coordinate $\tau = t + \varphi/\Omega_i$ which is only a translation in time.

II. Wave topology

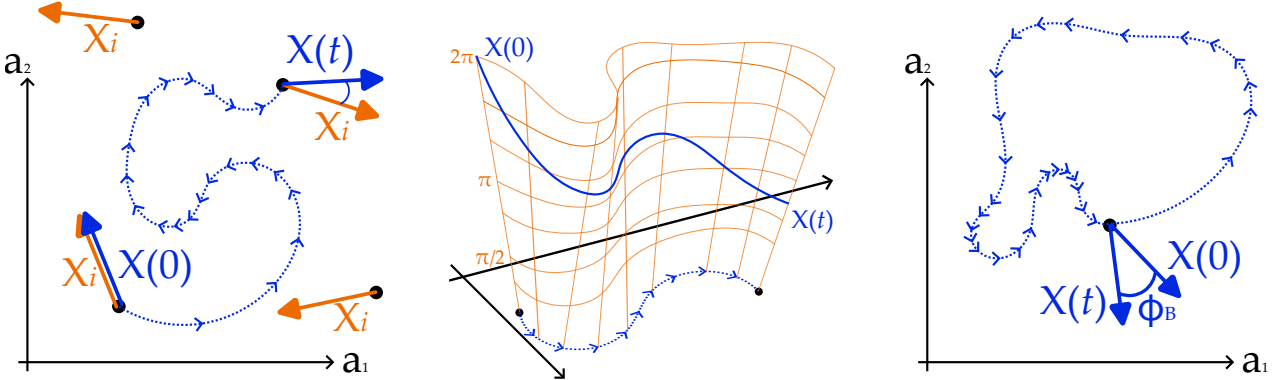


Figure II.1: Transport of a vector \mathbf{X} in a fiber bundle. **Left:** At each point in the parameter space a , one can arbitrarily choose the global phase of the eigenvector $e^{i\varphi} \mathbf{X}_i$ (orientation of orange vectors). A system initiated along \mathbf{X}_i at the starting point and slowly transported at an end point will not be aligned with \mathbf{X}_i there. **Middle:** the vector $\mathbf{X}(t)$ follows a parallel transport on a curved space, the fiber bundle (orange grid). The connection of this parallel transport is \mathcal{A} , emerging from the symmetry of invariance under global phase change. **Right:** the parallel transport-induced phase ϕ_B is independent on the choice of orientation of eigenvectors \mathbf{X}_i (orange) when the path is a closed loop. In that case, it is physically observable and is called the Berry phase.

On the other hand,

- The vector $\mathbf{X}_i \neq \tilde{\mathbf{X}}_i$,
- The gradients $\nabla_a \tilde{\mathbf{X}}_i = \nabla_a e^{i\varphi(a)} + \nabla_a \mathbf{X}_i \neq \nabla_a \mathbf{X}_i$,

are not gauge-invariant. This last point is the root of the manifestation of the Berry phase. Indeed, when \mathbf{X} follows a path Γ , the vector follows a *parallel transport* with respect to the gauge [165]. In essence, it implies that a gauge-dependent term must be added to ∇_a in order to obtain a gauge-invariant gradient. This term is generically called the *connection*, and we are dealing here with the Berry connection

$$\mathcal{A}_i \equiv i \mathbf{X}_i^\dagger \cdot \nabla_a \mathbf{X}_i. \quad (\text{II.10})$$

One checks that indeed

$$\left(\nabla_a + \tilde{\mathcal{A}}_i \right) \tilde{\mathbf{X}}_i = (\nabla_a + \mathcal{A}_i) \mathbf{X}_i, \quad (\text{II.11})$$

making for a gauge-invariant gradient.

One is free to make the selection on each fiber of the eigenvectors $\mathbf{X}_i(\mathbf{a})$ at each point of the parameter space. This amounts to choosing all the orange arrows on Figure II.1 (left), representing these eigenvectors, each one being able to be rotated freely. This is a local choice at each point. However, if an initial state (in blue) is chosen along one such orange eigenvector and evolved through time when following a path Γ (blue dots), it will be transported on a curved space, the fiber bundle (orange grid). Because of the curvature of the fiber bundle represented on Figure II.1 (right), it will rotate, and arrive at the end point with a certain angle φ . It thus ends with a certain angle with the orange arrow at the end point (Fig. II.1 (left)).

The Berry connection \mathcal{A}_i is not gauge-invariant and therefore cannot be measured. Indeed,

$$\tilde{\mathcal{A}}_i = i \tilde{\mathbf{X}}_i^\dagger \cdot \nabla_a \tilde{\mathbf{X}}_i = -\nabla_a \varphi + \mathcal{A}_i. \quad (\text{II.12})$$

Therefore, as it is an integral of this quantity, the Berry phase is not gauge-invariant on any path Γ but only on closed paths. Indeed, this is the only condition to have

$$\phi_B = \oint_{\Gamma} \tilde{\mathcal{A}}_i d\mathbf{a} = \oint_{\Gamma} \mathcal{A}_i d\mathbf{a} \quad (\text{II.13})$$

II. Wave topology

for an arbitrary choice of φ , as the difference between $\tilde{\mathcal{A}}_i$ and \mathcal{A}_i is a gradient, contributing to zero in a closed loop integral. Therefore, physical consequences of the Berry curvature can only be studied on situations like the one on Figure II.1 (right).

II.2 Polarization relations influence on ray-tracing

Let us come to an actual wave problem in which a non-zero Berry connection and Berry phase have been identified. In fluid waves context, a non-zero Berry phase have been found a few times [166, 167, 168, 169, 170]. Additionally, the topological analysis on the Chern number of [141] imposes a fortiori that these geophysical waves also have non-zero Berry curvature because of the rotation of the Earth, and manifested a Berry phase in close ties with Foucault's pendulum. This Section shows the direct consequence of the Berry connection has on these waves.

As it has been found in condensed matter, the Berry connection affects wavepackets by adding a virtual magnetic field, which makes them deviate from expected trajectories [171, 172, 173]. See the review on this effect in condensed matter physics [174].

Let us start by re-writing the Berry phase by using Stokes theorem, and formulate the close loop integral as a surface integral as

$$\phi_B = \oint_{\Gamma} \mathcal{A} da = \int_{\Sigma} \nabla_a \wedge \mathcal{A} d\Sigma, \quad (\text{II.14})$$

where Σ is any surface whose boundary is Γ . We defined the Berry curvature

$$\mathcal{F}_i = \nabla_a \wedge \mathcal{A}_i = i \nabla_a \wedge (\mathbf{X}_i^\dagger \cdot \nabla_a \mathbf{X}_i), \quad (\text{II.15})$$

for each waveband i . Note that this expression with the wedge product is only applicable in a 3D parameter space, which will mostly be the case in this thesis. However a general expression in any dimension exists in the framework of differential forms [165].

This quantity is named Berry *curvature* because it is indeed a curvature in the differential geometry sense, the curvature of the fiber bundle. This real vector field on the parameter space is gauge-invariant. Indeed, under a gauge transformation, one has

$$\tilde{\mathcal{F}}_i = \nabla_a \wedge \tilde{\mathcal{A}}_i = \nabla_a \wedge (\mathcal{A}_i - \nabla_a \varphi) = \nabla_a \wedge \mathcal{A}_i = \mathcal{F}_i. \quad (\text{II.16})$$

It is therefore an observable quantity. Equation (II.15) illustrates that this quantity measures the variations of the polarization relations \mathbf{X}_i , more specifically the way the orientation of \mathbf{X}_i twists in the parameter space. It therefore manifests in wave propagation in inhomogeneous media only.

In condensed matter, it has been found that the Berry curvature \mathcal{F} affects the trajectory of wavepackets of electrons in the semi-classical limit, seen as almost ballistic particles [175]. This semiclassical limit of quantum physics is in correspondence with the ray-tracing approach of waves in fluids.

Ray-tracing in fluids amounts to determine the trajectory of a wave in the medium if the degrees of freedom are reduced to only the position and impulsion of the center of mass of the wave. This approach accurately describes wavepackets of relatively small spatial extension. This technique is also sometimes called geometrical optics as it rests on the same approximation, which disregards that the perturbation is a wave and instead focuses on determining the path that it will follow. The interest for asteroseismology lying in this approximation is that it is able to characterize the frequencies of standing waves in stars and planets where eigenfunctions are non-separable, because of anisotropy or non-spherical geometry, caused respectively by a magnetic field and by deformation owing to fast rotation. It is close to the study of characteristics of the PDE governing the waves, for instance Equation (II.1). See the book of Whitham [158] and the applications of these techniques for asteroseismology [44, 159, 176].

Essentially, in the limit of geometrical optics, the coordinates of the center-of-mass of a wavepacket of the waveband i in a phase space (\mathbf{x}, \mathbf{k}) satisfy the equations of Hamilton

$$\frac{d\mathbf{x}}{dt} = +\partial_{\mathbf{k}} \Omega_i, \quad (\text{II.17})$$

$$\frac{d\mathbf{k}}{dt} = -\partial_{\mathbf{x}} \Omega_i, \quad (\text{II.18})$$

II. Wave topology

where the Hamiltonian is the dispersion relation $\Omega_i(\mathbf{x}, \mathbf{k})$. They are the phase-space equivalent of the eikonal equation, and can be used to explain acoustic mirages as they show the effects of spatially varying group velocity. Indeed, if a 2D (x, z) gas is stratified in temperature, the dispersion relations of acoustic waves is $\Omega = c_s(z)\sqrt{k_x^2 + k_z^2}$. Decoupling the ray-tracing Equations (II.17)-(II.18) yields $\ddot{z} = -c_s \frac{dc_s}{dz} + \frac{dc_s^2}{dz} (\dot{z}/c_s)^2$, a nonlinear equation which for low angles $k_z \ll k_x$ simplifies into $\ddot{z} = -\frac{d}{dz} \frac{1}{2} c_s^2$. In other words, the problem is reduced to a point-particle in a potential $V = \frac{1}{2} c_s(z)^2$, whose first integral of motion is $E = \frac{1}{2}(\dot{z}^2 + c_s(z)^2)$ which provides a simple description of the bending of the trajectories, the turning point of acoustic waves when c_s increases, and silent lightning storms [177]. No notion of polarization relations, fiber bundles or Berry curvature is involved in the establishment and solving of these equations. Indeed, they are only involved in the first order correction to the approximation of geometrical optics. It may be seen as the first order correction of the wavepacket being small but not totally reduced to a point. When it was found that there is a non-zero Berry curvature in the polarization relations of shallow-water waves, [178] established the ray-tracing equations of these waves using the semiclassical machinery of quantum physics, in order to obtain the first order correction to geometrical optics. They did find that this correction involved the Berry curvature. The derivations are quite involved and demand some manipulations. One key is the use of the Wigner-Weyl transforms, two famous transforms of quantum mechanics [179]. The Weyl transform is a quantization scheme, taking classical numbers like x and k to operators \hat{x} and $\hat{k} = -i\partial_x$ with appropriate properties for describing quantum mechanics. The Wigner transform is simply its reciprocal, taking operators to functions on a phase space (x, k) . In fluid wave problems, the linearized equations are expressed using differential operators, such that they are naturally formulated in the "quantum" context. We are therefore interested in the Wigner transform, which will provide a formulation of the wave equation in a phase space (x, k) . In this context, the Wigner transform is a generic formula to express the local propagation of waves in an otherwise inhomogeneous medium, providing their local polarization relations and local dispersion relation. For more details on the usefulness of these transforms for fluid mechanics, see [180].

The wave problem studied by [178] is the following: assume that a thin layer of incompressible fluid covers a rotating sphere under its centripetal gravity field g , with a hard impenetrable boundary below and a free surface at the top. The model of shallow water waves considers the linearized equations governing this problem in the limit of infinitesimally small height, i.e for wavelengths much larger than the height h [10]. Considering a point at a particular latitude and writing the coordinates as x for the West-East position and y for the South-North position with respect to this point, the linear waves equation in the rotating frame can be written as

$$\partial_t \begin{pmatrix} v_x \\ v_y \\ \eta \end{pmatrix} = \begin{pmatrix} 0 & f & -g\partial_x \\ -f & 0 & -g\partial_y \\ -h\partial_x & -h\partial_y & 0 \end{pmatrix} \begin{pmatrix} v_x \\ v_y \\ \eta \end{pmatrix}. \quad (\text{II.19})$$

$f = 2\Omega \cdot \mathbf{e}_r$ is twice the projection of the rotation rate with the local vertical, and is called the Coriolis parameter, while the variables v_x, v_y, η are the components of the velocity and the elevation of the surface. The simple case of study of shallow water waves considers short propagation on the sphere, which amounts to approximating f to a constant. This model is called the f -plane, as the sphericity is thus neglected, and is the classical model of study of atmospheric and oceanic inertial waves as presented on Figure I.1. When retaining a latitudinal dependence at first order of a Taylor expansion as $f = f_0 + \beta y$, the model is called the β -plane. The β parameter is essential for a number of phenomena, among which the Rossby waves which do not propagate in an f -plane [10].

Upon adimensionalizing the variables with height as h and velocities as $c = \sqrt{gh}$, one obtains

$$\partial_t \begin{pmatrix} v_x/c \\ v_y/c \\ \eta/h \end{pmatrix} = \begin{pmatrix} 0 & f(y) & -c\partial_x \\ -f(y) & 0 & -c\partial_y \\ -c\partial_x & -c\partial_y & 0 \end{pmatrix} \begin{pmatrix} v_x/c \\ v_y/c \\ \eta/h \end{pmatrix} \equiv -i\hat{\mathbf{H}} \begin{pmatrix} v_x/c \\ v_y/c \\ \eta/h \end{pmatrix}. \quad (\text{II.20})$$

The differential operator $\hat{\mathbf{H}}(y, \partial_y, \partial_x)$ describes all waves propagating in the model. It is a 3×3 operator, and its eigenvalues can be classified in three categories stemming from the three wavebands

II. Wave topology

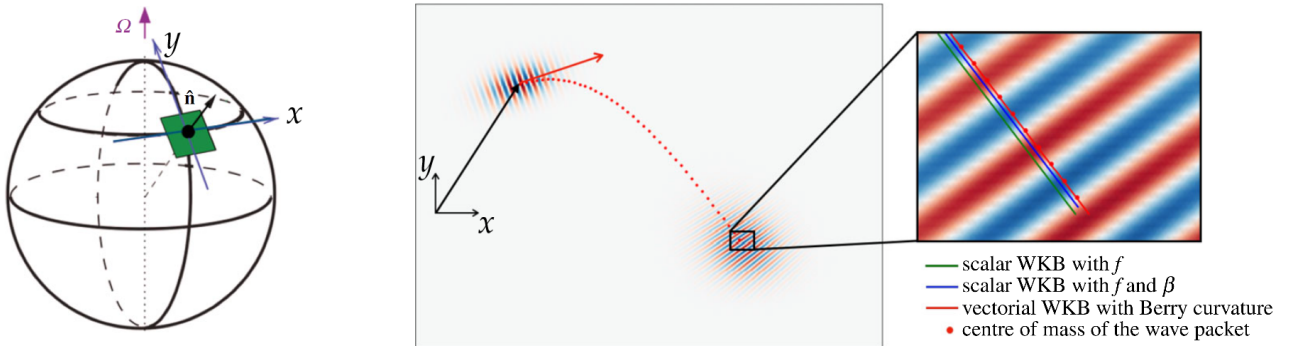


Figure II.2: Ray-tracing of shallow water waves in an inhomogeneous medium show a deviation from pure geometrical optics, due to the intervention of Berry curvature¹. The scalar theory with f and β accounts for inhomogeneity in the dispersion relation but neglects the deflection due to Berry curvature.

¹Adapted from [178].

of its symbol: two Poincaré wavebands with positive and negative frequencies respectively, and the Rossby waveband.

The Wigner-Weyl transforms propose a way to obtain the ray-tracing equations from $\hat{\mathbf{H}}$ as a semi-classical limit. Among the derivations needed, one calculates the Wigner symbol of $\hat{\mathbf{H}}$ which is

$$\mathbf{H} = \begin{pmatrix} 0 & f(y) & k_x \\ -f(y) & 0 & k_y \\ k_x & k_y & 0 \end{pmatrix}, \quad (\text{II.21})$$

a 3×3 matrix function on the parameter space (y, k_y, k_x) . Sometimes called microlocal analysis, this approach is equivalent as a local Fourier analysis. The eigenvalues of \mathbf{H} provide the local dispersion relations of the waves, which read

$$\Omega_{\text{poincaré}} = \pm \sqrt{k_x^2 + k_y^2 + f^2}, \quad \Omega_{\text{rossby}} = 0. \quad (\text{II.22})$$

From there, [178] found that the center-of-mass (x, k_x, y, k_y) of a wavepacket solution of Equation (II.20) of small relative size ϵ with respect to the size of the variations of the medium f_0/β satisfied the equations

$$\frac{dx}{dt} = +\partial_{k_x} \bar{\Omega}_i, \quad (\text{II.23})$$

$$\frac{dk_x}{dt} = -\partial_x \bar{\Omega}_i = 0, \quad (\text{II.24})$$

$$\frac{dy}{dt} = +\partial_{k_y} \bar{\Omega}_i + \epsilon \mathcal{F}_{y, k_y} \frac{dy}{dt}, \quad (\text{II.25})$$

$$\frac{dk_y}{dt} = -\partial_y \bar{\Omega}_i + \epsilon \mathcal{F}_{y, k_y} \frac{dk_y}{dt}, \quad (\text{II.26})$$

where $\mathcal{F}_{y, k_y} = i\{\mathbf{X}_i^\dagger, \mathbf{X}_i\}_{y, k_y}$ is the Berry curvature in the (y, k_y) phase space, which would be the first component $\mathcal{F} \cdot e_{k_x}$ of the Berry curvature \mathcal{F} in a 3D parameter space (k_x, y, k_y) . The Hamiltonian of this system is $\bar{\Omega}_i = \Omega_i + \epsilon \frac{i}{2} \mathbf{X}_i^\dagger \cdot \{\mathbf{H} - \Omega_i \mathbf{I}_3, \mathbf{X}_i\}_{y, k_y}$, with a correction at first order. We used the Poisson brackets on the (y, k_y) phase space $\{A, B\}_{y, k_y} = \partial_y A \partial_{k_y} B - \partial_y B \partial_{k_y} A$. The curvature in the x direction \mathcal{F}_{x, k_x} does not appear as it is zero because the x direction is homogeneous.

The form of Equations (II.23)-(II.24) is expected from the limit of geometrical optics. However, when the first order ϵ^1 is kept, the Berry curvature does appear in the ray-tracing equations in the (y, k_y) plane. We note that the Hamiltonian $\bar{\Omega}_i$ is also corrected at this order, and is not exactly Ω_i the dispersion relation of the f -plane. The intervention of the medium's spatial variations through β causes the non-trivial corrections in ray-tracing the trajectories in the phase space (y, k_y) . For instance, the Rossby waveband has $\Omega_{\text{rossby}} = 0$, but a non-zero $\bar{\Omega}_{\text{rossby}}$ which allows them to propagate when including β .

II. Wave topology

Through this derivation, [178] showed that the geometrical effects related to Berry curvature are indeed involved in the dynamics of the waves. It corrects the well-known eikonal equation by making the polarization relations of the waves intervene in the ray-tracing equations. It is an interesting result showing that the trajectories and travel times of waves do not only depend on the dispersion relation, which was also noted by Godin who wrote "knowledge of the dispersion relation is not sufficient for calculation of the wave phase" [170]. They confirmed their analysis with numerical experiments in a β -plane, by computing exactly the trajectory of a wavepacket of Poincaré waves and comparing with the expected trajectories from geometrical optics with and without the Berry correction. Their results are showed on Figure II.2.

Their results suggest similar corrections in any ray-tracing of waves in inhomogeneous media, which lead to the work presented in Chapter VII on acoustic waves in the Sun.

II.3 The Chern number and concept of spectral flow

Let us introduce a new level of mathematical concepts which characterize the topology of the fiber bundle described above. The topology of this abstract space has direct consequences on the physics of the waves through the so-called bulk-boundary correspondence presented below.

II.3.i Topology

A few years after the experimental discovery of the quantized conductivity of the Quantum Hall Effect [181], Thouless explained it by invoking a topological argument in 1982 [161, 182]. Laughlin showed in 1981 that the quantized Hall conductivity was a manifestation of a gauge invariance [183]. One year later, Simon explicitly linked the topological number of Thouless with the gauge invariance at the roots of Berry's connection [184]. With this insight he saw the link between the two, topology and Berry's curvature, as a manifestation of the Chern theorem [185]. This theorem states that the integral of the curvature of a fiber bundle is quantized by an integer number, the equivalent of its Euler characteristic. This number is therefore called the Chern number, and characterizes the topology of the fiber bundle. Through the Chern theorem, this number reads

$$\mathcal{C} = \frac{1}{2\pi} \int_{\Sigma} \mathcal{F} d\Sigma, \quad (\text{II.27})$$

where Σ is any closed surface in the 3D parameter space. Again, other dimensions of parameter space require the adaptation of this expression, which will not be required in this thesis. The fiber bundle on which the Chern theorem is applied here is the set of equivalent eigenvectors $\{e^{i\varphi} \mathbf{X}_i(\mathbf{a}) | \varphi \in [0, 2\pi]\}$ above Σ , i.e for all \mathbf{a} in Σ . One notes the interesting property that Σ can be deformed continuously without changing \mathcal{C} , as the only way for an integer to be continuous is to be constant. This is true as long as no singularity of \mathcal{F} is crossed. See the gray sphere on Figure II.3 (right).

Going back to the expression of Equation (II.15), one sees that in a 3D parameter space \mathcal{F} is the curl of \mathcal{A} , such that

$$\nabla_{\mathbf{a}} \cdot \mathcal{F} = 0. \quad (\text{II.28})$$

This equation may be seen either as an incompressibility condition, or as a Maxwell-Gauss equation in a vacuum. In any case, this implies that the flux through a closed surface Σ expressed as

$$\int_{\Sigma} \mathcal{F} d\Sigma \quad (\text{II.29})$$

can only be non-zero if the vector field is singular somewhere inside the enclosed region. If there is a point where $|\mathcal{F}| = +\infty$, then this point is a source/sink, or equivalently a "point charge" of Berry curvature radiating outward/inward from it, just as a point charge radiates an electrostatic field. The term monopole is usually used, and such points of singular Berry curvature are dubbed *Berry-Chern monopoles*. Then, Equation (II.27) must be seen as simply a Gauss theorem where \mathcal{C} plays the role of the charge. A difference with electrostatics is the additional condition that the charge \mathcal{C} must be an

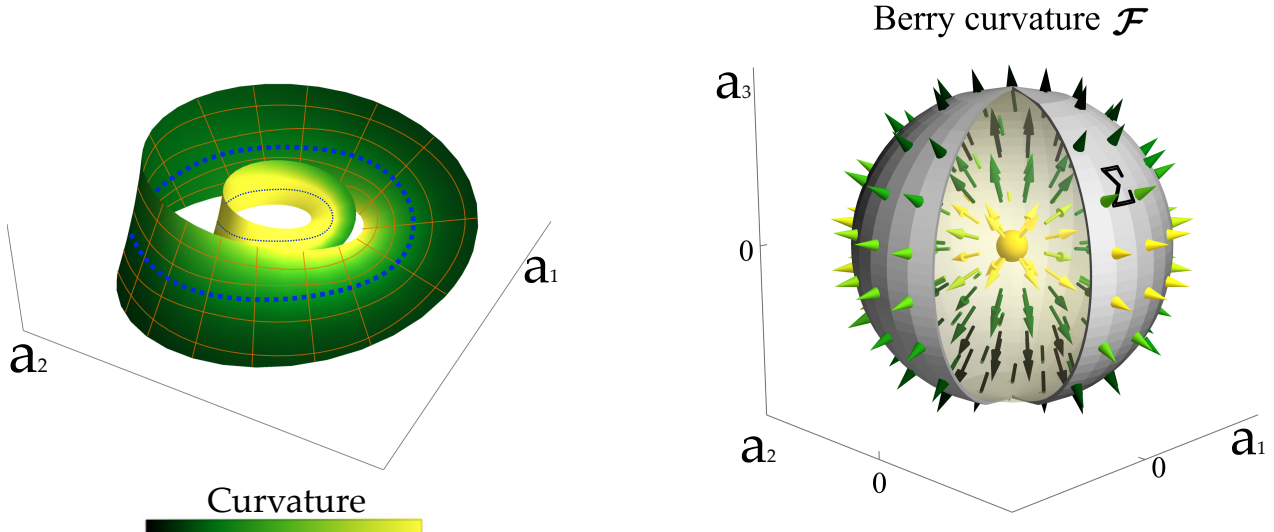


Figure II.3: Left: schematic representation of a fiber bundle with non-trivial topology with a 2D parameter space, here defining a Möbius strip. Similar to Fig. II.1 (middle). Here is represented the Riemannian curvature (green-yellow colormap), as the fiber bundle is a surface. When the path Γ (blue) is tightened, the curvature of the surface increases because of the topology of the Möbius strip which includes a twist. When tightened to a point, the curvature would diverge to infinity. Right: in a 3D parameter space, one looks directly at the Berry curvature vector field \mathcal{F} , as the fiber bundle cannot be represented. The Chern number of a singularity of \mathcal{F} is obtained by calculating the flux of \mathcal{F} through a closed surface Σ enclosing it. This point is a Berry-Chern monopole.

integer because it is a topological equation, imposing the quantization of this number.

Before we see below and in Section II.4 what consequences this topological number has on the physics of the waves, let us characterize where the monopoles occur in parameter space. This is particularly important to establish which parameters are relevant in a topological analysis when approaching a new wave problem.

For this aim, we use yet another expression of the Berry curvature [186], which one obtains by expressing the components $\mathcal{F}_i = (\mathcal{F}_{i,a_1}, \mathcal{F}_{i,a_2}, \mathcal{F}_{i,a_3})$ as

$$\mathcal{F}_{i,a_\lambda}(\mathbf{a}) = i \sum_{j \neq i} \frac{1}{(\Omega_i(\mathbf{a}) - \Omega_j(\mathbf{a}))^2} \epsilon_{\lambda\mu\nu} (\mathbf{X}_i^\dagger \cdot \partial_{a_\mu} \mathbf{H} \cdot \mathbf{X}_j) (\mathbf{X}_j^\dagger \cdot \partial_{a_\nu} \mathbf{H} \cdot \mathbf{X}_i). \quad (\text{II.30})$$

In this expression, ϵ is the Levi-Civita tensor and j spans the wavebands other than i . This cumbersome expression shows three things:

- (i) the curvature in the a_λ direction is given by the gradients of the matrix \mathbf{H} in the other two directions a_μ and a_ν .
- (ii) the curvature results from the interaction between the waveband i and the others $j \neq i$.
- (iii) the numerator is always finite as \mathbf{H} is assumed to be a sufficiently smooth function of the parameters.

This last point reveals where the singularities occur, as they necessarily come from the denominator going to zero. Therefore, Berry-Chern monopoles are located in parameter space where

$$\Omega_i(\mathbf{a}) = \Omega_j(\mathbf{a}). \quad (\text{II.31})$$

This condition states that singularities of Berry curvature occur at degeneracies of the frequencies of waves from different wavebands. As we will see in the next section, this result is of great help

II. Wave topology

when investigating a new wave problem, as one can start by investigating the dispersion relations of the various waves propagating in the system, and look for crossings which suggest the possibility of topological numbers.

This is also a way of establishing which parameters are relevant. Indeed, in order to find Berry-Chern monopoles in a 3D parameter space, one needs to find 3 parameters (a_1, a_2, a_3) which all can lift the degeneracy. It is only in such a case that degeneracies will be points in this 3D space.

II.3.ii Bulk-boundary correspondence

The consequence of a non-trivial topology underlying a wave equation is given by the *bulk-boundary correspondence*. It is the founding principle of wave topology, which relates the Chern number to particular spectral properties of waves.

In 1963, Atiyah and Singer established the Index theorem, an important piece of mathematics which connects analysis and topology [187]. They proved an equality between two indices of elliptic differential operators, one related to their eigenvalues (the *analytical* index) and the other related to the topology of the bundle they span (the *topological* index). The theorem strikingly asserts that these two integer numbers must be equal even though they characterize very different features of the operator of interest. A few years later they applied this theorem to relate the *spectral flow* of an operator to the Chern number [188], which is the application we are interested in here.

These two papers established these important results in a set of assumptions which does not quite adapt for geophysical, astrophysical or quantum waves settings. In particular, it was established for compact manifolds while many physical models require application in \mathbb{R}^n , for which the index theorem was recently proved to hold by [189]. This paper is focused on application for physics, and is therefore more accessible for physicists. Let us now present what a spectral flow is.

In the context of waves in fluids, a spectral flow is a particular phenomenon occurring in the dispersion relation of wave modes $\{\omega_n(a) \mid n \in \mathbb{N}\}$ discretized by boundary conditions and depending on a continuous parameter a . For instance, in stars as shown in Figure I.6 (left), the parameter to be varied is the horizontal wavenumber ℓ . For this discussion, we shall take an example from quantum physics, the Dirac operator [186] which is only taken here as a formal illustration.

Let us consider the operator eigenvalue equation

$$\omega \mathbf{X} = \begin{pmatrix} x & -i\partial_x - ik_y \\ -i\partial_x + ik_y & -x \end{pmatrix} \mathbf{X}, \quad (\text{II.32})$$

with solutions of normal modes of finite energy $\int \mathbf{X}^\dagger \cdot \mathbf{X} dx$, i.e decaying at infinity. These solutions correspond to standing waves in the x direction, travelling as $\cos(\omega t - k_y y)$ in the y direction.

This operator is simple enough so that de-coupling the two differential equations is tractable, and one finds the spectrum of normal modes as $\omega_n(k_y) = \pm \sqrt{k_y^2 + n + 1}$ for $n \in \mathbb{N}$, plus the additional solution $\omega = k_y$. This spectrum is shown on Figure II.4. The special behavior of the red branch is a spectral flow.

A spectral flow is the fact that, upon swiping the parameter k_y , one or several branches of modes *transit* from one waveband i to another j . More specifically, they follow the asymptotic behavior of the wavebands i or j in the two limits $k_y \rightarrow \pm\infty$ respectively.

Now let us make a local approach of Equation (II.32). Using the Wigner transform, or equivalently just replacing $-i\partial_x$ by k_x with the aim of solving for locally plane waves, one obtains the symbol

$$\omega \mathbf{X} = \begin{pmatrix} x & k_x - ik_y \\ k_x + ik_y & -x \end{pmatrix} \mathbf{X}, \quad (\text{II.33})$$

whose eigenvalues are $\Omega_{\pm}(k_y) = \pm \sqrt{k_y^2 + k_x^2 + x^2}$. These two dispersion relations degenerate at $x = k_x = k_y = 0$. Therefore, a Berry-Chern monopole is expected at the origin of the 3D parameter space (x, k_x, k_y) . Indeed, taking the waveband with positive frequencies $i = +$, one computes

$$\mathcal{F}_+ = \frac{\mathbf{a}}{2|\mathbf{a}|^3}, \quad (\text{II.34})$$

II. Wave topology

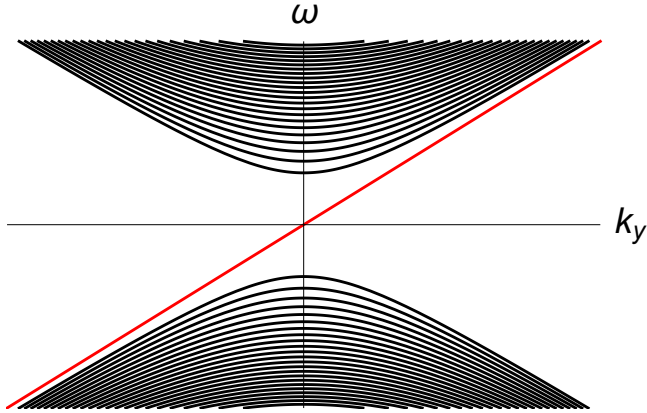


Figure II.4: A spectral flow of +1: one branch of modes transit from the lower waveband to the upper waveband when k_y is swiped from negative to positive values. This one mode is responsible for the fact that no gap in frequency exists in this system.

where $\mathbf{a} = (x, k_x, k_y)$. The curvature is singular at the origin, radiating from a charge $\mathcal{C}_+ = +1$. One also finds that $\mathcal{C}_- = -1$.

The index theorem can now be stated. For any waveband i of a differential operator, the analytical index \mathcal{N}_i is measured as the number of new modes between $k_y \rightarrow +\infty$ and $k_y \rightarrow -\infty$ counted algebraically. On the other hand, the Chern number of this same waveband is calculated by calculating the topology of the fiber bundles in its symbol. The index theorem states that

$$\mathcal{N}_i = \mathcal{C}_i. \quad (\text{II.35})$$

In other words, the number of modes gained by the waveband i is equal to its Chern number.

In the spectrum on Figure II.4, one notes that the upper waveband has $\mathcal{N}_+ = +1$. The lower waveband has $\mathcal{N}_- = -1$. These numbers, necessarily integers, are solely counted in the spectrum. On the other hand, one did indeed find that $\mathcal{C}_\pm = \pm 1$, in satisfaction of the index theorem. The situation is summarized on Figure II.5.

It may seem surprising that the Chern number, characterizing a space of local eigenvectors, imposes a number of global modes with such constraints on their eigenvalues. We propose the following interpretation: as shown in Equation (II.30), a Chern number appears at local degeneracies of the eigenvalues of different wavebands. Therefore, it manifests where the spectral gap is closed in the local problem. It can thus be expected that if the gap closes in the local analysis, the gap in the spectrum of global modes will also be closed. Thus a branch of global mode must cross the frequency gap. From this standpoint, the index theorem is then the statement that the gaps in the local and in the global spectrum are either both closed or both open.

Now, what if this problem was deformed into an equation with the operator

$$\begin{pmatrix} f(x) & -i\partial_x - ik_y \\ -i\partial_x + ik_y & -f(x) \end{pmatrix}, \quad (\text{II.36})$$

with a modulation $f(x)$ instead of simply linear variations x ? The spectrum of global modes will be deformed as well, but the spectral flow will remain as long as f increases past the value 0 at some x [189]. Indeed, this is the idea of a continuous deformation, which preserves the spectral flow as long as no additional degeneracy point $f(x) = 0$ is added or subtracted from the system. Indeed, it is protected by the topological number $\mathcal{C}_i = +1$. In a local analysis, the parameter space would become $\mathbf{a} = (f, k_x, k_y)$, but the degeneracies and the monopole would be left unchanged. This is the point of topology, which provides characteristics that are invariant under continuous deformations. Of course, one can find non-continuous deformations that break the spectral flow, for example with singular or non-differentiable modulation $f(x)$. For instance, the equatorial shallow-water waves with $f(y) = \beta y$ host the Kelvin and Yanai waves with a spectral flow of +2, but in the wave spectrum

II. Wave topology

with a step function $f(y) = \text{sign}(y)f_0$ only the Kelvin wave is found, the Yanai wave does not cross the frequency gap any more, such that the spectral flow is only +1 [190]. This fact is one of the main interests of wave topology, which is able to assert the existence and number of modes of spectral flow without solving for the modes or their eigenvalues.

However, the position at which the mode of spectral flow propagates will have to change, and follow the deformation $f(x)$. In the previous model with linear variations, the spectral flow branch with $\omega = k_y$ have the eigenfunctions $X = \begin{pmatrix} \exp(-x^2/2) \\ 0 \end{pmatrix}$. This mode is localized close to where $x = 0$.

This is generic of topological modes, whose eigenfunctions are trapped close to the spatial position of Berry-Chern monopole in parameter space ($x = 0$). Upon deforming the spatial profile of the diagonal components in Equation (II.32) as $x \mapsto f(x)$, the degeneracy will be located at $f(x) = 0$, which is where the mode of spectral flow will be trapped.

Such a point depends on the medium considered, and is sometimes called a *topological interface*. Indeed, it is at this point of contact between the regions $f > 0$ and $f < 0$ that this mode is trapped. This situation concerns many topological modes in fluid problems, as will be presented in Section II.4 and the rest of this thesis. However, it may be so that the system studied has boundaries, for instance one could solve Equation (II.32) in the domain $x \in [1, 2]$ with some boundary conditions². In this case a careful analysis is warranted, as the role of boundaries and boundary conditions and their interaction with topology is yet to be fully understood.

This behavior is quite striking, and is called the bulk-boundary correspondence. Degeneracies of the bulk problem – or equivalently the local problem – are characterized by the Chern number, which impose the existence in the global problem of a certain number of branches crossing the frequency gap between the wavebands. These modes, called *edge modes* or *topological modes*, or sometimes *zero modes* in the condensed matter community, are trapped in the medium as close as possible to the Berry-Chern monopoles. If the medium is such that the monopoles are not localized inside of it, the edge modes are trapped at the actual boundaries of the system. If the medium is such that the monopoles are located at a particular position inside of it, this is where the edge modes propagate, and this independently of the boundaries. It is as if the edge modes were repulsed by the bulk of the system because of its topology, and put at the boundaries, in the absence of a better place to propagate.

Going back to the quantum Hall effect, it has been identified that the quantized conductance was performed by edge modes [191], which later on were linked to the Chern number of the bulk by Hatsugai in 1993 [192]. The bulk-boundary correspondence was founded, stating the topology of the bulk problem is responsible for putting propagating modes at the edge [193, 194].

Before moving on to review the literature on such modes, let us stress some fundamental differences between the perspectives of topological modes in fluid waves compared to topological modes in condensed matter physics. In condensed matter, the crucial feature of these modes is that they determine whether the material is gapped or gapless in terms of energy bands. The few edge modes crossing the energy gap are connecting the valence band to the conductive band and directly explain quantized transport, making the sample slightly conductive instead of an insulator. The fact that the modes propagate at the edge of the sample is interesting but not important for transport. The main source of interest is rather the robustness of these modes to defaults in the crystal, which is guaranteed by their topological protection. The quantized conductance is thus exact and default-independent.

For fluid waves, there is no state-filling rule, statistics or Fermi level. Therefore, the property of filling the frequency gap may only be interesting for mode identification, when identifying an oscillation mode in what should have been a "forbidden" frequency band. But the more interesting feature of the bulk-boundary correspondence is the boundary: topological physics tells you where modes are going to be trapped spatially. In this thesis, this property was leveraged to predict that the f -modes of stars should be localized deep inside the star for low degree ℓ as they acquire a nature of topological modes, which then lead to the unveiling of mixed f/g modes in the Sun. This is presented

²which should preserve the Hermiticity of the operator

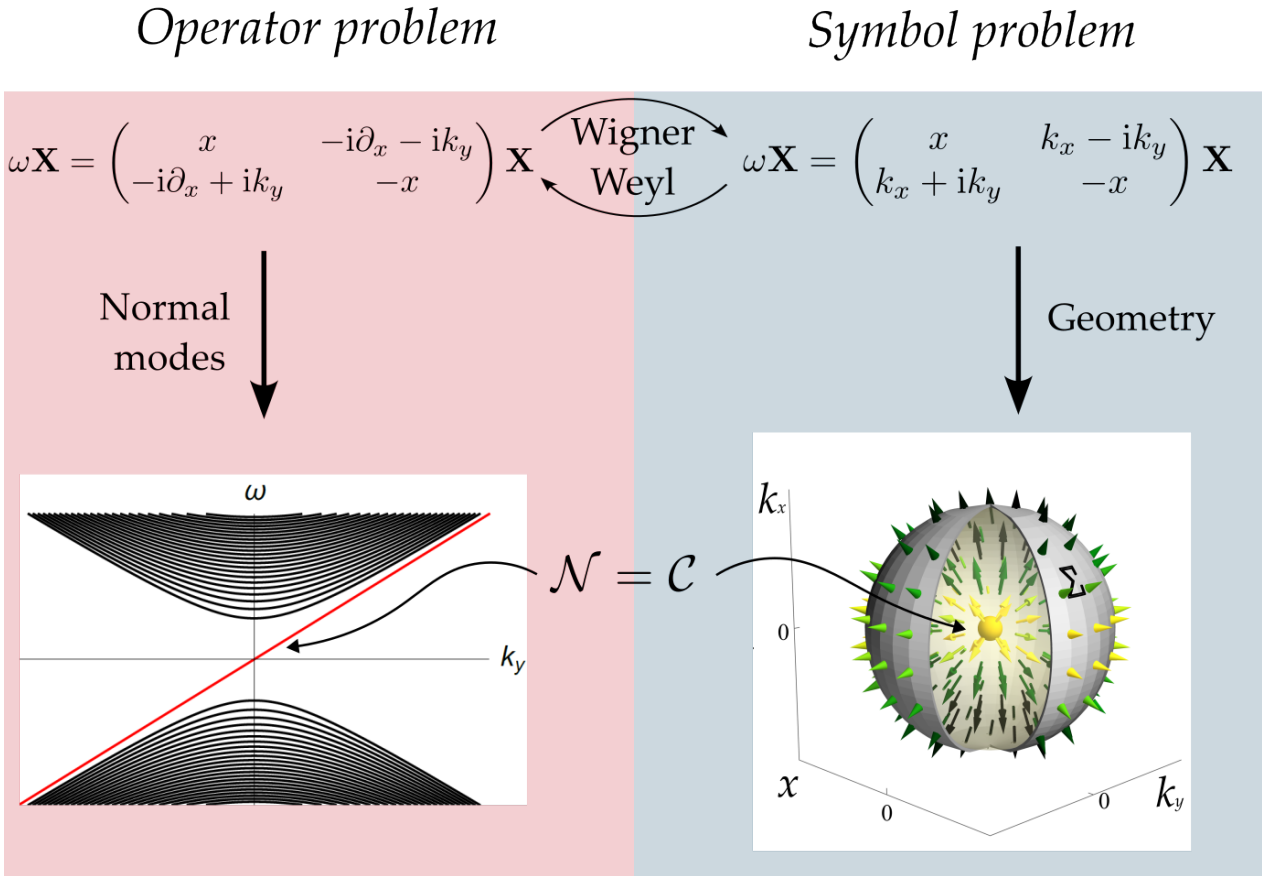


Figure II.5: Flowchart of the approach of wave topology . On the left, the problem of normal modes of an inhomogeneous system. Among the branches of modes, $\mathcal{N} = 1$ transits between wavebands, constituting a spectral flow. On the right, the Wigner transform maps this problem to a symbolic one in a phase space. The geometry of the fiber bundle of local eigenvectors shows Berry curvature and a Berry-Chern monopole of charge $\mathcal{C} = 1$, in satisfaction of the index theorem. Would the operator problem be deformed, and the diagonal terms change as $x \mapsto f(x)$, the spectral flow would be protected and guaranteed by \mathcal{C} , even though the normal modes computation would become untractable.

in Chapters V and VI. Furthermore, topological modes sometimes come with the unique property of being unidirectional, as is the case in the example above on Figure II.4 where the mode of spectral flow only propagates towards increasing y . This is true when time-reversal symmetry is broken, for instance by rotation which causes the purely eastward propagation of the Kelvin and Yanai waves at the equator. This non-reciprocal propagation is also a particularly interesting property which can be analyzed by topology.

The methodology of wave topology is thus the following: for a given wave problem, one must determine if time-reversal or mirror symmetry in one direction is broken. If that is the case, it is likely that the fiber bundles will not be flat and some Berry curvature exists.

Then, writing the linear wave equation as $i\partial_t \mathbf{X} = \hat{\mathbf{H}} \mathbf{X}$, perform a local approach by employing Wigner transform to obtain an equation $\omega \mathbf{X} = \mathbf{H}(a) \mathbf{X}$. The parameters a must be chosen so as to have isolated degeneracies in the 3D parameter space. In that case, these are likely to be Berry-Chern monopoles. Compute the eigenvectors of \mathbf{H} and the Berry curvature of a given waveband with Eq. (II.15), and look for singularities of \mathcal{F} . Around these singularities, compute the flux of Berry curvature through a closed surface to obtain the Chern number. If it is non-zero, some topological modes must propagate in the inhomogeneous medium considered, with possibly unique spectral or spatial properties.

II.4 Topological waves

This Section aims at reviewing topological modes that had been identified in the literature by the time this thesis started. Topological modes are the waves directly associated to a spectral flow, and/or a Chern number. It will present in details two examples in geophysical fluid dynamics which constituted the basis of this thesis. It ends by going over topological waves which have been found in other disciplines of physics, such as condensed matter, plasma physics, optics, ...

II.4.i The Kelvin and Yanai waves

In 2017, Delplace et al. found for the first time a Berry-Chern monopole in a problem of waves in a geophysical fluid: the equatorial shallow water waves [10]. It is the same problem as presented in Section II.2, but focusing on the equator. The equator is a particular latitude for this problem, as it is the place where the Coriolis parameter $f = 2\Omega \cdot e_r$ is zero. Therefore, rotation only enters the problem as an inhomogeneity term $f = 0 + \beta y$. The wave modes trapped latitudinally and propagating longitudinally in this situation were famously solved by Matsuno in 1966 [195], in the β -plane approximation presented above. He found unsurprisingly three infinite countable sets of modes: Poincaré with positive frequencies, Poincaré with negative frequencies, and Rossby waves. In addition to this triply infinite number of branches of modes, he found two branches which were neither Poincaré nor Rossby: the Kelvin and the Yanai waves, with frequencies shown on Figure II.6. At the time, this was a theoretical prediction which was confirmed by atmospheric detections afterwards. These two waves have their own dispersion relations $\omega(k_x)$ which depart from the behaviors of the wavebands of Poincaré and Rossby, and constitute a spectral flow of $\mathcal{N} = +2$ for the upper Poincaré waveband. Indeed, the two branches of frequencies cross the frequency gap between the wavebands, as shown on Figure II.6. This spectral flow, along the fact that the rotation of the Earth breaks time-reversal symmetry, raised the question as to whether these modes are topologically protected, which is what [141] found. Let us first explicitly show that time-reversal symmetry is broken by f . With the notations introduced in Section II.2, the wave equation is

$$\partial_t \begin{pmatrix} v_x/c \\ v_y/c \\ \eta/h \end{pmatrix} = \begin{pmatrix} 0 & f & -c\partial_x \\ -f & 0 & -c\partial_y \\ -c\partial_x & -c\partial_y & 0 \end{pmatrix} \begin{pmatrix} v_x/c \\ v_y/c \\ \eta/h \end{pmatrix}. \quad (\text{II.37})$$

Time-reversal symmetry is the reversal of the direction of the variable t as a coordinate. In other words, time-reversal amounts to change the sign of ∂_t and the velocities v_x and v_y . Under this transformation, the equation becomes

$$-\partial_t \begin{pmatrix} -v_x/c \\ -v_y/c \\ \eta/h \end{pmatrix} = \begin{pmatrix} 0 & f & -c\partial_x \\ -f & 0 & -c\partial_y \\ -c\partial_x & -c\partial_y & 0 \end{pmatrix} \begin{pmatrix} -v_x/c \\ -v_y/c \\ \eta/h \end{pmatrix}, \quad (\text{II.38})$$

yielding

$$\partial_t \begin{pmatrix} v_x/c \\ v_y/c \\ \eta/h \end{pmatrix} = \begin{pmatrix} 0 & -f & -c\partial_x \\ +f & 0 & -c\partial_y \\ -c\partial_x & -c\partial_y & 0 \end{pmatrix} \begin{pmatrix} v_x/c \\ v_y/c \\ \eta/h \end{pmatrix}. \quad (\text{II.39})$$

For non-zero f , one does not end up on the same equation. Therefore, the Coriolis force breaks time-reversal symmetry. This is the key ingredient identified in condensed matter for unidirectional topological modes to appear. What is interesting here, is that the equator is a point on the y axis where $f = 0$. At this particular point, time-reversal symmetry is restored. The interface between the Northern ($f > 0$) and Southern ($f < 0$) hemispheres is a point of contact between domains where time-reversal symmetry is broken. This is generic of the topological analysis: a discrete symmetry is broken almost everywhere, and a point where it is locally restored is a degeneracy point in local dispersion relations, which thus becomes a topological interface where a topological mode is trapped. [141] calculated that, in the parameter space (k_x, k_y, f) , the Berry curvature of the waves was singular at the origin. This Berry-Chern monopole bears a charge $\mathcal{C} = +2$ for the upper Poincaré waves,

II. Wave topology

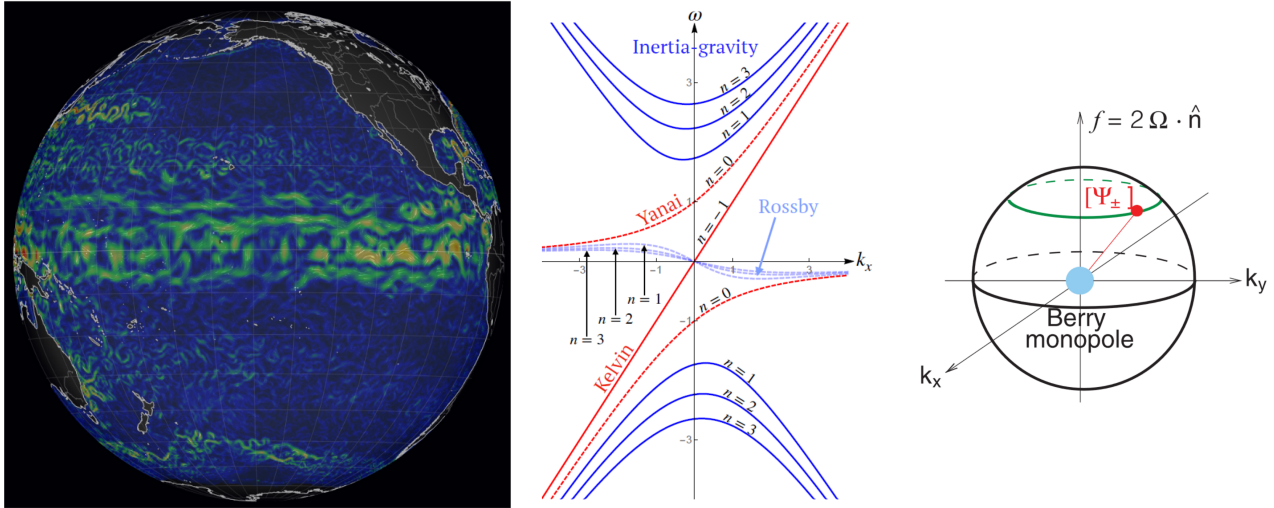


Figure II.6: Equatorial waves propagate in the ocean on Earth. **Left:** The currents of the pacific ocean on May 27th, 2018 show waves trapped at the equator¹. **Middle:** The Yanai and Kelvin waves cross the frequency gaps between the wavebands². **Right:** Their existence is imposed by the Berry-Chern monopole of charge $\mathcal{C} = +2$ found in parameter space, asserting that the equator is a topological interface³.

¹Credits: database <https://earth.nullschool.net> ²Credits: [198] ³Credits: [141].

$\mathcal{C} = -2$ for the lower Poincaré and $\mathcal{C} = 0$ for the Rossby waveband. In agreement with the index theorem, these topological charges explain the spectrum found by Matsuno. Indeed, the lower Poincaré waveband must lose two branches as k_x increases from $-\infty$ to $+\infty$, the upper Poincaré gains two, and the Rossby waveband gains as many as it lost. These exchanges of branches are realized by the Kelvin and Yanai waves.

These results opened an avenue of research, as one wonders what could be the other consequences of topological properties of waves in geophysical fluids. In the case of equatorial waves, the topological modes are trapped at the interface $f = 0$, and are therefore bulk modes of the atmosphere and the ocean. However, it has been known for a long time that coasts are able to trap waves. These coastal waves were found by Kelvin in 1880, who calculated that they were exponentially trapped close to the coast, i.e the edge of an oceanic basin [196]. Under the light of the previous study, this fact suggests a bulk-boundary correspondence between a Chern number and the actual edge of the ocean, which is indeed what was found by [197]. In this model, a boundary is put at $y = 0$ in an f -plane approximation of shallow water waves. Thus f is constant and the only inhomogeneity comes from the existence of the edge. They found that the unidirectional edge modes at the coast found by Kelvin were of topological origin from Berry-Chern monopoles of charge $\mathcal{C} = 1$.

II.4.ii The Lamb wave

Shortly after establishing the topological origin of Kelvin and Yanai waves, the same team investigated another famous wave problem of geophysical fluid dynamics: the disturbances of a compressible stratified atmosphere. When a non-rotating compressible fluid is in a gravity field \mathbf{g} , an equilibrium can only exist when a pressure force balances the weight in the hydrostatic equation

$$\nabla P_0 = \rho_0 \mathbf{g}. \quad (\text{II.40})$$

The gravity field imposes a pressure gradient in order to be balanced, which in turn imposes a density gradient by compressibility $\nabla \rho_0$ ³. Therefore, as a rule, gravity imposes density stratification. Two kinds of waves propagate in such a medium, the same which are found in stars: acoustic waves and internal gravity waves. Interestingly, Lamb [12] found an edge mode in isothermal atmospheres,

³This would not be true in an incompressible fluid, which would have $\rho_0 = \text{cst}$ and a non-zero pressure gradient, and only the pressure would be stratified. Incompressibility is never assumed for modelling atmospheres.

II. Wave topology

subsequently called Lamb wave which was presented in Section I.1. This acoustic mode is exponentially trapped at the bottom boundary of the atmosphere, close to the ground, which makes it able to travel long distances. The existence of this boundary mode, in addition to the fact that vertical mirror symmetry $z \mapsto -z$ is expected to be generically broken by gravity $-ge_z$ and stratification, suggested here a possible topological feature. In order to perform the topological analysis, the evolution equation of linear perturbations needed to be written down as a Schrödinger-like equation, which they managed to obtain for 2D isothermal plane-parallel atmospheres. The equation for linear adiabatic perturbations of this model reads

$$i\partial_t \begin{pmatrix} \tilde{v}_x \\ \tilde{v}_z \\ \tilde{\Theta} \\ \tilde{p} \end{pmatrix} = \begin{pmatrix} 0 & 0 & 0 & -ic_s \partial_x \\ 0 & 0 & iN & -ic_s \partial_z - iS \\ 0 & -iN & 0 & 0 \\ -ic_s \partial_x & -ic_s \partial_z + iS & 0 & 0 \end{pmatrix} \begin{pmatrix} \tilde{v}_x \\ \tilde{v}_z \\ \tilde{\Theta} \\ \tilde{p} \end{pmatrix}. \quad (\text{II.41})$$

This symmetric form, for which the 4×4 operator involved is Hermitian with respect to the canonical scalar product, was obtained thanks to the change of variables

$$\begin{aligned} v'_x, v'_z &\mapsto \tilde{v}_x, \tilde{v}_z = \rho_0^{1/2} v'_x, \rho_0^{1/2} v'_z, \\ p' &\mapsto \tilde{p} = \rho_0^{-1/2} c_s^{-1} p', \\ \rho' &\mapsto \tilde{\Theta} = \rho_0^{-1/2} \frac{g}{N} (\rho' - \frac{1}{c_s^2} p'), \end{aligned} \quad (\text{II.42})$$

where c_s is the speed of sound, N is the buoyancy frequency (see Section I.2) and S is the combination of terms

$$S = \frac{c_s}{2g} \left(N^2 - \frac{g^2}{c_s^2} \right). \quad (\text{II.43})$$

Interestingly, both S and N break the vertical mirror symmetry. Indeed, both take a sign in Equation (II.41) under the transformation $\partial_z \mapsto -\partial_z$ and $v'_z \mapsto -v'_z$. Upon studying the symmetries of this problem, [199] defined a new symmetry which they called *stratification symmetry*, which is closely related to the vertical mirror symmetry. It is defined by the action of $\partial_z \mapsto -\partial_z$ along with $v'_z \mapsto -v'_z$ and $\tilde{\Theta} \mapsto -\tilde{\Theta}$. This amounts to flipping the direction of the vertical axis while keeping identical buoyancy. It is therefore broken by $S \neq 0$ only. Indeed, under this stratification symmetry, Equation II.41 becomes

$$i\partial_t \begin{pmatrix} \tilde{v}_x \\ \tilde{v}_z \\ \tilde{\Theta} \\ \tilde{p} \end{pmatrix} = \begin{pmatrix} 0 & 0 & 0 & -ic_s \partial_x \\ 0 & 0 & iN & -ic_s \partial_z + iS \\ 0 & -iN & 0 & 0 \\ -ic_s \partial_x & -ic_s \partial_z - iS & 0 & 0 \end{pmatrix} \begin{pmatrix} \tilde{v}_x \\ \tilde{v}_z \\ \tilde{\Theta} \\ \tilde{p} \end{pmatrix}. \quad (\text{II.44})$$

Thus, non-zero values of S break this discrete symmetry, which is locally restored when $S = 0$.

This problem is 4×4 , and exhibits four wavebands. Two acoustic bands, and two internal gravity bands, each kind found with positive or negative frequencies. [199] found that, in the parameter space (k_x, k_z, S) where N is considered an external fixed value, there are two Berry-Chern monopoles. They are localized at $(k_x, k_z, S) = (\pm N/c_s, 0, 0)$ and bear charges $C = \mp 1$ for the upper acoustic waveband. One thus concludes that the Lamb wave is a topological edge mode, protected by these charges. Interestingly, these results suggest that if an atmosphere has a profile $S(z)$ which changes sign somewhere in the bulk of the atmosphere, this region would be a topological interface. In such a situation, a Lamb-like wave would be trapped at the altitude z^* where $S(z^*) = 0$. Unfortunately, the models of atmospheres considered by [199] showed that $S < 0$ in general. This is why Lamb waves are always edge modes at the bottom boundary of atmospheres, and have not been seen to propagate at mid-altitude.

As time-reversal symmetry is not broken in this problem, there is no net spectral flow. The Lamb or Lamb-like waves are found in pairs of branches, as is shown on Figure II.7. They are still topologically protected, but are not unidirectionally propagating. In a following study, [200] found that if

II. Wave topology

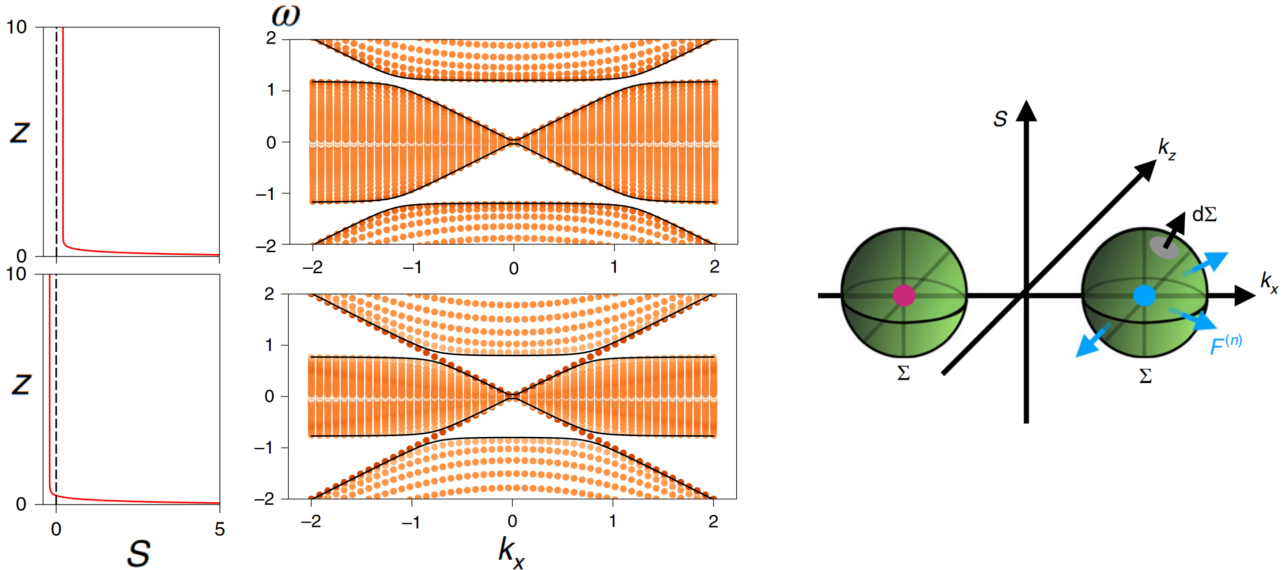


Figure II.7: Atmospheric Lamb-like waves propagate across the frequency gap between internal gravity waves and acoustic waves, as found by [199]. These waves propagate if an altitude where $S = 0$ exists in the atmosphere, as proved by the spectra of the two models $S(z)$ on the left¹. **Right:** in the parameter space (k_x, k_z, S) , two Berry-Chern monopoles are found, with opposite charges ± 1 .

¹Adapted from [199].

one would introduce a breaking of time-reversal symmetry with rotation in this problem, one could eliminate one of the two Lamb-like branches to obtain a solitary unidirectional topological branch.

II.4.iii Topological modes elsewhere in physics

As presented above, topological modes have been identified first in the condensed matter community in the 70s and 80s, explaining the quantized electrical transport of the Quantum Hall Effect discovered experimentally in 1980 by Klitzing [181]. This breakthrough was rewarded by the 2016 Physics Nobel Prize [161, 162, 201]. From there came an avalanche of engineering-oriented applications of topological properties of materials. Let us now review the key references of the considerable literature on this subject in condensed matter, fluid dynamics, plasma physics, acoustics, elasticity, optics and photonics, active and soft matter, chemistry, quantum computing, and modern developments of the theory. The aim is to present the wide range of applications of topology across the fields of physics, which motivated the investigation of its effects in astrophysical fluids.

After the successful explanation of the Quantum Hall Effect, topology in condensed matter gained a new level of attraction in 2005 with the arrival of graphene, in which was experimentally observed topology-protected modes [163, 164, 202, 203, 204]. This 2D material was readily adapted for the application of Dirac's equation. Generalizations to 3D materials came two years later [164, 205, 206], which unveiled a richer topological classification. From 2006 onward, experiments evidenced topological modes in quantum wells and semiconductors of various compositions, by showing directly the spectral flow in the dispersion relations using angle-resolved photoemission spectroscopy (ARPES) [207, 208, 209, 210, 211, 212, 213, 214, 215, 216]. Investigations on other broken symmetries protecting topological modes were lead, such as the mirror symmetry [217], strain gradients [218], or materials under time-periodic external parameters called Floquet topological insulators [219, 220]. Many reviews exist in the literature, in which more details can be found on topological insulators in general [221, 222], on the theory of topology [223], on experimental realizations [224, 225], or on 3D materials [206, 226].

As presented above, topology was applied to geophysical waves in 2017 [141], which triggered other developments of topology in fluids. For instance, a difficulty arose when it was noted that a

II. Wave topology

Chern number is well-defined on a compact space, which is the case of the Brillouin zone in materials. In 2D fluids however, (k_x, k_y) is an unbounded space, so the Chern number can only be well-defined as it was introduced in the sections above, as associated to a degeneracy point. Therefore in fluids and in continuum media, a Chern number is attributed to such a degeneracy point. In lattices, the (k_x, k_y) space is compact by periodicity, and a Chern number is attributed to the whole system. The bulk-boundary correspondence can either be re-established by adding odd viscosity [227, 228], which then attributes a Chern number per phase in the fluids and edge modes at interfaces as $\mathcal{N} = \Delta\mathcal{C}_{\text{left-right}}$. Or one can compute directly the Chern number of the interface in a 3D parameter space, in the way it was presented in Section II.3 and as [141] did. In the rest of this thesis, a 3D parameter space will always be used to avoid such complications. The bulk-boundary correspondence for equatorial waves was investigated from a mathematical standpoint by [190] who found what conditions make it break. The role of boundary conditions in fluids has also been investigated, as they sometimes appear to violate the bulk-edge correspondence [229].

Another specific difficulty of some waves in fluids is the incompressibility condition $\operatorname{div} \mathbf{v} = 0$ which does not fit in a Schrödinger-like equation $i\partial_t \mathbf{X} = \hat{\mathbf{H}}\mathbf{X}$. This was studied by [230] who gives a general way to still perform a topological analysis with such flows.

A unidirectional edge mode was found in rotating convection experiments and numerical simulations [231, 232], which had the additional property of being particularly robust to deformations of the boundary. These properties strongly hinted towards a topological mode, and the Chern number associated to its origin was found soon after [233].

Studies of topological waves in magnetized plasma started mid 2010s, when a few independent works found Berry curvature and Berry-Chern monopoles in linearized MHD equations [234, 235, 236]. After that, a number of different topological modes were found, starting with a gaseous plasmon polariton, propagating at an interface plasma-vacuum [237]. Simultaneously, the same team found that Alfvén waves have a Chern number $\mathcal{C} = 1$, associated with an edge mode observed in tokamaks which propagates where the magnetic shear goes to zero [238]. An other topological mode was found in plasma crystals recently [239], as well as a topological Langmuir-cyclotron wave in magnetized plasmas identified previously in numerical simulations [240, 241]. Studies of extensions to non-Hermitian situations are reported [242].

A comprehensive description of topology in plasma physics is found in the two reviews [243, 244].

The idea that topology could protect quantized, non-reciprocal emission of waves in condensed matter suggested interesting applications in acoustic waves. Topological acoustics were demonstrated first in 2015 by [245], [246] and [247] who all made the edge modes appear by breaking time-reversal symmetry with airflows. Soon after, [248] and [249] imaged directly the spectral flow of these acoustic edge modes, in two different types of sonic crystals. The theory of edge acoustic modes on curved surfaces was studied [250], as well as Floquet topological acoustics [251]. The cause for the great attraction that followed is the one-way acoustic transport whose exceptional robustness to defaults and obstacles is guaranteed by topology. This field is oriented towards engineering applications. It developed quickly in one decade, and already investigates non-Hermitian extensions [252] and nonlinear topological modes (e.g. [253]). Several reviews on the topic can be found [254, 255, 256].

Similar results have been found in elastic waves, first in 2009 when topological phonons were unveiled as modes of protein microtubes in cells [257], and later in filamentary structures [258], followed soon after by the general theory of topological phonons [259]. Studies of such modes in metamaterials [260, 261], phononic crystals [262], rotating media [263], optomechanical cavities [264] and graphene [265] followed, also interested in the potential applications of one-way robust transport. Various topological phonons were then found, and classified according to the broken symmetries involved [266]. Up to this point, the topological modes were edge modes, until interface modes were engineered by [267]. See these three reviews on topological elastic waves for more details and perspectives [268, 269, 270].

Topological modes of electromagnetic waves in crystals breaking time-reversal symmetry were

II. Wave topology

predicted in 2008 [271, 272]. They were observed in experiments one year later [273], with the signature of topological modes: unidirectional with no backscattering. It attracted many following studies of topological optics and photonics which took advantage of the one-way transport and its robustness [274, 275, 276, 277, 278] and managed to directly image the electromagnetic edge modes [279]. In parallel, Floquet topological modes were also designed and observed where a periodic spatial dimension plays the role of time [280]. Edge modes were then studied in 3D materials [281, 282]. Today, topological photonics is a full-fledged field of research oriented towards engineering applications, for instance the design of on-chip topological metamaterials [283] and topological lasers [284, 285, 286, 287]. Some topological electromagnetic modes have particularly great robustness to fabrication defaults [288].

More details on topological photonics in the reviews [289, 290, 282].

It is now clear that topological waves appear in any medium where some symmetry is broken, which is often the case in active and biological materials. In 2016, [291] showed that self-propelled bacteria could be directed by controlling topological defects of anisotropic media, the topological charges acting as attractors and repellers. They were not Chern numbers, and this study did not involve topological waves. One year later however, [292] designed an active liquid breaking time-reversal symmetry in which a topological sound wave propagated, opening the way to the role and applications of such waves in active matter. Colloidal particles and chiral grains [293, 294], dissipation by active processes [295, 296], and active metamaterials [297, 298] all manifest topologically protected sound edge modes. They even have been observed in bacterial colonies [299]. [300] presents a comprehensive review of the role of topology for active matter research. An extensive presentation of the role of topology in soft and biological matter is found in [301], which shows that topological numbers other than the Chern number are relevant, for instance linking numbers .

The suggested applications of topology reached the chemistry community, who saw interesting opportunities for materials chemistry [302, 303, 304] and catalytic chemistry [305, 306, 307], where the topological surface modes would be used for efficient surface reactions. Research is still ongoing towards harnessing edge modes for high-performance catalysts [308]. Conversely, quantum chemistry has been able to help in predicting many more topological insulators than what was previously known [309, 310].

Topological modes have attracted the attention of the quantum computing community, again for their robustness but especially for their energy levels isolated in an energy gap. Such an isolation leads to minimal coupling with other modes and immunity to quantum decoherence, the main issue for quantum computing. These considerations appeared in 2000, when topological modes in superconductors were discovered [311, 312, 313], with the promising perspective of fault-tolerant quantum computation [314, 315]. Once the statistics of these so-called non-Abelian anyons were elucidated, and they were identified as Majorana zero-modes, many teams worked towards experimental implementation in supraconducting nanowires [316, 317, 318, 319, 320], until their protection [321] and spin measures [322] were conclusively demonstrated. This year, Microsoft published the performance of the technology they use in their Majorana 1 quantum chip [323].

For more details, see the review [221] and an introduction on topological quantum computing in [324].

Today, topology has percolated in many domains of physics and belongs no longer to condensed matter but is now a transverse theory. The main frontiers of this theory are threefold, in the form of higher-order topological insulators [325, 326, 327, 328, 329, 330], non-Hermitian topology [331, 332, 333] and nonlinear topology [334, 335, 336].

This thesis comes back to non-Hermitian topology in Part IV.

See [337] for a transverse review on topological waves in classical systems, and [338] for a short introduction on topological mechanics.

Motivation and aims of the thesis

The general goal of this thesis has been to point the light of wave topology towards a number of selected wave problems in astrophysical fluids, a line of research which had not been pursued before, and there were two questions. The first was to identify whether indeed, some waves in some astrophysical fluids were submitted to underlying topological constraints. These waves would then be said to be topologically non-trivial, in the sense defined and discussed in Chapter II.

The works presented in this thesis are focused on waves in planetary and stellar interiors, whose great variety of structure, dynamical and thermodynamical processes are known to make rich wave problems, possibly favorable for topological properties. The second general question has been to establish what could be learned about waves and the objects in which they propagate from their topological properties. In other words, what can be predicted from the fact that such waves are topologically non-trivial? Tools from topology allow to establish constraints on the spatial localization, the robustness to perturbations, and sometimes on the unidirectionality of certain modes, the topological modes. If they are identified, the unique properties of these modes can be harnessed for an understanding of a particular phenomenology of the objects where they would be found. For instance, the topological modes identified by Delplace, Marston and Venaille in 2017, are known to propagate in the ocean at the equator, only towards the West. They cannot propagate eastward, and this property is implicated in the El Niño phenomenon, this heat wave from Asia to the Americas. Wave topology provides a way of analyzing whether the waves could support such a unidirectional phenomenon.

Waves in astrophysical fluids have long been studied, as they are an excellent way of probing stellar bodies like stars and planets, but also because they play crucial dynamical roles. Linear instabilities, transport of energy and angular momentum shape stars, accretion and protoplanetary discs, galaxies, planets and atmospheres. Every community studying these objects studies the waves propagating in them. As wave topology is a new, complementary technique of analysis yet to be exploited, to develop this technique serves to advance our understanding of a number of phenomena in all these astrophysical objects.

The order of the chapters of this manuscript does not reflect the chronology of the works of this thesis. Instead, the choice was made to present a synthesis with an increasing level of complexity of the topological analysis. Indeed, Chapter III is a problem of inertial waves with one monopole, and a clear spectral flow is identified. Chapter IV discusses three monopoles that may collide, and a spectral flow which may disappear. Chapter V studies waves in stellar interiors, showing the role of spherical geometry and the presence of two monopoles of opposite charges. Chapter VI studies these waves in a hydrodynamical simulation of the solar interior, and finds that the topological waves are rather delocalized, which is uncommon in the topological physics literature. Chapter VII also discusses the solar interior, exhibiting the importance of the Berry phase of acoustic modes. Chapters VIII and IX discuss linear instabilities from the point of view of non-Hermitian topology and the role of discrete symmetries.

Part II

Geophysical and astrophysical inertial waves

Inertial waves in convective zones

Résumé

La plupart des étoiles possède une zone convective. Cette région du fluide stellaire a la propriété particulière de n'avoir presque aucune flottaison, étant quasiment stratifiée adiabatiquement ($\frac{\partial P_0}{\partial \rho_0} \simeq (\frac{\partial P}{\partial \rho})_S$, ou de manière équivalente $\gamma \simeq \Gamma_1$), la force résultante de la compétition entre la poussée d'Archimède et du poids est presque nulle de sorte qu'on a $N^2 \sim 0$. Dans ces régions, aucune onde de gravité ne se propage ; mais si l'étoile est en rotation, des ondes inertielles peuvent se propager, soutenues par la force de Coriolis. Le travail présenté dans ce chapitre étudie ces ondes purement inertielles, et montre qu'elles ont une topologie non-triviale. Un monopole de Berry-Chern est trouvé à l'équateur de l'étoile, avec une charge $\mathcal{C} = 1$. Ce résultat est utilisé pour interpréter l'existence d'un mode d'oscillation des zones convectives en rotation parfois appelé mode de Busse, qui explique sa propriété unique d'être purement prograde. De plus, il est montré que les ondes inertielles ont une singularité de phase dans l'espace de Fourier, une signature topologique robuste et observable de leur propagation.

Most stars possess a convective region. These regions have the particular property of having close to no buoyancy as they are quasi adiabatically stratified $\frac{\partial P_0}{\partial \rho_0} \simeq (\frac{\partial P}{\partial \rho})_S$, or equivalently $\gamma \simeq \Gamma_1$. The net resultant of weight and Archimedes' force is thus almost zero, such that $N^2 \sim 0$. In these regions, no gravity wave therefore propagates; if the star rotates however, inertial waves freely propagate, being supported by the Coriolis force. The work presented in this Chapter focuses on these waves, and show that they have a non-trivial topological structure. A Berry-Chern monopole is found at the equator with a Chern number of $\mathcal{C} = 1$. I use this result to interpret the existence of a columnar mode of oscillation previously known as the Busse mode as being a topological mode, explaining its unidirectional motion. I further show that inertial waves present a phase degeneracy in Fourier space, an observable signature of their propagation imposed by topology.

This work was motivated by the presentation of Dr. Rekha Jain at AMS80, Mathematical Aspects of Geophysical and Astrophysical Fluid Dynamics in Newcastle, January 2024. Her own work on inertial waves in convective zones exhibited what appeared to be a spectral flow of +1, hinting to the possible topology of these waves. Furthermore, the physical conditions constituted an interesting complementary case to the previous study of Delplace et al. [141], as it is another inertial wave problem in which a Chern number is found. [141] discussed shallow water (2D) waves, and found a Chern number of 2 at the equator. Here is found a Chern number of 1 for inertial waves in 3D convective zones, again at the equator. The exhibition of a purely prograde topological mode in convective zone suggests a special involvement in angular momentum transport. Furthermore, it provides further characterization of oscillation modes which are currently actively searched in the Sun and other stars like γ Dor whose core inertial modes have been detected recently.

The results presented in this chapter have been published in *Wave topology of stellar inertial oscillations*, Leclerc, Laibe, Perez, **Physical Review Research** 2024 [339].

Wave Topology of Stellar Inertial Oscillations

Armand Leclerc,* Guillaume Laibe, and Nicolas Perez
ENS de Lyon, CRAL UMR5574, Université Claude Bernard Lyon 1, CNRS, Lyon, F-69007, France
(Dated: November 14, 2024)

Inertial waves in convective regions of stars exhibit topological properties linked to a Chern number of 1. The first of these is a unique, unidirectional, prograde oscillation mode within the cavity, which propagates at arbitrarily low frequencies for moderate azimuthal wavenumbers. The second one are phase singularities around which the phase winds in Fourier space, with winding numbers $\nu = \pm 1$ depending on the hemisphere. Phase winding is a collective effect over waves propagating in all directions that is strongly robust to noise. This suggests a topology-based method for wave detection in noisy observational data.

I. INTRODUCTION

Helioseismology has shed unparalleled light on the Sun's interior, and with it stellar interiors in general. While many acoustic modes with mHz frequencies have been identified and used to constrain the rotation and sound speed profiles [1], other waves are expected to bring complementary information to the surface. Solar internal gravity waves with $10^2 \mu\text{Hz}$ frequencies would bring constraints on the solar core, but confirmation of their observation is still missing [2]. In recent years, a third kind of waves has attracted a great deal of attention. Inertial waves propagate owing to solar rotation with 10^2nHz frequencies, and are sensitive to the entropy gradient in the convective zone, a quantity to which acoustic modes are essentially insensitive [3]. These waves control the differential rotation of the convective zone and cause it to depart from the Taylor-Proudman columnar structure [4]. Rossby waves [5–7] and inertial waves of higher frequencies [8, 9] have unequivocally been observed at the solar surface. Inertial modes of convective cores of γ Doradus stars have also been observed [10], as well as Rossby waves [11–13]. Inertial waves are thus an important channel of modern stellar seismology, which motivates further characterization of their oscillation modes.

In parallel, recent studies showed a connection between topology and geophysical and astrophysical waves, providing new insight on the properties of global modes [14–20]. In this study, we show that stellar inertial waves possess topological properties, characterized by Chern numbers of ± 1 . This result gives a topological origin to a unidirectional inertial wave propagating eastward at arbitrarily low frequencies. It also explains the existence of a phase singularity of the polarization relations of the waves in Fourier space, to which is associated a winding of the phase of ± 1 . This property provides a novel way of identifying waves. We give a procedure to use this singularity as a signature of the wave and help future identification of seismic signals.

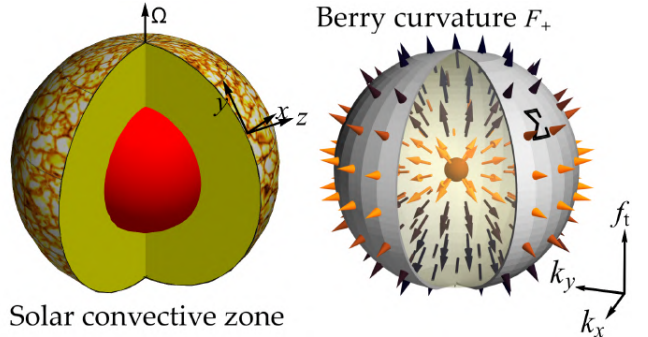


FIG. 1. Physical space and parameter space of solar inertial waves. Left: coordinates of the convective zone (yellow). Right: The Berry curvature of the upper inertial waveband is singular at the origin of the parameter space $k_x = k_y = f_t = 0$. Brightness indicates the norm of F_+ .

II. WAVE TOPOLOGY OF INERTIAL WAVES

Consider the rotating convective region of the Sun as represented on Fig. 1. The medium is radially stratified by the gravity field $-g\mathbf{e}_z$. Following [21, 22], we assume that the buoyancy frequency $N^2 = -g\frac{d\ln\rho_0}{dz} - \frac{g^2}{c_s^2}$ is zero and the sound speed c_s is uniform. The linearized equations of motions describing fully compressible adiabatic perturbations (v', p', p') of this rest state (ρ_0, p_0) are [23]

$$\partial_t v' = -2\Omega \wedge v' - \frac{1}{\rho_0} \nabla p' + \frac{\rho'}{\rho_0^2} \nabla p_0, \quad (1)$$

$$\partial_t \rho' = -\rho_0 \nabla \cdot v' - v' \cdot \nabla \rho_0, \quad (2)$$

$$\partial_t p' + v' \cdot \nabla p_0 = c_s^2 (\partial_t \rho' + v' \cdot \nabla \rho_0). \quad (3)$$

Velocity components are coupled by the so-called traditional and non-traditional Coriolis parameters $f_t = 2\Omega \sin \theta$ and $f_{nt} = 2\Omega \cos \theta$ with θ the latitude. We follow [21, 24–26] and retain compressibility in the equations. Compressibility allows to formulate the problem under the form of a linear eigenvalue problem $\mathcal{L}X = \omega X$, without bringing any additional complexity to the derivation. Enforcing $\operatorname{div} u' = 0$ would introduce unnecessary technical difficulties [27]. Incompressibility is recovered here as a genuine limit of the model.

* armand.leclerc@ens-lyon.fr

Essential properties of the inertial waves are captured by an f -plane approximation of the rotation, which amounts to assuming that f_t and f_{nt} are constants [28]. We perform the change of variables $(v, p) = (\rho_0^{1/2}v', \rho_0^{-1/2}p')$ which symmetrizes the equations. Plane-wave solutions $\exp(-i\omega t + ik_x x + ik_y y + ik_z z)$ are then solutions of

$$\omega \begin{pmatrix} v_y \\ v_z \\ v_x \\ p \end{pmatrix} = \begin{pmatrix} 0 & 0 & -if_t & c_s k_y \\ 0 & 0 & if_{nt} & c_s k_z + iS \\ if_t & -if_{nt} & 0 & c_s k_x \\ c_s k_y & c_s k_z - iS & c_s k_x & 0 \end{pmatrix} \begin{pmatrix} v_y \\ v_z \\ v_x \\ p \end{pmatrix}, \quad (4)$$

where $S \equiv \frac{c_s}{2} \frac{d \ln \rho_0}{dz} = -\frac{g}{2c_s}$ is the stratification parameter, which opens a frequency gap between acoustic and internal gravity waves [15, 17].

Equation (4) has four eigenvalues, corresponding to two acoustic wavebands and two inertial wavebands. Acoustic waves propagate at frequencies $\omega^2 \geq \max(4\Omega^2, S^2)$, whereas inertial waves propagate at frequencies $\omega^2 \leq 4\Omega^2$. Hence, stratification also opens a frequency gap between inertial and acoustic waves, as long as $S^2 > 4\Omega^2$, which is the case for the Solar convective region ($-S \sim 10^3 \Omega$ from [17] and [4]). In the following, we shall refer to waves with frequencies $0 < \omega_+ < 2\Omega$ as upper (+) inertial waves and wavebands, and those with frequencies $-2\Omega < \omega_- < 0$ as lower (-) inertial waves. Upon inspection of the plane-waves dispersion relation (i.e. the characteristic equation of the matrix in Eq. (4)), the upper and lower inertial waves degenerate at $\omega_+ = \omega_- = 0$ when $k_x = k_y = f_t = 0$, for any f_{nt} , k_z and S . As the degeneracy do not depend on f_{nt} , k_z and S , we treat them as external parameters.

We aim to determine the properties of the waves governed by Eq. (4) that come from topological constraints over the parameter space [14–20]. Let X_+ denote the eigenvector of Eq.(4) corresponding to the upper inertial waveband. The mathematical space of interest is the fiber bundle $\{\lambda X_+(k_x, k_y, f_t) | \lambda \in \mathbb{C}\}$, which contains all polarization vectors of these waves across the parameter space (k_x, k_y, f_t) . The curvature of the fiber bundle, so-called Berry curvature, is

$$F_+ \equiv i\tilde{\nabla} \wedge (X_+^\dagger \cdot \tilde{\nabla} X_+), \quad (5)$$

where $\tilde{\nabla} \equiv (\partial_{k_x}, \partial_{k_y}, \partial_{f_t/c_s})^\top$. F_+ is a real-valued vector field, which quantifies how the polarization vector X_+ is transported when changing the values of parameters (k_x, k_y, f_t) (similarly to Riemannian curvature for transport on Riemannian manifolds). This vector field is divergence-free where it is non-singular, similar to the electrostatic field generated by a point charge. The Berry curvature is singular whenever the frequency of the wave matches the frequency of another wave of the system, i.e when two eigenvalues of Eq. (4) degenerate. This occurs between the lower and upper inertial waves at $\omega_+ = \omega_- = 0$ for $k_x = k_y = f_t = 0$. Figure 1 shows F_+ around the singular degeneracy point. The topology of the manifold of polarization vectors is then characterized

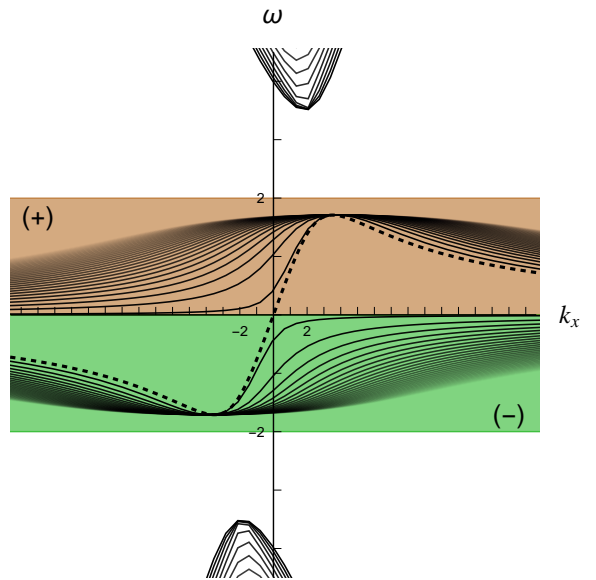


FIG. 2. Dispersion relation of the modes in the β -plane approximation. One mode transits from the lower (-) inertial waveband to the upper one (+), satisfying the spectral flow condition Eq.(9). Solid lines represent solutions with non-zero v_y , while dashed lines indicate solutions with zero v_y . Frequencies are shown for $k_z = 1.5$ and $S = -3$, in units of Ω and $c_s \Omega^{-1}$.

by an integer called the Chern number \mathcal{C} , which is analogous the Euler characteristic for geometric surfaces. It is defined by

$$\mathcal{C} \equiv \frac{1}{2\pi} \oint_{\Sigma} F \cdot d\Sigma, \quad (6)$$

where Σ is any surface enclosing the degeneracy (for example the gray sphere in Fig. 1). The Chern number is the flux of F_+ outward from its singular point. In this problem, the Chern number evaluates to

$$\mathcal{C}_+ = 1. \quad (7)$$

As the sum of Chern numbers over the bands must be zero [29], one necessarily has for the lower inertial waveband

$$\mathcal{C}_- = -1. \quad (8)$$

We conclude that stellar inertial waves are *topologically non-trivial*, similarly to other waves in geophysical and astrophysical media that were found to have topologically-charged degeneracy points [14–17, 23].

III. A SPECTRAL FLOW IN INERTIAL STANDING MODES

The propagation of peculiar edge or interface modes stands out as the manifestation of the existence of non-zero Chern numbers in wave problems [14–17, 23, 30].

They cross frequency gaps between wavebands, and exhibit unique properties such as unidirectionality. These modes exist in virtue of the index theorem [31], which characterizes the *spectral flow*, a property of the dispersion relation $\{\omega_n(k_x)\}_n$ (where n labels the branches) of modes propagating in a medium with varying parameters instead of plane waves in a homogeneous medium. In the case of a single degeneracy point, a waveband i is not composed by the same number of branches in the two limits $k_x \rightarrow \pm\infty$. Referring to the difference between these branch numbers as $\Delta\mathcal{N}_i$, the index theorem states that $\Delta\mathcal{N}_i = \mathcal{C}_i$: the Chern number gives the number of modes leaving/arriving into the waveband when k_x increases. For the inertial waves,

$$\Delta\mathcal{N}_+ = -\Delta\mathcal{N}_- = +1. \quad (9)$$

Equation 9 guarantees the presence of a mode of topological origin transiting between the (-) and the (+) bands, similarly to what has been found in other studies (e.g. Fig.10 of [32], or Fig.5 of [26]). This mode is the stable counterpart of Busse columns, the most unstable mode of a convectively unstable rotating fluid [33]. It is sometimes called the Busse mode. It is stable here as we study neutral stratification. This wave has been seen in numerical works [32, 34], as well as in the analytical study of [26] which models the equator as a channel with $f_t = 0$ and impenetrable boundaries. It also has been identified recently in a DNS of nonlinear inertial waves in the Sun [35]. The value of the Chern number provides an explanation as to why it is purely prograde.

We confirm the existence and the properties of this topological mode by finding the normal modes of Eqs. (1)-(3) under the β -plane approximation. The latter consists in expanding the spatial dependence of f_t and f_{nt} at first order in latitude y , which can be expressed as

$$f_t = \beta y, \quad (10)$$

$$f_{nt} = 2\Omega. \quad (11)$$

The plane-parallel geometry of the β -plane retains the frequency behavior of the modes, but does not capture the columnar structure found in shell cavities [33, 34].

The equations of normal modes associated to linear perturbations of the form $\exp(-i\omega t + ik_x x + ik_z z) (v_x(y) \ v_y(y) \ v_z(y) \ p(y))^\top$ are

$$\omega \begin{pmatrix} v_y \\ v_z \\ v_x \\ p \end{pmatrix} = \begin{pmatrix} 0 & 0 & -i\beta y & -ic_s \partial_y \\ 0 & 0 & i2\Omega & c_s k_z + iS \\ i\beta y & -i2\Omega & 0 & c_s k_x \\ -ic_s \partial_y & c_s k_z - iS & c_s k_x & 0 \end{pmatrix} \begin{pmatrix} v_y \\ v_z \\ v_x \\ p \end{pmatrix}. \quad (12)$$

Boundaries in the vertical direction discretize k_z . Imposing impenetrable boundary conditions $v_z = 0$ yields $k_z = \frac{p\pi}{L}$, where L is the width of the convective region and p is a positive integer.

Equation (12) can be reduced to a single ordinary differential equation on $\phi \equiv \exp\left(\frac{4i\beta\Omega c_s k_z}{\omega^2 - 4\Omega^2} \frac{y^2}{2}\right) v_y$ (see Appen-

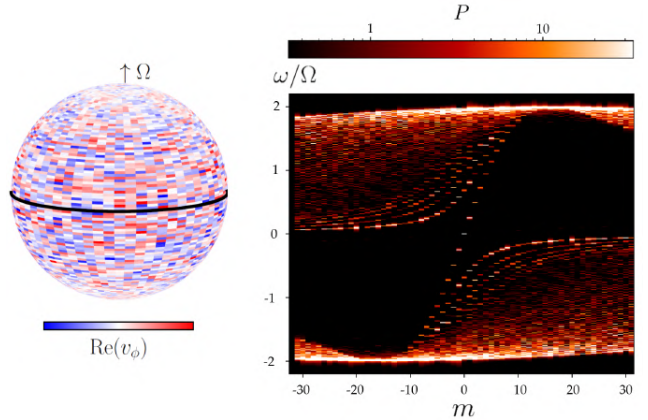


FIG. 3. A branch of modes transits between the inertial wavebands in numerical simulations of linear inertial waves on a sphere. Left: Snapshot of zonal velocity. Right: Power spectrum at the equator. Ridges, i.e. the bright regions of the power spectrum, are the normal modes. Power is measured in arbitrary units (equations are linear).

dices):

$$-\partial_{yy}\phi + (\gamma y^2 + \delta) \phi = 0, \quad (13)$$

where $\gamma = \frac{\beta^2}{\omega^2 - 4\Omega^2} (\omega^2 - c_s^2 k_z^2 - S^2 - \frac{4c_s^2 k_z^2 \Omega^2}{\omega^2 - 4\Omega^2})$, $\delta = \frac{1}{\omega^2 - 4\Omega^2} (\beta(c_s k_x \omega + 2S\Omega) + A\omega)$ and

$$A \equiv \det \begin{pmatrix} -\omega & i2\Omega & c_s k_z + iS \\ -i2\Omega & -\omega & c_s k_x \\ c_s k_z - iS & c_s k_x & -\omega \end{pmatrix}. \quad (14)$$

For $\gamma < 0$, Eq. (13) has no non-zero square-integrable solution. For $\gamma > 0$, Eq.(13) is transformed into a Weber differential equation [36] through the change of coordinate $\xi = \sqrt{2\gamma}y$

$$-\partial_{\xi\xi}\phi + \left(\frac{\xi^2}{4} - \frac{1}{2} - \left(\frac{-\delta}{2\gamma} - \frac{1}{2}\right)\right) \phi = 0. \quad (15)$$

Regularity of ϕ at infinity provides a condition for the normal modes in the β -plane model, imposing

$$\frac{-\delta}{2\gamma} - \frac{1}{2} = n - 1, \quad (16)$$

for $n \geq 1$ any positive integer. Combined with the condition $\gamma > 0$, Eq. (16) provides the dispersion relation for the normal modes. The typical latitudinal extent of the waves is $\gamma^{-1/2}$. The eigenfunctions of the modes are given by Hermite polynomials H_n with

$$\phi_n(\xi) = \exp\left(-\frac{\xi^2}{4}\right) H_{n-1}\left(\frac{\xi}{\sqrt{2}}\right). \quad (17)$$

These solutions are the normal modes that have non-zero latitudinal velocity v_y . To identify all the normal

modes, one must also determine those with zero v_y , denoted as $n = 0$. From Eq.(12), those satisfy

$$A = 0 = -\omega^3 + (4\Omega^2 + S^2 + c_s^2 k_x^2 + c_s^2 k_z^2)\omega + 4\Omega S c_s k_x. \quad (18)$$

Three modes are solutions of this equation: one inertial wave, and two acoustic waves. Analytical expressions of their dispersion relations are given in Appendices. These three modes complete the spectrum given by Eq.(16), for any radial order p and latitudinal order n . Figure 2 shows the dispersion relations obtained for all modes. It appears clearly that the $n = 0$ inertial branch transits from the lower inertial band to the upper one as k_x increases. This is the spectral flow expected from the Chern numbers $\mathcal{C} = \pm 1$ of the wavebands. This mode possesses the distinctive characteristic of being unidirectional, exclusively prograde, while the other modes can propagate either eastward or westward.

Fig. 3 confirms the presence of this prograde wave among the oscillation modes of spherical shells in numerical simulations.

IV. PHASE SINGULARITY AND WINDING

Beyond evidencing the spectral flow, we will now show a way to exploit another topological property of the inertial modes: a physical quantity known as phase winding, measuring the cumulative phase difference between two complex quantities over a closed path in the parameter space, which attracted interest in recent years, e.g. in geophysical waves [18, 19] or material sciences [37]. Non-zero Chern numbers imply the existence of phase singularities (see Appendices, or [38] for an example in condensed matter). The relative phase between two wave components exhibits a singular point in Fourier space, around which the phase winds. Phase winding changes sign when changing hemisphere. Figure 4 (left) shows that the relative phase between the zonal and vertical velocity perturbations v_x and v_z of plane-waves in an f -plane, i.e the components of the eigenvector of Eq. (4), is singular the origin of the (k_x, k_y) plane. Formally, the winding number of this phase is

$$\nu = \frac{1}{2\pi} \oint_{\Gamma} \tilde{\nabla} \arg(v_x^* v_z) \cdot dk, \quad (19)$$

where Γ can be any closed loop encircling the origin once with counterclockwise orientation. Depending on the upper (+) or lower (-) inertial waveband and the hemisphere, one finds

$$\nu_{+, \text{north}} = -1, \quad (20)$$

$$\nu_{+, \text{south}} = +1, \quad (21)$$

$$\nu_{-, \text{north}} = +1, \quad (22)$$

$$\nu_{-, \text{south}} = -1. \quad (23)$$

Physically, this value of ν means that the peaks of v_z have precisely shifted by one wavelength with respect to

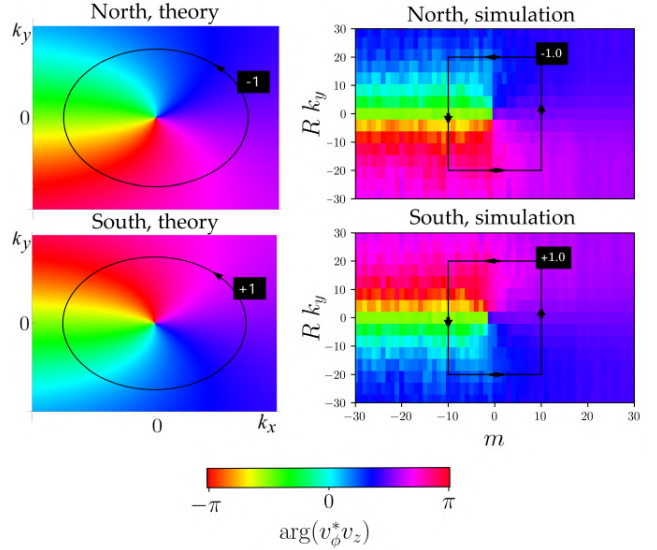


FIG. 4. Phase singularity of the upper (+) inertial waves. Left: phase in the f -plane. Right: phase found when analyzing the simulations Northern (Southern) hemisphere only.

the peaks of v_x after completing one full revolution along the contour. In contrast, the relative phases between v_y , or v_x and p , do not experience winding and remain non singular.

Using numerical simulations, we confirm that the phase singularity identified in the f -plane persists in spherical geometry. This aligns with the results of [19], who observed phase winding of Poincaré waves in the atmospheric data of the Earth, consistent with f -plane predictions. For this purpose, we solve Eqs. (1)-(3) within the solar convective zone. For simplicity, we fix the vertical wavenumber to $k_z = p\pi/L$, restricting the dynamics to a specific radial order p . We compute the two-dimensional dynamics in (θ, ϕ) for modes with radial order $p = 1$ with the code DEDALUS [39]. We use Ω^{-1} and $c_s \Omega^{-1}$ as units of time and length. The evolution equations of linear perturbations become

$$\partial_t u + 2\mathbf{e}_r \wedge u + \nabla p + 2 \sin(\theta) v_z \mathbf{e}_\phi = 0, \quad (24)$$

$$\partial_t v_z + (ik_z - S)p - 2 \sin(\theta) u \cdot \mathbf{e}_\phi = 0, \quad (25)$$

$$\partial_t p + \nabla \cdot u + (ik_z + S)v_z = 0, \quad (26)$$

where $u = (u_\theta, u_\phi) = (-v_y, v_x)$ are the angular components of the velocity in spherical coordinates, and ∇ is the nabla operator on the sphere. The evolution equations are written in a covariant way for the angular directions, a necessity for the spectral decomposition by DEDALUS. (See Appendices for details of implementation).

The fields are initialized with random values across the grid to excite all wavelengths. After solving for the evolution, the velocity data $u(t, \theta, \phi)$ and $v_z(t, \theta, \phi)$ are then Fourier-transformed in both space and time. For consis-

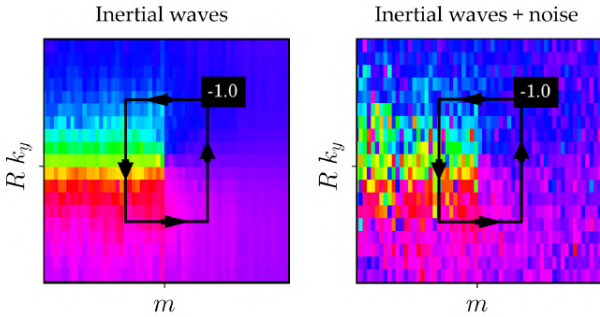


FIG. 5. The winding of the phase is robust to the addition of noise in the data. On a signal of pure inertial waves (left), or upon adding a random noise on the velocities data (right), the measurement of the winding ν still yields -1 . The amplitude of the noise is 10 times that of the initial condition of the simulation.

tency, we adopt the convention

$$\hat{f}(\omega, k_y, m) = \int f(t, \theta, \phi) e^{-i\omega t - ik_y R\theta + im\phi} dt d\theta d\phi. \quad (27)$$

This transform is computed numerically for all values of ϕ and t , but on various domains of latitude $y = R(\frac{\pi}{2} - \theta)$. The azimuthal wavenumber m is equated to Rk_x .

We compute the power spectrum of the kinetic energy $P = |\hat{v}_x|^2 + |\hat{v}_y|^2 + |\hat{v}_z|^2$ at the equator ($y = 0$) so as to extract equatorial waves. This yields the dispersion relation of the modes in an (m, ω) diagram. Figure 3 (right panel) shows this power spectrum; ridges of power indicate normal modes which are in agreement with the propagation of the topological mode found in the β -plane. In order to extract the phase singularities, we compute Fourier transforms of the data over an entire hemisphere exclusively, which yields the relative phase $\arg(\hat{u}_\phi^* \hat{v}_z)(\omega, m, k_y)$. This quantity is subsequently averaged on the frequencies of the upper inertial band $0 < \omega < 2\Omega$. Results are shown on Fig. 4(right), which reveals the phase singularity discussed above without any ambiguity. The phase winding values correspond to those of Eqs. (20)-(23).

We repeat the aforementioned analysis, adding various noises with intensities up to approximately 10 times higher than that of the initial signal (see Appendices for details). Figure 5 shows the relative phase in case of noisy data, for which the measurement of ν still yields -1 in the Northern hemisphere. The determination of the winding number is robust to a significant level of noise, a common characteristic of topological properties in physics [29].

V. CONCLUSION

Inertial waves in convective stellar regions have topological properties linked to a parameter space degeneracy at the equator and a Chern number of ± 1 . We derived

this result accounting for compressibility for both generality and simplicity, although compressible effects are not important in this problem, since frequencies of inertial and acoustic waves are of distinct orders of magnitude in the Sun.

Wave topology predicts the existence of a mode of spectral flow between the two (+) and (-) inertial bands. This mode uniquely propagates at arbitrarily low frequencies ω for moderate azimuthal wavelengths (Fig. 2) and as such, may be significant for certain stellar objects. For instance, it is expected to propagate at arbitrarily low frequencies within the convective cores of γ Dor stars, while gravity-inertial waves propagate in the outer layers. Because of their low frequencies, high-order g -modes are likely to couple with the core mode, making it a valuable probe for core dynamics [10]. This also implies that mixed modes should consistently appear in the spectra of γ Dor stars.

Wave topology further predicts a collective phase winding of ± 1 for sets of inertial waves propagating in multiple directions. Phase winding is calculated by accumulating the phase of the waves as their propagation direction varies along a closed loop in parameter space. Consequently, measuring phase winding may be more feasible using observational data than detecting individual waves, as it integrates the power spectrum across parts of the wavebands. This approach allows for observational diagnosis even when the signal is weak.

Topology ensures finally that the conclusions of this study apply to any cavity containing an equator, whether it involves a fully convective star or a convective shell zone. The rotation profile can be arbitrary as long as it is Rayleigh stable. Topological tools used in Hermitian physics are however not suited for discussing viscous damping (Ekman layer). Analyzing its effects requires a non-Hermitian topological approach [18, 40]. Fortunately, viscous damping in the Sun occurs on a much longer timescale than rotation [41], and may only affect the results of this study as small corrections.

ACKNOWLEDGMENTS

We acknowledge funding from the ERC CoG project PODCAST No 864965. AL is funded by Contrat Doctoral Spécifique Normalien.

Appendix A: Analytical derivation of modes

The system of equations Eq. (12) governing the evolution of normal modes in the β -plane can be written under the form

$$\omega v_y + i f_t v_x + i c_s \partial_y p = 0, \quad (\text{A1})$$

$$\begin{pmatrix} -\omega & i f_{nt} & c_s k_z + i S \\ -i f_{nt} & -\omega & c_s k_x \\ c_s k_z - i S & c_s k_x & -\omega \end{pmatrix} \begin{pmatrix} v_z \\ v_x \\ p \end{pmatrix} = \begin{pmatrix} 0 \\ -i f_t v_y \\ i c_s \partial_y v_y \end{pmatrix}. \quad (\text{A2})$$

The matrix in the left-hand side of Eq. (A2) involves no y -derivative, which allows us to express v_z , v_x and p as linear combinations of v_y and $\partial_y v_y$ by inverting it. Using the result in Eq. (A1) yields to an ordinary differential equation on v_y . In details, define

$$A \equiv \det \begin{pmatrix} -\omega & i 2\Omega & c_s k_z + i S \\ -i 2\Omega & -\omega & c_s k_x \\ c_s k_z - i S & c_s k_x & -\omega \end{pmatrix}, \quad (\text{A3})$$

such that $A \neq 0$ when v_y is a non-zero function. Hence,

$$v_z = \frac{1}{A} \left[\beta y \left(c_s k_x (-i c_s k_z + S) + 2\Omega \omega \right) v_y + \left((i c_s k_z - S) \omega - 2 c_s k_x \Omega \right) c_s \partial_y v_y \right], \quad (\text{A4})$$

$$v_x = \frac{1}{A} \left[i \beta y \left(S^2 + c_s^2 k_z^2 - \omega^2 \right) v_y + i \left(c_s k_x \omega - (i c_s k_z - S) 2\Omega \right) c_s \partial_y v_y \right], \quad (\text{A5})$$

$$p = \frac{1}{A} \left[-i \beta y \left(c_s k_x \omega + (i c_s k_z + S) 2\Omega \right) v_y + i \left(\omega^2 - 4\Omega^2 \right) c_s \partial_y v_y \right]. \quad (\text{A6})$$

Casting Eqs.(A5) and (A6) into Eq.(A1) yields

$$(\omega^2 - 4\Omega^2) c_s^2 \partial_{yy} v_y - 4i \beta \Omega c_s^2 k_z y \partial_y v_y + \left(\beta^2 (c_s^2 k_z^2 + S^2 - \omega^2) y^2 - \beta (c_s k_x \omega + 2\Omega (i c_s k_z + S)) - A \omega \right) v_y = 0 \quad (\text{A7})$$

The change of variable $\phi \equiv \exp \left(-\frac{i \beta \Omega k_z}{\omega^2 - 4\Omega^2} y^2 \right) v_y$ removes the second term of the left-hand side of Eq.(A7), which then reduces to

$$-\partial_{yy} \phi + (\gamma y^2 + \delta) \phi = 0, \quad (\text{A8})$$

with

$$\gamma = -\frac{\beta^2}{\omega^2 - 4\Omega^2} (c_s^2 k_z^2 + S^2 - \omega^2 + \frac{4c_s^2 k_z^2 \Omega^2}{\omega^2 - 4\Omega^2}), \quad (\text{A9})$$

$$\delta = \frac{1}{\omega^2 - 4\Omega^2} (c_s \beta (c_s k_x \omega + 2S\Omega) + A\omega), \quad (\text{A10})$$

yielding Eq. (13) discussed in the main text.

From Eq. (A1), the modes with $v_y = 0$ must satisfy $A = 0$. The three roots of this third order polynomial describe one inertial wave ($-2\Omega \leq \omega \leq 2\Omega$) and two acoustic waves ($\omega^2 \geq S^2$). Following the method of [42], we obtain the expressions of the three roots. The one corresponding to the inertial mode is

$$\begin{aligned} \omega_{\text{inertial}, n=0} &= \frac{2}{\sqrt{3}} \sqrt{c_s^2 (k_x^2 + k_z^2) + S^2 + 4\Omega^2} \times \quad (\text{A11}) \\ &\cos \left(\frac{\arccos \left(\frac{6\sqrt{3} c_s k_x S \Omega}{\sqrt{(c_s^2 (k_x^2 + k_z^2) + S^2 + 4\Omega^2)^3}} \right) - 2\pi}{3} \right). \end{aligned}$$

The two $n = 0$ acoustic modes have frequencies

$$\begin{aligned} \omega_{\text{acoustic}, n=0} &= \frac{2}{\sqrt{3}} \sqrt{c_s^2 (k_x^2 + k_z^2) + S^2 + 4\Omega^2} \times \quad (\text{A12}) \\ &\cos \left(\frac{\arccos \left(\frac{6\sqrt{3} c_s k_x S \Omega}{\sqrt{(c_s^2 (k_x^2 + k_z^2) + S^2 + 4\Omega^2)^3}} \right) + 2s\pi}{3} \right), \end{aligned}$$

where the case $s = 0$ and $s = +1$ corresponds to positive and negative frequencies respectively.

Appendix B: Non-zero Chern numbers and phase winding

Under the appropriate gauge choice ϕ_a , a normalised eigenvector of the upper inertial waveband can be written

$$\begin{aligned} \Psi &\equiv \begin{pmatrix} a \\ b e^{i\phi_b} \\ c e^{i\phi_c} \\ d e^{i\phi_d} \end{pmatrix}, \quad (\text{B1}) \\ &= e^{-i\phi_a} \begin{pmatrix} i f_t k_x + \frac{2\Omega}{\omega} f_t k_z + i \frac{2\Omega}{\omega} f_t S - k_y \omega + \frac{4\Omega^2}{\omega} k_y \\ \frac{2\Omega}{\omega} (f_t k_y - i k_x \omega) + \frac{f_t^2 - \omega^2}{\omega} (k_z + i S) \\ -i f_t k_y - k_x \omega + 2i k_z \Omega - 2S\Omega \\ f_t^2 - \omega^2 + 4\Omega^2 \end{pmatrix}, \end{aligned}$$

where a, b, c, d are real numbers satisfying $a^2 + b^2 + c^2 + d^2 = 1$. The Chern number of the band is the gauge-

invariant quantity

$$\mathcal{C} = \frac{1}{2\pi} \oint_{\Sigma} i\nabla \times (\Psi^\dagger \cdot \nabla \Psi) \cdot d\Sigma, \quad (\text{B2})$$

where Σ is a closed oriented surface enclosing the degeneracy point located at the origin of parameter space

$(k_x, k_y, f_t) = (0, 0, 0)$. With the functional form given by Eq. (B1), one obtains

$$2\pi\mathcal{C} = \oint_{\Sigma} i\nabla \wedge (\Psi^\dagger \cdot \nabla \Psi) \cdot d\Sigma, \quad (\text{B3})$$

$$= i \oint_{\Sigma} \nabla \wedge (a\nabla a + b\nabla b + c\nabla c + d\nabla d + i(b^2\nabla\phi_b + c^2\nabla\phi_c + d^2\nabla\phi_d)) d\Sigma, \quad (\text{B4})$$

$$= \frac{i}{2} \oint_{\Sigma} \nabla \wedge \underbrace{\nabla(a^2 + b^2 + c^2 + d^2)}_{=0} - \oint_{\Sigma} \nabla \wedge (b^2\nabla\phi_b + c^2\nabla\phi_c + d^2\nabla\phi_d) d\Sigma, \quad (\text{B5})$$

$$= - \oint_{\Sigma} \nabla \wedge R d\Sigma, \quad (\text{B6})$$

where $R \equiv b^2\nabla\phi_b + c^2\nabla\phi_c + d^2\nabla\phi_d$. Hence, if R is smooth everywhere on Σ , $\mathcal{C} = -\frac{1}{2\pi} \int_{\partial\Sigma} R dp = 0$ from Stokes theorem. Conversely, a non-zero Chern number implies for R to be singular, i.e. the existence of phase singularity in the parameter space.

Appendix C: Simulations

The equations of linear inertial waves on the sphere Eqs. (24)-26 are solved using the spectral code DEDALUS [39]. The spatial solver decomposes the fields on bases of polynomials in angular coordinates (θ, ϕ) . The bases are truncated at order $(N_\theta, N_\phi) = (128, 64)$. The timestepping solver is a Runge-Kutta method of order 2, with constant timestep $dt = 10^{-2}\Omega^{-1}$. The four fields u_θ, u_ϕ, v_z, p are initiated with uniformly sampled random values between -1 and 1 on the 128×64 grid points. The evolution is then solved until $t = 200\Omega^{-1}$. In these units, the solar radius is $R = 2.0 \cdot 10^{-2} c_s \Omega^{-1}$. We set $S = -800\Omega$ (values discussed e.g. in [17] and [4]).

The Fourier transforms of the output of the simulations are computed by the Fast Fourier Transforms (FFT) methods of Numpy. The spatial Fourier transform in the Northern hemisphere is computed on all the points $0 < y/R < \pi/2$. The Fourier transform in the Southern hemisphere is computed on all the points $0 > y/R > -\pi/2$.

The winding number is measured by unwrapping the signal of the phase along the closed path (black loop on Fig. 4). Unwrapping the signal involves adjusting large jumps by multiples of the period 2π to obtain a continuous function that is not restricted to $[-\pi, \pi]$. The winding number is then given by the difference between the first and last values of the signal, which is an integer multiple of 2π . Figure 6 shows the raw signal of the phase along the points Γ_i of the loop Γ , and the result

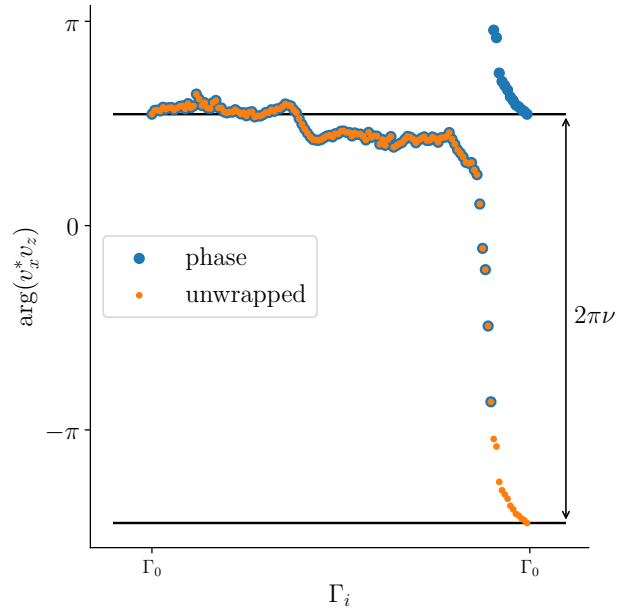


FIG. 6. The winding number of the closed loop Γ is measured by unwrapping the phase. A continuous curve is obtained, and the difference between the first and last point is $2\pi\nu$.

of its unwrapping. This procedure is guaranteed to yield an integer result for ν , ensuring that any error would be at least 100%.

The full Python script used for this study is available at <https://www.github.com/ArmandLeclerc/topo-inertial-waves>.

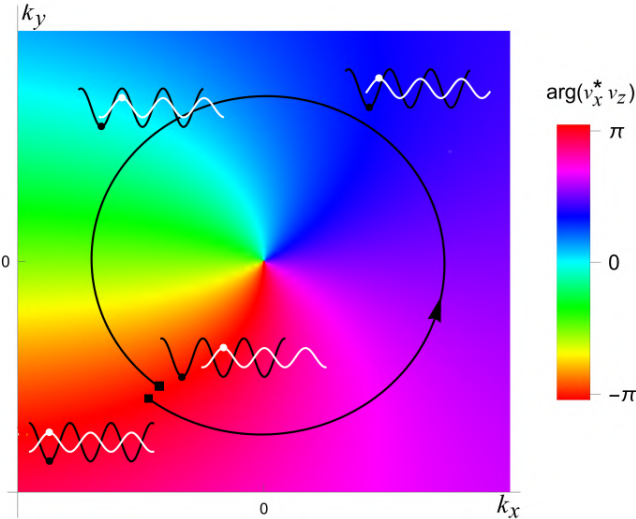


FIG. 7. The phase winding of 1 corresponds to a 2π shift of the phase when completing a closed path around the topological singularity in the Fourier space.

Appendix D: Interpretation of phase winding

When the eigenvector associated with the inertial wave in Fourier space is continuously varied, the relative phase between v_x and v_z changes. Starting and coming back to given point on a closed path in the parameter space, the resulting plane wave is physically identical to the initial one. This requirement implies the phase accumulated along the closed path is not identically zero, but a multiple of 2π . Figure 7 shows phase evolution along the path that corresponds to a winding of 1 for the inertial wave. The crests of v_z are shifted exactly by one wavelength with respect to the crests of v_x when moving along the black loop that encloses the singularity.

Appendix E: Robustness to noise

An artificial amount of noise is added to the velocity data calculated by the simulation by

$$u_{\text{tot}} = u_{\text{sim}} + u_{\text{noise}}, \quad (\text{E1})$$

$$v_{z,\text{tot}} = v_{z,\text{sim}} + v_{z,\text{noise}}, \quad (\text{E2})$$

where the noise fields are generated by sampling random values between $-a$ and a on the 128×64 grid points at every time step. a is the noise amplitude relative to the amplitude of the initial amplitude of the linear perturbation. The winding number ν_+ in the northern hemisphere is then measured, and shown on Fig. 8. Up to a noise factor $a = 10$, the winding number is still measured to be -1 , demonstrating the robustness of the method against

noise. Physical noise sources can produce noise with a structured power spectrum, such as Gaussian noise or power-law noise. Figure 9 shows that by employing a

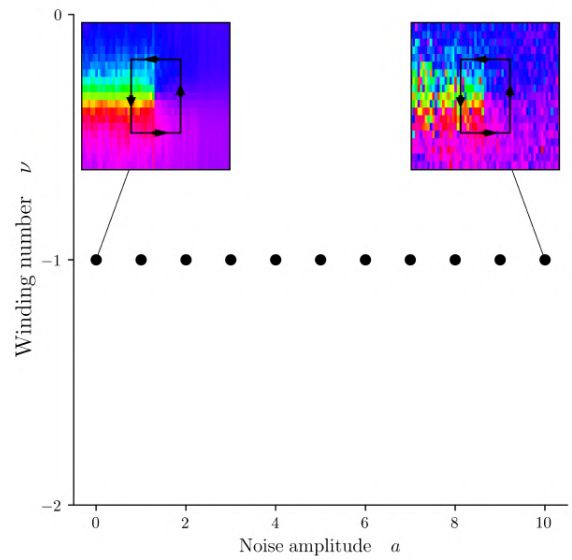


FIG. 8. Winding numbers measured as a function of the relative amplitude of noise with respect to the initial linear perturbation. Up to a ratio of $a = 10$, winding numbers are still measured to be -1 .

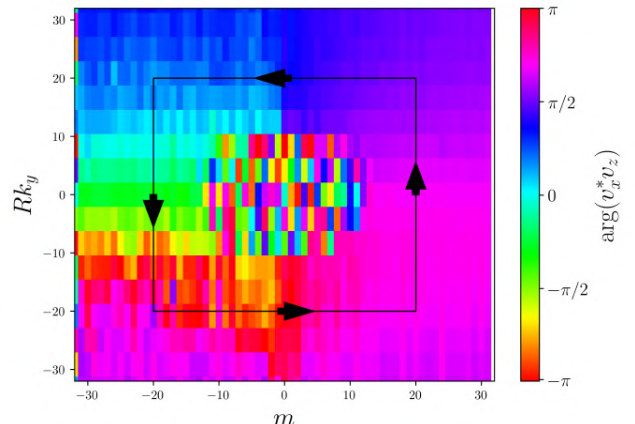


FIG. 9. Example of phase winding measurement with isotropic noise whose power spectrum decreases at high spatial frequencies.

contour of integration where the noise has significantly diminished relative to the wave signal, it is possible to measure the phase winding.

-
- [1] S. Basu, Global seismology of the sun, *Living Reviews in Solar Physics* **13**, 2 (2016).
- [2] R. A. García, S. Turck-Chièze, S. J. Jiménez-Reyes, J. Ballot, P. L. Pallé, A. Eff-Darwich, S. Mathur, and J. Provost, Tracking solar gravity modes: the dynamics of the solar core, *Science* **316**, 1591 (2007).
- [3] C. Jones, K. Kuzanyan, and R. Mitchell, Linear theory of compressible convection in rapidly rotating spherical shells, using the anelastic approximation, *Journal of Fluid Mechanics* **634**, 291 (2009).
- [4] Y. Bekki, R. H. Cameron, and L. Gizon, The sun's differential rotation is controlled by high-latitude baroclinically unstable inertial modes, *Science Advances* **10**, eadk5643 (2024).
- [5] B. Löptien, L. Gizon, A. C. Birch, J. Schou, B. Proxauf, T. L. Duvall Jr, R. S. Bogart, and U. R. Christensen, Global-scale equatorial rossby waves as an essential component of solar internal dynamics, *Nature Astronomy* **2**, 568 (2018).
- [6] D. H. Hathaway and L. A. Upton, Hydrodynamic properties of the sun's giant cellular flows, *The Astrophysical Journal* **908**, 160 (2021).
- [7] L. Gizon, R. H. Cameron, Y. Bekki, A. C. Birch, R. S. Bogart, A. S. Brun, C. Damiani, D. Fournier, L. Hyest, K. Jain, *et al.*, Solar inertial modes: Observations, identification, and diagnostic promise, *Astronomy & Astrophysics* **652**, L6 (2021).
- [8] C. S. Hanson, S. Hanasoge, and K. R. Sreenivasan, Discovery of high-frequency retrograde vorticity waves in the sun, *Nature Astronomy* **6**, 708 (2022).
- [9] S. A. Triana, G. Guerrero, A. Barik, and J. Rekier, Identification of inertial modes in the solar convection zone, *The Astrophysical Journal Letters* **934**, L4 (2022).
- [10] R.-M. Ouazzani, F. Lignières, M.-A. Dupret, S. Salmon, J. Ballot, S. Christophe, and M. Takata, First evidence of inertial modes in γ doradus stars: The core rotation revealed, *Astronomy & Astrophysics* **640**, A49 (2020).
- [11] T. Van Reeth, A. Tkachenko, and C. Aerts, Interior rotation of a sample of γ doradus stars from ensemble modelling of their gravity-mode period spacings, *Astronomy & Astrophysics* **593**, A120 (2016).
- [12] H. Saio, D. W. Kurtz, S. J. Murphy, V. L. Antoci, and U. Lee, Theory and evidence of global rossby waves in upper main-sequence stars: r-mode oscillations in many kepler stars, *Monthly Notices of the Royal Astronomical Society* **474**, 2774 (2018).
- [13] G. Li, T. Van Reeth, T. R. Bedding, S. J. Murphy, and V. Antoci, Period spacings of γ doradus pulsators in the kepler field: Rossby and gravity modes in 82 stars, *Monthly Notices of the Royal Astronomical Society* **487**, 782 (2019).
- [14] P. Delplace, J. Marston, and A. Venaille, Topological origin of equatorial waves, *Science* **358**, 1075 (2017).
- [15] M. Perrot, P. Delplace, and A. Venaille, Topological transition in stratified fluids, *Nature Physics* **15**, 781 (2019).
- [16] N. Perez, P. Delplace, and A. Venaille, Unidirectional modes induced by nontraditional coriolis force in stratified fluids, *Physical Review Letters* **128**, 184501 (2022).
- [17] A. Leclerc, G. Laibe, P. Delplace, A. Venaille, and N. Perez, Topological modes in stellar oscillations, *The Astrophysical Journal* **940**, 84 (2022).
- [18] Z. Zhu, C. Li, and J. Marston, Topology of rotating stratified fluids with and without background shear flow, *Physical Review Research* **5**, 033191 (2023).
- [19] W. Xu, B. Fox-Kemper, J.-E. Lee, J. Marston, and Z. Zhu, Topological signature of stratospheric poincare-gravity waves, *Journal of the Atmospheric Sciences* (2024).
- [20] R. Lier, R. Green, J. de Boer, and J. Armas, Topological plasma oscillations in the solar tachocline (2024), arXiv:2401.07622 [astro-ph.SR].
- [21] K. H. Lockitch and J. L. Friedman, Where are the r-modes of isentropic stars?, *The Astrophysical Journal* **521**, 764 (1999).
- [22] P. Ivanov and J. Papaloizou, Inertial waves in rotating bodies: a wkbj formalism for inertial modes and a comparison with numerical results, *Monthly Notices of the Royal Astronomical Society* **407**, 1609 (2010).
- [23] N. Perez, *Topological waves in geophysical and astrophysical fluids*, Ph.D. thesis, Ecole normale supérieure de Lyon-ENS LYON (2022).
- [24] J. Papaloizou and J. Pringle, Non-radial oscillations of rotating stars and their relevance to the short-period oscillations of cataclysmic variables, *Monthly Notices of the Royal Astronomical Society* **182**, 423 (1978).
- [25] J. Vidal and D. Cébron, Acoustic and inertial modes in planetary-like rotating ellipsoids, *Proceedings of the Royal Society A* **476**, 20200131 (2020).
- [26] R. Jain and B. W. Hindman, Latitudinal propagation of thermal rossby waves in stellar convection zones, *The Astrophysical Journal* **958**, 48 (2023).
- [27] Y. Onuki, A. Venaille, and P. Delplace, Bulk-edge correspondence recovered in incompressible geophysical flows, *Physical Review Research* **6**, 033161 (2024).
- [28] G. K. Vallis, *Atmospheric and oceanic fluid dynamics* (Cambridge University Press, 2017).
- [29] P. Delplace, Berry-chern monopoles and spectral flows, *SciPost Physics Lecture Notes* , 039 (2022).
- [30] H. Qin and Y. Fu, Topological langmuir-cyclotron wave, *Science Advances* **9**, eadd8041 (2023).
- [31] F. Faure, Manifestation of the topological index formula in quantum waves and geophysical waves, *Annales Henri Lebesgue* **6**, 449 (2023).
- [32] Y. Bekki, R. H. Cameron, and L. Gizon, Theory of solar oscillations in the inertial frequency range: Linear modes of the convection zone, *Astronomy & Astrophysics* **662**, A16 (2022).
- [33] F. H. Busse, Thermal instabilities in rapidly rotating systems, *Journal of Fluid Mechanics* **44**, 441 (1970).
- [34] G. A. Glatzmaier and P. A. Gilman, Compressible Convection in a Rotating Spherical Shell - Part Three - Analytic Model for Compressible Vorticity Waves, *Astrophys. J.* **45**, 381 (1981).
- [35] C. C. Blume, B. W. Hindman, and L. I. Matilsky, Inertial waves in a nonlinear simulation of the sun's convection zone and radiative interior, *The Astrophysical Journal* **966**, 29 (2024).
- [36] E. T. Whittaker and G. N. Watson, *A Course of Modern Analysis*, 5th ed., edited by V. H. Moll (Cambridge University Press, 2021).
- [37] M. S. Ergoktas, A. Kecebas, K. Despotelis, S. Soleymani, G. Bakan, A. Kocabas, A. Principi, S. Rotter, S. K.

- Ozdemir, and C. Kocabas, Localized thermal emission from topological interfaces, *Science* **384**, 1122 (2024).
- [38] T. Fösel, V. Peano, and F. Marquardt, L lines, c points and chern numbers: understanding band structure topology using polarization fields, *New Journal of Physics* **19**, 115013 (2017).
- [39] K. J. Burns, G. M. Vasil, J. S. Oishi, D. Lecoanet, and B. P. Brown, Dedalus: A flexible framework for numerical simulations with spectral methods, *Physical Review Research* **2**, 023068 (2020).
- [40] L. Jezequel and P. Delplace, Non-hermitian spectral flows and berry-chern monopoles, *Physical Review Letters* **130**, 066601 (2023).
- [41] V. Canuto and J. Christensen-Dalsgaard, Turbulence in astrophysics: Stars, *Annual review of fluid mechanics* **30**, 167 (1998).
- [42] K. B. Oldham, J. C. Myland, and J. Spanier, The cubic function $x^3 + ax^2 + bx + c$, in *An Atlas of Functions: with Equator, the Atlas Function Calculator* (Springer US, New York, NY, 2009) pp. 139–146.

Shallow water waves on a sphere

Résumé

Quand Deplace et al. [141] découvrent l'origine topologique des ondes équatoriales, ils trouvent une charge $\mathcal{C} = 2$ qui expliquait l'existence des ondes de Kelvin et Yanai dans un modèle: le plan β . Ce modèle simplifie la forme de l'atmosphère en ôtant la courbure de la planète du problème, en gardant simplement la dépendance en latitude au premier ordre du paramètre de Coriolis $f = 2\Omega \cdot e_r \sim \beta y$, ce qui est une bonne approximation pour les atmosphères tournant rapidement.

Le travail de ce chapitre discute les limites de cette approximation à la lumière de la topologie des ondes. Plus précisément, il s'attache à mesurer les différences de l'analyse topologique et ses prédictions quand on garde la géométrie sphérique de l'atmosphère. Le but était d'étudier un problème d'onde à géométrie courbe. Il est trouvé que deux charges topologiques $\mathcal{C} = -1$ additionnelles existent à des latitudes moyennes, causées par la courbure de l'espace, en plus de la charge $\mathcal{C} = 2$ à l'équateur. De manière intéressante, ces deux charges additionnelles peuvent fusionner avec la charge équatoriale quand la rotation devient suffisamment lente. Alors, il n'existe plus qu'une charge nulle $\mathcal{C} = 0$, en concordance avec le fait que les ondes de Kelvin et Yanai disparaissent du spectre.

When [141] unveiled the Berry-Chern monopole of equatorial waves, they identified a topological charge with a Chern number $\mathcal{C} = 2$, which explained the presence of the Kelvin and Yanai waves in an approximation: the β -plane model. In this model, the curvature of the planet is removed, only retaining the geometry in a first-order latitude y dependence of the Coriolis parameter $f = 2\Omega \cdot e_r \sim \beta y$. This approximation is good for atmospheres and oceans at the surface of spherical bodies rotating rapidly, as rapid rotation traps the waves close to the equator. The work presented in this chapter discusses the limits of this approximation, under the light of wave topology. More specifically, it focuses on how the topological analysis and its predictions change when retaining the full spherical geometry of the atmosphere. The point was to deal with a problem of waves on a curved space. This work finds two additional topological charges at mid-latitudes with Chern numbers $\mathcal{C} = -1$, caused by the curvature of the space. Interestingly, the position of these charges depend on the rotation rate, and may collide with the original one with charge +2. At this collision, occurring for low rotation rates, a transition occurs which makes the Kelvin and Yanai waves disappear from the spectrum.

I wrote the code to compute the spectrum on the full sphere, and numerically calculated the Chern numbers of mid-latitude degeneracies and participated in the redaction of the article. My personal interest in this study was directed towards obtaining a grasp of the effects of a curved space in a topological analysis. Indeed, the vast majority of the literature of topological analyses is performed on 1D flat geometries. For the construction of an topological analysis of stellar oscillations, sphericity must obviously be fully included. The shallow water problem on the sphere separates vertical and horizontal directions, and provides a good problem to highlight the effects of sphericity. Here, the results show that the curvature of the sphere strongly dictates whether topological equatorial modes exist or not. It is an elegant way to unveil a limit of the β -plane approximation. For stellar seismology applications, this study is a foothold for future topological studies of waves in rotating stars where rotation is non-perturbative. The results presented in this chapter have been published in *Topology of shallow-water waves on the rotating sphere*, Perez, Leclerc, Delplace, Laibe, **Journal of Fluid Mechanics** 2025 [340]. The article is shown here, truncated of its appendices.

Topology of shallow-water waves on the rotating sphere

Nicolas Perez¹, Armand Leclerc¹, Guillaume Laibe¹ and Pierre Delplace²

¹ Univ Lyon, ENS de Lyon, Univ Claude Bernard, CNRS, Centre de Recherche Astrophysique de Lyon (UMR CNRS 5574), F-69230 Saint-Genis-Laval, France

² Univ Lyon, ENS de Lyon, Univ Claude Bernard, CNRS, Laboratoire de Physique (UMR CNRS 5672), F-69342 Lyon, France

email: nicolas.perez@ens-lyon.fr

Abstract

Topological properties of the spectrum of shallow-water waves on a rotating spherical body are established. Particular attention is paid to its spectral flow, i.e. the modes whose frequencies transit between the Rossby and inertia-gravity wavebands as the zonal wave number is varied. Organising the modes according to the number of zeros of their meridional velocity, we conclude that the net number of modes transiting between the shallow-water wavebands on the sphere is null, in contrast with the Matsuno spectrum. This difference can be explained by a miscount of zeros under the β -plane approximation. We corroborate this result with the analysis of [1] by showing that the curved metric discloses a pair of degeneracy points in the Weyl symbol of the wave operator, non-existent under the β -plane approximation, each of them bearing a Chern number -1 .

1 Introduction

The rotating shallow-water model is certainly one of the most significant for modeling two-dimensional large-scale fluid motions in the ocean, the atmosphere and even stellar media [2–7]. It was originally introduced by Laplace in 1775 to address the problem of the dynamical response of the oceans to the tidal forces generated by the Moon. The strength of this model relies on the fact that it focuses mainly on the effects of the Coriolis force, produced by the solid-body rotation of the planet or star at rate Ω , on the dynamics of surface waves, without losing so much generality. Owing to the curvature of the surface, these Coriolis effects, i.e. the projection of the Coriolis term $-2\Omega \times \mathbf{v}$ on the surface (with \mathbf{v} the fluid velocity field on this surface), naturally depend on the latitude θ , more specifically on the normal component of 2Ω , called the *Coriolis parameter*, which is

$$f = 2\Omega \sin(\theta) , \quad (1)$$

for a spherical body. A hundred years after the work of Laplace, Lord Kelvin used this model (free of tidal forcing) to compute the normal-mode oscillations of a local plane, assuming a constant Coriolis parameter f [8]. He exhibited different kinds of plane-wave solutions, namely the *surface gravity* (*Poincaré*) modes, the *geostrophic* modes (for which the flow is stationary as the pressure gradient is exactly balanced by the Coriolis force) and *coastal Kelvin* modes which exist only in the presence of a boundary and propagate in one direction. However, this *f-plane approximation* is not relevant at the equator, where the parameter f vanishes, thus virtually cancelling the Coriolis effects within the frame of this approximation. Rossby bypassed this problem by introducing the so-called *β -plane approximation*, which amounts to assuming locally linear variation of the Coriolis parameter

f with latitude [9]. This simple approximation led to qualitatively accurate understanding of many previously observed phenomena in geophysical fluid dynamics, such as the western intensification of wind-driven currents [10, 11], the oscillations of mid-latitude jets [12] or the equatorial trapping of gravity waves. Using this approximation at the equator with constant $\beta = df/dy$, where y is the meridional distance from the equator, Matsuno computed the spectrum of equatorial waves of the shallow-water model [13]. This spectrum has a discrete set of low-frequency *planetary (Rossby)* waves and *inertia-gravity* waves, plus two branches of modes transiting from the first to the second as the zonal wave number k goes from negative to positive values, namely the *Yanai* (or *mixed-Rossby-gravity*) and *equatorial Kelvin* modes.

However, the equatorial β -plane approximation used by [1, 13] (and many other studies of geophysical fluid dynamics) is limited in the sense that it only accounts for the curvature of the surface in the variation of the Coriolis parameter, at linear order, and not in the metric. It thus ignores the existence of the poles, and generates a spectrum of solutions defined on the unbounded domain across the equator, which seems paradoxical. Nevertheless, the solutions are accurate as long as they remain trapped around the equator, in the so-called *Yoshida waveguide* [13, 14], where the linear approximation holds. The trapping length, called the *equatorial radius of deformation*, is given by

$$L_{\text{eq}} = \sqrt{\frac{c}{\beta}}, \quad (2)$$

where c is the speed of surface waves without rotation. L_{eq} thus needs to be much smaller than R , the radius of the planet. This condition is satisfied for fast-rotating planets, compared to the timescale of propagation of the waves at their surface. For the first baroclinic mode (i.e. the fastest one) in the equatorial ocean on Earth, the equatorial radius of deformation is approximately 300 kilometers (see e.g. [3], p. 304), so the β -plane approximation is quite accurate in this context. However, when it comes to global oscillations of larger scales, both the curved metric and the actual sine variation of f with latitude must be taken into account. Moreover, the quantisation of the zonal wave number k cannot be ignored, especially when the wavelength is not small compared to the radius R . The full spectrum of shallow-water waves on the sphere is a peculiar problem, as the sphere is an unbounded but finite domain. The eigenvalue problem has no exact solution in the general case, however it has been extensively investigated through a variety of analytic approaches (e.g. [15–21]), and the frequencies and wave functions can be well-approximated with analytical expressions in the different asymptotic regimes. In particular, in the regime $L_{\text{eq}} \ll R$ (hereafter referred to as *Matsuno limit*), the spectrum of equatorial shallow-water waves is well-approximated by Matsuno's spectrum and thus clearly exhibits two branches of modes with eastward group velocity transiting through the frequency gap between the different *wavebands* (in the rest of the paper, we will refer to the different groups of shallow-water modes as wavebands). There are three wavebands in the shallow-water model: the Rossby waveband and two equivalent inertia-gravity wavebands). In contrast, those seem to be absent from the frequency spectrum in the other limit (see Figure 1), i.e. when Ω is small compared to c/R , hereafter referred to as *Margules limit* [15]. One would think that these branches somehow disappear as L_{eq} and R become comparable, however there is no analytical solution of the eigenvalue problem in this intermediate situation to show exactly how.

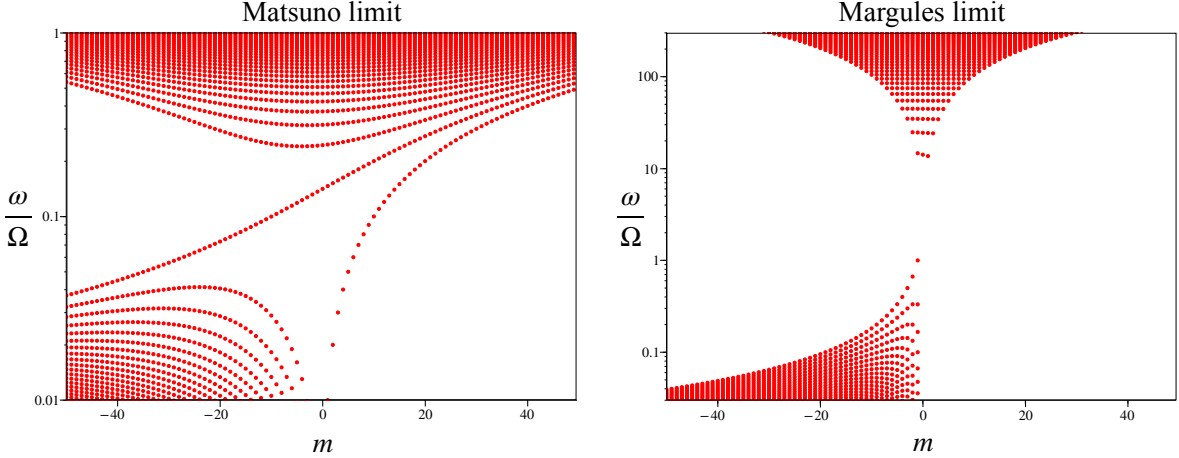


Figure 1: Dimensionless frequencies of the shallow-water model on the rotating sphere for two values of the parameter $\epsilon = c/\Omega R$ (left: $\epsilon = 0.01$, strong rotation; right: $\epsilon = 10$, weak rotation), in function of the azimuthal wave number $m \in \mathbb{Z}$, computed with **Dedalus** [22] (see Appendix 6.1 for numerical methods). In the Matsuno limit (left panel, $\epsilon \ll 1$), two distinct branches of frequencies transit through the gap between Rossby and inertia-gravity waves, whereas in the Margules limit (right panel, $\epsilon \gg 1$) these are clearly separated by an unfilled frequency gap. Note that the frequency axes in this figure are in logarithmic scale, as well as in Figure 4, in order to visually appreciate the transition between the Matsuno and Margules regimes. All the other frequency plots in the article are displayed in linear scale.

Alternatively, a few years ago, the presence of these two transiting branches in the spectrum of shallow-water waves on the unbounded β -plane was interpreted as a manifestation of an underlying topological property. Indeed, after noticing the strong resemblance of this *+2 spectral flow* of modes with the topologically-protected modes crossing the gap in certain insulating materials, [1] applied the same arguments used in condensed matter physics to define topological integers associated to this spectral flow, the *Chern numbers* or *topological charges*. These integers characterise the phase singularities of Kelvin's plane-wave solutions, which are computed for constant f and thus require only to diagonalise a 3-by-3 matrix. Nevertheless, they happen to be equal to the number of modes gained by the associated *wavebands* in the more elaborated β -plane model. This counter-intuitive result, which connects the topological properties of Kelvin's f -plane modes to a spectral property of Matsuno's β -plane spectrum, is a consequence of the more general *index theorem* [23–25]. It has been applied to predict the conditions of existence and number of modes transiting across the frequency gap in a variety of models from a great variety of domains [26–36].

This paper intends to shed a new light on the loss of gapless Kelvin and Yanai modes on the sphere, not with exact analytical resolution but by combining the study of the structure of modes with spectral topology. This analysis relies on numerous previous works in which topology brought new insights on wave properties in geophysical and astrophysical media [1, 26–29, 37]. In the first part, we introduce the equations of the rotating shallow-water model on the sphere, and the relevant dimensionless parameters that characterise it. We recall the asymptotic solutions in both Matsuno and Margules limits. In the second part, we discuss the concept of *modal flow* and show that the latter is equal to zero for the spectrum of shallow-water waves on the rotating sphere, whereas it is equal to +2 on the unbounded β -plane. In the third part, we provide a topological interpretation of this result. We compute the Chern numbers, which are associated to the points where the symbol of the wave operator has multiple eigenvalues. We show that the metric term induces degeneracy points of non-zero Chern numbers, in addition to the one exhibited by [1]. This analysis reconciles the bulk-interface correspondence established by Delplace *et al* on the unbounded β -plane with the disappearance of the equatorial spectral flow in spherical geometry.

2 The linearised shallow-water model on the rotating sphere

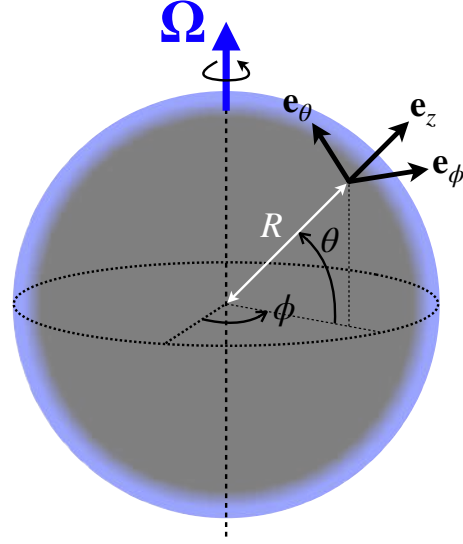


Figure 2: Geometry of the rotating shallow-water model on the sphere. The spherical coordinates and associated unit vectors are different than the usual ones, θ being the latitude instead of the colatitude.

2.1 Linearised equations

We consider the linearised shallow-water equations of an inviscid fluid layer on top of a sphere of radius R , rigidly rotating with constant rate Ω (Figure 2). The fluid is initially at rest in the rotating frame. Besides, assuming that the gravity g at the surface is such that $g \gg R\Omega^2$, we ignore the centrifugal effects. Therefore, the rest state is that of a quiet layer of constant depth h_0 . Noting the perturbed fields with $'$, we define $\mathbf{v} = \mathbf{v}'(\mathbf{x}, t)$ and $h = h_0 + h'(\mathbf{x}, t)$ the two-component velocity and height of the fluid, respectively, both functions of time t and position \mathbf{x} on the sphere. The linearised shallow-water equations can be conveniently expressed in terms of rescaled perturbation fields, i.e. $\tilde{\mathbf{v}} = \sqrt{h_0} \mathbf{v}' = \tilde{u} \mathbf{e}_\phi + \tilde{v} \mathbf{e}_\theta$ and $\tilde{h} = \sqrt{g} h'$, as

$$\frac{\partial \tilde{\mathbf{v}}}{\partial t} = -c\nabla \tilde{h} - \mathbf{f} \times \tilde{\mathbf{v}}, \quad (3a)$$

$$\frac{\partial \tilde{h}}{\partial t} = -c\nabla \cdot \tilde{\mathbf{v}}, \quad (3b)$$

where $c = \sqrt{gh_0}$ is the constant phase speed and $\mathbf{f} = (2\Omega \cdot \mathbf{e}_z)\mathbf{e}_z$ is the projection of 2Ω on the local unit vector \mathbf{e}_z normal to the surface (traditional Coriolis parameter). Since none of the parameters appearing in Equations (3) depend on time or longitude, the rotating sphere acts as a waveguide trapping zonally-propagating waves in the meridional direction. We can thus expand any perturbation on the set of Fourier modes $X(\theta)e^{i(m\phi-\omega t)}$, where X is any of the three dependent variables of Equations (3), (ϕ, θ) the longitudinal and latitudinal coordinates, respectively, and (m, ω) the azimuthal wave number and frequency associated with the Fourier mode, which corresponds to the solutions of

$$\omega \tilde{\mathbf{v}} = -ic\nabla \tilde{h} - i\mathbf{f} \times \tilde{\mathbf{v}}, \quad (4a)$$

$$\omega \tilde{h} = -ic\nabla \cdot \tilde{\mathbf{v}}. \quad (4b)$$

The core of the discussion of this article is the metric term that arises from the divergence operator $\nabla \cdot$ in Equation (4b), owing to the geometrical curvature of the surface. This point will be discussed in section 4.

2.2 Lamb parameter and asymptotic solutions

If one rather considers the dimensionless frequency ω/Ω , the eigenvalue problem (4) depends only on one dimensionless parameter:

$$\epsilon = \frac{c}{R\Omega} . \quad (5)$$

The quantity $2/\epsilon$ is sometimes called the *Lamb parameter* [19], not to be confused with the Lamb frequency used in asteroseismology [38]. $1/\epsilon$ gives the traversal time of a gravity wave over the spherical body in planetary days. Equations (4) in dimensionless units are

$$(\omega/\Omega)\tilde{\mathbf{v}} = -i\epsilon\tilde{\nabla}\tilde{h} - 2i\sin(\theta)\mathbf{e}_z \times \tilde{\mathbf{v}} , \quad (6a)$$

$$(\omega/\Omega)\tilde{h} = -i\epsilon\tilde{\nabla} \cdot \tilde{\mathbf{v}} , \quad (6b)$$

where $\tilde{\nabla} = R\nabla$ is the gradient operator on the unit sphere. The parameter ϵ naturally appears in asymptotic expansions to compute the approximate spectrum of shallow-water waves [19, 21] or their ray paths [39] on the sphere. One can expect to asymptotically recover the Matsuno spectrum as $\epsilon \rightarrow 0$. Indeed, Expression (2) yields $L_{\text{eq}}/R = \sqrt{\epsilon/2}$ for the equatorial radius of deformation, which means that, for small ϵ , the wave functions are equatorially trapped with angular spreading of order $\sqrt{\epsilon}$, thus recovering the Cartesian β -plane approximation made by Matsuno. In this limit, the solutions of (4) are appropriately described with Hermite polynomials, which are exact solutions on the unbounded β -plane (see 3.1).

Conversely, for larger values of ϵ , the solutions are expected to spread away from the equator and eventually over the whole sphere. In the limit $\epsilon \gg 1$, sometimes called the *Margules limit* [19], there are two kinds of eigenvalues, originally found by Margules [15] and Hough [16], that we recall here:

- The ones such that $\omega = \mathcal{O}(c/R)$. One recovers the non-rotating shallow-water equations from (4). The wave functions are those of the Laplacian operator on a prolate spheroid, i.e. the prolate spheroidal wave functions [6], and we have $R\omega/c \simeq \sqrt{\ell(\ell+1)} - m/\epsilon$ (see e.g. [19, 40]) with non-zero integers ℓ and $|m| \leq \ell$. These are global surface gravity oscillations on the sphere, perturbed by a small Coriolis term. For these solutions, the number of zeros of \tilde{v} on the open interval $(-\pi/2, \pi/2)$ is given by $p = \ell - |m| + 1$ [19].
- The ones such that $\omega = \mathcal{O}(\Omega)$. These are quasi-geostrophic planetary (Rossby) modes. From (4), it is straightforward to check that they obey $|\tilde{\nabla} \cdot \mathbf{v}'| = \mathcal{O}(|\mathbf{v}'|/\epsilon^2)$, i.e. that these modes have asymptotically divergence-free velocity. Eliminating the other variables from Equations (4a), we end up with a second-order differential equation for $V = \cos^{\frac{3}{2}}(\theta)\tilde{v}$:

$$-\frac{d^2V}{d\theta^2} + \left[\left(m^2 - \frac{1}{4} \right) \tan^2(\theta) + \left(m^2 - \frac{1}{2} + \frac{2m\Omega}{\omega} \right) \right] V = 0 . \quad (7)$$

Solutions of Equation (7) are provided for instance by [41]. They yield

$$\frac{\omega}{\Omega} = \frac{-2m}{m^2 + (2p+1)|m| + p(p+1)} \quad (\text{with } p = 0, 1, 2, \dots) , \quad (8)$$

where the index p indicates the number of zeros of the meridional velocity \tilde{v} in the open interval $(-\pi/2, \pi/2)$. In the Margules limit, the largest Rossby frequency is thus $\omega = \Omega$, for $m = -1$ and $p = 0$. The Rossby modes with $p = 0$ constitute the westward Yanai modes [42]. Expression (8), which is exact for any azimuthal wave number m in the Margules limit $\epsilon \gg 1$, is the same as (3.2c) obtained by [19] through a covariant formulation of the wave equations (3). Figure 3 provides a comparison of Expression (8) with numerical simulations, demonstrating the convergence of the Rossby waveband toward the Margules limit as ϵ increases.

There is a large frequency gap between these two wavebands, in which the Kelvin and Yanai modes of the Matsuno spectrum are absent (see Figure 1).

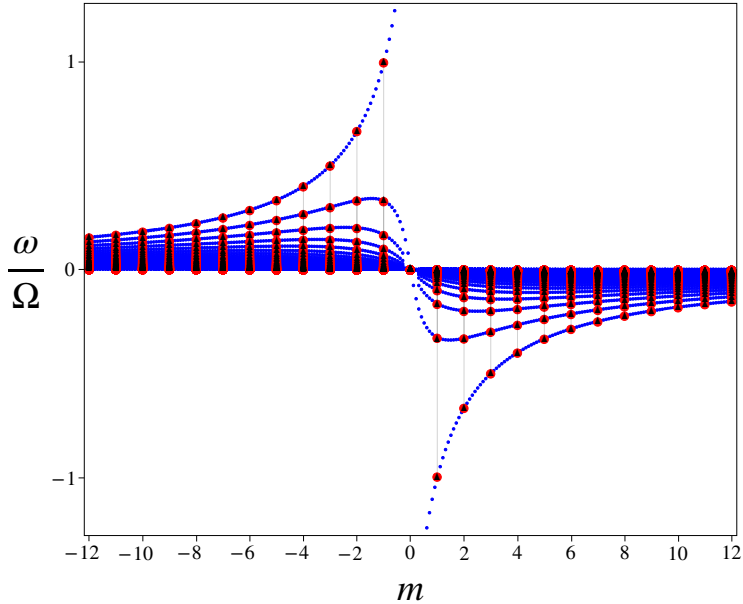


Figure 3: Comparison between Expression (8) (black triangles) and numerically-computed Rossby frequencies for $\epsilon = 5$. The red dots are obtained by projecting Equations (4) on `Dedalus`' curvilinear spectral basis [22], whereas the blue dots are computed from the problem (11) on $(-\pi/2, \pi/2)$, not necessarily with integer values of m , projecting the wave functions on the basis of Chebyshev polynomials [43] (see Appendix 6.1). The accuracy between the numerically-converged frequencies for $\epsilon = 5$ and Margules' asymptotic formula (8) is approximately 0.4%.

2.3 Matsuno and Margules limits on planets and stars

As far as the shallow-water model is valid, the Matsuno regime is common to most fast-rotating planets, but also stars like brown dwarfs [44]. Observations of the δ Scuti star Rasalhague allows one to estimate $\epsilon \simeq 0.36$ [45]. Atmospheres of exoplanets cover a large range of values of ϵ (see e.g. [46], Table 1), as well as the atmosphere of Earth, on which there is a variety of values of ϵ depending on the type of waves considered [19, 47]. For instance, the measurements of Kelvin and Rossby-Haurwitz waves in the atmosphere of Venus presented by [48] lead to the estimation $\epsilon \simeq 0.9$, whereas $\epsilon \approx 70$ for the atmospheric waves considered by [46]. On Earth, equatorial Kelvin waves have been detected both in the equatorial ocean [49, 50] and atmosphere [51], and their implication in a variety of geophysical phenomena (e.g. the El Niño event and the Madden-Julian Oscillation) is well understood. The first baroclinic modes (the fastest ones) are such that $c \simeq 2 \text{ m s}^{-1}$ in the equatorial ocean, thus $\epsilon \simeq 4.3 \cdot 10^{-3}$, and $c \simeq 25 \text{ m s}^{-1}$ in the atmosphere, thus $\epsilon \simeq 5.4 \cdot 10^{-2}$ (see [3], p. 304). However, the barotropic modes in the terrestrial atmosphere propagate at phase speed $c \simeq 300 \text{ m s}^{-1}$, which corresponds to $\epsilon \simeq 0.65$. This value is consistent with the data studied by [52]. Surface motions on giant planets of our solar system are the subject of many recent works [46, 53–55]. Atmospheric waves on Jupiter and Saturn are mostly in the Matsuno regime. For instance, eastward-propagating motions strongly localised at the equator on Jupiter have been interpreted as Kelvin waves [56], which is consistent with the estimation $\epsilon \simeq 1.4 \cdot 10^{-4}$.

2.4 Opening of a spectral gap as ϵ increases

In the Margules limit ($\epsilon \gg 1$), the minimal inertia-gravity frequency is equal to $\sqrt{2} c/R$ and the maximum Rossby frequency is Ω , which yields a frequency gap of width $\Omega(\sqrt{2}\epsilon - 1)$ in which there is no mode. Conversely, in the Matsuno limit ($\epsilon \ll 1$), the frequency gap between Rossby and inertia-gravity modes is filled with the Yanai and Kelvin modes. However, talking about a frequency gap and branches of modes is abusive in this situation. Indeed, contrary to the zonal wave number k of zonally-propagating waves on the unbounded β -plane, the azimuthal wave number m is not a continuous parameter, since it only takes discrete integer values. Therefore the spectrum (m, ω) does not consist of continuous branches but rather a discrete set of points, which means that, strictly speaking, there are frequency gaps between any allowed values of ω . Nevertheless, the equatorial Yanai and Kelvin modes define a clear connection between the Rossby and inertia-gravity wavebands on the unbounded β -plane, which is still visible in the shallow-water spectrum on the sphere with small ϵ , even if m takes discrete values (see Figures 1 and 4). Such a connection in the spectrum is referred to as spectral flow, which is usually defined for a continuous *spectral parameter* such as k in unbounded flow models [1, 26–30, 34, 57]. The purpose of the following section is to extend the concept of spectral flow to the present situation, i.e. with a discrete wave number m , and show that the net number of modes gained by the inertia-gravity waveband, when those modes are naturally labelled by the zeros of their meridional velocity, is actually zero for any value of ϵ , even if there are transiting frequencies for small ϵ (see Figure 4).

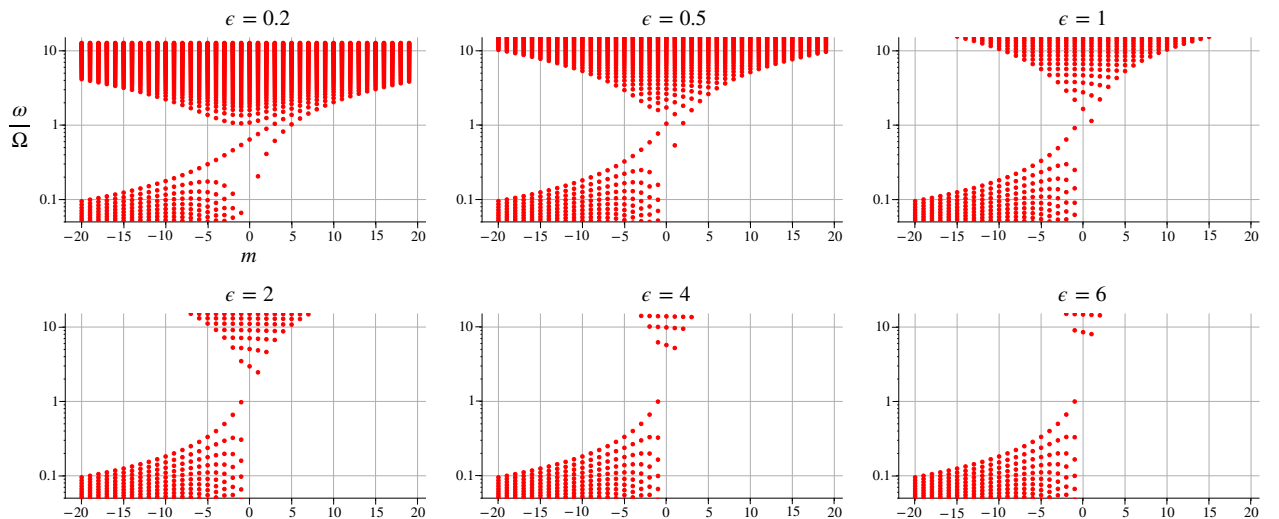


Figure 4: Numerically-computed frequencies ω for increasing values of ϵ and $|m| \leq 20$. These converged values are obtained by projecting Equations (4) on a basis of spin-weighted harmonics, a spectral method implemented in the **Dedalus** solver [22] (see Appendix 6.1). While for small ϵ two distinguishable spectral branches, the Yanai and Kelvin modes, transit through the gap between Rossby and gravity modes, these branches progressively break down and a clear gap opens up, separating Rossby and gravity frequencies.

3 Modal flow and zeros of the meridional velocity

To this day, Equations (4) do not have an exact solution for arbitrary values of ϵ , although good approximations have been found in certain limits, especially in short wavelength ranges [17, 21], or for special values of ω and ϵ [19]. In this study, we are interested in the transition between the Matsuno and Margules limits, i.e. the evolution of modes and frequencies for finite values of ϵ . For this reason, the analysis of this section is mostly based on numerical integration of Equations (4), with the spectral solver **Dedalus** [22]. The point of this section is the following: the Matsuno spectrum,

i.e. the frequencies ω of zonally-propagating equatorial waves on the unbounded β -plane, consists of a discrete set of continuous functions of the zonal wave number k , or *spectral branches*. These branches can be indexed by the number of zeros of the meridional velocity $\tilde{v}(\theta)$. For shallow-water waves on the sphere, however, the modes and frequencies depart from Matsuno's solutions as ϵ increases, wave functions spread away from the equator and new zeros of $\tilde{v}(\theta)$ appear at non-zero latitudes, modifying the natural order of mode branches established by Matsuno. This affects the conclusion regarding the very concept of spectral flow in this model, which must be replaced by a more accurate notion that we name the modal flow.

3.1 Reminder: the Matsuno spectrum and wave functions

The shallow-water equations for equatorial waves on the unbounded β -plane are the same as (4), only with Cartesian coordinates instead of the spherical ones (x is the zonal coordinate pointing eastward and y is the meridional coordinate pointing northward, with $y = 0$ defining the equator), and $f = \beta y$. Once again, we focus on plane waves propagating in the zonal direction, i.e. solutions in the form $X(y)e^{i(kx-\omega t)}$, where the wave number k can take continuous values. As explained in the introduction, this model captures the physics of equatorial waves in the limit of small ϵ . The solutions found by [13] obey the dispersion relation

$$\frac{\omega^2}{c^2} - k^2 - \frac{\beta k}{\omega} - \frac{\beta}{c}(2p+1) = 0 \quad (\text{with } p = -1, 0, 1, 2, \dots) , \quad (9)$$

and the corresponding wave functions for the meridional velocity are given by

$$\begin{aligned} \tilde{v}(y) &\propto H_p \left(y \sqrt{\frac{\beta}{c}} \right) e^{-\frac{\beta}{2c}y^2} \quad \text{for } p \geq 0 , \\ \tilde{v}(y) &= 0 \quad \text{for } p = -1 , \end{aligned} \quad (10)$$

with the Hermite polynomials H_p . As depicted in Figure 5, the dispersion relation (9) can be represented by a discrete set of continuous branches in (k, ω) , each indexed by the integer p . For $p \geq 0$, this index is equal to the number of zeros of \tilde{v} in the meridional direction y . Branches with $p \geq 1$ are the Rossby and inertia-gravity modes. The branches $p = 0$ and $p = -1$ are those of the Yanai and Kelvin modes, respectively. The Kelvin modes are purely zonal, i.e. with $\tilde{v} = 0$. The dispersion relation (9) formally associates Kelvin modes with the index $p = -1$ and, even though it does not make sense in terms of number of zeros of $\tilde{v}(y)$, it will be convenient to keep this index -1 in mind. It is also worth noticing that, for $p = 0$, Equation (9) admits an additional solution $\omega = -ck$. This solution corresponds to a diverging mode on the unbounded β -plane, thus it is discarded as it is not physically acceptable.

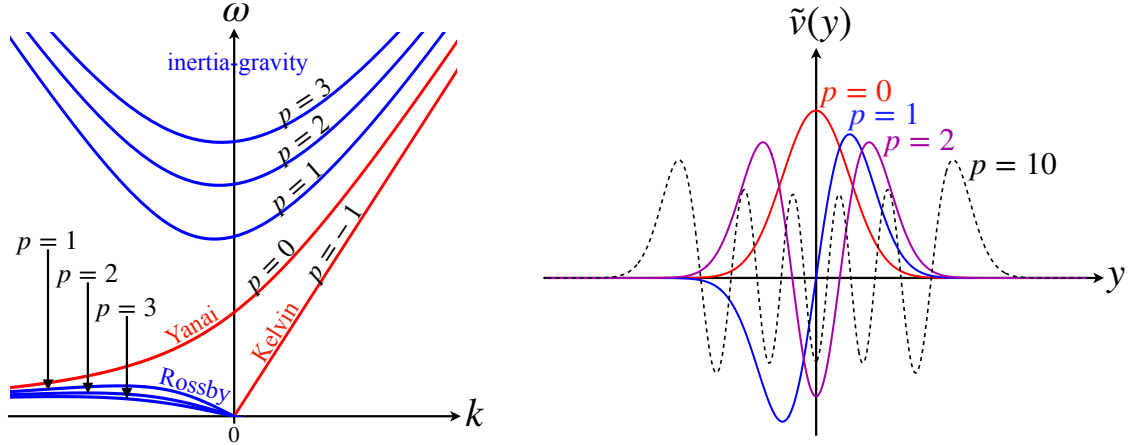


Figure 5: The Matsuno spectrum and wave functions for equatorial shallow-water waves on the unbounded β -plane [13]. Left: plot of the dispersion relation (9), showing the branches $-1 \leq p \leq 3$ for positive frequencies. The Yanai and Kelvin branches transit across the frequency gap between the Rossby and inertia-gravity wavebands, as k increases. Right: Amplitude of the meridional velocity in the y direction, given by Expression (10). The branch index p is equal to the number of zeros of $\tilde{v}(y)$.

3.2 Zeros of the meridional velocity

The +2 spectral flow studied by [1] corresponds to the Yanai and Kelvin modes, which transit from the Rossby waveband to the inertia-gravity waveband as k increases. Beyond the fact that these modes form continuous curves in (k, ω) , what identifies each of them is the number of zeros of the meridional velocity in the y direction, as previously shown. Generally speaking, it is straightforward to define the spectral flow of an eigenvalue problem if there is a continuous parameter such as the zonal wave number k , because the spectrum thus consists of continuous branches. However, if the spectral parameter takes discrete values, one must find an alternative way to count the number of modes gained or lost by a waveband as this spectral parameter is swept. For shallow-water waves on the rotating sphere, the azimuthal wave number m is a discrete parameter, nevertheless we will extrapolate the relation existing between the spectral flow of inertia-gravity waves and the number of zeros of \tilde{v} for the unbounded β -plane model. In other words, we will adopt the number of zeros of $\tilde{v}(\theta)$ on the open interval $(-\pi/2, +\pi/2)$ as an ordering parameter for the modes of the problem (4) (see Figure 6). In fact, many works on the spectrum of shallow-water waves associate or *label* modes according to the number of zeros of their meridional velocity [16, 17, 19, 42, 58]. In the Matsuno spectrum, at negative k , there are modes with no zero of \tilde{v} in the Rossby waveband but not in the inertia-gravity waveband, whereas there are modes with no zero in the inertia-gravity waveband at positive k . Connecting them together forms the spectral flow of Yanai modes, which transits between the Rossby and inertia-gravity wavebands as k increases. To clarify, in the rest of the paper, we will employ the term *modal branch* to refer to modes with the same number of zeros of $\tilde{v}(\theta)$ on the open interval $(-\pi/2, \pi/2)$, as m varies, and say that there is a *modal flow* when such a modal branch transits between the Rossby and inertia-gravity wavebands. In contrast, the terms *spectral branch* and *spectral flow* will be used to refer to the continuous curves formed by the frequencies, which is a well-defined concept only if the spectral parameter is continuous, strictly speaking. Spectral and modal branches of the Matsuno spectrum are the same (see Figure 5). In the shallow-water spectrum on the sphere, the spectral parameter m is not continuous, yet one can argue that there is a spectral flow of frequencies in the Matsuno limit (see Figures 1 and 4), but not in the Margules limit.

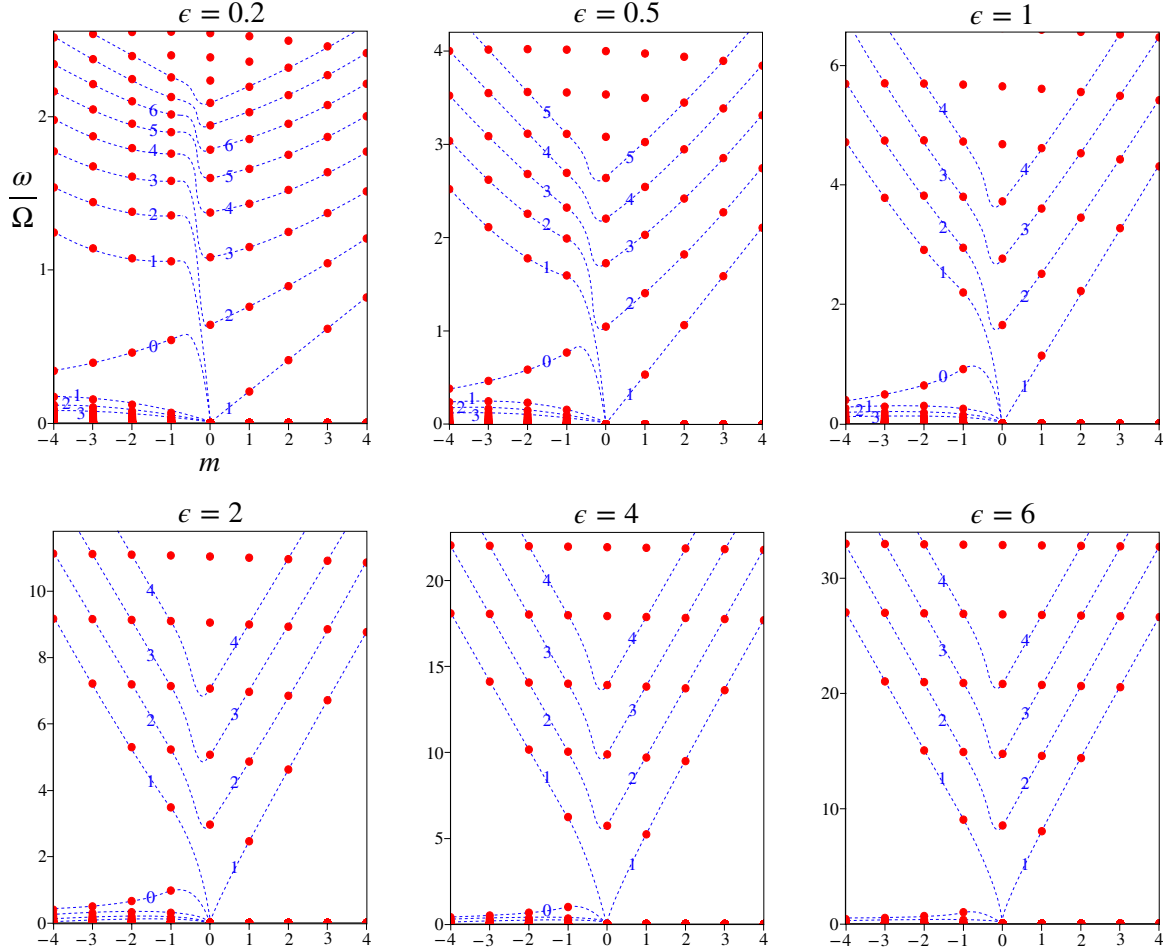


Figure 6: Numerically-calculated frequencies of Equations (4) (red dots). The modes with same number of zeros of $\tilde{v}(\theta)$ are connected by dashed blue curves, which have no physical meaning. The number of zeros is indicated on the curves. For small ϵ , the modal branches display an abrupt jump right before $m = 0$. As ϵ increases, the spectrum progressively loses its east-west asymmetry and the spectral flow collapses.

As shown in the previous section, for small ϵ , the ratio between the equatorial radius of deformation and the sphere's radius is of order $\sqrt{\epsilon}$, which implies that the wave functions spread across the whole sphere even for moderate values of ϵ , and thus the modes experience the discrepancy with the unbounded β -plane. The spreading of all the wave functions reveals additional zeros of \tilde{v} at non-zero latitude, which are virtually invisible when ϵ is too small and the modes are strongly trapped at the equator. In fact, all modes with positive phase speed (i.e. positive m , considering only the positive frequencies) have two additional zeros at opposite latitudes (see Figures 7 and 8), compared to the same modes of the unbounded β -plane. However, the zeros of Rossby modes, which propagate westward, are unchanged. In other words, the index p of the Matsuno modes propagating eastward is increased by +2 in spherical geometry. In particular, Yanai modes with negative m have $p = 0$ meridional zeros and $p = 2$ zeros for positive m . Similarly, in contrast with the unbounded β -plane, Kelvin modes have a non-zero meridional velocity which cancels once at the equator, i.e. $p = 1 = -1 + 2$. This +2 jump in number of zeros, which was already discussed by [19], is illustrated in Figure 6.

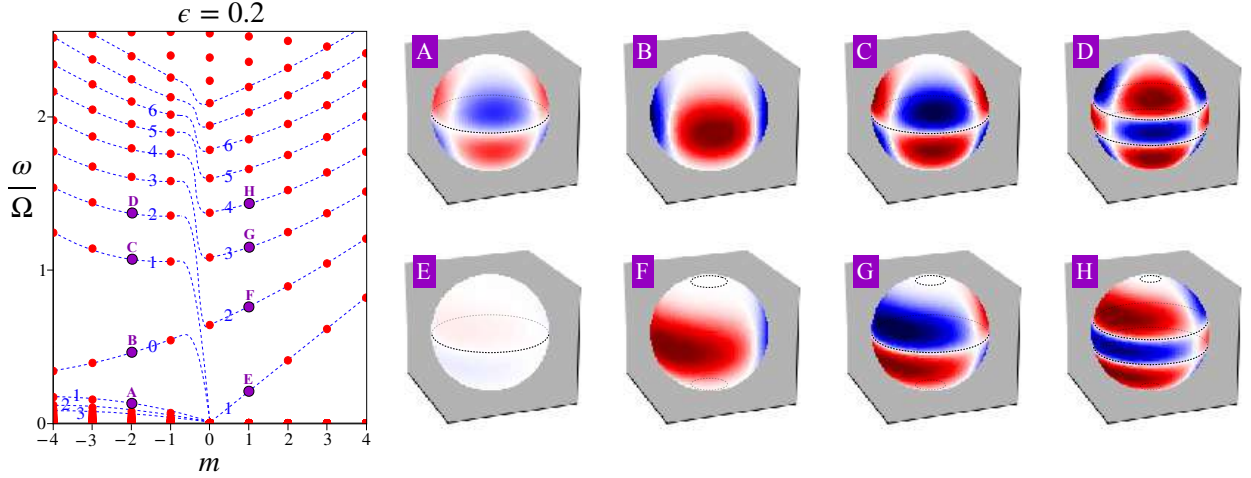


Figure 7: Meridional velocity $\text{Re}(\tilde{v}(\theta)e^{im\phi})$ of modes for $\epsilon = 0.2$ and $m = -2, +1$, computed with Dedalus (red: positive values; blue: negative values). A is a Rossby mode, B and F are Yanai modes, E is a Kelvin mode, C, D, G and H are inertia-gravity modes. On the left, modes are connected by dashed blue curves according to number of zeros of $\tilde{v}(\theta)$ on $(-\pi/2, \pi/2)$. Modes F, G and H have zeros at high latitude, which are not visible on the plot since the wave functions vanish away from the equator (see Appendix 6.1). Dashed black lines indicate the zeros of $\tilde{v}(\theta)$, and the meridional lines of zeros correspond to the term $e^{im\phi}$ with $m \neq 0$ for travelling waves.

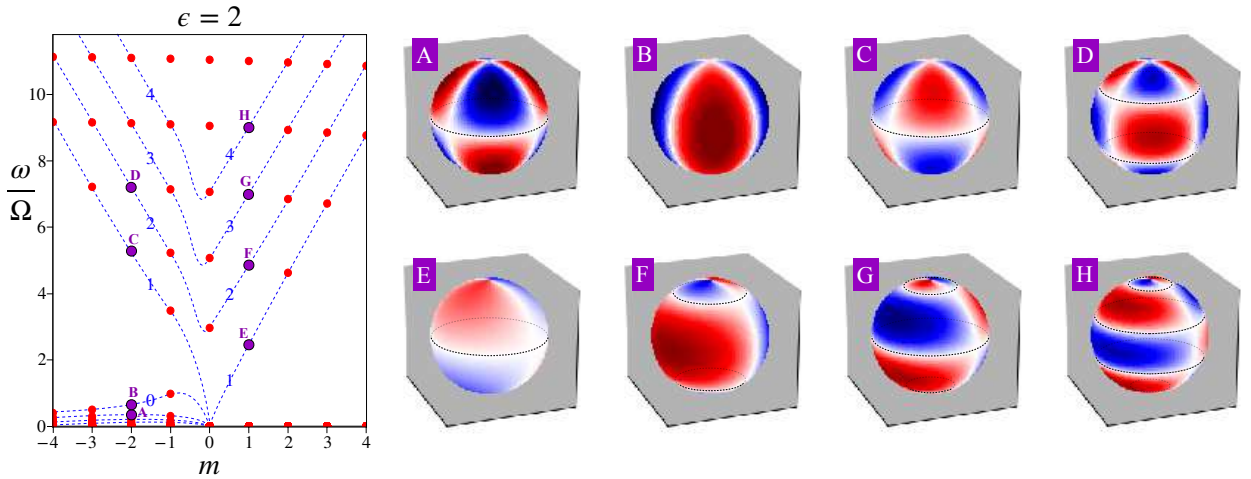


Figure 8: Same modes as Figure 7, for $\epsilon = 2$. The wave functions are more spread in latitude and extend up to the poles, clearly revealing zeros at high latitudes. The meridional velocity of a Yanai mode has no zero for negative m (B), but changes sign at two opposite latitudes for positive m (F), contrary to the Yanai mode computed by Matsuno on the equatorial β -plane. Generally speaking, the meridional velocity of modes with eastward phase speed has two more zeros, compared to Matsuno's wave functions. Similarly, Kelvin modes (E) have zero meridional velocity on the unbounded β -plane, which is not true on the sphere. Note that the north-south symmetry of the wave functions is preserved on the sphere, which implies the parity of these additional zeros. This point is discussed in Appendix 6.2.

To conclude this part, we have shown that the net modal flow of shallow-water waves, equal to $+2$ on the unbounded β -plane, is null on the sphere. This is evident for large ϵ since the spectrum displays a strong east-west symmetry, i.e. the frequencies ω and wave functions are nearly the same for m and $-m$. As ϵ becomes smaller, the spectrum loses this east-west symmetry, displays an apparent spectral flow of frequencies but the net modal flow remains zero. At small ϵ , the spectrum resembles

the Matsuno one as there are Kelvin and Yanai modes transiting across the gap for increasing wave number m . However, the Yanai modes do not form a modal branch because the eastward ones have two more zeros than the westward ones. In the present case, the nullity of this modal flow can be surprising regarding the bulk-interface correspondence established by [1, 24, 59], which states that the number of transiting modes of the Matsuno spectrum is equal to a robust topological charge +2 at the equator. In the following we will show that the nullity of the net modal flow is actually in agreement with the index theorem, as the Chern numbers of the shallow-water spectrum on the sphere add up to zero, in contrast with the unbounded β -plane.

4 Topology of the shallow-water model on the sphere

Identifying modes with the number of zeros of their \tilde{v} wave function, we showed that the net modal flow of shallow-water waves on the sphere is null, while it is +2 for the unbounded β -plane. Many studies [1, 24, 26–30, 60, 61] showed that, when the frequencies ω can be expressed as the eigenvalues of a Hermitian differential wave operator \mathcal{H} , the number of modes gained by a waveband as the spectral parameter increases is equal to a topological invariant characterising the *Weyl symbol* H of the operator \mathcal{H} , in virtue of the *index theorem* [23]. As demonstrated for instance by [1, 23, 24, 62], the presence of +2 transiting equatorial modes on the unbounded β -plane is ensured by a +2 Chern number characterising the degeneracy point of the symbol at $f = 0$. More precisely, the Yanai and Kelvin branches constitute a footprint, in the spectrum of \mathcal{H} , of a degeneracy point of its symbol bearing a Chern number +2. In light of the discussion of section 3, the aim of this section is to show that the previous conclusions can be inferred with the index theorem, as accounting for the spherical metric reveals new degeneracy points of the symbol of the wave operator, in addition to the unique degeneracy point of the problem on the unbounded β -plane. We will demonstrate that these additional degeneracy points bear topological charges which compensate the +2 Chern number of the equatorial degeneracy point, thus making the eigenbands of the symbol have zero total Chern numbers, which justifies the absence of transiting modes and the breaking of Yanai and Kelvin mode branches on the sphere for large ϵ .

4.1 Hermitian form, analogy with topographic shallow-water waves

In order to apply the index theorem, we first need to express Equations (4) in the form $\mathcal{H}X = \omega X$, where \mathcal{H} is a Hermitian differential wave operator and the complex vector X contains the three dependent variables $\tilde{u}(\theta)$, $\tilde{v}(\theta)$ and $\tilde{h}(\theta)$. To do this, we introduce the rescaled fields $u = \sqrt{\cos(\theta)} \tilde{u}$, $v = \sqrt{\cos(\theta)} \tilde{v}$ and $\eta = \sqrt{\cos(\theta)} \tilde{h}$. Equations (4) can thus be recast in the form of a matrix eigenvalue equation:

$$\omega \begin{pmatrix} u \\ v \\ \eta \end{pmatrix} = \begin{pmatrix} 0 & \mathrm{i}f(\theta) & \frac{c}{R \cos \theta} \frac{m}{\sin \theta} \\ -\mathrm{i}f(\theta) & 0 & -\mathrm{i}\frac{c}{R} \frac{\mathrm{d}}{\mathrm{d}\theta} - \mathrm{i}\beta_g(\theta) \\ \frac{c}{R \cos \theta} \frac{m}{\sin \theta} & -\mathrm{i}\frac{c}{R} \frac{\mathrm{d}}{\mathrm{d}\theta} + \mathrm{i}\beta_g(\theta) & 0 \end{pmatrix} \begin{pmatrix} u \\ v \\ \eta \end{pmatrix} = \mathcal{H} \begin{pmatrix} u \\ v \\ \eta \end{pmatrix}, \quad (11)$$

with the Coriolis parameter $f = 2\Omega \sin(\theta)$ and a *metric β -term*

$$\beta_g = \frac{c}{2R} \tan(\theta). \quad (12)$$

The problem is that of identifying the eigenvalues of the wave operator \mathcal{H} , the 3-by-3 matrix of differential operators appearing in the RHS of Equation (11). It is a Hermitian matrix operator for the canonical scalar product of complex vector functions of θ (see Appendix 6.3). In consequence,

unsurprisingly, the spectrum of shallow-water waves on the sphere is purely real. We now introduce the Weyl symbol of the wave operator \mathcal{H} :

$$H = \begin{pmatrix} 0 & if & M \\ -if & 0 & K_\theta - i\beta_g \\ M & K_\theta + i\beta_g & 0 \end{pmatrix}, \quad (13)$$

where we have also defined $M = c m / (R \cos \theta)$, and K_θ the symbol of the Hermitian differential operator $-id/d\theta$ times c/R , which is therefore a real quantity (see [63], Theorem 13.8). Generally speaking, the symbol of a wave operator, which is obtained via the Wigner transform (see appendix 6.3), provides a local representation of the wave equations in phase space (see e.g. [62, 64–66]). It extends the Fourier transform to systems of wave equations with non constant coefficients. In the present case, the symbol H represents quasi-local dispersion and polarisation relations of shallow-water waves on the sphere. H is a continuous matrix function of the conjugated variables θ , K_θ , and m . To be clear, m must be an integer so that the wave functions of \mathcal{H} are regular on the sphere, but we can formally consider the symbol H as a continuous function of m or M . In the context of this paper, we introduce it in order to apply the index theorem, following [23], i.e. we investigate the topological properties of the degeneracy points of H . This theorem relates the Chern numbers of these degeneracy points to the number and direction of transiting modes of the wave operator \mathcal{H} , which can be interpreted as the spectral footprint of a degeneracy point of non-zero Chern number in the quasi-local dispersion relations. The symbol (13) is a generalisation of the one studied by [1] for the unbounded β -plane: indeed, in the Matsuno limit, $\beta_g/f \approx \epsilon/4 \ll 1$ in the Yoshida waveguide, thus the metric term β_g can be dropped, as far as equatorially-trapped waves are concerned.

A recent paper [67] wrongly states that the shallow-water wave operator on the sphere is non-Hermitian and admits complex eigenvalues, which is not true since this system is linearly stable in the absence of a background flow. The mistake originates from using the Fourier transform (which is wrong since the coefficients of \mathcal{H} vary with θ) on the wave operator, instead of the more relevant Wigner transform. It is known that the Wigner transform must include additional terms on curved manifolds [68], which yields a Hermitian symbol in this case. Moreover, the equivalence between the respective Hermiticity of an operator and its symbol is a known property [63], and the symbol (13) is Hermitian as we used an appropriate rescaling of the variables, implying the Hermiticity of the operator \mathcal{H} for the canonical scalar product. Besides, we wish to point out that the topological properties that are presented in the following section do not depend on the choice of θ (and thus its conjugated symbol K_θ) as coordinate to express the differential operator \mathcal{H} and its symbol. Indeed, one would obtain the same symbol H using any alternative coordinate $x = F(\theta)$, as long as the fields are appropriately rescaled so as to preserve the Hermiticity of \mathcal{H} (see appendix 6.3).

We also wish to point out that Equations (11) are formally equivalent to the shallow-water model in planar geometry with varying topography, whose transiting modes were investigated by [27]. The metric term β_g plays the exact same role as the topographic parameter β_t , although [27] only considered an f -plane. In other words, the metric β -term is mathematically analogous to topography in flat metric. Actually, one could consider together the effect of a curved metric (spherical or oblate for rapidly rotating celestial bodies, for instance) with a topography $h_0(\theta)$ varying with latitude (thus the velocity $c = \sqrt{gh_0}$ is also a function of latitude). It can be shown that the symbol of this problem is the same as (13), with a total β -term that is the sum of β_g and β_t . For the spherical metric with topography, this adds up to $\beta_{\text{total}} = (c/2R)(\tan \theta - d \ln c/d\theta)$. We will not be considering a varying topography, as we wish to focus on the curved metric. However, we bring to the analysis of [27] the case of varying f and the additional geometric/topographic term with latitude, which was already addressed by [37] (part 3.5.1), in the context of the equatorial channel.

4.2 Degeneracy points of the symbol and their Chern numbers

Let us now determine the topological properties of the matrix H of Expression (13). As a function of (m, K_θ, θ) and a 3-by-3 Hermitian matrix, H has generically 3 eigenvalues which are real-valued functions defined over the parameter space (m, K_θ, θ) . These will be referred to as *eigenbands* in the following, noted λ_n with $n = -1, 0, +1$ for increasing eigenvalues. It is important to understand that these eigenvalues are not the same as the frequencies ω , i.e. the eigenvalues of the operator \mathcal{H} as defined in (11).

The fields in Equations (3) are real-valued. As such, we have $\overline{\mathcal{H}(m)} = -\mathcal{H}(-m)$, where the overline stands for the complex conjugation of all coefficients of \mathcal{H} . Consequently, the spectrum of \mathcal{H} is completely symmetric under the inversion $(m, \omega) \rightarrow (-m, -\omega)$. In the same way, all eigenvalues of H verify

$$\lambda_{-n}(m, K_\theta, \theta) = -\lambda_{+n}(-m, -K_\theta, \theta), \quad (14)$$

for any band index $n = -1, 0, +1$. Therefore, it is sufficient to consider only the positive frequencies ω of \mathcal{H} , and the eigenbands $n = 0$ (quasi-local representation of Rossby waves) and $n = +1$ (quasi-local representation of inertia-gravity waves) of H . For this reason, even though a given degeneracy point of H has three Chern numbers (one for each eigenband $n = -1, 0, +1$), we will mostly consider the $n = +1$ one and simply refer to it as Chern number (without mentioning the band index). The characteristic polynomial of the matrix H reads as

$$X^3 - (M^2 + K_\theta^2 + f^2 + \beta_g^2) X - 2f\beta_g M. \quad (15)$$

The polynomial (15) has a multiple root, i.e. H has a degenerated eigenvalue ($\lambda_0 = \lambda_{+1}$ and/or $\lambda_0 = \lambda_{-1}$), if and only if

$$\beta_g = \pm f, \quad (16)$$

as computed by [27] for the topographic shallow-water model. The degenerated positive eigenvalue ($\lambda_0 = \lambda_{+1}$) is equal to $|f|$, and the corresponding degeneracy points in parameter space are the ones such that $\beta_g(\theta) = \pm f(\theta)$, $M = \mp |f|$ and $K_\theta = 0$. Now the modal flow of \mathcal{H} for an eigenband n , i.e. the number of modes gained by the Rossby (for $n = 0$) or the inertia-gravity (for $n = +1$) waveband as m goes from $-\infty$ to $+\infty$, is constrained by the presence of at least one of these degeneracy points in the real system, and the value of this modal flow is given by the Chern number (a negative Chern number corresponds to a net loss of modes as m increases) held by this degeneracy point for the band n of the symbol [1, 23, 37]. Since f and β_g have the same sign (negative in the southern hemisphere and positive in the northern one), the problem amounts to solving $c \tan(\theta)/2R = 2\Omega \sin(\theta)$, which yields

$$\theta = 0 \quad \text{or} \quad \cos(\theta) = \frac{\epsilon}{4}. \quad (17)$$

Therefore one can distinguish two situations, as illustrated in Figure 9:

- If $\epsilon < 4$, there are three latitudes at which a degeneracy between the eigenvalues of the symbol occurs, one at the equator (3-fold since all three eigenvalues of H are degenerated there) and two (2-fold) degeneracy points near the poles, at opposite latitude. As ϵ increases, these get closer to the equator, where they eventually merge with the equatorial degeneracy point for $\epsilon = 4$. The value of m at the non-equatorial degeneracy points for the positive eigenbands is

$$m_c = -\frac{1}{2} \sqrt{1 - \left(\frac{\epsilon}{4}\right)^2} \in (-1/2, 0). \quad (18)$$

- If $\epsilon \geq 4$, there is a unique degeneracy point at the equator. This can be seen as a threshold in the competition between two different β -effects, the traditional one owing to the variation

of f with latitude, which tends to trap waves at the equator, and the geometric one, which conversely tends to spread the wave functions away from it, over the whole sphere.

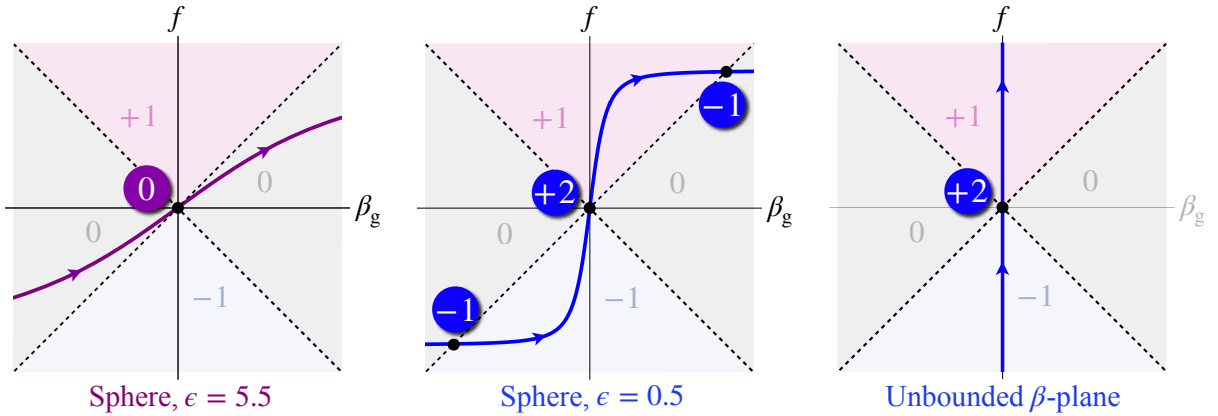


Figure 9: Phase diagram of H , inspired by [69]. The colored curves represent the trajectory of (β_g, f) as θ goes from $-\pi/2$ to $+\pi/2$. H has a degenerated eigenvalue when $f = \pm\beta_g$ (dashed lines), thus splitting the parameter space (β_g, f) in 4 areas, each of which is characterised by an integer 0, -1 or $+1$. The Chern number C_{+1} (colored discs) of a degeneracy point (black dots) involving the eigenband $n = +1$ is given by their difference as θ increases past the degeneracy point. Middle: if $\epsilon < 4$, the equatorial degeneracy point has $C_{+1} = +2$, same as in [1], and there are two additional mid-latitude degeneracy points with $C_{+1} = -1$. Left: as ϵ increases and reaches 4, they merge with the equatorial degeneracy point, which still exists for $\epsilon > 4$ and has zero Chern number. Right: the symbol of shallow-water waves on the unbounded β -plane is obtained by taking $\beta_g = 0$ and $f = \beta y$ in (13), which yields the unique degeneracy point of Chern number $+2$ studied by [1].

Each of these degeneracy points can be assigned a set of Chern numbers, one for each eigenband involved in the degeneracy (see Appendix 6.4). Again, two situations can be distinguished:

- For $\epsilon < 4$, the equatorial 3-fold degeneracy point has a set of Chern numbers $(C_{-1}, C_0, C_{+1}) = (-2, 0, +2)$ for the three eigenbands ($n = -1, 0, +1$) of H , which are all degenerated. This is the result of [1] for the β -plane shallow-water model, and it still holds with the contribution of the spherical metric, as long as $\epsilon < 4$. The other 2-fold non-equatorial degeneracy points bear the Chern numbers $(C_0, C_{+1}) = (+1, -1)$ (for the positive-eigenband degeneracies) and $(C_{-1}, C_0) = (+1, -1)$ (for the negative-eigenband degeneracies). Note that, for small ϵ , the latter are pushed toward the poles, which are then discarded by Matsuno's β -plane approximation. This is why the β -plane shallow-water model does not have them accounted for. These negatively-charged degeneracy points also appear at wave number $m = m_c \in (-1/2, 0)$, given by Expression (18), which is why their footprint is appreciable in the form of a jump of the modal branches right before m reaches 0 (see Figures 6 and 7).
- For $\epsilon \geq 4$, all degeneracy points merge at the equator – and their respective Chern numbers add up – into a unique three-fold degeneracy point which is topologically neutral, i.e. of zero Chern numbers: $(C_{-1}, C_0, C_{+1}) = (0, 0, 0)$. In the spectrum of the wave operator, this fusion manifests as a symmetrisation of the modes between positive and negative m , whereas the east-west asymmetry of the spectrum is appreciable for small ϵ , when the degeneracy points are separated.

In conclusion, the metric term β_g generates systematic degeneracy points whose Chern numbers compensate that of the equatorial degeneracy point. For small ϵ , these degeneracy points are located

near the poles and bear the Chern number -1 for the eigenband $n = +1$, and for $\epsilon \geq 4$ there is a unique degeneracy point at the equator whose Chern numbers are 0 . The eigenbands of H thus have zero total Chern numbers, which confirms that the net number of modes gained by the inertia-gravity waveband as m is swept from $-\infty$ to $+\infty$ is zero, in virtue of the index theorem. As explained in section 3, there is a direct correspondence between this mode imbalance and the evolution of the number of zeros of \tilde{v} for waves on the unbounded β -plane. While the same correspondence can only be inferred by extrapolation for waves on the rotating sphere, we showed here that the absence of modal flow is in agreement with the predictions of topology. For the unbounded β -plane, [62] provides a formal proof of the equality between the modal flow (i.e. the difference in number of positive-frequency inertia-gravity modes between the two limits $k \rightarrow +\infty$ and $k \rightarrow -\infty$) and the Chern number of the symbol's degeneracy point at the equator, based on geometric WKB analysis of the waves in both limits. This study, which provides an alternative point of view to the index theorem, could also be extended here to demonstrate the nullity of this mode imbalance on the sphere, with the wave number m instead of k .

4.3 Collapse of the spectral flow

For $\epsilon < 4$, one could expect that each of the degeneracy points exhibited in 4.2 should be associated with its own branch of modes, two of them localised near the equator, transiting from the Rossby waveband to the inertia-gravity waveband as m increases (corresponding to the $+2$ topological charge at the equator), and two localised near the latitudes $\pm\theta$ such that $\cos\theta = \epsilon/4$, transiting from the inertia-gravity waveband to the Rossby waveband as m increases (corresponding to the -1 charges). However there is no footprint of the modes transiting from the inertia-gravity waveband to the Rossby waveband, and this happens for two reasons:

- Although the index theorem applies individually for each degeneracy point of the symbol, the resulting spectral flows are visible only in a semi-classical limit [23], i.e. as long as the transiting modes are well-separated in phase space [70]. In the case of shallow-water waves on the rotating sphere, the semi-classical limit in question corresponds to $\epsilon \ll 1$. Indeed, the equatorial waves spread up to the poles even for moderate values of ϵ ($\epsilon \sim 1$), which means that the modes corresponding to the opposite spectral flows overlap and hybridise, thus manifesting an avoided crossing between their respective spectral branches (see e.g. the cases studied by [71] and [37], part 3.5.1), which is precisely why the spectral flow of frequencies collapses as ϵ increases.
- Even for $\epsilon \ll 1$ the modes of negative spectral flow are not visible in the spectrum. We showed in 4.2 that these are expected to be localised near the poles, as the corresponding degeneracy points of the symbol are, and transit around $m \approx -1/2$. These modes are the spherical counterpart of Matsuno's spurious solutions (for $\omega = -ck$), or coastal Kelvin waves in the equatorial channel [21,27,37], if the edges of the channel were moved up to the poles. Owing to the spherical geometry, the dispersion relation of coastal Kelvin modes propagating along a longitudinal wall at latitude θ is $\omega = -cm/R\cos\theta$. Therefore, the slope of the branches formed by these hypothetical polar modes is large, and they do not appear in the spectrum for integer values of the wave number m since they transit around $m \approx -1/2$. For small ϵ , the strong east-west asymmetry is the manifestation of these opposite topological charges being separated, the gap-crossing Kelvin and Yanai frequencies are the footprint of the $+2$ topological charge at the equator, while the abrupt $+2$ modal jump happening between $m = -1$ and $m = 0$ (see Figure 6) is the footprint of the degeneracy points of charges -1 located near the poles.

5 Concluding remarks

The goal of this work is to investigate the topological properties of the shallow-water spectrum on the rotating sphere. In particular, we aimed at answering the following questions: how do the results of [1], which were established using the β -plane approximation, extend to the spherical case? What does topology tell us about the transition between the Matsuno and Margules limits? Both regimes have been extensively investigated, and the corresponding solutions can be well-approximated, however there is no analytic solution for arbitrary values of ϵ . In the Matsuno limit ($\epsilon \ll 1$ or large Lamb parameter), there seems to be a continuous spectral connection between the Rossby and inertia-gravity modes, which is embodied by the Yanai and Kelvin modes, whose frequencies cross the gap as m increases (see Figure 1). This spectral feature is reminiscent of the Matsuno spectrum on the unbounded β -plane, for which the connection with topological invariant is well-established [1, 23, 24, 62]. In the Margules limit (large ϵ or small Lamb parameter), this gapless connection progressively breaks down. All the inertia-gravity modes plus the positive-phase-speed Yanai (with $m \geq 0$) and Kelvin modes (with $m \geq 1$) move up to values $\omega = \mathcal{O}(c/R)$, while the largest Yanai frequency ($m = -1$) remains smaller than Ω (see Equation (8) with $n = 0$ and Figure 4), thus separating the spectrum into two distinct wavebands with an open frequency gap.

For small ϵ , the frequencies of shallow-water waves on the sphere and those of the Matsuno spectrum on the unbounded β -plane are nearly identical, however the \tilde{v} component of the modes of positive (eastward) phase speed has two more zeros located at opposite latitudes. The latter being close to the poles, they are not captured by the β -plane approximation. Modes on the sphere have been extensively studied, in particular the Yanai modes [42, 72]. Nevertheless, to our knowledge, the existence of these additional zeros is usually not discussed in the geophysical literature. Yet they are consistent with the evolution of the shallow-water spectrum as ϵ varies continuously. To explain why, let us consider a mode with wave number m and frequency ω , for a large value of ϵ (Margules limit). The number p of zeros of $\tilde{v}(\theta)$ is established by the classification given in 2.2. The inertia-gravity modes are essentially those of the Laplacian on the sphere, which are insensitive to the sign of m . As ϵ continuously decreases, the effect of rotation becomes stronger and the spectrum progressively loses this east-west symmetry. For the mode picked in the large ϵ regime, its frequency ω and the wave function \tilde{v} change as well in a continuous manner. However, the number p cannot change as the structure of \tilde{v} is governed by a generalised Sturm-Liouville problem (see the arguments of [58]), whose eigenvalue equation is the spherical generalisation of Matsuno's equation (Equation (3.3) of [19] is given for the perturbation of potential vorticity, which is proportional to $\cos(\theta)\tilde{v}$). When decreasing ϵ , the frequencies of the eastward modes decrease faster than the westward ones, leading to a dislocation (or +2 branch jump) in the spectrum. This dislocation eventually results in the spectral flow of Yanai and Kelvin modes in the small ϵ (Matsuno) limit. In the Matsuno limit on the sphere, this spectral flow is thus obtained as a continuous deformation of the Margules spectrum with no spectral flow. It arises from the isolated +2 topological charge at the equator, whereas the opposite topological charges near the poles generate invisible modes with opposite spectral flow, which manifest in the spectrum through the change in number of \tilde{v} zeros of Yanai modes as m changes sign. In other words, this spectral flow is not a modal flow, since the westward and eastward Yanai modes do not constitute a single modal branch. In contrast, the shallow-water spectrum on the unbounded β -plane arises from a single non-zero topological charge, because there is no such way to continuously deform it into a spectrum with no modal flow, as the parameters β and c can be absorbed in the definition of length and time units, and thus do not affect the shape of the spectrum discussed in 3.1. Conversely, for waves on the sphere, both R and the Rossby radius of deformation $c/2\Omega$ deeply affect the shape of the solutions, and their ratio define the effective equatorial trapping of waves.

We then highlighted furthermore this distinction between the unbounded β -plane and the sphere

by investigating the topology of the symbol of the shallow-water model on the sphere. We showed that the shallow-water eigenbands on the sphere have zero total Chern numbers, in contrast with the eigenbands on the unbounded β -plane. Consequently, in virtue of the index theorem, there is no net modal flow of modes in the spectrum. Precisely, we found that when ϵ becomes higher than 4, several degeneracy points merge into a unique, topologically neutral degeneracy point at the equator. This manifests in the shallow-water spectrum as the loss of east-west asymmetry and the complete collapse of the spectral flow of equatorial Yanai and Kelvin waves. However, for $\epsilon < 4$, the symbol of the wave operator on the sphere has several charged degeneracy points: an equatorial one with non-zero Chern numbers, which is reminiscent of the unbounded β -plane [1], plus two others (considering the positive eigenbands $n = 0, +1$) with opposite charges. As discussed in 4.3, the spectral footprint of the former are the Yanai and Kelvin waves, whose transiting frequencies are characteristic of the east-west asymmetry at small ϵ , and that of the latter is the +2 modal jump, i.e. the fact that opposite topological charges of the symbol lead, for small ϵ , to a spectral flow that is not a modal flow.

This work joins recent efforts toward the comprehension of how topology applies in the spectral properties of continuous physical systems on curved surfaces [34, 67, 73–75], a subject that still lacks a unified framework. In that sense, we wish to stress the importance of the Weyl symbol and the spectral parameter. With this study, we have shown that the shallow-water model on the rotating sphere has a counter-intuitive topology that is either neutral (all Chern numbers are null for $\epsilon \geq 4$) or *polar* in the sense that it has several degeneracy points of non-zero Chern numbers which sum to zero (for $\epsilon < 4$), whereas its β -plane counterpart in unbounded flat geometry has a unique, topologically charged degeneracy point. Besides, we exhibited a peculiar situation, in which different degeneracy points (with different multiplicity) merge and yield a unique degeneracy point which is topologically neutral, yet without the gap opening afterward. This situation is not usual in topological physics. Further investigation is necessary to better understand the spectral properties of continuous systems on curved surfaces, and the manifestation of topology in their dynamics.

NP and GL acknowledge funding from the ERC CoG project PODCAST No 864965. AL is funded by a PhD grant allocation Contrat doctoral Normalien. PD is supported by the national grant ANR-18-CE30-0002-01.

References

- [1] P. Delplace, J. Marston, and A. Venaille, “Topological origin of equatorial waves,” *Science*, vol. 358, no. 6366, pp. 1075–1077, 2017.
- [2] A. E. Gill, *Atmosphere-ocean dynamics*, vol. 30. Academic press, 1982.
- [3] G. K. Vallis, *Atmospheric and oceanic fluid dynamics*. Cambridge University Press, 2017.
- [4] V. Zeitlin, *GEOPHYSICAL FLUID DYNAMICS: Understanding (almost) everything with rotating shallow water models*. Oxford University Press, 2018.
- [5] P. A. Gilman, “Magnetohydrodynamic “shallow water” equations for the solar tachocline,” *The Astrophysical Journal*, vol. 544, no. 1, p. L79, 2000.
- [6] T. Zaqrashvili, R. Oliver, and J. Ballester, “Global shallow water magnetohydrodynamic waves in the solar tachocline,” *The Astrophysical Journal*, vol. 691, no. 1, p. L41, 2009.
- [7] T. Zaqrashvili, M. Albekioni, J. Ballester, Y. Bekki, L. Biancofiore, A. Birch, M. Dikpati, L. Gizon, E. Gurgenashvili, E. Heifetz, et al., “Rossby waves in astrophysics,” *Space Science Reviews*, vol. 217, pp. 1–93, 2021.

- [8] W. Thomson, “1. on gravitational oscillations of rotating water,” *Proceedings of the Royal Society of Edinburgh*, vol. 10, pp. 92–100, 1880.
- [9] C.-G. Rossby, “Relation between variations in the intensity of the zonal circulation of the atmosphere and the displacements of the semi-permanent centers of action,” *J. mar. Res.*, vol. 2, pp. 38–55, 1939.
- [10] H. Stommel, “The westward intensification of wind-driven ocean currents,” *Eos, Transactions American Geophysical Union*, vol. 29, no. 2, pp. 202–206, 1948.
- [11] W. H. Munk and G. F. Carrier, “The wind-driven circulation in ocean basins of various shapes,” *Tellus*, vol. 2, no. 3, pp. 158–167, 1950.
- [12] C. Rossby, “On displacements and intensity changes of atmospheric vortices,” *Journal of Marine Research*, vol. 7, no. 3, 1948.
- [13] T. Matsuno, “Quasi-geostrophic motions in the equatorial area,” *Journal of the Meteorological Society of Japan. Ser. II*, vol. 44, no. 1, pp. 25–43, 1966.
- [14] K. Yoshida, “A theory of the cromwell current (the equatorial undercurrent) and of the equatorial upwelling an interpretation in a similarity to a costal circulation,” *Journal of the Oceanographical Society of Japan*, vol. 15, no. 4, pp. 159–170, 1960.
- [15] M. Margules, *Air motions in a rotating spheroidal shell*. Advanced Study Program, National Center for Atmospheric Research, 1980.
- [16] S. S. Hough, “V. on the application of harmonic analysis to the dynamical theory of the tides.—part ii. on the general integration of laplace’s dynamical equations,” *Philosophical Transactions of the Royal Society of London. Series A, Containing Papers of a Mathematical or Physical Character*, vol. 191, pp. 139–185, 1898.
- [17] M. S. Longuet-Higgins, “The eigenfunctions of laplace’s tidal equation over a sphere,” *Philosophical Transactions of the Royal Society of London. Series A, Mathematical and Physical Sciences*, vol. 262, no. 1132, pp. 511–607, 1968.
- [18] A. F. Bridger and D. E. Stevens, “Long atmospheric waves and the polar-plane approximation to the earth’s spherical geometry,” *Journal of the Atmospheric Sciences*, vol. 37, no. 3, pp. 534–544, 1980.
- [19] D. Müller and J. O’Brien, “Shallow water waves on the rotating sphere,” *Physical Review E*, vol. 51, no. 5, p. 4418, 1995.
- [20] P. J. Dellar, “Variations on a beta-plane: derivation of non-traditional beta-plane equations from hamilton’s principle on a sphere,” *Journal of Fluid Mechanics*, vol. 674, pp. 174–195, 2011.
- [21] N. Paldor, *Shallow water waves on the rotating Earth*. Springer, 2015.
- [22] G. M. Vasil, D. Lecoanet, K. J. Burns, J. S. Oishi, and B. P. Brown, “Tensor calculus in spherical coordinates using jacobi polynomials. part-i: Mathematical analysis and derivations,” *Journal of Computational Physics: X*, vol. 3, p. 100013, 2019.
- [23] F. Faure, “Manifestation of the topological index formula in quantum waves and geophysical waves,” *Annales Henri Lebesgue*, vol. 6, pp. 449–492, 2023.
- [24] P. Delplace, “Berry-chern monopoles and spectral flows,” *SciPost Physics Lecture Notes*, p. 039, 2022.

- [25] H. Qin and Y. Fu, “Topological langmuir-cyclotron wave,” *Science Advances*, vol. 9, no. 13, p. eadd8041, 2023.
- [26] M. Perrot, P. Delplace, and A. Venaille, “Topological transition in stratified fluids,” *Nature Physics*, vol. 15, no. 8, pp. 781–784, 2019.
- [27] A. Venaille and P. Delplace, “Wave topology brought to the coast,” *Physical Review Research*, vol. 3, no. 4, p. 043002, 2021.
- [28] N. Perez, P. Delplace, and A. Venaille, “Unidirectional modes induced by nontraditional coriolis force in stratified fluids,” *Physical Review Letters*, vol. 128, no. 18, p. 184501, 2022.
- [29] A. Leclerc, G. Laibe, P. Delplace, A. Venaille, and N. Perez, “Topological modes in stellar oscillations,” *The Astrophysical Journal*, vol. 940, no. 1, p. 84, 2022.
- [30] J. B. Parker, J. Marston, S. M. Tobias, and Z. Zhu, “Topological gaseous plasmon polariton in realistic plasma,” *Physical Review Letters*, vol. 124, no. 19, p. 195001, 2020.
- [31] H. Qin and Y. Fu, “Topological langmuir-cyclotron wave,” *Science Advances*, vol. 9, no. 13, p. eadd8041, 2023.
- [32] Z. Wang, Y. Chong, J. D. Joannopoulos, and M. Soljačić, “Observation of unidirectional backscattering-immune topological electromagnetic states,” *Nature*, vol. 461, no. 7265, pp. 772–775, 2009.
- [33] A. Souslov, B. C. Van Zuiden, D. Bartolo, and V. Vitelli, “Topological sound in active-liquid metamaterials,” *Nature Physics*, vol. 13, no. 11, pp. 1091–1094, 2017.
- [34] S. Shankar, M. J. Bowick, and M. C. Marchetti, “Topological sound and flocking on curved surfaces,” *Physical Review X*, vol. 7, no. 3, p. 031039, 2017.
- [35] L. M. Nash, D. Kleckner, A. Read, V. Vitelli, A. M. Turner, and W. T. Irvine, “Topological mechanics of gyroscopic metamaterials,” *Proceedings of the National Academy of Sciences*, vol. 112, no. 47, pp. 14495–14500, 2015.
- [36] A. B. Khanikaev, R. Fleury, S. H. Mousavi, and A. Alu, “Topologically robust sound propagation in an angular-momentum-biased graphene-like resonator lattice,” *Nature communications*, vol. 6, no. 1, p. 8260, 2015.
- [37] N. Perez, *Topological waves in geophysical and astrophysical fluids*. PhD thesis, Ecole normale supérieure de Lyon-ENS LYON, 2022.
- [38] C. Aerts, J. Christensen-Dalsgaard, and D. W. Kurtz, *Asteroseismology*. Springer Science & Business Media, 2010.
- [39] M. S. Longuet-Higgins, “Planetary waves on a rotating sphere. ii,” *Proceedings of the Royal Society of London. Series A. Mathematical and Physical Sciences*, vol. 284, no. 1396, pp. 40–68, 1965.
- [40] D. Müller, B. Kelly, and J. O’brien, “Spheroidal eigenfunctions of the tidal equation,” *Physical review letters*, vol. 73, no. 11, p. 1557, 1994.
- [41] H. Taşeli, “Exact analytical solutions of the hamiltonian with a squared tangent potential,” *Journal of mathematical chemistry*, vol. 34, pp. 243–251, 2003.

- [42] N. Paldor, I. Fouxon, O. Shamir, and C. I. Garfinkel, “The mixed rossby–gravity wave on the spherical earth,” *Quarterly Journal of the Royal Meteorological Society*, vol. 144, no. 715, pp. 1820–1830, 2018.
- [43] K. J. Burns, G. M. Vasil, J. S. Oishi, D. Lecoanet, and B. P. Brown, “Dedalus: A flexible framework for numerical simulations with spectral methods,” *Physical Review Research*, vol. 2, p. 023068, Apr. 2020.
- [44] X. Tan and A. P. Showman, “Atmospheric circulation of tidally locked gas giants with increasing rotation and implications for white dwarf–brown dwarf systems,” *The Astrophysical Journal*, vol. 902, no. 1, p. 27, 2020.
- [45] J. Monnier, R. Townsend, X. Che, M. Zhao, T. Kallinger, J. Matthews, and A. Moffat, “Rotationally modulated g-modes in the rapidly rotating δ scuti star rasalhague (α ophiuchi),” *The Astrophysical Journal*, vol. 725, no. 1, p. 1192, 2010.
- [46] A. P. Showman, J. Y. Cho, and K. Menou, “Atmospheric circulation of exoplanets,” *Exoplanets*, vol. 526, pp. 471–516, 2010.
- [47] O. Shamir, C. I. Garfinkel, E. P. Gerber, and N. Paldor, “The matsuno–gill model on the sphere,” *Journal of Fluid Mechanics*, vol. 964, p. A32, 2023.
- [48] A. D. Del Genio and W. B. Rossow, “Planetary-scale waves and the cyclic nature of cloud top dynamics on venus,” *Journal of Atmospheric Sciences*, vol. 47, no. 3, pp. 293–318, 1990.
- [49] E. S. Johnson and M. J. Mc Phaden, “Structure of intraseasonal kelvin waves in the equatorial pacific ocean,” *Journal of physical oceanography*, vol. 23, no. 4, pp. 608–625, 1993.
- [50] J. Sprintall, A. L. Gordon, R. Murtugudde, and R. D. Susanto, “A semiannual indian ocean forced kelvin wave observed in the indonesian seas in may 1997,” *Journal of Geophysical Research: Oceans*, vol. 105, no. C7, pp. 17217–17230, 2000.
- [51] G. N. Kiladis, M. C. Wheeler, P. T. Haertel, K. H. Straub, and P. E. Roundy, “Convectively coupled equatorial waves,” *Reviews of Geophysics*, vol. 47, no. 2, 2009.
- [52] T. Sakazaki and K. Hamilton, “An array of ringing global free modes discovered in tropical surface pressure data,” *Journal of the Atmospheric Sciences*, vol. 77, no. 7, pp. 2519–2539, 2020.
- [53] K. Menou and E. Rauscher, “Atmospheric circulation of hot jupiters: a shallow three-dimensional model,” *The Astrophysical Journal*, vol. 700, no. 1, p. 887, 2009.
- [54] A. P. Showman, A. P. Ingersoll, R. Achterberg, and Y. Kaspi, “The global atmospheric circulation of saturn,” *Saturn in the 21st Century*, vol. 20, p. 295, 2018.
- [55] N. Gavriel and Y. Kaspi, “The number and location of jupiter’s circumpolar cyclones explained by vorticity dynamics,” *Nature geoscience*, vol. 14, no. 8, pp. 559–563, 2021.
- [56] J. Legarreta, N. Barrado-Izagirre, E. García-Melendo, A. Sanchez-Lavega, and J. M. Gómez-Forrellad, “A large active wave trapped in jupiter’s equator,” *Astronomy & Astrophysics*, vol. 586, p. A154, 2016.
- [57] Z. Zhu, C. Li, and J. Marston, “Topology of rotating stratified fluids with and without background shear flow,” *Physical Review Research*, vol. 5, no. 3, p. 033191, 2023.
- [58] K. Iga, “Transition modes of rotating shallow water waves in a channel,” *Journal of Fluid Mechanics*, vol. 294, pp. 367–390, 1995.

- [59] C. Tauber, P. Delplace, and A. Venaille, “A bulk-interface correspondence for equatorial waves,” *Journal of Fluid Mechanics*, vol. 868, p. R2, 2019.
- [60] F. Faure and B. Zhilinskii, “Topological chern indices in molecular spectra,” *Physical review letters*, vol. 85, no. 5, p. 960, 2000.
- [61] Y. Fu and H. Qin, “Topological phases and bulk-edge correspondence of magnetized cold plasmas,” *Nature Communications*, vol. 12, no. 1, p. 3924, 2021.
- [62] A. Venaille, Y. Onuki, N. Perez, and A. Leclerc, “From ray tracing to waves of topological origin in continuous media,” *SciPost Physics*, vol. 14, no. 4, p. 062, 2023.
- [63] B. C. Hall, *Quantum theory for mathematicians*. Springer, 2013.
- [64] R. G. Littlejohn and W. G. Flynn, “Geometric phases in the asymptotic theory of coupled wave equations,” *Physical Review A*, vol. 44, no. 8, p. 5239, 1991.
- [65] Y. Onuki, “Quasi-local method of wave decomposition in a slowly varying medium,” *Journal of Fluid Mechanics*, vol. 883, p. A56, 2020.
- [66] N. Perez, P. Delplace, and A. Venaille, “Manifestation of the berry curvature in geophysical ray tracing,” *Proceedings of the Royal Society A*, vol. 477, no. 2248, p. 20200844, 2021.
- [67] D. S. Ageev and A. A. Iliasov, “Unveiling topological modes on curved surfaces,” *Physical Review B*, vol. 109, no. 8, p. 085435, 2024.
- [68] C. Gneiting, T. Fischer, and K. Hornberger, “Quantum phase-space representation for curved configuration spaces,” *Physical Review A*, vol. 88, no. 6, p. 062117, 2013.
- [69] F. D. M. Haldane, “Model for a quantum hall effect without landau levels: Condensed-matter realization of the” parity anomaly”,” *Physical review letters*, vol. 61, no. 18, p. 2015, 1988.
- [70] L. Jezequel and P. Delplace, “Mode-shell correspondence, a unifying phase space theory in topological physics – part i: Chiral number of zero-modes,” *arXiv preprint arXiv:2310.05656*, 2023.
- [71] A. Kaufman, J. Morehead, A. Brizard, and E. Tracy, “Mode conversion in the gulf of guinea,” *Journal of Fluid Mechanics*, vol. 394, pp. 175–192, 1999.
- [72] C. I. Garfinkel, I. Fouxon, O. Shamir, and N. Paldor, “Classification of eastward propagating waves on the spherical earth,” *Quarterly Journal of the Royal Meteorological Society*, vol. 143, no. 704, pp. 1554–1564, 2017.
- [73] R. Green, J. Armas, J. de Boer, and L. Giomi, “Topological waves in passive and active fluids on curved surfaces: a unified picture,” *arXiv preprint arXiv:2011.12271*, 2020.
- [74] C. Finnigan, M. Kargarian, and D. K. Efimkin, “Equatorial magnetoplasma waves,” *Physical Review B*, vol. 105, no. 20, p. 205426, 2022.
- [75] G. Li and D. K. Efimkin, “Equatorial waves in rotating bubble-trapped superfluids,” *Physical Review A*, vol. 107, no. 2, p. 023319, 2023.
- [76] M. V. Berry, “Quantal phase factors accompanying adiabatic changes,” *Proceedings of the Royal Society of London. A. Mathematical and Physical Sciences*, vol. 392, no. 1802, pp. 45–57, 1984.
- [77] T. Fukui, Y. Hatsugai, and H. Suzuki, “Chern numbers in discretized brillouin zone: efficient method of computing (spin) hall conductances,” *Journal of the Physical Society of Japan*, vol. 74, no. 6, pp. 1674–1677, 2005.

Part III

A topological wave in stellar oscillations

The nature of f -modes

Résumé

Ce chapitre présente une étude des ondes propagatives dans les intérieurs d'étoiles, l'objet d'étude de l'astérosismologie. Le but était d'adapter et généraliser les résultats de [199] qui étudiait des atmosphères isothermes à des intérieurs stellaires, ce qui demande de traiter deux obstacles : la stratification sphérique et la variation de vitesse du son. Les résultats obtenus montrent que des ondes Lamb-like devraient génériquement se propager dans les étoiles, grâce à la géométrie sphérique. Ce sont des modes d'oscillations de grandes longueurs d'ondes radiales et horizontales, donc avec des ordres et degrés $n = 0$ et $\ell \sim 1$. Cette situation est difficile à étudier théoriquement car elle échappe aux approximations locales type WKB habituellement utilisées comme présenté au Chapitre I. Cette étude a été le premier travail de cette thèse.

The work presented in this chapter discusses waves propagating inside stars, the main subjects of asteroseismology studies. The aim of the analysis is to generalize the results of [199] on isothermal atmospheres to stars, which demands to overcome two main obstacles: spherical stratification and varying sound speed. The results show that Lamb-like waves should generically propagate in stars. They are their oscillation modes with radial and horizontal wavelengths comparable to the size of the star, i.e $n = 0$ and $\ell \sim 1$. This case is difficult to analyze theoretically, as it falls out of WKB domains of validity, as presented in Chapter I.

This work was the starting point of this thesis. The results presented in this Chapter have been published in *Topological modes in stellar oscillations*, Leclerc, Laibe, Delplace, Venaille, Perez, The Astrophysical Journal 2022 [341]. The decomposition on spherical harmonics was not used in the most efficient way, which was improved later. Here, we redo the derivation using an improved way relying upon vectorial spherical harmonics.

The main result is the prediction that Lamb-like waves must propagate in stars, in the form of a large scale bulk mode. At the time, this prediction was difficult to put in perspective of the asteroseismology literature, as such a mode was not described. It was therefore required to pursue the characterization of this mode, and understand whether it did indeed propagate in stars and where was its place in the literature. This lead to the works presented in Chapter VI and Chapter IX.

V.1 A practical set of variables

Derivation of the wave equation

We are interested in the seminal case of adiabatic perturbations of a non-rotating, non-magnetic, stably stratified star, neglecting gravity perturbations, as was presented in Section I.2 of Chapter I. Let us then recall that the equations of such perturbations are

$$\partial_t \mathbf{v}' = -\frac{1}{\rho_0} \nabla P' + \frac{\rho'}{\rho_0^2} \nabla P_0, \quad (\text{V.1})$$

$$\partial_t \rho' + \rho_0 \nabla \cdot \mathbf{v}' + v'_r \frac{d\rho_0}{dr} = 0, \quad (\text{V.2})$$

$$\partial_t P' + v'_r \frac{dP_0}{dr} = c_s^2 (\partial_t \rho' + v'_r \frac{d\rho_0}{dr}), \quad (\text{V.3})$$

where $\rho_0(r)$, $P_0(r)$ and $c_s(r)$ are the equilibrium profiles of density, pressure and sound speed of the star. The steady state is spherically symmetric, such that these profiles only depend on the r coordinate of spherical geometry. \mathbf{v}' , ρ' , P' are the Eulerian perturbation of velocity, density and pressure.

In order to perform a topological analysis, one needs to re-write this system of equations into a Schrödinger-like equation $i\partial_t \mathbf{X} = \hat{\mathbf{H}}\mathbf{X}$, in order to extract the eigenvectors as described in Chapter II (e.g. Figure II.5). Furthermore, $\hat{\mathbf{H}}$ must be self-adjoint with respect to the canonical scalar product for an easy application of Wigner transform.

With this aim and inspiration from [199], it was found that this is accomplished by the change of variable

$$\mathbf{v}' \mapsto \tilde{\mathbf{v}} = \rho_0^{1/2} r \mathbf{v}', \quad (\text{V.4})$$

$$p' \mapsto \tilde{p} = \rho_0^{-1/2} c_s^{-1} r P', \quad (\text{V.5})$$

$$\rho' \mapsto \tilde{\Theta} = \rho_0^{-1/2} r \frac{g}{N} (\rho' - \frac{1}{c_s^2} P'). \quad (\text{V.6})$$

Let us go through the steps of applying the change of variable Equations (V.4)-(V.6) on the evolution equations (V.1)-(V.3). At some point in the derivations, one needs the two equations from the background

$$\frac{dP_0}{dr} = -g\rho_0, \quad (\text{V.7})$$

$$N^2 = g \left(\frac{1}{\Gamma_1} \frac{d \ln P_0}{dr} - \frac{d \ln \rho_0}{dr} \right) = -g \frac{d \ln \rho_0}{dr} - \frac{g^2}{c_s^2}, \quad (\text{V.8})$$

as well as the re-writing of Equation (V.6) to eliminate the ρ' terms as

$$\frac{g}{\sqrt{\rho_0}} \rho' = \frac{N}{r} \tilde{\Theta} + \frac{g}{c_s r} \tilde{p}. \quad (\text{V.9})$$

Let us start with the radial component of Equation (V.1):

$$\begin{aligned} \partial_t v'_r &= -\frac{1}{\rho_0} \partial_r P' + \frac{\rho'}{\rho_0^2} \frac{dP_0}{dr} = -\frac{1}{\rho_0} \partial_r \left(\frac{c_s \sqrt{\rho_0}}{r} \tilde{p} \right) - \frac{\rho'}{\rho_0} g = -\frac{1}{\rho_0} \partial_r \left(\frac{c_s \sqrt{\rho_0}}{r} \tilde{p} \right) - \frac{1}{\sqrt{\rho_0} r} \left(N \tilde{\Theta} + \frac{g}{c_s} \tilde{p} \right) \\ &= \frac{1}{r \sqrt{\rho_0}} \partial_t \tilde{v}_r \end{aligned} \quad (\text{V.10})$$

Developing the radial derivative in the r.h.s and using Eq. (V.8) yields

$$\partial_t \tilde{v}_r = -c_s \partial_r \tilde{p} - \frac{1}{2} \frac{dc_s}{dr} \tilde{p} + \left(\frac{c_s}{r} - \frac{1}{2} \frac{dc_s}{dr} + \frac{c_s}{2g} (N^2 - \frac{g^2}{c_s^2}) \right) \tilde{p} - N \tilde{\Theta}. \quad (\text{V.11})$$

V. The nature of f -modes

We will justify the choice of isolating the $\frac{1}{2} \frac{dc_s}{dr}$ term below.

Let us now establish the evolution of \tilde{p} . From Equation (V.3) and Equation (V.2), one has

$$\partial_t P' + v'_r \frac{dP_0}{dr} = c_s^2 \left(\partial_t \rho' + v'_r \frac{d\rho_0}{dr} \right) = -c_s^2 \rho_0 \nabla \cdot \mathbf{v}'. \quad (\text{V.12})$$

We now split the radial and horizontal directions as $\mathbf{v}'_h = (0, v'_\theta, v'_\phi)^\top$ and $\nabla_h = (0, \frac{1}{r} \partial_\theta, \frac{1}{r \sin \theta} \partial_\phi)^\top$. Equation (V.12) thus transforms as

$$\begin{aligned} \partial_t P' &= -c_s^2 \rho_0 \frac{1}{r^2} \partial_r (r^2 v'_r) - \frac{dP_0}{dr} v'_r - c_s^2 \rho_0 \nabla_h \cdot \mathbf{v}_h = -c_s^2 \rho_0 \frac{1}{r^2} \partial_r \left(\frac{r}{\sqrt{\rho_0}} \tilde{v}'_r \right) - \frac{1}{r \sqrt{\rho_0}} \frac{dP_0}{dr} \tilde{v}'_r - \frac{c_s^2 \sqrt{\rho_0}}{r} \nabla_h \cdot \tilde{\mathbf{v}}_h \\ &= \frac{c_s \sqrt{\rho_0}}{r} \partial_t \tilde{p}. \end{aligned} \quad (\text{V.13})$$

Once again developing the radial derivative in the r.h.s and using Eq. (V.8), one has

$$\partial_t \tilde{p} = -c_s \partial_r \tilde{v}'_r - \frac{1}{2} \frac{dc_s}{dr} \tilde{v}'_r - \left(\frac{c_s}{r} - \frac{1}{2} \frac{dc_s}{dr} + \frac{c_s}{2g} \left(N^2 - \frac{g^2}{c_s^2} \right) \right) \tilde{v}'_r - c_s \nabla_h \cdot \tilde{\mathbf{v}}_h. \quad (\text{V.14})$$

There are two more equations to establish, namely the evolutions of $\tilde{\Theta}$ and \tilde{v}_h . From Equation (V.3), re-arranging the terms yields

$$\begin{aligned} \partial_t \left(\rho' - \frac{1}{c_s^2} P' \right) &= \left(\frac{1}{c_s^2} \frac{dP_0}{dr} - \frac{d\rho_0}{dr} \right) v'_r = \frac{\rho_0}{g} N^2 v'_r = \frac{\sqrt{\rho_0}}{rg} N^2 \tilde{v}'_r \\ &= \frac{N \sqrt{\rho_0}}{rg} \partial_t \tilde{\Theta} \\ \Rightarrow \partial_t \tilde{\Theta} &= N \tilde{v}'_r. \end{aligned} \quad (\text{V.15})$$

The last equation is the easiest to establish, as the horizontal directions are insensitive to the change of variable, yielding

$$\begin{aligned} \partial_t \mathbf{v}'_h &= -\frac{1}{\rho_0} \nabla_h P' = -\frac{c_s}{r \sqrt{\rho_0}} \nabla_h \tilde{p} \\ &= \frac{1}{r \sqrt{\rho_0}} \partial_t \tilde{\mathbf{v}}_h \\ \Rightarrow \partial_t \tilde{\mathbf{v}}_h &= -c_s \nabla_h \tilde{p}. \end{aligned} \quad (\text{V.16})$$

Defining the quantity

$$S \equiv \frac{c_s}{r} - \frac{1}{2} \frac{dc_s}{dr} + \frac{c_s}{2g} \left(N^2 - \frac{g^2}{c_s^2} \right), \quad (\text{V.17})$$

which reads as a characteristic frequency of the medium, one obtains that the set of evolution equations as

$$\partial_t \tilde{\mathbf{v}}_h = -c_s \nabla_h \tilde{p}, \quad (\text{V.18})$$

$$\partial_t \tilde{v}'_r = -c_s \partial_r \tilde{v}'_r - \frac{1}{2} \frac{dc_s}{dr} \tilde{v}'_r + S \tilde{p} - N \tilde{\Theta}, \quad (\text{V.19})$$

$$\partial_t \tilde{\Theta} = N \tilde{v}'_r, \quad (\text{V.20})$$

$$\partial_t \tilde{p} = -c_s \partial_r \tilde{v}'_r - \frac{1}{2} \frac{dc_s}{dr} \tilde{v}'_r - S \tilde{v}'_r - c_s \nabla_h \cdot \tilde{\mathbf{v}}_h. \quad (\text{V.21})$$

We now deal with the horizontal directions by projecting onto spherical harmonics, by first defining

$$\mathbf{Y}_\ell^m \equiv Y_\ell^m \mathbf{e}_r, \quad (\text{V.22})$$

$$\Psi_\ell^m \equiv \frac{ir}{\sqrt{\ell(\ell+1)}} \nabla Y_\ell^m \quad \text{or 0 if } \ell = 0, \quad (\text{V.23})$$

$$\mathbf{T}_\ell^m \equiv \frac{i}{\sqrt{\ell(\ell+1)}} \mathbf{r} \wedge \nabla Y_\ell^m \quad \text{or 0 if } \ell = 0. \quad (\text{V.24})$$

Y_ℓ^m is the spherical harmonic function of harmonic and azimuthal degrees (ℓ, m) , \mathbf{e}_r is the unit vector in the radial direction. The normalization slightly differs from [342]. These complex vector fields are orthonormal with respect to the scalar product on the sphere, satisfying

$$\int d\Phi \quad \mathbf{Y}_\ell^m \cdot \mathbf{Y}_{\ell'}^{m'*} = \delta_{\ell\ell'} \delta_{mm'}, \quad (\text{V.25})$$

$$\int d\Phi \quad \mathbf{\Psi}_\ell^m \cdot \mathbf{\Psi}_{\ell'}^{m'*} = \delta_{\ell\ell'} \delta_{mm'}, \quad (\text{V.26})$$

$$\int d\Phi \quad \mathbf{T}_\ell^m \cdot \mathbf{T}_{\ell'}^{m'*} = \delta_{\ell\ell'} \delta_{mm'}, \quad (\text{V.27})$$

$$\int d\Phi \quad \mathbf{Y}_\ell^m \cdot \mathbf{\Psi}_{\ell'}^{m'*} = \int d\Phi \quad \mathbf{\Psi}_\ell^m \cdot \mathbf{T}_{\ell'}^{m'*} = \int d\Phi \quad \mathbf{T}_\ell^m \cdot \mathbf{Y}_{\ell'}^{m'*} = 0. \quad (\text{V.28})$$

Φ is the solid angle ($d\Phi = \sin \theta d\theta d\phi$). One can thus decompose the (rescaled) velocity perturbations as $\tilde{\mathbf{v}}(r, \theta, \phi, t) = \tilde{v}_r(r, t)\mathbf{Y}_\ell^m(\theta, \phi) + \tilde{v}_h(r, t)\mathbf{\Psi}_\ell^m(\theta, \phi)$, along with $\tilde{\Theta}, \tilde{p} \propto Y_\ell^m$. Using relations on vectorial spherical harmonics, one has from Equations (V.18) and (V.21) that

$$\partial_t \tilde{v}_h(r, t) = \int d\Phi \quad \partial_t \tilde{\mathbf{v}} \cdot \mathbf{\Psi}_\ell^{m*} = \int d\Phi \quad (-c_s \nabla \tilde{p}) \cdot \mathbf{\Psi}_\ell^{m*} = i c_s \frac{\sqrt{\ell(\ell+1)}}{r} \tilde{p}, \quad (\text{V.29})$$

$$\begin{aligned} \partial_t \tilde{p}(r, t) &= \int d\Phi \left(-(S + \frac{c'_s}{2} + c_s \partial_r) \tilde{v}_r Y_\ell^m - c_s \nabla_h \cdot (\tilde{v}_h \mathbf{\Psi}_\ell^m) \right) Y_\ell^{m*} \\ &= -(S + \frac{c'_s}{2} + c_s \partial_r) \tilde{v}_r - i c_s \frac{\sqrt{\ell(\ell+1)}}{r} \tilde{v}_h. \end{aligned} \quad (\text{V.30})$$

Introducing the Lamb frequency $L_\ell = c_s \frac{\sqrt{\ell(\ell+1)}}{r}$, one obtains the desired equation which reads

$$i\partial_t \begin{pmatrix} \tilde{v}_h \\ \tilde{v}_r \\ \tilde{\Theta} \\ \tilde{p} \end{pmatrix} = \begin{pmatrix} 0 & 0 & 0 & L_\ell \\ 0 & 0 & -iN & -i c_s \partial_r - \frac{i}{2} \frac{dc_s}{dr} + iS \\ 0 & iN & 0 & 0 \\ L_\ell & -i c_s \partial_r - \frac{i}{2} \frac{dc_s}{dr} - iS & 0 & 0 \end{pmatrix} \begin{pmatrix} \tilde{v}_h \\ \tilde{v}_r \\ \tilde{\Theta} \\ \tilde{p} \end{pmatrix}. \quad (\text{V.31})$$

This equation is a re-writing of the evolution of linear, adiabatic waves in non-rotating non-magnetic stars. By enforcing the symmetrisation of the equations, we revealed a third characteristic frequency S , which in addition to the well-known Lamb L_ℓ and Brunt-Väisälä N frequencies, govern the waves. The operator

$$\hat{\mathbf{H}} = \begin{pmatrix} 0 & 0 & 0 & L_\ell \\ 0 & 0 & -iN & -i c_s \partial_r - \frac{i}{2} \frac{dc_s}{dr} + iS \\ 0 & iN & 0 & 0 \\ L_\ell & -i c_s \partial_r - \frac{i}{2} \frac{dc_s}{dr} - iS & 0 & 0 \end{pmatrix} \quad (\text{V.32})$$

is self-adjoint for the boundary conditions $\tilde{v}_r(r=0) = \tilde{v}_r(r=R) = 0$.

Topological analysis

Employing the wave topology methodology described on Figure II.5, we compute the Wigner symbol of the operator $\hat{\mathbf{H}}$ as being

$$\mathbf{H} = \begin{pmatrix} 0 & 0 & 0 & L_\ell \\ 0 & 0 & -iN & K_r + iS \\ 0 & iN & 0 & 0 \\ L_\ell & K_r - iS & 0 & 0 \end{pmatrix}. \quad (\text{V.33})$$

In other words, locally plane waves $\mathbf{X} \propto e^{-i\omega t - ik_r r}$ are solutions of $\omega \mathbf{X} = \mathbf{H} \mathbf{X}$, where $K_r = c_s k_r$. Interestingly, we find the exact same symbol as [199] did for waves in atmospheres. The sphericity and variations of sound speed correct the expression of S , but do not impact the local propagation

V. The nature of f -modes

of the waves. Therefore, the Berry curvature and Berry-Chern monopoles are identical, and the full expression of the former is derived and given in Appendix B. We recall that they are located at

$$K_r = S = 0 \quad \text{and} \quad L_\ell = \pm N, \quad (\text{V.34})$$

with Chern numbers $\mathcal{C} = \mp 1$ for the acoustic wavebands, and $\mathcal{C} = \pm 1$ for the internal gravity wavebands.

We therefore expect generically a spectral flow between the two wavebands in the spectrum of a star. Interestingly, where [199] found that S was never changing sign in the bulk of atmospheres, we find that the curvature term c_s/r crucially helps in having radii where it goes to zero. It is thus expected that Lamb-like waves would be trapped at these radii in stars.

This analysis is equivalent and more straightforward than the one published in [341], the article which is shown below, truncated of its appendices.

Topological modes in stellar oscillations

ARMAND LECLERC ,¹ GUILLAUME LAIBE,^{1,2} PIERRE DELPLACE,³ ANTOINE VENAILLE,³ AND NICOLAS PEREZ³

¹ Univ Lyon, Univ Lyon1, ENS de Lyon, CNRS, Centre de Recherche Astrophysique de Lyon
 UMR5574, F-69230, Saint-Genis-Laval, France

² Institut Universitaire de France

³ ENS de Lyon, CNRS, Laboratoire de Physique (UMR CNRS 5672), F-69342 Lyon, France

ABSTRACT

Stellar oscillations can be of topological origin. We reveal this deep and so-far hidden property of stars by establishing a novel parallel between stars and topological insulators. We construct an hermitian problem to derive the expression of the stellar *acoustic-buoyant frequency* S of non-radial adiabatic pulsations. A topological analysis then connects the changes of sign of the acoustic-buoyant frequency to the existence of Lamb-like waves within the star. These topological modes cross the frequency gap and behave as gravity modes at low harmonic degree ℓ and as pressure modes at high ℓ . S is found to change sign at least once in the bulk of most stellar objects, making topological modes ubiquitous across the Hertzsprung-Russel diagram. Some topological modes are also expected to be trapped in regions where the internal structure varies strongly locally.

Keywords: Stellar oscillations – Internal waves – Theoretical techniques

1. INTRODUCTION

Stars are opaque. Fortunately, deformations of the stellar surface depend on their interiors Cowling (1941); Gough (1993); Ledoux & Walraven (1958); Unno et al. (1979); Christensen-Dalsgaard et al. (1996); Aerts et al. (2010) and as such, asteroseismology is the Rosetta Stone to infer details of stellar structures Christensen-Dalsgaard et al. (1996); Aerts et al. (2010). Stellar spectra consist principally of low-frequencies gravity (g-) modes and high-frequencies pressure (p-) modes, defining two bands separated by a finite interval of frequencies, also referred as a gap. The stellar spectrum may also be enriched by additional branches, such as surface wave modes confined in the outer regions. In recent years, a novel type of waves propagating in stratified compressible fluids has been discovered. This so-called *Lamb-like* wave fills the gap between the p- and the g- band. Although this mode bears similarities with the Lamb wave Lamb (1911); Iga (2001), it is confined around peculiar values specific of the stratification profile, and not at the boundaries. The key point is that

these waves have been postulated using arguments from topology Perrot et al. (2019). Modes in the original spatially homogeneous system can be predicted from the analysis of the topological invariant of a simpler dual wave problem with constant coefficients. Similar topological approaches were developed in condensed matter since the eighties, and flourished across all field of physics, including fluid dynamics and plasma over the last few years Hasan & Kane (2010); Delplace et al. (2017); Shankar et al. (2020); Parker (2021).

The Lamb wave has been detected in the atmosphere, but the Lamb-like wave is hardly expected to propagate on Earth, neither in the atmosphere nor in oceans. Stars were speculated to provide favourable conditions for it to propagate Perrot et al. (2019). However, this study lacked the treatment of self-gravity, spherical geometry and variations of sound speed, three critical processes as we shall show. We therefore adapt tools that have been originally developed by the topological insulator community to study the seminal case of adiabatic perturbations of a non-rotating, non-magnetic, stably stratified stellar fluid neglecting gravity perturbations (Cowling's approximation Cowling (1941)). The physical quantities are first rescaled to express the evolution of linear perturbations under the form of a Schrödinger-like wave

Corresponding author: Guillaume Laibe
 guillaume.laibe@ens-lyon.fr

equation

$$i\partial_t \mathbf{Y} = \mathcal{H}\mathbf{Y} \quad (1)$$

where $\mathcal{H} =$

$$i \begin{pmatrix} 0 & 0 & 0 & 0 & -\frac{c_s}{r}\partial_\theta \\ 0 & 0 & 0 & 0 & -\frac{c_s}{r\sin(\theta)}\partial_\phi \\ 0 & 0 & 0 & -N & S - c_s\partial_r - \frac{c'_s}{2} \\ 0 & 0 & N & 0 & 0 \\ -\frac{c_s}{r\sin(\theta)}\partial_\theta(\sin(\theta)\cdot) & -\frac{c_s}{r\sin(\theta)}\partial_\phi & -S - c_s\partial_r - \frac{c'_s}{2} & 0 & 0 \end{pmatrix},$$

and the perturbation vector contains rescaled velocities, density and pressure

$$\mathbf{Y} = {}^\top (\tilde{u}, \tilde{v}, \tilde{w}, \tilde{\Theta}, \tilde{p}). \quad (2)$$

See Appendix A for details.

As such, the 5×5 wave operator \mathcal{H} of the problem is explicitly Hermitian. \mathcal{H} depends on the sound speed c_s , the Brunt-Väisälä frequency N and a characteristic frequency further referred to as the *acoustic-buoyant frequency* S that emerges explicitly

$$S \equiv \frac{c_s}{2g} \left(N^2 - \frac{g^2}{c_s^2} \right) - \frac{1}{2} \frac{dc_s}{dr} + \frac{c_s}{r}. \quad (3)$$

All three parameters vary with radius r . Usually, these equations are combined into a single differential equation of high order. Instead, preserving the vectorial structure of the problem is better suited for a topological analysis.

2. ACOUSTIC-BUOYANT FREQUENCY S

The acoustic-buoyant frequency S is a coupling parameter for momentum exchange between buoyant and acoustic oscillations, and was called *stratification parameter* in Perrot et al. (2019). This role of mode coupling is shown in details below. Two extra terms appear compared to the plan-parallel case Perrot et al. (2019): c_s/r , which accounts for sphericity effects at small radii, and $\frac{1}{2} \frac{dc_s}{dr}$, which becomes important when the internal structure of the object varies strongly. S combines the four physical processes responsible for mirror-symmetry breaking in the radial direction: gravity, density stratification, curvature, and radial variations of sound speed. The profile $S(r)$ varies between stellar objects ; however the sound speed is expected to go to 0 at the surface as a positive power law of the density Chandrasekhar (1939); Horedt (1987). S is then $-\infty$ at the surface. At small radii, the curvature term guarantees S to reach $+\infty$. $S(r)$ being continuous, it must change sign in the bulk of the star at least once. We confirm this analytically on a stellar polytrope in Appendix B and numerically on models of typical stellar objects computed with the MESA code Paxton et al. (2011) (Fig. 2).

The physical nature of the acoustic-buoyant frequency S is disclosed by considering the equivalent of Eq. (1) in the 2D plane-parallel (y, z) geometry. After performing a Fourier transform in time and space in the invariant direction y and performing the rescaling $(u, w, \Theta, p) \mapsto c_s^{1/2}(u, w, \Theta, p)$, one obtains

$$\partial_t u = i c_s k_y p, \quad (4)$$

$$\partial_t \Theta = N w, \quad (5)$$

$$\partial_t w = -N \Theta - c_s \partial_z p + S p, \quad (6)$$

$$\partial_t p = i c_s k_y u - c_s \partial_z w - S w. \quad (7)$$

Combining the equations gives

$$(\partial_{tt} + N^2)w = -\partial_t(c_s \partial_z p - S p), \quad (8)$$

$$(\partial_{tt} + c_s^2 k_y^2)p = -\partial_t(c_s \partial_z w + S w), \quad (9)$$

a system where acoustic and buoyant vibrations are explicitly coupled (no Boussinesq or anelastic approximation is assumed). The first term of the right-hand side of Eq. (8) consists of local pressure forces that competes with buoyancy. The first term of the right-hand side of Eq. (9) comes from fluid compression in the direction z and is generic from 2D purely acoustic waves. In the long wavelength limit in the stratification direction z , these two terms become negligible and

$$(\partial_{tt} + N^2)w = S \partial_t p, \quad (10)$$

$$(\partial_{tt} + c_s^2 k_y^2)p = -S \partial_t w, \quad (11)$$

showing that S is the frequency of periodic exchanges of momentum between acoustic and buoyant vibrations. Non-Boussinesq contributions allow local densities to be affected by acoustic compression, providing an effect that competes with buoyancy when S is large. Conversely, pressure increases not only through compression, but also through advection in a differential background. These two effects on coupling between g-modes and p-modes were identified by Lighthill (1978). Multiplying Eq. (10) by $\partial_t p$ and Eq. (11) by $\partial_t w$ shows that the power transmitted by one mode to the other occurs without losses, as expected from the adiabatic assumption. Such a coupling has been widely studied in polariton physics, and shown to result in gap opening Lagoudakis (2013). The condition $S = 0$ is therefore associated to local mode decoupling (see Fig. 1).

3. TOPOLOGICAL PROPERTIES OF THE PROBLEM

Eigenvalues of \mathcal{H} are constrained by topology when varying the physical parameters. These constraints can be efficiently studied by associating a simple matrix to

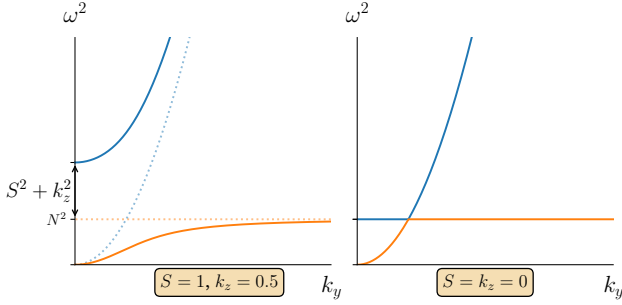


Figure 1. Local dispersion relation of the problem, as modelled by Eqs. (8)-(9). The p-mode and the g-mode (solid lines) result from the coupling of acoustic and buoyant oscillations (dashed lines for $k_z = 0$). Both S and k_z pull the bands away. For any mode, including $k_z = 0$, a gap exists as soon as $S \neq 0$.

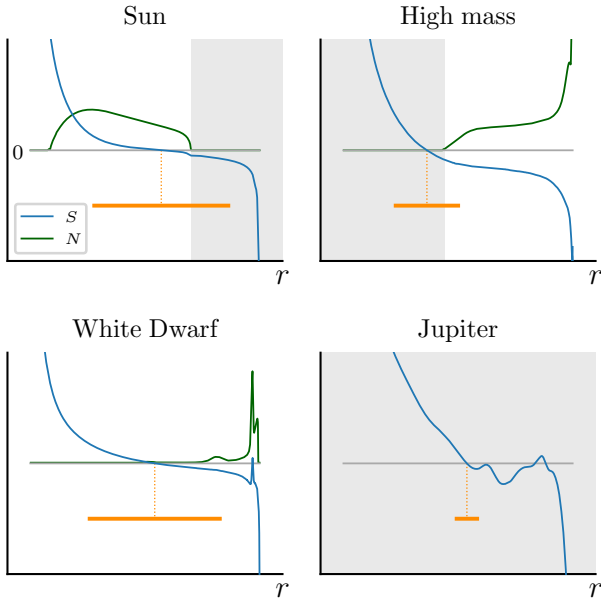


Figure 2. Profiles of S for four different typical stellar objects. N is plotted for comparison. Solid orange line indicates the region where the topological mode is trapped, as measured by the trapping length \mathcal{L} defined by Eq. (25). Stellar interiors are computed with MESA. The High mass star is an $M = 100M_{\odot}$ main-sequence star. The White Dwarf mass is $0.6M_{\odot}$, during its cooling phase. The Jupiter model has a solid core of 10 Earth masses. S cancels always at least once, whether in the radiative or convective region. Light grey area indicates the convective zone.

\mathcal{H} that retains the topological constraints. The correspondence is established via a Wigner transform, which allows us to define rigorously a wave that is locally plane without any hypothesis of scale separation (Appendix C). Here, topological properties of \mathcal{H} can be charac-

terised through the eigenvalue problem of the matrix

$$M \equiv \begin{pmatrix} N^2 & -NS - iNc_s k_r \\ -NS + iNc_s k_r & L_{\ell}^2 + S^2 + c_s^2 k_r^2 \end{pmatrix}, \quad (12)$$

$$\omega \mathbf{X} = M \mathbf{X}, \quad (13)$$

where the Lamb frequency is $L_{\ell} \equiv c_s \sqrt{\ell(\ell+1)}/r$. M is Hermitian and parametrised by a radial wavenumber k_r and parameters L_{ℓ} , c_s , N and S that are constant.

As expected, the two eigenvalues of M correspond to the square of the frequencies of the local pressure and gravity modes. Interestingly, these two bands intersect when $k_r = 0$, $L_{\ell} = N$, $S = 0$ for any value of c_s and N , i.e. the two frequencies degenerate into a single one (see Appendix C). Such a degeneracy point behaves like a topological monopole in parameter space (k_r, L_{ℓ}, S) , which is characterised by an integer called the Chern number Chern (1946). A non-zero Chern number translates the topological obstruction to smoothly define the phase of the eigenvectors – that describe the local polarization relations of M – all around the degeneracy point in parameter space. In that case, the eigenvectors can only be defined smoothly over patches in parameter space, corresponding to different gauge choices. The $U(1)$ gauge transformation that connects the different patches is a phase whose winding is the Chern number. In our case, we find the Chern numbers associated to the gravity and the pressure bands to be $\mathcal{C}^g = +1$ and $\mathcal{C}^p = -1$ respectively (see Appendix D for computations). These topological considerations can be back-connected to the original problem : any change of sign of the acoustic-buoyant frequency $S(r)$ is associated to the existence of a branch that transits from the g-band towards the p-band as ℓ increases. Mathematically, this correspondence is ensured by index theorems Atiyah & Singer (1963); Chern (1946); Perrot et al. (2019); Faure (2019); Delplace (2022); Nakahara (1990); Esposito (1997). The transiting branch flows from the upper-band to the lower-band or *vice-versa*, depending on the sign of S' at the change of sign of S . In stars, $S' < 0$ and the mode transits from the g- to the p- band: this mode is the Lamb-like wave Perrot et al. (2019). Fig. 3 confirms the deep relation between a change of sign of $S(r)$ and the existence of a mode transiting from the g-band at small ℓ to the p-band at large ℓ . The physical validity of this mode is carefully verified in Appendix E.

By analogy with similar modes encountered in a variety of other physical systems Hasan & Kane (2010); Delplace et al. (2017); Shankar et al. (2020); Parker (2021), one may expect for the global stellar mode to have no node, and to transit between the bands at a value of ℓ such that $L_{\ell} \sim N$. One may also expect for

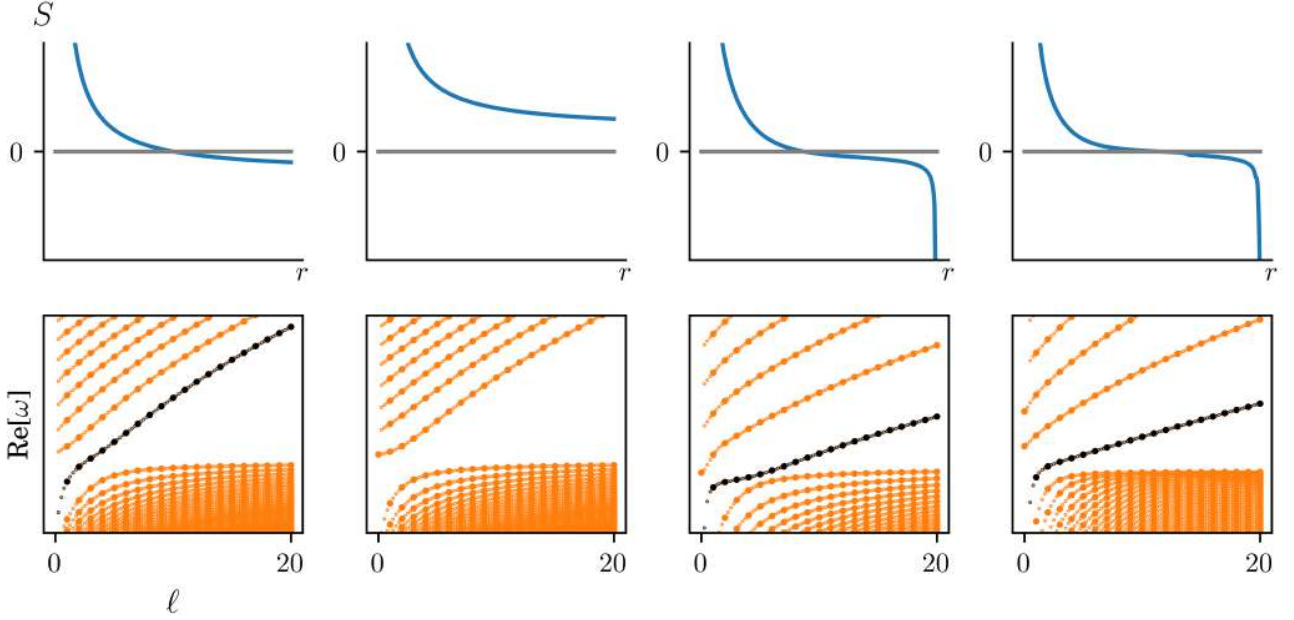


Figure 3. A mode develops between the gravity band and the pressure band (bottom) when the acoustic-buoyant frequency S (top) of Eq. (3) changes sign. From left to right: toy profile that cancels in the bulk, decaying positive profile of S , polytrope with polytropic index $n = 3$ and a MESA Solar-like profile. Physical values of the harmonic degree ℓ are integer, and plotted with large points, from 0 to 20. Non-integer values are plotted with small points for readability. Surface gravity waves are filtered out by appropriate boundary conditions. The mode transiting between bands is highlighted in black. These values are computed by solving Eq. (1) numerically using `Dedalus` Burns et al. (2020).

the eigenfunctions to be located around the radius r_0 where $S(r_0) = 0$. These properties of the topological mode can be verified on a simple analytically solvable model presented in the next section.

4. TOPOLOGICAL MODE IN ANALYTICAL MODEL

We present a simple analytical model featuring a cancellation in S , and show that the analytical solution of the wave equation include the topological mode. Consider a fluid where all quantities but S are constant in space:

$$S(r) = -\alpha(r - r_0), \quad (14)$$

$$N(r) = N_0, \quad (15)$$

$$c_s(r) = c_{s,0}, \quad (16)$$

$$L_\ell^2(r) = L_{\ell,0}^2 = c_{s,0} \frac{\ell(\ell+1)}{r_0^2}. \quad (17)$$

This parametrisation mimics a situation where variations of S would be infinitely more abrupt than the other quantities. In this minimal model, S vary linearly and cancels in r_0 . This model may thus be thought of as the compressible-stratified analogue to the equatorial shallow water model solved by Matsuno Mat-

suno (1966). Perform the transform $(u, v, w, \Theta, p) \mapsto c_s^{1/2}(u, v, w, \Theta, p)$ in Eq. (1), then apply a time-Fourier Transform and project on spherical harmonics. The variables combine into a single ODE on p

$$\left(\frac{d^2}{dr^2} - \left(\frac{S(r)}{c_{s,0}} \right)^2 - \left(\frac{S(r)}{c_{s,0}} \right)' + k_{r,0}^2 \right) p = 0, \quad (18)$$

where we denote

$$k_{r,0}^2 = \frac{(L_{\ell,0}^2 - \omega^2)(N_0^2 - \omega^2)}{c_{s,0}^2 \omega^2}, \quad (19)$$

and use the symbol $'$ for derivatives with respect to r for background quantities. Eq. (18) holds for any $S(r)$, and can be seen as a Schrödinger equation describing a particle of energy $k_{r,0}^2$ in the potential $V = S^2/c_{s,0}^2 + S'/c_{s,0}$. For the model of Eq. (14), this reduces to

$$\left[\frac{d^2}{dx^2} - \left(\frac{1}{4}x^2 - \frac{1}{2}(1 + \frac{c_{s,0}}{\alpha} k_{r,0}^2) \right) \right] p = 0, \quad (20)$$

using the dimensionless quantity $x \equiv \sqrt{2}\sqrt{\frac{\alpha}{c_{s,0}}}(r - r_0)$. The solution is a Parabolic Cylinder Function U Abramowitz & Stegun (1972)

$$p = U \left(-\frac{1}{2}(1 + \frac{c_{s,0}}{\alpha} k_{r,0}^2), x \right). \quad (21)$$

Regularity at infinity imposes the first argument to be negative half-integer, leading to the quantization

$$\frac{c_{s,0}}{\alpha} k_{r,0}^2 = 2n + 1, \quad (22)$$

for any $n \in \mathbb{N}$.

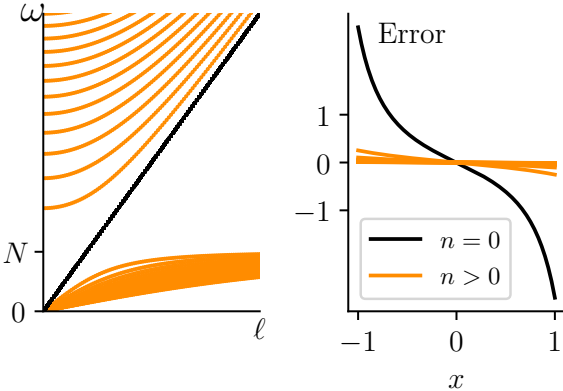


Figure 4. Left: spectrum of the minimal model parametrized by Eq. (14). The topological mode is the $n = 0$ mode, and transits between the bands. Right: Measure of the error a JWKB approximation of the solutions would make. The error on the $n = 0$ mode is not small.

Solutions reduce then to Hermite functions $p = e^{-x^2/2} H_n(x)$, where H_n denotes the n th Hermite polynomial. Fig. 4 shows the spectrum associated to this problem. The values of ω can be inverted in Eq. (22). For $n \geq 1$, each value of $k_{r,0}$ give two eigenfrequencies, the n th g-mode and the n th p-mode. The expected topological mode corresponds to $n = 0$. One of the two eigenfrequencies associated with this solution is unphysical, since the eigenfunctions diverges quickly at infinity. The other verifies

$$\omega = L_{\ell,0}, \quad (23)$$

which transits between the bands as ℓ increases, as shown on Fig. 4. This property is associated to the fact that $S'(r_0) = -\alpha < 0$ at the cancellation point.

The topological mode has the profile

$$p(r) = p_0 \exp \left(-\frac{\alpha}{c_{s,0}} (r - r_0)^2 \right), \quad (24)$$

an expression that provides a definition of the length over which the mode has significant amplitude

$$\mathcal{L} \equiv \sqrt{\frac{c_{s,0}}{\alpha}} = \sqrt{c_{s,0} / \left| \frac{dS}{dr} \right|_{S=0}}, \quad (25)$$

which we call the *trapping length*. Denoting $R(x) \equiv -\frac{1}{4}x^2 + n + 1/2$ the second term of Eq. (20)

that corresponds to a solution for a given n , we find for JWKB approximation of the solution to be valid when the condition $|R^{-3/2} \frac{dR}{dx}| \ll 1$ is satisfied (Daghig & Green 2012). Fig. 4 shows this quantity for the first modes. The topological mode $n = 0$ breaks strongly this validity condition. As expected, JWKB techniques cannot capture the topological mode.

This analytical solution confirms that the topological mode is the mode with zero node of the system, and that this mode is not accessible with scale separation methods.

5. DISCUSSION

Interestingly, the topological mode and the surface-gravity mode have both zero node and similar dispersion relations. Numerical experiments show that when they coexist, they hybridize to form a unique $n = 0$ mode. A comprehensive study including various boundary conditions is performed in Appendix F. We interpret this hybridised mode as the *f-mode* of asteroseismology Gough (1993); Rozelot & Neiner (2011), revealing its previously unexpected hybrid nature.

Finally, strong local gradients of thermodynamical quantities may give rise to peaks of acoustic-buoyant frequency where S changes sign twice over a short scale, as in the White Dwarf model showed on Fig. 2. This results in two modes of topological origin that may be used to probe fine details of the structure of the stellar object. The white dwarf is the canonical object for application of this study, as it is fully radiative. Its profile of S cancels three times, two of them resulting from a phase transition close to the surface. For this model, we predict three topological modes, one for each cancellation. One crossing the gap, with long trapping length \mathcal{L} , as the slope of S where it changes sign is low at the first cancellation. Two more modes with zero nodes are predicted close to the peak of S just underneath the surface, with much smaller trapping lengths \mathcal{L} , as the slope of S is high when S changes sign. They potentially overlap each other, such that they would hybridise. This hybridisation could serve as a measure of the peak in S , meaning the modes could serve as probes for the associated phase transition. This hybridization is illustrated on Fig. 5.

The current study focuses on stably stratified stars, for which index theorems on Hermitian systems apply. However the effect of a convective zone on the Lamb-like wave remains to be investigated. Such a region, where N^2 vanishes, is indeed sustained by the convective circulation of the background. Fig. 2 shows that in the Sun, S cancels in the radiative zone, close to the convective zone. The trapping length of the topological mode in-

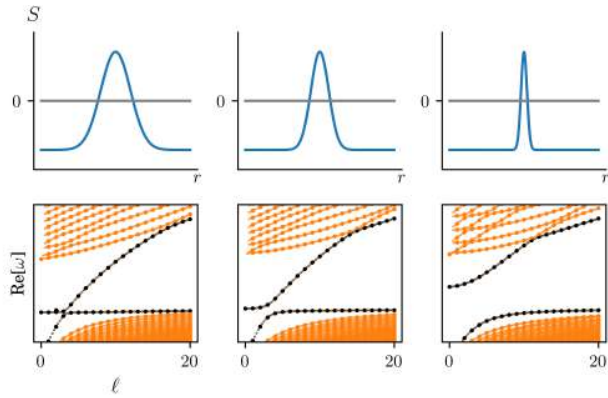


Figure 5. Peaks of S through positive values imply the existence of two topological modes in the spectrum. The sharper the peak, the more the modes hybridize, and their branches avoid crossing in the spectrum.

dicates interactions with the convective zone, although convection is out of the scope of this study. In High Mass stars, S cancels within the convective core where the topological mode is not guaranteed by this study, as no background flow is considered in the wave equation Eq. (1). The same conclusion applies to Jupiter, which is fully convective, and has interesting multiple cancellations of S .

Lamb-like waves are neither Lamb waves, surface-gravity waves, nor mixed modes Dziembowski et al. (2001); Dupret et al. (2009); Deheuvels & Michel (2010). Mixed modes are linear combinations of g-modes and p-modes standing in different cavities in the star, due to spatial variations of N and L_ℓ and can have a high number of nodes. The Lamb-like wave emanates as a mode $n = 0$ of a single cavity hosting both g-modes and p-modes.

We expect generic properties of stellar pulsations related to topology such as ray tracing to be encoded in $S(r)$ Perez et al. (2021). Other discrete symmetries can be broken in the presence of rotation Perez et al. (2021) and magnetic fields Cally (2006); Parker et al. (2020), and one should expect the emergence of new classes of topological waves when these additional ingredients are taken into account, potentially at the stellar tachocline where strong shear develops. The resilience of these topological modes on unstable stratification when $N^2 < 0$, or with the inclusion of dissipative effects, is a highly promising avenue of research in the currently flourishing field of non-Hermitian topological waves Delplace et al. (2021); Gong et al. (2018); Yao & Wang (2018); Bergholtz et al. (2021).

In this study, we revisit the old field of stellar pulsations under the bright new prism of topology. By doing a novel parallel between stars and topological insulators, we establish for the first time the existence of a wave of topological origin in stars. We derive the expression of a novel key physical parameter, the acoustic-buoyant frequency. We demonstrate in a comprehensive analysis that topological modes are associated to zeros of this frequency, and show the ubiquitous existence of at least one topological mode across the entire spectrum of stellar object in the Universe. More importantly, we show that local phase transitions, which are key for understanding the evolution of stars within the cosmological context, may give rise to pairs of robust topological modes. The hunt of these modes may therefore become a critical target for future cutting-edge instruments such as the *PLATO* mission.

ACKNOWLEDGMENTS

A.L. lead the derivation of the acoustic-buoyant frequency and performed numerical simulations. G.L. lead the astrophysical analysis and the writing of the manuscript. P.D. and A.V. lead the topological analysis and the analogy with the plane-parallel case. N.P. performed the numerical experiments on surface-gravity wave and topological mode hybridisation.

G.L. acknowledges funding from the ERC CoG project PODCAST No 864965. This project has received funding from the European Union’s Horizon 2020 research and innovation programme under the Marie Skłodowska-Curie grant agreement No 823823. This project was partly supported by the IDEXLyon project (contract nANR-16-IDEX-0005) under the auspices University of Lyon. We acknowledge financial support from the national programs (PNP, PNPS, PCMI) of CNRS/INSU, CEA, and CNES, France. AV and PD were supported by the national grant ANR-18-CE30-0002-01 and Idex Tore. N.P. was funded by a PhD grant allocation Contrat doctoral Normalien. We thank S. Deheuvels, I. Baraffe, G. Chabrier, E. Jaupart, J. Fensch and E. Lynch for useful comments and discussions. The authors are grateful to the anonymous referee, whose thorough comments helped to improved the quality of this article significantly.

6. CONCLUSION

REFERENCES

- Abramowitz, M., & Stegun, I. A. 1972, Handbook of Mathematical Functions with Formulas, Graphs, and Mathematical Tables. National Bureau of Standards Applied Mathematics Series 55. Tenth Printing. (ERIC)
- Aerts, C., Christensen-Dalsgaard, J., & Kurtz, D. W. 2010, Asteroseismology (.)
- Atiyah, M. F., & Singer, I. M. 1963, Bull. Amer. Math. Soc., 69, 422.
<https://projecteuclid.org:443/euclid.bams/1183525276>
- Bergholtz, E. J., Budich, J. C., & Kunst, F. K. 2021, Rev. Mod. Phys., 93, 015005, doi: [10.1103/RevModPhys.93.015005](https://doi.org/10.1103/RevModPhys.93.015005)
- Bernevig, B. A. 2013, Topological Insulators and Topological Superconductors (Princeton University Press), doi: [doi:10.1515/9781400846733](https://doi.org/10.1515/9781400846733)
- Burns, K. J., Vasil, G. M., Oishi, J. S., Lecoanet, D., & Brown, B. P. 2020, Physical Review Research, 2, 023068, doi: [10.1103/PhysRevResearch.2.023068](https://doi.org/10.1103/PhysRevResearch.2.023068)
- Cally, P. 2006, Philosophical Transactions of the Royal Society A: Mathematical, Physical and Engineering Sciences, 364, 333, doi: [10.1098/rsta.2005.1702](https://doi.org/10.1098/rsta.2005.1702)
- Chandrasekhar, S. 1939, An introduction to the study of stellar structure (.)
- Chern, S. 1946, Annals of Mathematics, 47, 85
- Christensen-Dalsgaard, J., et al. 1996, Science, 272, 1286, doi: [10.1126/science.272.5266.1286](https://doi.org/10.1126/science.272.5266.1286)
- Cowling, T. G. 1941, Monthly Notices of the Royal Astronomical Society, 101, 367, doi: [10.1093/mnras/101.8.367](https://doi.org/10.1093/mnras/101.8.367)
- Daghigh, R. G., & Green, M. D. 2012, Phys. Rev. D, 85, 127501, doi: [10.1103/PhysRevD.85.127501](https://doi.org/10.1103/PhysRevD.85.127501)
- Deheuvels, S., & Michel, E. 2010, Ap&SS, 328, 259, doi: [10.1007/s10509-009-0216-2](https://doi.org/10.1007/s10509-009-0216-2)
- Delplace, P. 2022, SciPost Phys. Lect. Notes, 39, doi: [10.21468/SciPostPhysLectNotes.39](https://doi.org/10.21468/SciPostPhysLectNotes.39)
- Delplace, P., Marston, J., & Venaille, A. 2017, Science, 358, 1075
- Delplace, P., Yoshida, T., & Hatsugai, Y. 2021, Phys. Rev. Lett., 127, 186602, doi: [10.1103/PhysRevLett.127.186602](https://doi.org/10.1103/PhysRevLett.127.186602)
- Dupret, M. A., Belkacem, K., Samadi, R., et al. 2009, A&A, 506, 57, doi: [10.1051/0004-6361/200911713](https://doi.org/10.1051/0004-6361/200911713)
- Dziembowski, W. A., Gough, D. O., Houdek, G., & Sienkiewicz, R. 2001, Monthly Notices of the Royal Astronomical Society, 328, 601, doi: [10.1046/j.1365-8711.2001.04894.x](https://doi.org/10.1046/j.1365-8711.2001.04894.x)
- Esposito, G. 1997, arXiv, doi: [10.48550/ARXIV.HEP-TH/9704016](https://arxiv.org/abs/1004.0489)
- Faure, F. 2019, arXiv e-prints, arXiv:1901.10592.
<https://arxiv.org/abs/1901.10592>
- Gong, Z., Ashida, Y., Kawabata, K., et al. 2018, Phys. Rev. X, 8, 031079, doi: [10.1103/PhysRevX.8.031079](https://doi.org/10.1103/PhysRevX.8.031079)
- Gough, D. O. 1993, in Astrophysical Fluid Dynamics - Les Houches 1987, 399–560
- Hasan, M. Z., & Kane, C. L. 2010, Reviews of modern physics, 82, 3045
- Horedt, G. P. 1987, A&A, 172, 359
- Iga, K. 2001, Fluid Dynamics Research, 28, 465, doi: [10.1016/S0169-5983\(01\)00011-9](https://doi.org/10.1016/S0169-5983(01)00011-9)
- Lagoudakis, K. 2013, The Physics of Exciton-Polariton Condensates (.), 1–165, doi: [10.1201/b15531](https://doi.org/10.1201/b15531)
- Lamb, H. 1911, Proceedings of the Royal Society of London Series A, 84, 551, doi: [10.1098/rspa.1911.0008](https://doi.org/10.1098/rspa.1911.0008)
- Ledoux, P., & Walraven, T. 1958, Handbuch der Physik, 51, 353, doi: [10.1007/978-3-642-45908-5_6](https://doi.org/10.1007/978-3-642-45908-5_6)
- Lighthill, J. 1978, Waves in fluids (Cambridge university press)
- Matsuura, T. 1966, Journal of the Meteorological Society of Japan. Ser. II, 44, 25, doi: [10.2151/jmsj1965.44.1.25](https://doi.org/10.2151/jmsj1965.44.1.25)
- Nakahara, M. 1990, Geometry, topology and physics, Graduate student series in physics (Bristol: Hilger).
<https://cds.cern.ch/record/206619>
- Onuki, Y. 2020, Journal of Fluid Mechanics, 883
- Parker, J. B. 2021, Journal of Plasma Physics, 87, 835870202, doi: [10.1017/S0022377821000301](https://doi.org/10.1017/S0022377821000301)
- Parker, J. B., Marston, J. B., Tobias, S. M., & Zhu, Z. 2020, PhRvL, 124, 195001, doi: [10.1103/PhysRevLett.124.195001](https://doi.org/10.1103/PhysRevLett.124.195001)
- Paxton, B., Bildsten, L., Dotter, A., et al. 2011, The Astrophysical Journal Supplement Series, 192, 3, doi: [10.1088/0067-0049/192/1/3](https://doi.org/10.1088/0067-0049/192/1/3)
- Perez, N., Delplace, P., & Venaille, A. 2021, Proceedings of the Royal Society A: Mathematical, Physical and Engineering Sciences, 477, 20200844
- Perez, N., Delplace, P., & Venaille, A. 2021, arXiv e-prints, arXiv:2110.02002. <https://arxiv.org/abs/2110.02002>
- Perrot, M., Delplace, P., & Venaille, A. 2019, Nature Physics, 15, 1, doi: [10.1038/s41567-019-0561-1](https://doi.org/10.1038/s41567-019-0561-1)
- Rozelot, J., & Neiner, C. 2011, The Pulsations of the Sun and the Stars, Vol. 832 (.), doi: [10.1007/978-3-642-19928-8](https://doi.org/10.1007/978-3-642-19928-8)
- Shankar, S., Souslov, A., Bowick, M. J., Marchetti, M. C., & Vitelli, V. 2020, arXiv preprint arXiv:2010.00364
- Unno, W., Osaki, Y., Ando, H., & Shibahashi, H. 1979, Nonradial oscillations of stars (.)
- Venaille, A., & Delplace, P. 2021, Phys. Rev. Research, 3, 043002, doi: [10.1103/PhysRevResearch.3.043002](https://doi.org/10.1103/PhysRevResearch.3.043002)
- Yao, S., & Wang, Z. 2018, Phys. Rev. Lett., 121, 086803, doi: [10.1103/PhysRevLett.121.086803](https://doi.org/10.1103/PhysRevLett.121.086803)

Topological mixed f/g modes in the Sun

Résumé

Ce chapitre est le résultat d'un travail collaboratif avec Arthur Le Saux, et constituait la naturelle étape suivant les résultats du Chapitre V. L'existence de l'onde topologique dans les oscillations d'étoiles était prédictive dans le cas général ; cette étude se concentre sur le cas particulier de l'étoile la mieux connue, le Soleil.

En comparant les prédictions sur cette onde avec des simulations hydrodynamiques de pointe de l'intérieur du Soleil, deux choses ont été montrées :

- L'onde topologique Lamb-like est naturellement excitée et se propage effectivement dans les étoiles de type solaire. Elle constitue la partie à bas degré ℓ de la branche f .
 - Cette onde s'hybride avec les modes g solaires tant recherchés. Le résultat de cette hybridation est une oscillation du Soleil agitant aussi bien la surface que son coeur. Elle est donc observable et sensible à la dynamique du coeur, offrant la perspective intéressante de le sonder sans observer les modes g directement.
-

This chapter is the next step following the results obtained in Chapter V, and is the result of a collaborative work with Arthur Le Saux. The existence of a topological mode in stellar oscillations was suggested in the general case; this work investigates the particular case of the most well-known star: the Sun.

Comparing state-of-the-art numerical simulations of the flows happening inside the Sun with the predictions on the topological wave, two important things are shown:

- The stellar topological wave propagates and is naturally excited in solar-like stars. It is part of the f branch of modes, at low harmonic degree ℓ .
- This wave hybridizes with the long-sought solar g -modes. The result of this hybridization is an oscillation of the Sun agitating both its core and its surface. It is thus observable *and* sensitive to the Sun's core, a unique feature offering interesting seismic probing perspectives without requiring observations of g -modes directly.

The results presented in this chapter have been published in **The Astrophysical Journal Letters** as *A one-hour topological oscillation explores the Sun's core*, Le Saux, Leclerc, Laibe, Delplace, Venaille, 2025 [343]. My personal interest in this work was to test the predictions on the topological modes with a realistic, non-linear simulation. I performed the linear calculations of the spectrum, eigenprofiles and rotation kernels, as well as the interpretation of the Lamb-like to free-surface wave transition using the effective potential.

The results, beyond confirming the predictions on this mode, suggested a way to probe the Sun's core which may be much more accessible than the currently pursued one, which rests on pure g -modes. This suggestion was obtained because of the special focus the topological analysis brought on the f -mode, and may provide the value and profile of the solar core rotation rate, a strong link on the advancement of angular momentum scenarios. This perspective makes this study the culmination of the project, where topology truly contributed to asteroseismology.

DRAFT VERSION JUNE 16, 2025
 Typeset using **LATEX** **preprint** style in AASTeX7

A core-sensitive mixed f/g mode of the Sun predicted by wave topology and hydrodynamical simulation

ARTHUR LE SAUX ^{1,2,*} ARMAND LECLERC ^{3,*} GUILLAUME LAIBE,^{3,4} PIERRE DELPLACE,⁵ AND ANTOINE VENAILLE⁵

¹ Université Paris-Saclay, Université Paris Cité, CEA, CNRS, AIM, Gif-sur-Yvette, F-91191, France.

² Laboratoire de Météorologie Dynamique / Institut Pierre-Simon Laplace (LMD/IPSL), Sorbonne Université, Centre National de la Recherche Scientifique (CNRS), École Polytechnique, École Normale Supérieure (ENS)

³ ENS de Lyon, CRAL UMR5574, Université Claude Bernard Lyon 1, CNRS, Lyon, F-69007, France

⁴ Institut Universitaire de France

⁵ ENS de Lyon, CNRS, Laboratoire de physique, F-69342 Lyon, France

ABSTRACT

Helioseismology has revolutionized our understanding of the Sun by analyzing its global oscillation modes. However, the solar core remains elusive, limiting a full understanding of its evolution. In this work, we study a previously unnoticed global oscillation mode of the Sun using a fully compressible, hydrodynamical simulation of the solar interior, and assess that it is a mixed f/g mode with a period of about one hour. This is the first global stellar hydrodynamics simulation that successfully couple compressible and gravity modes. To understand this coupling, we invoke a recent theory on the nature of f -modes seen through the prism of wave topology, characterizing their ability to propagate deep into stellar interiors. We demonstrate that the mixed f/g mode is highly sensitive to the core's rotation rate, providing a new promising pathway to explore the Sun's core.

1. INTRODUCTION

The Sun, our closest star, serves as a fundamental reference for understanding stellar evolution. Its proximity offers a unique window into the physical processes governing the life cycles of stars, with broader implications for astrophysics, as stars are the building blocks of galaxies and hosts of exoplanets. In recent decades, helioseismology - the science that studies solar oscillations - has revolutionized our understanding of the Sun. Seismic inversion techniques of these modes have provided precise constraints of the Sun's internal structure and dynamics, such as the location of the interface between the radiative and convective zones, the abundance of helium in the convective envelope, the efficiency of chemical diffusion or the rotation profile of the solar interior (R. Howe 2009; S. Basu 2016). These advances have been driven by high-precision data from space telescopes (A. Gabriel et al. 1997; J. T. Hoeksema et al. 2018) and ground-based networks of solar observatories (E. Fossat 1991; W. J. Chaplin et al. 1996; J. Harvey et al. 1996). Today, we know most of the Sun's internal structure (outer 90 % of the total radius) and rotation profile (outer 80 %) (see the

Email: arthur.lesaux@cea.fr

* These authors contributed equally to this work

detailed review by [J. Christensen-Dalsgaard 2021](#)). However, a global understanding of the theories of angular momentum transport and mixing of elements in stellar interiors requires observational constraints for the innermost 10-20% of the Sun's radial layers ([J. Leibacher et al. 2023](#)).

Unfortunately, the solar core remains inaccessible to helioseismology. Indeed, the non-radial acoustic modes, or *p*-modes, used for inversion are refracted before reaching the core, where their horizontal wavelength becomes infinitesimally small, confining them outside. Recently, inertial and Rossby waves, supported by solar rotation, have provided new insights into superadiabaticity and turbulent viscosity in the deep convection zone ([L. Gizon et al. 2021](#)), and on the Sun's latitudinal differential rotation ([Y. Bekki et al. 2024](#)). But these modes are confined to the convective envelope and do not probe the core.

So far, the only constraints on the solar core come from neutrinos, which have recently revealed the Carbon-Nitrogen-Oxygen cycle and provided insights into stellar metallicity and energy production ([M. Borexino Collaboration et al. 2020](#)). A long-standing goal of helioseismology is the detection of solar internal gravity waves, or *g*-modes, buoyant oscillations that could provide unprecedented information about the Sun's interior. While some claims of detection exist ([R. A. García et al. 2007](#); [E. Fossat et al. 2017](#)), these results remain unconfirmed ([T. Appourchaux et al. 2010](#); [H. Schunker et al. 2018](#)). Their detection is difficult due to their small amplitude at the surface, and frequency domain overlapping with solar granulation noise ([K. Belkacem et al. 2022](#)), making them elusive to current instruments.

In this study, we show that some *g*-modes couple with *f*-modes at large horizontal wavelength and form mixed *f/g* modes, which have amplitude both in the core and at the surface. This key property makes them potential observational probes of the Sun's deep interior dynamics. This result, evidenced by state-of-the-art hydrodynamical simulations, challenge the usual depiction of *f*-modes as being surface waves ([F.-L. Deubner & D. Gough 1984](#); [D. Gough 1993](#); [C. Aerts et al. 2010](#)), a description which only holds at short horizontal wavelength. We demonstrate that at large horizontal wavelength, *f*-modes are topological waves that propagate in the bulk of the star, as recently predicted by [A. Leclerc et al. \(2022\)](#). Topological waves are a class of large-scale modes characterized by topological arguments inherited from condensed matter physics ([P. Delplace et al. 2017](#); [M. Perrot et al. 2019](#); [N. Perez 2022](#)). The identification of such topological *f*-modes explains their ability to couple with *g*-modes, as they have spatial and frequency overlaps.

2. THE TWO KINDS OF *F*-MODES

The normal modes of non-rotating non-magnetic stars are classified as *p*-modes, *g*-modes or *f*-modes as by the seminal paper [T. G. Cowling \(1941\)](#). Each mode is identified by two numbers: its radial order n and angular degree $\ell \geq 0$, which correspond to the numbers of radial and angular nodes of the perturbation of pressure respectively. The *p*-modes, characterized by high frequencies, permeate the entire solar interior, whereas the *g*-modes, with lower frequencies, are confined to the radiative region. The *f*-modes are the $n = 0$ modes and as such are fundamental modes with generically intermediate frequencies ([W. Unno et al. 1979](#)). In the literature, *f*-modes have mostly been described as motion of the free surface of the Sun as surface gravity waves in the plane-parallel approximation ([F.-L. Deubner & D. Gough 1984](#); [D. Gough 1993](#)), which works for short horizontal wavelengths with $\ell \gg 1$ and in good agreement with numerical models and helioseismic data ([J. Christensen-Dalsgaard 2002](#); [S. Basu 2016](#)). These surface waves are mostly unaffected by the Sun's interior and cannot provide information about its internal structure. Instead, they have been used

to measure the solar radius and its variations (H. M. Antia 1998; S. Lefebvre et al. 2007). Nevertheless, the interpretation of f -modes as surface waves does not hold at low ℓ . Recent studies show that for long horizontal wavelengths ($\ell \sim 1$), f -modes are Lamb-like waves (M. Perrot et al. 2019; A. Leclerc et al. 2022). These waves have been named due to similarities with the atmospheric Lamb waves (H. Lamb 1911; F. Bretherton 1969). While atmospheres support Lamb waves trapped at their bottom solid boundary, Lamb-like waves in stars occur at a specific radius, depending on sphericity. This radius is defined at the location where the characteristic frequency

$$S = \frac{c_s}{2g} \left(N^2 - \frac{g^2}{c_s^2} \right) - \frac{1}{2} \frac{dc_s}{dr} + \frac{c_s}{r}, \quad (1)$$

goes to zero and changes sign. In this equation g is the gravity field, c_s is the sound speed, and N is the buoyancy frequency. Therefore, f -modes at low degree ℓ are Lamb-like waves, and propagate close to the radius where $S = 0$. In spherical geometry, the curvature term c_s/r in Eq. (1) ensures that the frequency S will change sign at least once in any star. This property was never identified before, and is key to understanding why f -modes leave the surface and hybridize with g -modes.

The prediction of stellar Lamb-like waves relies on an analysis of the topological properties of the propagation equation of local plane waves (A. Leclerc et al. 2022). In summary, this topological analysis shows that the region where $S = 0$ is a phase singularity for plane waves, which results in a branch of modes, here the Lamb-like modes, whose frequencies transition from the low-frequency (g -modes) to the high-frequency (p -modes) wavebands as ℓ increases. These modes, classified as topological modes, are imposed to localize where $S = 0$ as predicted by the bulk-boundary correspondence. For further details on wave topology, we refer the reader to (B. A. Bernevig 2013; M. Perrot et al. 2019; P. Delplace 2022; N. Perez 2022).

Then, as ℓ increases, the f -modes is confined in outer layers, and become the surface wave usually described. These two types of waves forming the f branch - Lamb-like and surface - arise from competing effects between the buoyant-acoustic S and the Lamb frequencies, the latter being defined as $L_\ell = \sqrt{\ell(\ell+1)}c_s/r$. As shown in Supplementary Materials Eq. (E15), the profile of S tends to trap low ℓ modes where it is zero, while L_ℓ tends to repulse high-frequency modes to the surface. The competition between the two effects place the f -modes in different regions of the star depending on the value of ℓ .

To show clearly these two regimes of f -modes, we create a model of a fictitious star, in which the buoyant-acoustic frequency S_{deformed} has been deformed from the solar case S_\odot , as presented in the panel A of Fig. 1. We then numerically solve for the frequencies of linear eigenmodes of this model (see Appendix A). Looking at the wave spectrum in the panel B of Fig. 1, we can see that for $\ell \lesssim 15$ the $n = 0$ mode propagates in the bulk of the star as a Lamb-like wave close to the $S_{\text{deformed}} = 0$ radius, while for $\ell \gtrsim 15$, it is confined at the surface. In the case of the Sun, the repulsive effect of L_ℓ overcomes the trapping at $S_\odot = 0$, causing Lamb-like modes at low ℓ to delocalize, making it more difficult to clearly distinguish the two regimes. This situation is atypical in topological physics and explains why solar Lamb-like waves are difficult to identify at first glance (see Fig. 7 of Supplementary Materials).

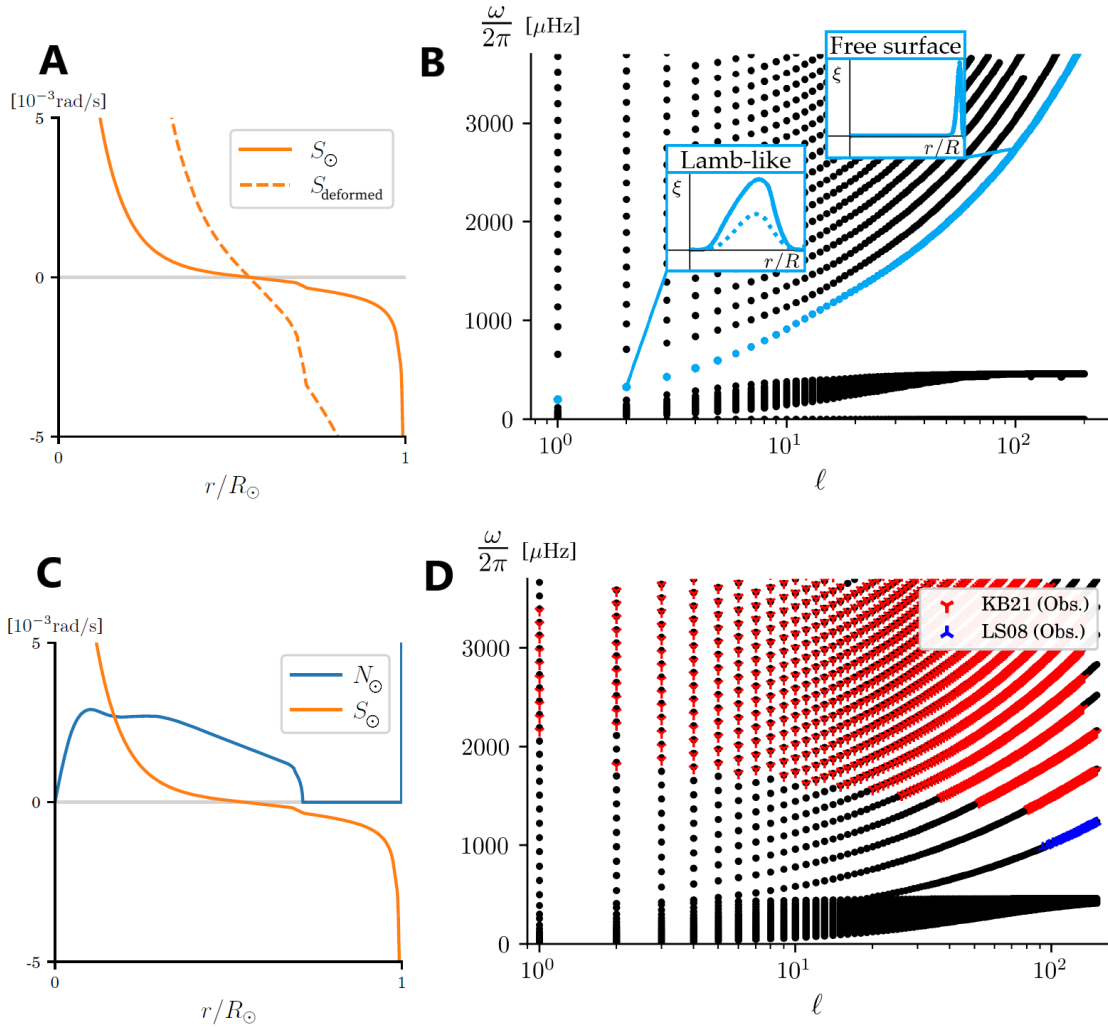


Figure 1. Normal linear adiabatic modes of oscillations. **(A)** Model and **(B)** frequencies of a fictitious star with $S_{\text{deformed}}(r) = 10S_\odot(r)$. The spectrum show that the low- ℓ part of the f branch consists in bulk modes localized where $S = 0$. The radial ξ_r and horizontal ξ_h displacements are represented by dotted and solid lines, respectively. **(C)** Model and **(D)** frequencies of the modes of our solar model for the first hundreds of harmonic degree ℓ . Linear theory predicts frequencies matching observed modes (colored crosses indicate data from T. Larson & J. Schou (2008); R. Kiefer & A.-M. Broomhall (2021)). Lamb-like modes are difficult to identify when the f -branch penetrates the g -band.

3. NON-LINEAR COMPRESSIBLE 2D SIMULATIONS WITH MUSIC

In this study, we demonstrate the natural excitation of Lamb-like waves in the Sun. Similar to acoustic waves, Lamb-like waves can only propagate in compressible media, necessitating the use of a fully compressible hydrodynamics code. Given that both anelastic and Boussinesq approximations inherently filter out acoustic waves including Lamb-like, these methods are unsuitable for the present investigation.

We present a 2D simulation of the solar interior using the MUSIC code (M. Viallet et al. 2013, 2016; T. Goffrey et al. 2017), one of the few stellar hydrodynamic codes that solves the fully compressible equations of hydrodynamics. This code uses a time-implicit method to solve the continuity, the

momentum and internal energy equations for a fully compressible, inviscid fluid, which are described in Appendix C.1. The initial conditions of the 2D MUSIC simulation are obtained from a 1D structure of the Sun computed with the stellar evolution code MESA (B. Paxton et al. 2011), calibrated to match observed characteristics of the Sun (see Appendix B). We will refer to the latter as the 1D model in the following. Linear modes of this 1D model agree excellently with the frequencies of the observed solar oscillation modes, as shown in panel D of Fig. 1, confirming that it accurately describes the Sun.

The numerical domain of the MUSIC simulation is a two-dimensional shell shown in the left panel of Fig. 2, covered by two spherical coordinates: the radius r and the co-latitude θ . This domain is large enough to model realistic properties of waves and their excitation by convective motions (A. Le Saux et al. 2022). The boundary conditions are described in details in Appendix C.2. In order to conclusively prove that Lamb-like waves propagate in the Sun, we apply solid boundary conditions at the outer surface for the radial velocity. This setup thus prevents the propagation of free surface gravity waves, ensuring that any $n = 0$ mode consists exclusively of a Lamb-like mode.

4. SOLAR LAMB-LIKE WAVES UNVEILED IN SIMULATIONS

Panel (A) of Fig. 2 shows a snapshot of the horizontal velocity in the simulation. The large-scale coherent flows, characteristic of convective motions in the Sun’s envelope, appear prominently. In the radiative interior ($r < 0.7 R$), the tightly wound spirals are characteristic of the wavefronts of internal gravity waves. These features are similar to what is usually observed in solar hydrodynamical simulations in two- (T. M. Rogers et al. 2006) or three-dimensions (A. S. Brun et al. 2011; L. Alvan et al. 2014).

The wave analysis is based on the methodology described in A. Le Saux et al. (2022, 2023). To compute the power spectra of the velocity components v_i , with $i = r$ or h , we first perform a temporal Fourier transform to obtain a pulsation ω dependence, and then use wedge harmonics to get an angular wavenumber $\tilde{\ell}$ dependence, transforming $v_i(r, \theta, t)$ into $\hat{v}_i(r, \tilde{\ell}, \omega)$. Wedge harmonics extend spherical harmonics to wedge-shaped domains, resulting in non-integer harmonic degrees $\tilde{\ell}$ (see Appendix D). Panel (B) of Fig. 2 shows the power spectrum of the horizontal velocity v_h as a function of frequency $\omega/2\pi$ and effective angular degree $\tilde{\ell}$ averaged over a few radial cells around $r = 0.55R_{\text{star}}$. This spectrum is characteristic of the radiative zone. At the surface ($r = R_{\text{star}}$), the frequencies of the modes would remain unchanged compared to the radiative zone, but the spectrum would be much more noisy due to surface convection. Detection and identification of normal modes in the simulation is performed by looking for peaks in the amplitude of the power spectrum localized in $(\omega, \tilde{\ell})$. The colored symbols (red for p -modes, green for g -modes and blue for f -modes) are linear modes calculated independently. We observe excellent agreement between these frequencies and those measured in the simulation. Taking a slice of the power spectrum at a specific $(\omega, \tilde{\ell})$, we extract the targeted mode, which provides the radial profile of the squared horizontal velocity $|v_h|^2(r)$ obtained in the simulation. This measurement is shown for four selected modes on panel (C) of Fig. 2. The modes’ amplitude are normalised to 1 at $r = 0.6R_{\text{star}}$ for better comparison (this radius was chosen to be close to the radiative boundary, but not too close to avoid contamination by convective boundary mixing). The modes $(\omega/2\pi, \tilde{\ell}) = (428 \mu\text{Hz}, 6.7), (508 \mu\text{Hz}, 9.1)$ and $(588 \mu\text{Hz}, 11.5)$, represented by the yellow, orange and red curves respectively, are f -modes. As predicted by Eq. (E15), the f -modes are confined to outer layers as $\tilde{\ell}$, or equivalently ℓ , increases. We compare the simulated velocities with the eigenfunctions of the corresponding linear modes (shown as dotted lines) and

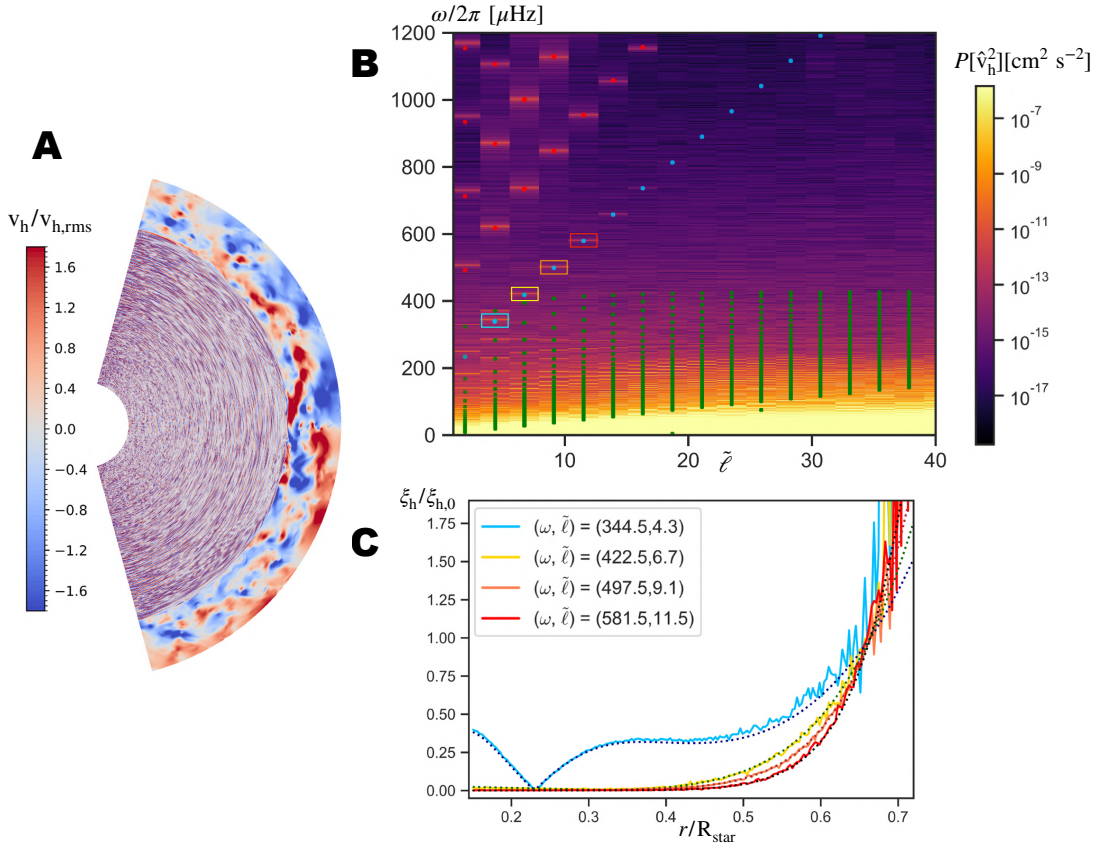


Figure 2. Non-linear simulation of the solar interior shows the Lamb-like wave among the standing waves. The simulation results demonstrate that f -modes propagate within the Sun, driven by convective excitation, even at low values of ℓ . **(A)** A snapshot of horizontal velocities, with values normalized at each radius by their root-mean-square. **(B)** The power spectrum of the horizontal velocity in the radiative zone displays peaks corresponding to normal modes. Red, blue, and green symbols indicate the numerically computed frequencies for linear standing p -modes, f -modes, and g -modes, respectively. The frequencies of the normal modes show excellent agreement with linear theory. At the surface and in observations, the power spectrum is more noisy due to convection and granulation. **(C)** When a normal mode frequency is selected, the radial profile of the horizontal displacement from the simulation (solid line) aligns perfectly with the numerically computed linear eigenfunction of the corresponding mode (dotted line). Displayed here are the profiles for a mixed f/g -mode (blue) and three pure f -modes (yellow, orange, red). The corresponding modes are marked by matching-colored boxes in the power spectrum in panel B.

find excellent agreement. This demonstrates that Lamb-like waves are indeed excited and propagate within the Sun, exhibiting the properties predicted by linear theory. Now, these Lamb-like waves reveal another notable feature: they can couple with other modes deep within the solar interior.

5. MIXED F/G -MODES IN THE SUN

In the simulation, the mode at $(\omega/2\pi, \tilde{\ell}) = (344 \mu\text{Hz}, 4.3)$ represented by the blue curve, shows a different structure than the other three f -modes: it has a node in the radiative zone. We identify here a mixed mode, resulting from the coupling of the f -mode with the g_1 -mode. Mixed modes occur when two oscillations of different nature propagating in distinct layers of a star become coupled. One of the major successes of asteroseismology has been to predict and detect p/g modes in

stars evolving beyond the main sequence (R. Scuflaire 1974; H. Kjeldsen et al. 1995), thus having amplitude not only in the deep core but also at the surface, making it possible to probe the entire interior of a star (see S. Hekker & J. Christensen-Dalsgaard 2017, and references therein).

The results of our simulation predict that mixed f/g modes should exist in the Sun, at possibly different frequency and degree because of the shorter size of the simulated domain. By examining the linear modes of the full Sun (Fig. 1 D), we do find a mixed mode at $\ell = 4$ between the f -mode and the fifth g -mode oscillating at a frequency $\omega/2\pi = 265 \mu\text{Hz}$, an oscillation period of almost an hour. We predicted the overlapping of f -modes and g -modes eigenfunctions from the properties of Lamb-like waves inherited from their topological origin. Indeed, for decreasing ℓ , the f -mode frequency crosses the values of g -modes frequencies (Fig. 1 D), and has more and more amplitude in the interior (Figs. 1 B and Fig. 2 C) leading to an overlap of their eigenfunctions. These two conditions cause the hybridization of the modes.

We show this hybridization by considering the kinetic energy-weighted average position of the modes

$$\langle r \rangle = \frac{\int dr r r^2 \rho_0 (\xi_r^2 + \xi_h^2)}{\int dr r^2 \rho_0 (\xi_r^2 + \xi_h^2)}, \quad (2)$$

which provides a diagnosis for mode coupling in the simulations. Panel (A) of Fig. 3 shows that the average position of the fifth g -mode is much higher than that of the other g -modes, all located close to the maximum of buoyancy frequency N^2 as expected for pure gravity modes. Panel (B) displays the standard diagnostic of mixed modes commonly used in observations (R.-M. Ouazzani et al. 2020). The periods P_n of pure g -modes are expected to be nearly uniformly spaced (W. Unno et al. 1979; D. Gough 1993). However, due to mode mixing, the period spacing $\Delta P \equiv P_{n+1} - P_n$ dips significantly at $n = 5$.

The value of the order n of the g -mode implicated in the coupling with the f -mode is sensitive to the exact frequency of the latter, and could thus depend on the 1D model. Still, we find that a mixed f/g mode at $\ell = 4$ happens with radial order $n = 5$ also for the standard model S of the Sun (J. Christensen-Dalsgaard et al. 1996) and the seismic solar model of (G. Buldgen et al. 2020), such that we do not expect a very different order in the Sun.

Mixed f/g modes have not been noticed in the solar spectrum before. To our knowledge, the existence of a coupling between solar f and g -modes was only studied in the dipolar case $\ell = 1$ when discussing the effect of Cowling's approximation (J. Christensen-Dalsgaard & D. Gough 2001). J. Provost et al. (2000) observed that the fifth solar g -mode at low ℓ exhibited a mixed nature, but did not realize this was due to its coupling with a deeply propagating f -mode. K. Belkacem et al. (2022) noticed a coupling of g -modes with an external mode in recent seismic solar models as well, which in the light of our results appears to be these mixed f/g modes.

6. SENSITIVITY TO THE SOLAR CORE ROTATION RATE

To date, the solar rotation rate $\Omega(r, \theta)$ has been accurately determined using p -modes in both the radiative and convective zones, but only for radii greater than 20% of the solar radius. We demonstrate here that the mixed $f/g5$ mode identified above is very sensitive to the rotation rate of the solar core and thus provides a new method to potentially probe the innermost layer of the Sun. Rotation causes a peak in the power spectrum of a given (n, ℓ) mode to split into $2\ell+1$ distinct peaks that correspond to each value of the azimuthal order m upon action of the Doppler effect and Coriolis

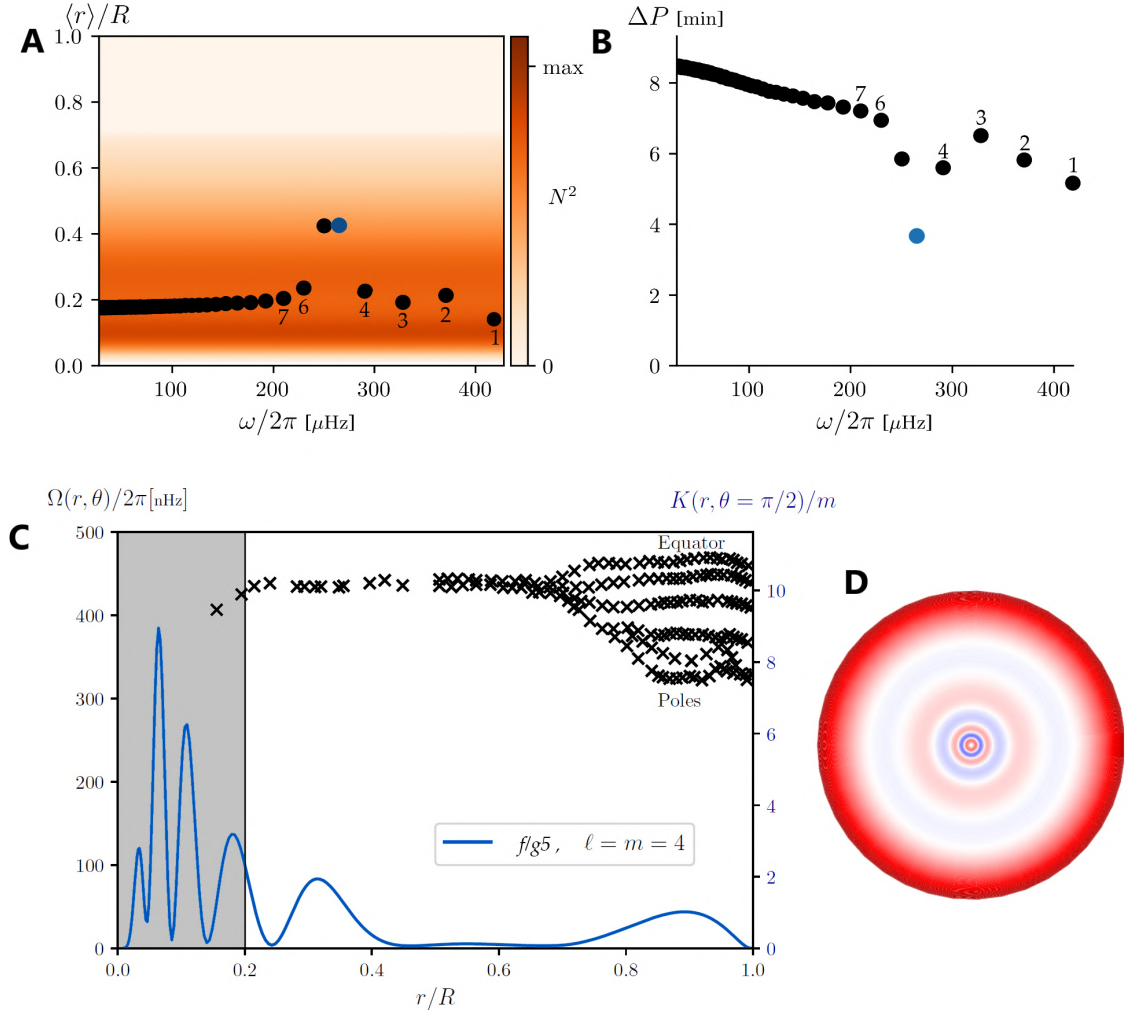


Figure 3. Identification of mixed f/g -modes in the solar spectrum. The $\ell = 4$ Lamb-like wave couples with the $g5$ mode to form a mixed mode. **(A)** The average position $\langle r \rangle$ of the g -modes defined in the main text is close to the maximum of buoyancy frequency N^2 , except for two: they result from the coupling of the f -mode and the $g5$ mode, which thus have more amplitude in the outer layers. **(B)** The period spacing $\Delta P = P_{n+1} - P_n$ shows a dip at the fifth g -mode. **(C)** The kernel K of the $f/g5$ mixed mode, in dark blue, shows significant amplitude in the solar core ($r/R_\odot < 0.2$), implying a significant sensitivity to the core rotation rate. Dark crosses are data points for Ω from M. J. Thompson et al. (2003) obtained observationally. **(D)** Representation of the horizontal displacement ξ_h of the mixed mode at frequency $265 \mu\text{Hz}$ in the Sun (red for positive, blue for negative, linear scale). It has amplitude at the surface, as well as in the deep interior.

force. By measuring this splitting, one can infer the solar rotation rate $\Omega(r, \theta)$ by inversion (R. Howe 2009). The split is generically expressed $\Delta\omega_{n,\ell,m} \equiv \omega_{n,\ell,m} - \omega_{n,\ell,0} = \int K_{n,\ell,m}(r, \theta)\Omega(r, \theta)drd\theta$, where $K_{n,\ell,m}$ is the kernel of the mode computed without rotation. The expression of $K_{n,\ell,m}$ for a given mode is given in J. Schou et al. (1994). In the following, subscripts (n, ℓ, m) are omitted.

To quantify how effectively a mode can probe the core rotation rate Ω^c , we define the sensitivity for solid body rotation of the core as

$$s \equiv \frac{\partial\omega}{\partial\Omega^c} = \int_{r<0.2R_\odot} K \, drd\theta, \quad (3)$$

such that the splitting specifically due to the rotation of the core is $\Delta\omega_{\text{core}} = s\Omega^c$. The solar modes used for inversion of rotation so far are acoustic and have limited sensitivity to core rotation since they do not travel in such deep layers. For instance, the mode $n = 5$ and $\ell = m = 1$, one of the deepest propagating p -modes, has $s = 7.27 \times 10^{-2}$. This implies that a core rotation of ~ 400 nHz would cause its splitting to increase by around 30 nHz. This change is too small to be conclusively measured with the current frequency resolution of approximately 10 nHz provided by the BiSON dataset (R. Howe et al. 2023).

In contrast, we find that the $f/g5$ mixed mode at $\ell = m = 4$ has a sensitivity $s = 2.24$, thirty times more than p -modes. Figure 3 shows the substantial amplitude of the kernel K of this mixed mode in the core, explaining its high sensitivity. For this mode, the known rotation rate in the radiative and convective regions account for a splitting of 786 nHz, leading to the expression

$$\Delta\omega/2\pi = 786 \text{ nHz} + 2.24 \Omega^c/2\pi. \quad (4)$$

The frequency resolution of 10 nHz in observations implies that the method presented here allows for the determination of Ω^c with a precision of ~ 5 nHz. For a hypothetical rotation rate of ~ 400 nHz, similar to that of the radiative region, the additional splitting would be around 10^3 nHz. As a comparison, at $\ell = m = 4$, a g -mode at $\omega/2\pi = 103\mu\text{Hz}$ has $s = 3.16$. It is thus as sensitive as the mixed mode, but we argue that it is a more difficult observational target because of its evanescence in the radiative zone and its lower frequency.

From an observational perspective, the mixed f/g mode is found in a frequency range that is not accessible yet with currently available data. However, using the MUSIC simulation, the eigenfunction computed from the 1D model and observational data from G. R. Davies et al. (2014), we can estimate the relative surface amplitudes between different modes. We find that the mixed f/g -mode at 265 μHz have a surface amplitude comparable to those of p -modes within the same frequency range, whereas g -modes in this range exhibit significantly lower surface amplitudes (see details in Appendix G). Instead, we find that g -modes have comparable surface amplitudes at lower frequencies (~ 50 –100 μHz), where they are expected to have largest surface amplitudes (K. Belkacem et al. 2022). But as background noise from granulation and turbulence increases at lower frequencies in the solar spectrum, the detection threshold at 265 μHz is two to three times lower (K. Belkacem et al. 2022). Consequently, despite having similar sensitivities, we conclude that the higher frequency of the mixed $f/g5$ mode makes it an easier target and a more promising opportunity for probing the solar core in the future than pure g -modes.

7. SUMMARY & DISCUSSION

For decades, f -modes have been thought to “provide no information about the solar interior” (C. Aerts et al. 2010). Indeed, f -modes are often considered to be only surface gravity waves. We overturn this longstanding belief by demonstrating that low degree f -modes are bulk modes in the form of topological waves, in the process making a novel use of a topological wave as a probe rather

than for transport properties as done in condensed matter physics. By performing a state-of-the-art simulation of the solar interior using the fully compressible hydrodynamical code MUSIC, we demonstrate that not only low-degree f -modes in the Sun have this topological origin, but also that they are naturally excited by solar convection. In addition, we identify a previously unnoticed mixed f/g mixed mode of the Sun. The coupling is due to properties inherited from the topological origin of the f -mode at low degree which imposes that it propagates deep in the solar interior. This mixed mode, oscillating every hour, is found to exhibit significant amplitude both in the Sun’s core and at its surface. Its sensitivity to the core’s rotation rate is over 30 times greater than currently observed modes. Thus, it provides a novel way to measure this rotation rate, that represents to date our most promising opportunity for future measurements as it is located in a less noisy region of power spectra than g -modes with expected maximum amplitudes ($100 \mu\text{Hz}$).

The argument is general, implying that topological mixed modes should universally be found in bodies having a stably stratified interior. We suspect that the f/g mode found in Saturn is such a mode (J. W. Dewberry et al. 2021). Our study highlights the key role of compressible hydrodynamics in modelling stellar interiors, presenting the first-ever simulation of the coupling between compressible and gravity modes. Altogether, this holds great promise for asteroseismology with the upcoming launch of the PLATO mission (H. Rauer et al. 2014) in 2026, which will provide low degree oscillations of solar-like stars, whose cores could be accessed with mixed f/g modes.

ACKNOWLEDGMENTS

The authors thank T. Guillet and A. Morison for their support with MUSIC, as well as R. A. Garcia and S. Korzennik for fruitful discussions on observational perspectives. We gratefully acknowledge support from the PSMN (Pôle Scientifique de Modélisation Numérique) of the ENS de Lyon and the Alfven facility of CEA Paris-Saclay for the computing resources. A.L. and G.L. acknowledge funding from the European Research Council (ERC) CoG project PODCAST No. 864965. A.L. is funded by Contrat Doctoral Spécifique Normalien. A.L.S. acknowledges support from the European Research Council (ERC) under the Horizon Europe programme (Synergy Grant agreement 101071505: 4D-STAR). While partially funded by the European Union, views and opinions expressed are however those of the author only and do not necessarily reflect those of the European Union or the European Research Council. Neither the European Union nor the granting authority can be held responsible for them.

AUTHOR CONTRIBUTIONS

A.L.S. ran the simulations, calibrated the 1D model, and performed their post-processing analysis. A.L. computed the linear spectra and the inversion kernels. All authors participated in the redaction of the manuscript. Numerical scripts and data are available on a Zenodo repository at doi.org/10.5281/zenodo.15600943.

APPENDIX

A. LINEAR THEORY

The Sun is stratified by gravity and maintains a state of hydrostatic equilibrium. Two types of motion perturb this static balance. In the convective zone, turbulent motion occurs in the form of convective eddies driven by the convective instability. In addition, acoustic and internal gravity waves propagate inside different layers of the Sun, depending on their nature and frequency (T. G. Cowling 1941; W. Unno et al. 1979; D. Gough 1993; C. Aerts et al. 2010). These waves are primarily excited by the convective motion and are classified by their normal modes, with frequencies characteristic of the Sun. Since the background structure through which they propagate is spherically symmetric, the normal modes generally take the form $e^{-i\omega t} Y_\ell^m(\theta, \phi) f(r)$, where ω is the frequency, $Y_\ell^m(\theta, \phi)$ is a spherical harmonics. f is a function to be determined for each component of the wave (radial and horizontal velocities, pressure, density, temperature).

Assuming linear and adiabatic perturbations, along with no perturbations in the gravitational potential (Cowling's approximation T. G. Cowling 1941), the normal modes of the sun are solutions of

$$\omega X = \mathcal{H}X, \quad \text{with} \quad \mathcal{H} \equiv \begin{pmatrix} 0 & 0 & 0 & L_\ell(r) \\ 0 & 0 & iN & -iS + \frac{i}{2}c'_s + ic_s \partial_r \\ 0 & -iN & 0 & 0 \\ L_\ell(r) & iS + \frac{i}{2}c'_s + ic_s \partial_r & 0 & 0 \end{pmatrix}, \quad (\text{A1})$$

where the perturbation vector $X(r) \equiv \left(\tilde{v}_h \ \tilde{v}_r \ \tilde{\Theta} \ \tilde{p} \right)^\top$ is based on re-scaled perturbed quantities of the horizontal velocity, radial velocity, entropy and pressure respectively, by

$$\begin{aligned} v' &\mapsto \tilde{v} = \rho_0^{1/2} r \ v' = \tilde{v}_r(r) Y_\ell^m e_r + \tilde{v}_h(r) \frac{ir}{\sqrt{\ell(\ell+1)}} \nabla(Y_\ell^m e_r), \\ p' &\mapsto \tilde{p} = \rho_0^{-1/2} c_s^{-1} r \ p', \\ \rho' &\mapsto \tilde{\Theta} = \rho_0^{-1/2} r \frac{g}{N} (\rho' - \frac{1}{c_s^2} p'), \end{aligned} \quad (\text{A2})$$

The buoyant-acoustic frequency S is given by Eq. (1), the buoyancy frequency squared is $N^2 \equiv -g \frac{d \ln \rho_0}{dr} - \frac{g^2}{c_s^2}$, the Lamb frequency squared $L_\ell^2 \equiv c_s^2 \ell(\ell+1)/r^2$ and $c'_s \equiv \frac{dc_s}{dr}$. Equation (A1) must be accompanied by appropriate boundary conditions. Solar boundaries require $v_r = 0$ at $r = 0$ and a free surface condition at the surface $\partial_t p + v_r \frac{dp_0}{dr} = 0$. The numerical wedge domain used in MUSIC requires $v_r = 0$ at $r = r_{\text{out}}$.

The eigenfrequencies and eigenvectors of \mathcal{H} are obtained by solving Eq. (A1) numerically, for a given model of the Sun which provides $N(r)$, $S(r)$ and $c_s(r)$. The numerical procedure utilizes the EVP class of the DEDALUS code (K. J. Burns et al. 2020). It allows us to find the set of $(\omega, X(r))$ which satisfy Eq. (A1) for any value of ℓ . DEDALUS uses spectral methods which decompose solutions on N_r Chebyshev polynomials, in order to obtain a matrix eigenvalue problem which is then solved by linear algebra techniques. This method can capture eigenmodes with radial order up to N_r . Examples of eigenfunctions of different solar modes are shown in Fig. 4.

B. SOLAR 1D MODEL

To investigate the oscillation modes of the Sun, we construct a one-dimensional model of the Sun using MESA (B. Paxton et al. 2011, 2013, 2015, 2018, 2019; A. S. Jermyn et al. 2023). This involves

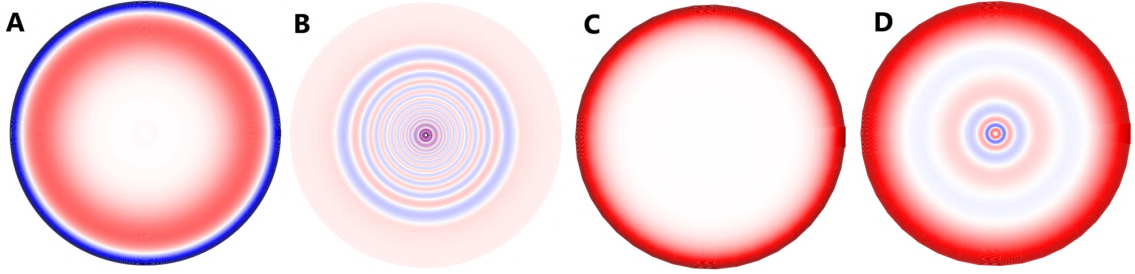


Figure 4. Modes of different types are located in different regions of the Sun. Red and blue are regions of positive and negative horizontal displacement ξ_h . (A) is the $n = 1, \ell = 4$ p -mode, (B) is the $n = 35, \ell = 4$ g -mode, (C) is the $\ell = 10$ f -mode, (D) is the mixed f/g mode discussed in the main text.

Table 1. Characteristics of the Sun and of our solar model. Obtained after calibration.

Parameter	Obs.	σ_j	Model	Model/Obs
Age (Gyr)	4.57	-	4.57	1.0
M (g)	1.9884×10^{33}	-	1.9884×10^{33}	1.0
T_{eff} (K)	5772.0	-	5760.1	0.998
R (cm)	6.957×10^{10}	3.211×10^8	6.9575×10^{10}	1.00007
L (erg.s $^{-1}$)	3.828×10^{33}	1.4×10^{30}	3.797×10^{33}	0.992
(Z/X) $_{\text{surf}}$	0.0252	10^{-3}	0.0259	0.972
Y_{surf}	0.2485	0.0035	0.2537	1.021
R_{CZ}/R_{\odot}	0.713	10^{-3}	0.714	0.999

calibrating a 1D solar model with the *simplex solar calibration* routine provided by MESA. This method aims at minimizing a χ^2 function, which is defined as

$$\chi^2 = \sum_j \frac{(O_j - M_j)^2}{\sigma_j^2}, \quad (\text{B3})$$

with O_j the observed characteristics of the Sun and M_j the modelled ones. These characteristics used to calibrate the model are the luminosity L , the radius R , surface metals $(Z/X)_{\text{surf}}$ and helium Y_{surf} abundances, the position of the interface between the radiative and the convective zones R_{CZ} and the sound speed profile of the solar interior. The measured values of L and T_{eff} are the ones given by the *Resolution B3* of the International Astronomical Union (E. E. Mamajek et al. 2015) and are the default values used in MESA. For the metals surface abundances, we use the values recently determined by E. Magg et al. (2022), which are similar to those from N. Grevesse & A. J. Sauval (1998) and correspond to the high metal abundance case. The helium surface abundance is based on measurements by S. Basu & H. M. Antia (2004), and the position of the radiative/convective interface is taken from S. Basu & H. M. Antia (1997). For the sound speed profile, we use the default profile in MESA, which is derived from helioseismology by S. Basu et al. (1996). All observed values for these parameters are summarized in Table 1, with the associated uncertainties σ_j , except for the sound speed profile, for which we refer the reader to the original paper (S. Basu et al. 1996).

For the calibration process, the parameters to be adjusted are the iron-to-hydrogen number ratio $[\text{Fe}/\text{H}] = \log((Z/X)/(Z/X)_{\odot})$ and the helium abundance Y in the convective zone, as well as the

mixing length α_{MLT} and the overshooting f_{ov} parameters. The subscript in $(Z/X)_{\odot}$ denotes the reference solar value, and it is equal to the one given for surface value, $(Z/X)_{\text{surf}}$, in Table 1. In evolutionary 1D models, convective mixing is assumed to be instantaneous, thus the convective region is assumed homogenous. As a result of the calibration process, the obtained iron-to-hydrogen number ratio is $[\text{Fe}/\text{H}] = 0.0531$, the helium abundance is $\text{Y} = 0.25375$, the mixing length and overshooting parameters are $\alpha_{\text{MLT}} = 2.0678$ and $f_{\text{ov}} = 0.0253$. For this best calibrated model, the value of the loss function is $\chi^2 = 4.33$. The results of the calibration are presented in Table 1, where the last column compares our solar model parameters to the observed values. The parameters presented in Table 1 for which no uncertainties are given, were not included in the calibration process.

To validate the seismic accuracy of our calibrated model, we compute the eigenfrequencies of its oscillation modes using the DEDALUS code as described above. The right panel of Fig. 1 confirms that our model accurately reproduces the eigenfrequencies for the global oscillation modes of the Sun, allowing for a precise comparison with helioseismic observations. In this figure, the red crosses represent the observed oscillations frequencies of p -modes measured by [R. Kiefer & A.-M. Broomhall \(2021\)](#) and the blue crosses the oscillation frequencies of the f -modes measured by [T. Larson & J. Schou \(2008\)](#). This good agreement between our model and the observed oscillations frequencies is the result of using the sound speed profile for the calibration. Indeed, the sound speed profile itself is inferred from helioseismology ([S. Basu et al. 1996](#)). The 1D model used in this study is publicly available, as well as the numerical treatment of the linear theory.

C. NUMERICAL SIMULATIONS

C.1. *The MUSIC code*

We present a 2D simulation of the solar interior using the stellar hydrodynamics code MUSIC ([M. Viallet et al. 2016; T. Goffrey et al. 2017](#)). This code employs a time-implicit method ([M. Viallet et al. 2013](#)) to solve for the mass, the momentum and internal energy for a fully compressible, inviscid fluid, i.e.,

$$\frac{\partial \rho}{\partial t} = -\vec{\nabla} \cdot (\rho \vec{v}), \quad (\text{C4})$$

$$\frac{\partial \rho \vec{v}}{\partial t} = -\nabla \cdot (\rho \vec{v} \otimes \vec{v}) - \vec{\nabla} p + \rho \vec{g}, \quad (\text{C5})$$

$$\frac{\partial \rho e}{\partial t} = -\vec{\nabla} \cdot (\rho e \vec{v}) - p \vec{\nabla} \cdot \vec{v} - \vec{\nabla} \cdot \vec{F}_r + \rho \epsilon_{\text{nuc}}, \quad (\text{C6})$$

where ρ is the density, e the specific internal energy, \vec{v} the velocity field, p the gas pressure, ϵ_{nuc} is the specific energy released by nuclear burning and \vec{g} the gravitational acceleration. The radial profile of nuclear energy ϵ_{nuc} is taken from the 1D model, and is assumed constant during the simulation time, as nuclear burning evolves on much longer timescales. The hydrodynamical simulation run for this work assumes spherically symmetric gravitational acceleration, $\vec{g} = -g \vec{e}_r$, which is updated after each time step:

$$g(r) = 4\pi \frac{G}{r^2} \int_0^r \bar{\rho}(u) u^2 du, \quad (\text{C7})$$

with $\bar{\rho}(r)$ radial density profile given by

$$\bar{\rho}(r) = \langle \rho \rangle_S \quad (\text{C8})$$

where the operator $\langle \cdot \rangle_S$ is an angular average over the whole unit sphere, defined as

$$\langle h \rangle_S := \frac{1}{4\pi} \int_S h(\theta, \phi) 2\pi \sin \theta d\theta d\phi. \quad (\text{C9})$$

For the solar simulations considered in this work, the major heat transport that contributes to thermal conductivity is radiative transfer characterised by the radiative flux \vec{F}_r , given within the diffusion approximation by

$$\vec{F}_r = -\frac{16\sigma T^3}{3\kappa\rho} \vec{\nabla}T = -\chi \vec{\nabla}T, \quad (\text{C10})$$

with κ denotes the Rosseland mean opacity of the gas, σ the Stefan–Boltzmann constant and χ the thermal conductivity respectively. MUSIC incorporates realistic stellar opacities (OPAL, C. A. Iglesias & F. J. Rogers 1996) for solar metallicity and equations of state (OPAL EOS, F. J. Rogers & A. Nayfonov 2002) suitable for describing the solar interior.

C.2. 2D solar simulations

The radial extent of the simulation described in the main text spans from $r_{\text{in}} = 0.15R_{\text{star}}$ to $r_{\text{out}} = 0.9R_{\text{star}}$. The co-latitudinal range is $\theta \in [\frac{\pi}{12}; \frac{11\pi}{12}]$. We use a grid resolution of $N_r \times N_\theta = 1024 \times 1024$ cells, with uniform distribution in the radial direction. The size of a unit radial grid cell is $dr = 5.1 \times 10^7 \text{ cm}$. The characteristic size of an angular grid cell is $d\theta = 2.3 \times 10^{-3} \text{ rad}$. The resolution in the θ -direction is defined by the requirement to preserve a satisfying aspect ratio of the grid cells on the whole domain on a spherical grid, ensuring adequate resolution for both the excited wave and convective motions (I. Baraffe et al. 2021; D. G. Vlaykov et al. 2022; A. Le Saux et al. 2022). The simulation takes into account the variable helium mass fraction Y, which is set from the 1D model and do not evolve during the simulation, and we impose the metallicity $Z = 0.02$.

The boundary conditions in the radial direction are the imposition of a constant radial derivative on the density at the inner and outer radial boundaries (see discussion in J. Pratt et al. 2016). The energy flux at both r_{in} and r_{out} is fixed and equal to the value of the energy flux at the corresponding radii in the calibrated 1D model. In terms of velocity, we impose reflective conditions at the radial boundaries as

- $v_r = 0$ and $\frac{\partial v_\theta}{\partial r} = 0$ at r_{in} and r_{out} .

The boundaries in the latitudinal directions are periodic for the density, the energy and the velocities. For instance, for the velocity this is expressed as

- $v_r(\theta_{\min}) = v_r(\theta_{\max})$,
- $v_\theta(\theta_{\min}) = v_\theta(\theta_{\max})$,

with $\theta_{\min} = \pi/12$ to $\theta_{\max} = 11\pi/12$ in this case.

In panel A of Fig. 2 shows a snapshot of the horizontal velocity in the simulation as a function of radius and co-latitude. For better visibility, we normalize its values at each radius by the root-mean-square value of the horizontal velocity. Indeed, the amplitude of the velocity in the radiative zone is much smaller than in the convective zone. The root-mean-square of the component v_i of the velocity $v_{i,\text{rms}}$ is defined as

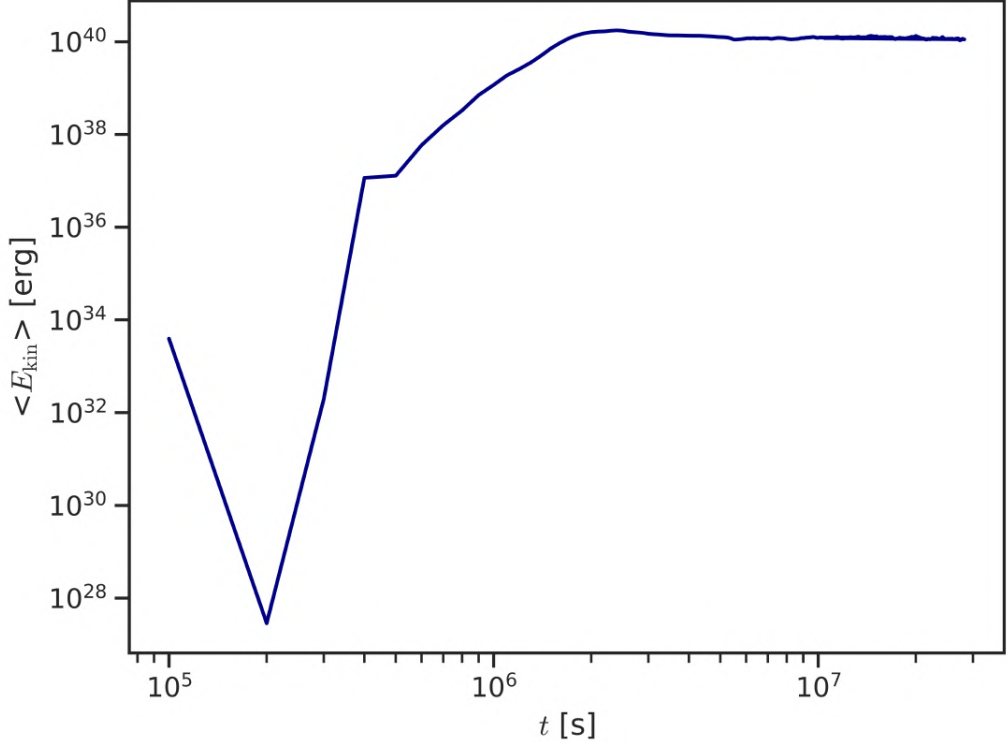


Figure 5. Evolution of the total kinetic energy in the simulation over time. The convective instability begins to develop around 2×10^5 s and then saturates as the convective layer fully develops. The simulation reaches a dynamical steady state once the plateau in kinetic energy is reached, around 3×10^6 s. The wave analysis is performed after that time.

$$v_{i,\text{rms}}(r) := \sqrt{\langle v_i^2(r, \theta, t) \rangle_{S,t}} \quad (\text{C11})$$

with $i = r, h$ denotes the radial and horizontal components of the velocity vector. The operator $\langle \cdot \rangle_S$ is defined in Eq. C9 and $\langle \cdot \rangle_t$ denotes the temporal average, and it is defined by

$$\langle f(t) \rangle_t := \frac{t_0}{T} \int_0^T f(t) dt, \quad (\text{C12})$$

with t_0 the time when the simulation reaches steady state convection and T the final time of the simulation. To estimate when the convection reaches a steady state, we plot on Fig. 5 the evolution of the total kinetic energy in the numerical model as a function of time. The initial peak in kinetic energy comes from strong acoustic waves generated at the start of the simulation. Then, convection starts around 2×10^5 s and then reaches a plateau around 3×10^6 s, which define the value of t_0 in Eq. (C12). We then run the simulation for a total time of $T \sim 3 \times 10^7$ s.

D. WEDGE HARMONICS DECOMPOSITION

The wedge harmonics basis is a basis of eigenfunctions of the Laplacian on wedge-shaped domains that do not span an entire hemisphere in the latitudinal direction, as in the case used in this study (see

Appendix C of [A. Le Saux 2023](#)). It is a generalization of the spherical harmonics basis, designed for wedges. This alternative choice of angular basis is the reason why the power spectra computed from MUSIC work with effective angular degrees $\tilde{\ell}$ that take non integer values, rather than the classical angular degree ℓ used in spherical harmonics. $\tilde{\ell}$ still measures an angular wavenumber of waves with typical angular wavelength $\pi/\tilde{\ell}$. In the case of the spherical harmonics, eigenvalues of $-r^2\Delta$ on the sphere are $\lambda_{\text{sphere}} = \lambda_{\ell}^{\text{SH}} = \ell(\ell + 1)$. By equating the eigenvalues in the spherical harmonics case and wedge harmonics cases, an effective angular degree $\tilde{\ell}$ can be defined such that

$$\lambda_{\text{wedge}} = \lambda_{\tilde{\ell}}^{\text{WH}} = \tilde{\ell}(\tilde{\ell} + 1), \quad (\text{D13})$$

yielding

$$\tilde{\ell} = \sqrt{\lambda_{\ell}^{\text{WH}} + \frac{1}{4}} - \frac{1}{2}. \quad (\text{D14})$$

The wedge harmonics basis and effective wavenumbers are only consequences of the removal of the north and south poles in the simulation, and have no impact on the underlying physics. For the wedge geometry used in the simulation, i.e. $\theta \in [\frac{\pi}{12}; \frac{11\pi}{12}]$, the first values of $\tilde{\ell}$ are $(0, 1.9, 4.3, 6.7, 9.1, 11.5, 13.9, \dots)$.

E. EFFECTIVE POTENTIAL THEORY

To highlight why both surface-intensified waves and interior-localized waves can exist on the f -branch, we derive an effective potential theory within the Cowling approximation. Building on the work of [S. Vorontsov & V. N. Zharkov \(1989\)](#), we find that in the high-frequency limit $\omega \gg N$, the linear perturbation equations reduce to the Schrödinger equation

$$\left(-\frac{d^2}{d\tau^2} + S^2 + \frac{dS}{d\tau} + L_\ell^2 \right) \bar{p} = \omega^2 \bar{p}, \quad (\text{E15})$$

with effective potential $V_{\text{eff}} \equiv S^2 + \frac{dS}{d\tau} + L_\ell^2$. τ denotes the acoustic radius ($d\tau = dr/c_s$), $\bar{p} \equiv \frac{r}{\sqrt{\rho_0 c_s}} p'$ and p' is the Eulerian pressure perturbation and $L_\ell = c_s \sqrt{\ell(\ell + 1)}/r$ is the Lamb frequency measuring the angular wavelength in spherical geometry. The competition between $S^2 + \frac{dS}{d\tau}$ and L_ℓ^2 in V_{eff} determines whether the modes are localized in the bulk of the star, where $S^2 + \frac{dS}{d\tau}$ is minimum, or in the outer layers where L_ℓ^2 is minimum. Figure 6 shows profiles of effective potential V_{eff} at $\ell = 6$ obtained for the Sun and a fictitious star, where the buoyant-acoustic frequency has been amplified $S = 10S_\odot$.

For the fictitious star, the effective potential is dominated by the contribution of $S^2 + \frac{dS}{d\tau}$, as in the academic case derived by [A. Leclerc et al. \(2022\)](#). As such, topological waves are trapped locally in the bulk of the star. For the Sun, the contribution of $S^2 + \frac{dS}{d\tau}$ is counterbalanced by the repulsive effect of L_ℓ^2 , implying mode delocalization.

F. DISTORSION OF THE BUOYANT-ACOUSTIC FREQUENCY $S(R)$

In order to confirm that the f -modes at low l are indeed of topological origin, we deform continuously deform the values of $S(r)$ in order to make the contribution $S^2 + \frac{dS}{d\tau}$ dominate the effective potential, similarly to the normal form analysed in [A. Leclerc et al. \(2022\)](#). This academic situation corresponds to a case of high coupling, where S exhibits large positive and negative values around the cancellation point and varies rapidly. In this regime, the Lamb-like wave consists solely of horizontal

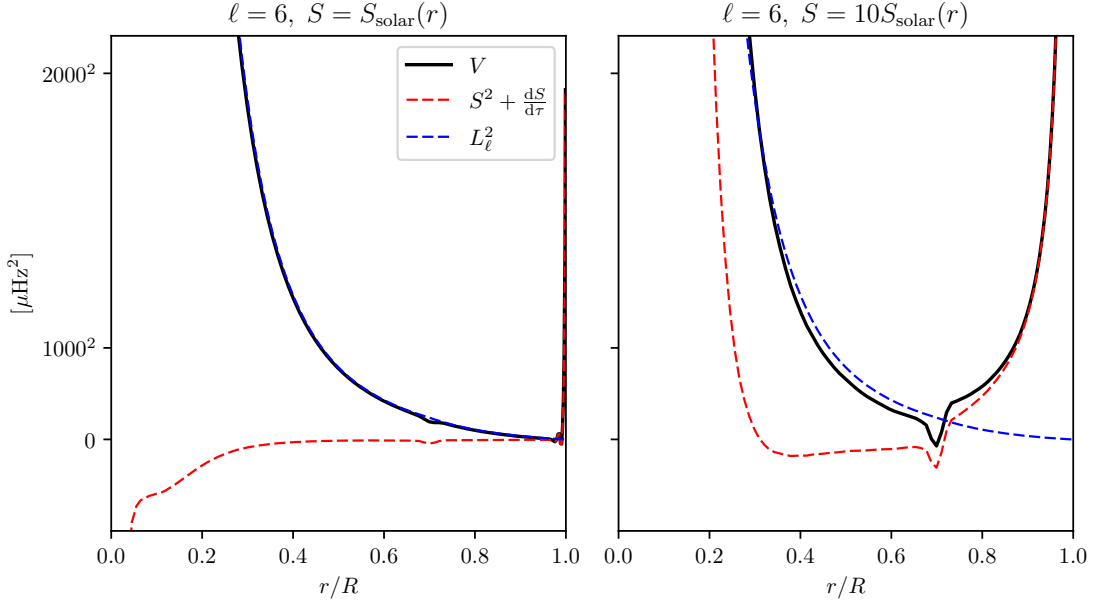


Figure 6. Effective potential of Eq. E15 for the p - and f -modes in the high-frequency limit. In the case $\ell = 6$, the minimum of the potential in the Sun is at the surface. In the fictitious star discussed in the main text for which $S(r) = 10S_\odot(r)$, the minimum is located inside the bulk of the star, where the f -mode is much more closely described by a Lamb-like mode.

velocity with no radial velocity, and its eigenfunctions are confined around the cancellation point of $S(r)$.

We compute the linear normal modes of the solar interior with $S = S_\odot(r)$, $S = 10S_\odot(r)$, and $S = 50S_\odot(r)$, where $S_\odot(r)$ is derived from the calibrated 1D solar model used in the simulation. We compare the eigenfunctions of the Lamb-like wave at $\ell = 6.754$ in these three spectra. Figure 7 shows the results, the blue curves being the solar model simulated in MUSIC.

As the values of S increase, the Lamb-like waves become more confined around their cancellation point, and the horizontal displacement ξ_h dominates the vertical displacement ξ_r , as calculated in A. Leclerc et al. (2022). Although properties of f -modes at low l are inherited from topology, the procedure above explains why these modes are additionally delocalized in the Sun. We expect topological modes in stars with steeper profiles of buoyant-acoustic frequencies to be closer to the academic situation studied in A. Leclerc et al. (2022).

G. AMPLITUDE OF THE MODES AT THE SURFACE AND OBSERVABILITY

Due to numerical constraints, the radial domain of the simulations is restricted to $r = 0.15R_{\text{star}}$ and $r = 0.9R_{\text{star}}$. Starting from data on this restricted domain, we identify normal modes excited by convective motion, and estimate their amplitude at the surface of the Sun. We begin by measuring the amplitude of the normal mode in the simulation at a selected radius within the radiative zone (outside the convective envelope and penetration zone to avoid measuring velocities from convective motions). This is done using the radial velocity extracted from the power spectrum. We choose $r = 0.6R_{\text{star}}$, and verify that this choice does not affect the subsequent results. Next, we calculate the amplitudes of the linear modes for a non-truncated star to determine the ratio of the mode amplitude

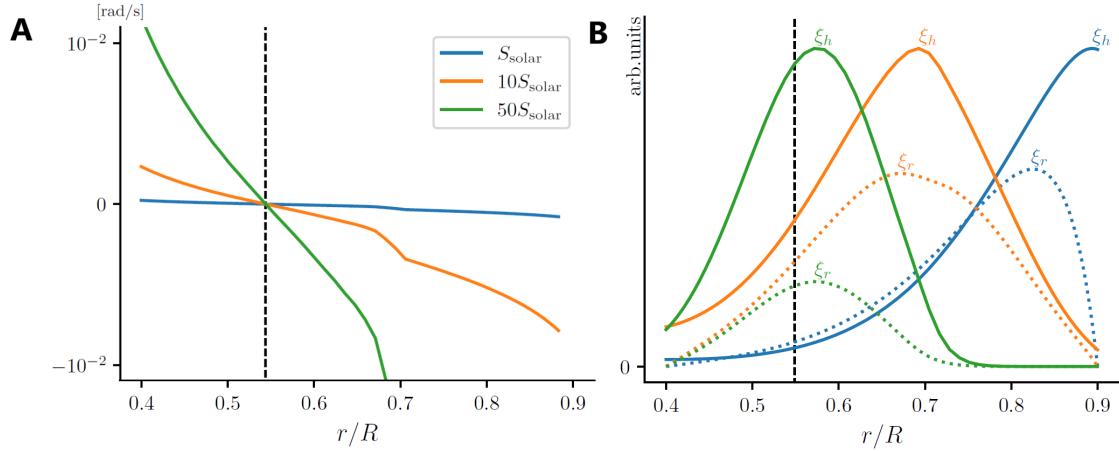


Figure 7. Displacements of the Lamb-like wave for increasing values of $S(r)$. (A) Three deformed profiles of $S(r)$. (B) Displacements of the $n = 0$, $\ell = 4$ modes for the 3 profiles. As the values of S increase, the wave becomes more localized around the point where S cancels (black dashed line). The horizontal displacement is also larger, consistent with the analysis of [A. Leclerc et al. \(2022\)](#).

at $r = 0.6R_{\text{star}}$ to that at the surface. This correction factor is then applied to estimate the mode amplitude at the surface of the Sun. Due to the difference in cavity size between the simulation and the complete 1D model, the eigenfunctions and eigenfrequencies of the normal modes are not exactly identical. In particular, the mixed f/g -mode in the simulation is at $344 \mu\text{Hz}$, the hybridization occurring with the g_1 mode, whereas in the extended 1D model and thus in the Sun, its frequency is $265 \mu\text{Hz}$, the hybridization being with the g_5 mode. The left panel of Figure 8 shows the mixed modes for the simulation (blue line) and for the extended linear model (red dashed line).

Estimates for the surface amplitude of different modes are presented in the column v_{surf} of Table 2. We obtain an estimate of $2.1 \times 10^{-4} \text{ cm s}^{-1}$ for the surface amplitude of the mixed f/g mode, similar as p -modes in the same frequency range. However, in this frequency range, g -modes have significantly lower surface amplitudes. The only g -modes with similar amplitude as the mixed f/g mode are at much lower frequencies, typically around ~ 50 or $100 \mu\text{Hz}$. Because stellar hydrodynamical simulations are far from stellar interior regimes, we find it more pertinent to compare the relative amplitudes between different modes rather than using the absolute amplitude of a given mode in cm s^{-1} . This frequency dependence of the highest amplitude mode plays a key role in observational detection. In helioseismology, surface convection noise, which is the main obstacle to detecting normal modes, intensifies with decreasing frequencies ([C. Pinçon et al. 2021](#)). Thus, despite having similar surface amplitudes, the mixed f/g_5 mode presents a significantly higher likelihood of detection compared to g -modes.

A limitation of our study is that the convection zone is truncated at $r = 0.9R_{\text{star}}$. However, it is well known that the outer layers of the convection zone play a major role in the excitation of the modes, at least for the high frequency ones. To test this, we run an additional simulation of the same solar model that extends from $r = 0.3R_{\text{star}}$ to $r = 0.98R_{\text{star}}$. We do not include more convective layers for numerical reasons. The extension of the numerical domain to the photosphere ($r = R_{\text{star}}$) is an open challenge for stellar hydrodynamical simulations given the sharp decrease of the pressure scale height with increasing radius. Because the size of the cavity is different, modes frequencies are shifted compared to our main simulations. We now identify the mixed f/g mode at $252.8 \mu\text{Hz}$.

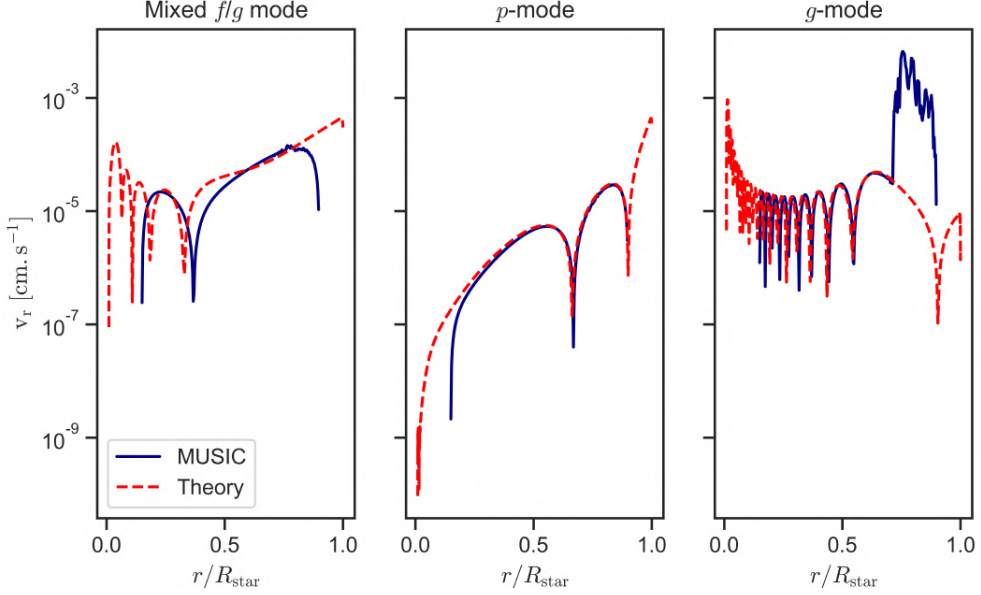


Figure 8. Amplitude of standing modes To estimate the surface amplitude of a mode, we compute its linear eigenfunction (dashed red lines) and fix its amplitude at $r = 0.6R_{\text{star}}$ with the one measured in the MUSIC simulations (blue lines). We can then extrapolate the amplitude of the mode at $r = R_{\text{star}}$.

Table 2. Surface amplitude v_{surf} of normal modes estimated using MUSIC simulation. The angular degree and frequency of the normal modes correspond to those of the complete 1D model and are therefore consistent with the predictions for the Sun. See the text for details on the methodology used for this estimation. As there are no g -modes with a frequency of $230 \mu\text{Hz}$ in the simulation extended to $r = 0.98R_{\text{star}}$, we take instead the highest frequency g -mode for $\ell = 4$, which is $177 \mu\text{Hz}$.

Mode	ℓ	$\omega/2\pi (\mu\text{Hz})$	$v_{\text{surf}} (\text{cm.s}^{-1})$	$v_{\text{surf,ro98}} (\text{cm.s}^{-1})$
Mixed f/g	4	265	2.1×10^{-4}	3.3×10^{-2}
p	4	610	2.6×10^{-4}	4.3×10^{-2}
p	2	543	1.1×10^{-4}	2.4×10^{-2}
g	4	230	3.7×10^{-5}	-
g	4	177	-	3.3×10^{-3}
g	4	93	5.3×10^{-6}	9.6×10^{-3}
g	2	100	2.1×10^{-5}	1.7×10^{-2}
g	4	51	1.1×10^{-4}	3.7×10^{-3}

The estimated surface amplitude using this simulation, $v_{\text{surf,ro98}}$, are presented in the last column of Table 2. The amplitudes of all modes increase significantly. This is expected as the inclusion of more external layers of the convective envelope drives convection stronger as was shown in D. G. Vlaykov et al. (2022). Nevertheless, our conclusions regarding the relative amplitudes of the modes remain unchanged.

Based on these results, an alternative estimate of the f/g mode amplitude at the surface can be obtained by using the observed amplitudes for p -modes, and assuming that the ratio of these

amplitudes to that of the f/g mode is accurately described by linear theory. This method was already used in K. Belkacem et al. (2022). G. R. Davies et al. (2014) use observations of low-order, low-degree p -modes to estimate their amplitude as a function of frequency (see their Fig. 4). Using their results and assuming that the amplitude-frequency relationship remains valid at low frequencies, we estimate the surface amplitude of a p -mode with frequency $\sim 265\mu\text{Hz}$, and therefore of the mixed f/g mode, to be approximately 0.02 cm s^{-1} , which is similar to amplitude estimated using our simulation extended to $r = 0.98R_{\star}$. To date, the most accurate data available comes from the GOLF mission. With a time series spanning over 22 years, the detection threshold is approximately 0.3 cm s^{-1} around $265 \mu\text{Hz}$ (K. Belkacem et al. 2022).

REFERENCES

- Aerts, C., Christensen-Dalsgaard, J., Kurtz, D. W., et al. 2010, *Asteroseismology* (Springer)
- Alvan, L., Brun, A. S., & Mathis, S. 2014, *A&A*, 565, A42, doi: [10.1051/0004-6361/201323253](https://doi.org/10.1051/0004-6361/201323253)
- Antia, H. M. 1998, *A&A*, 330, 336
- Appourchaux, T., Belkacem, K., Broomhall, A.-M., et al. 2010, *The Astronomy and Astrophysics Review*, 18, 197
- Baraffe, I., Pratt, J., Vlaykov, D., et al. 2021, *Astronomy & Astrophysics*, 654, A126
- Basu, S. 2016, *Living Reviews in Solar Physics*, 13, 2, doi: [10.1007/s41116-016-0003-4](https://doi.org/10.1007/s41116-016-0003-4)
- Basu, S., & Antia, H. M. 1997, *MNRAS*, 287, 189, doi: [10.1093/mnras/287.1.189](https://doi.org/10.1093/mnras/287.1.189)
- Basu, S., & Antia, H. M. 2004, *ApJL*, 606, L85, doi: [10.1086/421110](https://doi.org/10.1086/421110)
- Basu, S., Christensen-Dalsgaard, J., Schou, J., Thompson, M. J., & Tomczyk, S. 1996, *ApJ*, 460, 1064, doi: [10.1086/177032](https://doi.org/10.1086/177032)
- Bekki, Y., Cameron, R. H., & Gizon, L. 2024, *Science Advances*, 10, eadk5643, doi: [10.1126/sciadv.adk5643](https://doi.org/10.1126/sciadv.adk5643)
- Belkacem, K., Pinçon, C., & Buldgen, G. 2022, *Solar Physics*, 297, 147
- Bernevig, B. A. 2013, *Topological insulators and topological superconductors* (Princeton university press)
- Borexino Collaboration, Agostini, M., Altenmüller, K., Appel, S., et al. 2020, *Nature*, 587, 577, doi: [10.1038/s41586-020-2934-0](https://doi.org/10.1038/s41586-020-2934-0)
- Bretherton, F. 1969, *Quarterly Journal of the Royal Meteorological Society*, 95, 754
- Brun, A. S., Miesch, M. S., & Toomre, J. 2011, *ApJ*, 742, 79, doi: [10.1088/0004-637X/742/2/79](https://doi.org/10.1088/0004-637X/742/2/79)
- Buldgen, G., Eggenberger, P., Baturin, V., et al. 2020, *Astronomy & Astrophysics*, 642, A36
- Burns, K. J., Vasil, G. M., Oishi, J. S., Lecoanet, D., & Brown, B. P. 2020, *Physical Review Research*, 2, 023068, doi: [10.1103/PhysRevResearch.2.023068](https://doi.org/10.1103/PhysRevResearch.2.023068)
- Chaplin, W. J., Elsworth, Y., Howe, R., et al. 1996, *Solar Physics*, 168, 1
- Christensen-Dalsgaard, J. 2002, *Reviews of Modern Physics*, 74, 1073
- Christensen-Dalsgaard, J. 2021, *Living Reviews in Solar Physics*, 18, 2, doi: [10.1007/s41116-020-00028-3](https://doi.org/10.1007/s41116-020-00028-3)
- Christensen-Dalsgaard, J., & Gough, D. 2001, *Monthly Notices of the Royal Astronomical Society*, 326, 1115
- Christensen-Dalsgaard, J., Däppen, W., Ajukov, S., et al. 1996, *Science*, 272, 1286
- Cowling, T. G. 1941, *Monthly Notices of the Royal Astronomical Society*, Vol. 101, p. 367, 101, 367
- Davies, G. R., Broomhall, A. M., Chaplin, W. J., Elsworth, Y., & Hale, S. J. 2014, *MNRAS*, 439, 2025, doi: [10.1093/mnras/stu080](https://doi.org/10.1093/mnras/stu080)
- Delplace, P. 2022, *SciPost Physics Lecture Notes*, 039
- Delplace, P., Marston, J., & Venaille, A. 2017, *Science*, 358, 1075
- Deubner, F.-L., & Gough, D. 1984, *Annual review of astronomy and astrophysics*, 22, 593
- Dewberry, J. W., Mankovich, C. R., Fuller, J., Lai, D., & Xu, W. 2021, *The Planetary Science Journal*, 2, 198
- Fossat, E. 1991, *SoPh*, 133, 1, doi: [10.1007/BF00149818](https://doi.org/10.1007/BF00149818)
- Fossat, E., Boumier, P., Corbard, T., et al. 2017, *A&A*, 604, A40, doi: [10.1051/0004-6361/201730460](https://doi.org/10.1051/0004-6361/201730460)

- Gabriel, A., Charra, J., Grec, G., et al. 1997, *Solar Physics*, 175, 207
- García, R. A., Turck-Chièze, S., Jiménez-Reyes, S. J., et al. 2007, *Science*, 316, 1591, doi: [10.1126/science.1140598](https://doi.org/10.1126/science.1140598)
- Gizon, L., Cameron, R. H., Bekki, Y., et al. 2021, *A&A*, 652, L6, doi: [10.1051/0004-6361/202141462](https://doi.org/10.1051/0004-6361/202141462)
- Goffrey, T., Pratt, J., Viallet, M., et al. 2017, *A&A*, 600, A7, doi: [10.1051/0004-6361/201628960](https://doi.org/10.1051/0004-6361/201628960)
- Gough, D. 1993, *Astrophysical Fluid Dynamics-Les Houches* 1987, 399
- Grevesse, N., & Sauval, A. J. 1998, *SSRv*, 85, 161, doi: [10.1023/A:1005161325181](https://doi.org/10.1023/A:1005161325181)
- Harvey, J., Hill, F., Hubbard, R., et al. 1996, *Science*, 272, 1284
- Hekker, S., & Christensen-Dalsgaard, J. 2017, *A&A Rv*, 25, 1, doi: [10.1007/s00159-017-0101-x](https://doi.org/10.1007/s00159-017-0101-x)
- Hoeksema, J. T., Baldner, C. S., Bush, R. I., Schou, J., & Scherrer, P. H. 2018, *Solar Physics*, 293, 1
- Howe, R. 2009, *Living Reviews in Solar Physics*, 6, 1, doi: [10.12942/lrsp-2009-1](https://doi.org/10.12942/lrsp-2009-1)
- Howe, R., Chaplin, W., Elsworth, Y., Hale, S., & Nielsen, M. 2023, *Monthly Notices of the Royal Astronomical Society*, 526, 1447
- Iglesias, C. A., & Rogers, F. J. 1996, *ApJ*, 464, 943, doi: [10.1086/177381](https://doi.org/10.1086/177381)
- Jermyn, A. S., Bauer, E. B., Schwab, J., et al. 2023, *ApJS*, 265, 15, doi: [10.3847/1538-4365/acae8d](https://doi.org/10.3847/1538-4365/acae8d)
- Kiefer, R., & Broomhall, A.-M. 2021, *Monthly Notices of the Royal Astronomical Society*, 500, 3095
- Kjeldsen, H., Bedding, T. R., Viskum, M., & Frandsen, S. 1995, *AJ*, 109, 1313, doi: [10.1086/117363](https://doi.org/10.1086/117363)
- Lamb, H. 1911, *Proceedings of the Royal Society of London. Series A, Containing Papers of a Mathematical and Physical Character*, 84, 551
- Larson, T., & Schou, J. 2008, in *Journal of Physics: Conference Series*, Vol. 118, IOP Publishing, 012083
- Le Saux, A. 2023, PhD thesis, University of Exeter. <https://www.proquest.com/docview/2925385787?pq-origsite=gscholar&fromopenview=true&sourcetype=Dissertations%20&%20Theses>
- Le Saux, A., Baraffe, I., Guillet, T., et al. 2023, *MNRAS*, 522, 2835, doi: [10.1093/mnras/stad1067](https://doi.org/10.1093/mnras/stad1067)
- Le Saux, A., Guillet, T., Baraffe, I., et al. 2022, *A&A*, 660, A51, doi: [10.1051/0004-6361/202142569](https://doi.org/10.1051/0004-6361/202142569)
- Leclerc, A., Laibe, G., Delplace, P., Venaille, A., & Perez, N. 2022, *The Astrophysical Journal*, 940, 84
- Lefebvre, S., Kosovichev, A. G., & Rozelot, J. 2007, *The Astrophysical Journal*, 658, L135
- Leibacher, J., Appourchaux, T., Buldgen, G., et al. 2023, *Bulletin of the AAS*, 55
- Magg, E., Bergemann, M., Serenelli, A., et al. 2022, *A&A*, 661, A140, doi: [10.1051/0004-6361/202142971](https://doi.org/10.1051/0004-6361/202142971)
- Mamajek, E. E., Prsa, A., Torres, G., et al. 2015, arXiv e-prints, arXiv:1510.07674, doi: [10.48550/arXiv.1510.07674](https://doi.org/10.48550/arXiv.1510.07674)
- Ouazzani, R.-M., Lignières, F., Dupret, M.-A., et al. 2020, *Astronomy & Astrophysics*, 640, A49
- Paxton, B., Bildsten, L., Dotter, A., et al. 2011, *ApJS*, 192, 3, doi: [10.1088/0067-0049/192/1/3](https://doi.org/10.1088/0067-0049/192/1/3)
- Paxton, B., Cantiello, M., Arras, P., et al. 2013, *ApJS*, 208, 4, doi: [10.1088/0067-0049/208/1/4](https://doi.org/10.1088/0067-0049/208/1/4)
- Paxton, B., Marchant, P., Schwab, J., et al. 2015, *ApJS*, 220, 15, doi: [10.1088/0067-0049/220/1/15](https://doi.org/10.1088/0067-0049/220/1/15)
- Paxton, B., Schwab, J., Bauer, E. B., et al. 2018, *ApJS*, 234, 34, doi: [10.3847/1538-4365/aaa5a8](https://doi.org/10.3847/1538-4365/aaa5a8)
- Paxton, B., Smolec, R., Schwab, J., et al. 2019, *ApJS*, 243, 10, doi: [10.3847/1538-4365/ab2241](https://doi.org/10.3847/1538-4365/ab2241)
- Perez, N. 2022, PhD thesis, Ecole normale supérieure de Lyon-ENS LYON
- Perrot, M., Delplace, P., & Venaille, A. 2019, *Nature Physics*, 15, 781
- Pinçon, C., Appourchaux, T., & Buldgen, G. 2021, *A&A*, 650, A47, doi: [10.1051/0004-6361/202040003](https://doi.org/10.1051/0004-6361/202040003)
- Pratt, J., Baraffe, I., Goffrey, T., et al. 2016, *A&A*, 593, A121, doi: [10.1051/0004-6361/201628296](https://doi.org/10.1051/0004-6361/201628296)
- Provost, J., Berthomieu, G., & Morel, P. 2000, *Astronomy and Astrophysics*, v. 353, p. 775-785 (2000), 353, 775
- Rauer, H., Catala, C., Aerts, C., et al. 2014, *Experimental Astronomy*, 38, 249, doi: [10.1007/s10686-014-9383-4](https://doi.org/10.1007/s10686-014-9383-4)

- Rogers, F. J., & Nayfonov, A. 2002, ApJ, 576, 1064, doi: [10.1086/341894](https://doi.org/10.1086/341894)
- Rogers, T. M., Glatzmaier, G. A., & Jones, C. A. 2006, ApJ, 653, 765, doi: [10.1086/508482](https://doi.org/10.1086/508482)
- Schou, J., Christensen-Dalsgaard, J., & Thompson, M. J. 1994, ApJ, 433, 389, doi: [10.1086/174653](https://doi.org/10.1086/174653)
- Schunker, H., Schou, J., Gaulme, P., & Gizon, L. 2018, SoPh, 293, 95, doi: [10.1007/s11207-018-1313-6](https://doi.org/10.1007/s11207-018-1313-6)
- Scuflaire, R. 1974, Astronomy and Astrophysics, Vol. 36, p. 107 (1974), 36, 107
- Thompson, M. J., Christensen-Dalsgaard, J., Miesch, M. S., & Toomre, J. 2003, Annual Review of Astronomy and Astrophysics, 41, 599
- Unno, W., Osaki, Y., Ando, H., & Shibahashi, H. 1979, Tokyo: University of Tokyo Press
- Viallet, M., Baraffe, I., & Walder, R. 2013, A&A, 555, A81, doi: [10.1051/0004-6361/201220725](https://doi.org/10.1051/0004-6361/201220725)
- Viallet, M., Goffrey, T., Baraffe, I., et al. 2016, A&A, 586, A153, doi: [10.1051/0004-6361/201527339](https://doi.org/10.1051/0004-6361/201527339)
- Vlaykov, D. G., Baraffe, I., Constantino, T., et al. 2022, MNRAS, 514, 715, doi: [10.1093/mnras/stac1278](https://doi.org/10.1093/mnras/stac1278)
- Vorontsov, S., & Zharkov, V. N. 1989, Astrophysics and Space Physics Reviews, 7, 1

Berry phase importance of solar p -modes

Résumé

Le Chapitre V montre que les ondes dans les étoiles ont une courbure de Berry non nulle, qui émane de deux monopoles de Berry-Chern de charge $\mathcal{C} = \pm 1$ dans leur espace des paramètres. C'est la propriété topologique causant l'existence des ondes topologiques.

Comme discuté dans le Chapitre II, une courbure de Berry cause également une phase de Berry non-nulle, amassée par les ondes lors de changements périodiques lents. Ce chapitre montre que de tels changements périodiques ont lieu quand on considère le tracé de rayon des ondes astéroismiques, ce qui amène à l'identification d'un terme de phase de Berry dans les fréquences propres des modes stellaires. Une phase de Berry a été trouvée dans les modes d'ondes équatoriales par [142], suggérant sa présence aussi dans les modes stellaires. Ce résultat donne un nouveau pont conceptuel entre physique quantique et dynamique des fluides. De plus, l'expression de ce terme de phase de Berry est obtenue exactement, et il corrige les lois classiques de Duvall et Tassoul, notamment à bas ordre radial n .

Chapter V showed that waves in stars have a non-zero Berry curvature, emanating from Berry-Chern monopoles with Chern numbers $\mathcal{C} = \pm 1$ in their parameter space. This is the topological property, causing the presence of the topological wave in stellar spectra.

As discussed in Chapter II, a non-zero Berry curvature also causes a non-zero Berry phase, picked up by the waves upon performing periodic slow changes. This chapter shows that such periodic slow changes can be found in ray-tracing solutions in asteroseismic context, leading to the identification of a Berry phase term in the frequencies of stellar modes. A Berry phase was identified in the equatorial shallow water modes in [142] which inspired this work, investigating its presence in asteroseismic waves.

This result strengthens the conceptual bridge between quantum physics and fluid dynamics. Additionally, it provides the expression of this term of Berry phase, which is shown to be a corrective term to the well-known laws of Duvall and Tassoul. These laws are obtained by WKB approximation of the normal modes' equation yielding the behavior of modes with high radial order n . The Berry phase corrects the laws at low n .

The results presented in this chapter have been published in *The importance of Berry phase in solar acoustic modes*, Leclerc & Laibe, *The Astrophysical Journal Letters* 2025 [344].

The importance of Berry phase in solar acoustic modes

ARMAND LECLERC  ^{1,*} AND GUILLAUME LAIBE ^{1,2}

¹*ENS de Lyon, CRAL UMR5574, Universite Claude Bernard Lyon 1, CNRS, Lyon, F-69007, France*

²*Institut Universitaire de France*

ABSTRACT

An analytic expression for the frequencies of standing waves in stars, applicable to any radial order n , is derived from ray-tracing equations by the mean of Wigner-Weyl calculus. A correction to previous formulas currently employed in asteroseismology is identified as the Berry phase, which accounts for the vectorial nature of wave propagation in stars. Accounting for this quantity significantly improves upon previous laws for low n modes of the Sun, and we show that the Berry phase is indeed present in the available observational data of solar modes. This phase is due to inhomogeneities of the medium.

Keywords: waves — helioseismology — analytical

1. INTRODUCTION

Mechanical waves that travel through the interiors of stars provide the most accurate insights into their inner structures (e.g. Basu 2016; Christensen-Dalsgaard 2021). Since these waves manifest as standing oscillations on the surface, a standard approach consists in deriving the equations that describe standing waves to obtain the theoretical frequency distributions of pulsations for large radial orders ($n \gg 1$). The frequencies are expressed as functions of the harmonic degree ℓ and the physical parameters of the star: the sound speed c_s and the buoyant frequency N , which both vary with radius r . Acoustic modes follow a relationship known as Duvall's law: frequencies are distributed approximately uniformly, as given by the formula $\nu = (n + \frac{\ell}{2} + \frac{3}{4})\Delta\nu$, where $\Delta\nu = (2 \int_0^R dr/c_s)^{-1}$ is the so-called large frequency separation (Duvall Jr 1982). Gravity modes obey Tassoul's law: periods are approximately uniformly spaced and expressed as $P = \frac{2\pi^2(n+\frac{1}{2})}{\sqrt{\ell(\ell+1)}} (\int_{r_1}^{r_2} \frac{N}{r} dr)^{-1}$ (Shibahashi 1979; Tassoul 1980). These laws give explicit constrain on N and c_s from the observed oscillation frequencies. At large radial orders n , deviations from these distributions are caused by the acoustic cut-off frequency $\omega_c^2 = c_s^2/4H^2(1 - 2dH/dr)$, where H is the pressure scale height. For acoustic modes, these corrections are usually grouped into a parameter called the phase function $\alpha(\omega)$ (e.g. Deubner and Gough 1984; Christensen-Dalsgaard and Pérez Hernández 1992), which leads to a small frequency separation $\delta\nu = \nu_{n,\ell} - \nu_{n+1,\ell-2}$, offering valuable information about the temperature gradient of the star (Tassoul 1980).

* Corresponding author: armand.leclerc@ens-lyon.fr

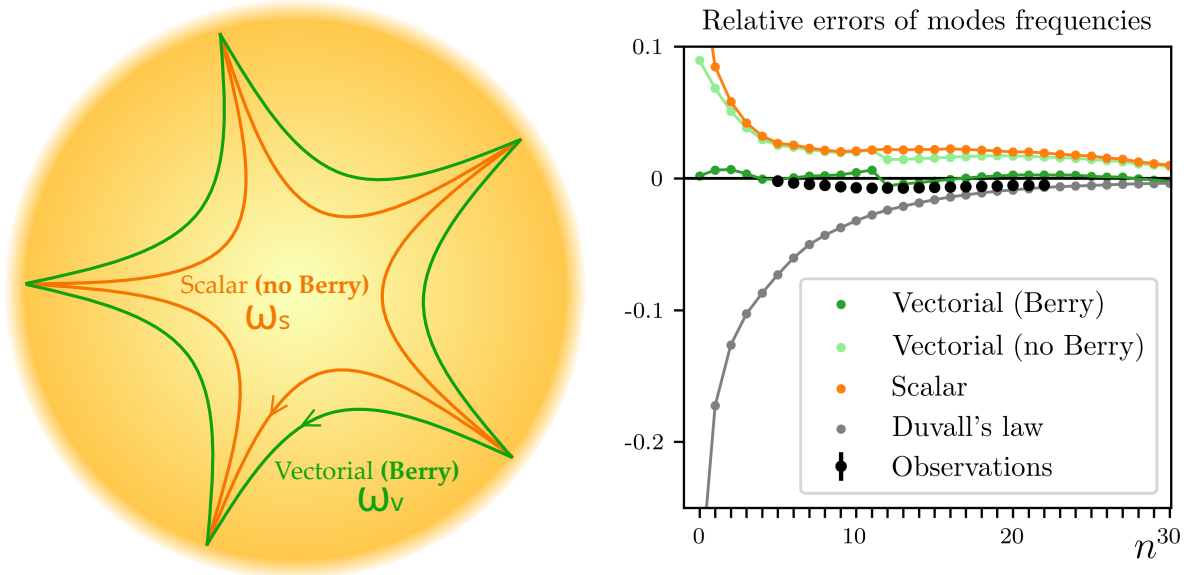


Figure 1. Ray-tracing equations accounting for the Berry curvature are slightly deviated, correcting the frequencies of standing waves. **Left:** The polarization of the wave adds a Berry term in the ray-tracing equations, changing the bending of the ray between a scalar and fully vectorial theory. The resulting standing wave traced by the rays have a different frequency. **Right:** Frequency estimates of solar acoustic modes for azimuthal degree $\ell = 25$ significantly improve when accounting for the Berry phase, in particular for low radial orders n . The scalar and the two vectorial theories account for the phase function $\alpha(\omega)$, the "vectorial (no Berry)" theory accounts for correction of Ω arising from spatial variation of background quantities, the "vectorial (Berry)" theory further incorporate ϕ_B . For $n \leq 20$, only the predictions accounting for ϕ_B match the observed frequencies to the current degree of precision of the 1D model (1%). The observational uncertainties (vertical bars) are undistinguishable at this scale (0.1% in (Hill et al. 1996)).

In this study, we provide a more precise equation for the frequencies of standing waves that is valid for all radial orders. Importantly, this equation introduces a correction term to the previously established laws that improves significantly their accuracy for low n . It is possible to relax the usual high n approximation by relying instead on a high ℓ approximation. For this, we treat asteroseismology from the alternate perspective of geometrical optics, which describes the paths of wave rays (Gough 1986, 1993; Loi 2020). While ray-tracing is generally based on a scalar description of the wave, we account here for polarization effects due to the multicomponent nature of the perturbations in the equations, resulting in a more accurate formulation. This result is obtained by treating the full perturbations equations as a Schrödinger equation, and taking its semi-classical limit which yields the dynamics of p -quasi-particles and g -quasi-particles.

2. RAY-TRACING WITH VARYING POLARIZATIONS

The evolution of linear, adiabatic perturbations of a non-rotating, non-magnetic stars under the Cowling approximation can be expressed in a symmetric form by adopting the appropriate change

of variables

$$\mathbf{v} = \rho_0^{1/2} c_s^{1/2} r \mathbf{v}', \quad (1)$$

$$p = \rho_0^{-1/2} c_s^{-1/2} r p', \quad (2)$$

$$\Theta = \rho_0^{-1/2} r \frac{g}{N} (\rho' - \frac{1}{c_s^2} p'), \quad (3)$$

where p' , ρ' and \mathbf{v}' are the Eulerian perturbations in pressure, density and velocity. It slightly differs here from the changes of variables performed in (Leclerc et al. 2022, 2024), in which the detailed derivations are presented.

Further decomposing the velocity perturbation onto the basis of vectorial spherical harmonics, one has

$$\mathbf{v}(r, \theta, \phi) = v_r(r) \mathbf{Y}_\ell^m + v_h(r) \Psi_\ell^m, \quad (4)$$

where $\mathbf{Y}_\ell^m = Y_\ell^m \mathbf{e}_r$ and $\Psi_\ell^m = \frac{ir}{\sqrt{\ell(\ell+1)}} \nabla Y_\ell^m$. By introducing the acoustic radius z_s defined by $dz_s = dr/c_s$ as a new radial coordinate, the equations of perturbation read

$$i\partial_t \begin{pmatrix} v_h \\ v_r \\ \Theta \\ p \end{pmatrix} = \begin{pmatrix} 0 & 0 & 0 & L_\ell \\ 0 & 0 & -iN - i\partial_{z_s} + iS & 0 \\ 0 & iN & 0 & 0 \\ L_\ell - i\partial_{z_s} - iS & 0 & 0 & 0 \end{pmatrix} \begin{pmatrix} v_h \\ v_r \\ \Theta \\ p \end{pmatrix}. \quad (5)$$

Defining the slow acoustic radius and slow time as $z = \epsilon z_s$, $\tau = \epsilon t$ with $\epsilon = 1/\sqrt{\ell(\ell+1)}$, one obtains the wave equation

$$i\epsilon\partial_\tau \mathbf{X} = \hat{\mathbf{H}}\mathbf{X}, \quad (6)$$

$$\text{with } \hat{\mathbf{H}} = \begin{pmatrix} 0 & 0 & 0 & L_\ell \\ 0 & 0 & -iN - i\epsilon\partial_z + iS & 0 \\ 0 & iN & 0 & 0 \\ L_\ell - i\epsilon\partial_z - iS & 0 & 0 & 0 \end{pmatrix}, \quad (7)$$

where $\mathbf{X} = (v_h \ v_r \ \Theta \ p)^\top$, $L_\ell = c_s/\epsilon r$ and $N^2 = g(\frac{1}{\Gamma_1} \frac{d \ln P_0}{dr} - \frac{d \ln \rho_0}{dr})$ are the Lamb and the buoyancy frequencies and $S = \frac{c_s}{2g} \left(N^2 - \frac{g^2}{c_s^2} \right) - \frac{1}{2} \frac{dc_s}{dr} + \frac{c_s}{r}$. The parameter $\epsilon \equiv 1/\sqrt{\ell(\ell+1)}$ is the angular wavelength which acts as a small parameter for large azimuthal degrees ℓ .

In principle, other small parameters ϵ can be chosen, as long as the limit $\epsilon \rightarrow 0$ is a limit in which the frequencies of p -modes and g -modes are well-separated which is needed in the following. This choice of variables $(v_h \ v_r \ \Theta \ p)^\top$ and coordinate z yields an operator which is self-adjoint with respect to the scalar product $\langle \mathbf{X}_1, \mathbf{X}_2 \rangle = \int dz \ \mathbf{X}_1^\dagger \cdot \mathbf{X}_2$. The expressions of our results are obtained for those specific variables and coordinate.

Obtaining the equations of rays from Eq. (7) at order ϵ^1 is involved and requires a number of technical steps. The derivation is analogous to the ones of Perez et al. 2021 and Venaille et al. 2023. We first aim to transform the vectorial equation (7) to a scalar one by transforming it to the form

$$i\epsilon\partial_\tau \psi = \hat{\Omega}\psi, \quad (8)$$

and this, for a selected waveband (either acoustic or internal gravity). The idea is to reconstruct the multicomponent perturbations field $\mathbf{X}(\tau, z)$ from the scalar field $\psi(\tau, z)$ through a vectorial operator $\hat{\chi}(z, \partial_z)$ by $\mathbf{X} = \hat{\chi}\psi$. ψ is the scalar field that evolves according to the dispersion relation, and $\hat{\chi}$ is a vector of differential operators used to reconstruct all perturbed fields of the wave from the scalar field. In general, such transform is not possible. It becomes however feasible when $\epsilon \ll 1$, which ensures that the wave bands are well-separated. This section shows that the ray-tracing equations for \mathbf{X} and ψ differ slightly, by a term involving the polarization relations given by $\hat{\chi}$.

The expressions of $\hat{\Omega}$ and $\hat{\chi}$ are unknown and have to be determined. The condition $\hat{\chi}^\dagger \cdot \hat{\chi} = \mathbf{1}$ is imposed, so that the energy of the wave is $E = \int dz \mathbf{X}^\dagger \cdot \mathbf{X} = \int dz \psi^* \psi = 1$. The symbol \dagger denotes the conjugate-transpose in the sense of 4×4 complex matrices and vectors. Consistency of time evolution imposes

$$\hat{\mathbf{H}}\hat{\chi} = \hat{\chi}\hat{\Omega}. \quad (9)$$

The operators are then expanded to first order in ϵ as

$$\hat{\mathbf{H}} = \hat{\mathbf{H}}_0 + \epsilon \hat{\mathbf{H}}_1, \quad (10)$$

$$\hat{\Omega} = \hat{\Omega}_0 + \epsilon \hat{\Omega}_1, \quad (11)$$

$$\hat{\chi} = \hat{\chi}_0 + \epsilon \hat{\chi}_1. \quad (12)$$

We now apply the Wigner transform, which transforms a differential operator $\hat{A}(z, \partial_z)$ into a function on the phase space $A(z, k_z)$. It is the reciprocal transform of the Weyl transformation, which is a quantization rule. See (Onuki 2020) for a detailed description of the Wigner transform and its usefulness in fluid mechanics. For instance, the Wigner transform gives the maps

$$-i\partial_z \mapsto k_z, \quad (13)$$

$$c_s(\hat{z}) \mapsto c_s(z). \quad (14)$$

It is a way of representing the local action of operators on plane waves. Wigner-Weyl calculus comes with a general way of computing products of operators, the so-called Moyal product \star , such that

$$\hat{A}\hat{B} = \widehat{A \star B}, \quad (15)$$

which is particularly useful to treat Eq. (9). The Moyal product is defined as the expansion on ϵ (Onuki 2020)

$$A \star B \equiv \sum_{p,q \in \mathbb{N}^2} \frac{(-1)^p}{p!q!} \left(\frac{i}{2}\epsilon \right)^{p+q} (\partial_z^q \partial_{k_z}^p A)(\partial_z^p \partial_{k_z}^q B), \quad (16)$$

which gives at first order in ϵ the r.h.s of Eq. (9) as

$$\hat{\chi}\hat{\Omega} = \widehat{\chi \star \Omega} \quad (17)$$

$$\text{and } \chi \star \Omega = \chi_0 \Omega_0 + \epsilon \left(\chi_1 \Omega_0 + \chi_0 \Omega_1 + \frac{i}{2} \{ \chi_0, \Omega_0 \} \right), \quad (18)$$

where $\{, \}$ are the Poisson bracket in the phase space (z, k_z) defined in the main text.

From Eq. (18), one determines the symbols Ω_0 , Ω_1 and χ_0 . At zeroth order in ϵ , one has

$$\mathbf{H}_0 \Omega_0 = \chi_0 \Omega_0, \quad (19)$$

where Ω_0 and χ_0 are an eigenvalue and an eigenvector of the matrix \mathbf{H}_0 , as obtained with direct linear algebra. The matrix \mathbf{H}_0 reads

$$\mathbf{H}_0(z, k_z) = \begin{pmatrix} 0 & 0 & 0 & L_\ell \\ 0 & 0 & -iN & k_z + iS \\ 0 & iN & 0 & 0 \\ L_\ell & k_z - iS & 0 & 0 \end{pmatrix}. \quad (20)$$

The full expressions of χ_0 , Ω_0 are given in Appendix A for both acoustic and internal gravity waves. Exploiting the limit $\epsilon \ll 1$, Wigner-Weyl calculus has therefore provided the mathematical framework to project the operator $\hat{\mathbf{H}}$ onto the acoustic band, by separating the scalar propagation operator $\hat{\Omega}$ and the polarisation operator $\hat{\chi}$. Pursuing the expansion of Eq. (9) at order ϵ^1 , one finds

$$\Omega_1 = \frac{i}{2} \chi_0^\dagger \{ \mathbf{H}_0 - \Omega_0 \mathbf{I}_4, \chi_0 \} + \frac{i}{2} \chi_0^\dagger \{ \Omega_0 \mathbf{I}_4, \chi_0 \}. \quad (21)$$

The first term of the r.h.s is involved in the ray-tracing dynamics. The second term is not involved in the ray-tracing equations (Perez et al. 2021; Venaille et al. 2023).

We can now establish the time evolution of a wavepacket of the form $\mathbf{X}(\tau, z) = \hat{\chi}(z, k(\tau, z))\psi(\tau, z)$, where

$$\psi(\tau, z) = a_0(\tau, z) e^{\frac{i}{\epsilon}(\phi_0 + \epsilon\phi_1)}. \quad (22)$$

The envelope a_0 is chosen to have significant values within a narrow spatial region Δz that is small compared to any other length-scale in the star. From Venaille et al. (2023), one has at order ϵ

$$\mathbf{X} = a_0 e^{\frac{i}{\epsilon}(\phi_0 + \epsilon\phi_1)} \chi_0(z, k(\tau, z)), \quad (23)$$

$$k(\tau, z) \equiv \partial_z \phi_0 + \epsilon \partial_z \phi_1. \quad (24)$$

The average position and momentum of the wavepacket are then determined by a_0 and $\phi_0 + \epsilon\phi_1$ respectively. The coordinates of the scalar wavepacket in phase space are

$$\langle z \rangle_\psi \equiv \int dz \psi^* z \psi = \int dz z a_0^2, \quad (25)$$

$$\langle k_z \rangle_\psi \equiv \int dz \psi^* (-i\epsilon \partial_z) \psi = (\partial_z \phi_0 + \epsilon \partial_z \phi_1) \Big|_{z=\langle z \rangle_\psi}. \quad (26)$$

Taking the derivative with respect to time, using the property that $\hat{\Omega}$ is self-adjoint and the identities $\hat{z}\hat{\Omega} - \hat{\Omega}\hat{z} = i\epsilon \widehat{\partial_{k_z} \Omega}$ and $\partial_z \hat{\Omega} - \hat{\Omega} \partial_z = \widehat{\partial_z \Omega}$ (Venaille et al. 2023), one obtains the dynamical evolution

$$\dot{\langle z \rangle}_\psi = \int dz (\partial_\tau \psi^* \cdot \hat{z} \psi + \psi^* \cdot \hat{z} \partial_\tau \psi), \quad (27)$$

$$= \int dz \frac{i}{\epsilon} (\psi^* \cdot \hat{\Omega} \hat{z} \psi - \psi^* \cdot \hat{z} \hat{\Omega} \psi), \quad (28)$$

$$= \int dz \psi^* \widehat{\partial_{k_z} \Omega} \psi, \quad (29)$$

and

$$\langle \dot{k}_z \rangle_\psi = \int dz (\partial_\tau \psi^* \cdot (-i\epsilon \partial_z) \psi + \psi^* \cdot (-i\epsilon \partial_z) \partial_\tau \psi), \quad (30)$$

$$= \int dz (\psi^* \cdot \hat{\Omega} \partial_z \psi - \psi^* \cdot \partial_z \hat{\Omega} \psi), \quad (31)$$

$$= - \int dz \psi^* \widehat{\partial_z \Omega} \psi. \quad (32)$$

Using the general result that for a scalar wavepacket of small extension and any operator \hat{A} , one has $\int dz \psi^* \hat{A} \psi \sim A(\langle z \rangle_\psi, \langle k_z \rangle_\psi)$ (Venaille et al. 2023), one obtains for the scalar wavepacket

$$\langle \dot{z} \rangle_\psi = +\partial_{k_z} \Omega, \quad (33)$$

$$\langle \dot{k}_z \rangle_\psi = -\partial_z \Omega. \quad (34)$$

This is a canonical system for the Hamiltonian $\Omega = \Omega_0 + \epsilon \Omega_1$. Littlejohn and Flynn (1991) showed that this expression is not gauge-invariant under a change of global phase $\chi_0 \mapsto e^{ig(z, k_z)} \chi_0$ due to the last term in Ω_1 in Eq. (21). On the other hand, the coordinates of the vectorial wavepacket

$$\langle z \rangle_{\mathbf{X}} \equiv \int dz \mathbf{X}^\dagger \cdot z \mathbf{X}, \quad (35)$$

$$\langle k_z \rangle_{\mathbf{X}} \equiv \int dz \mathbf{X}^\dagger \cdot (-i\epsilon \partial_z) \mathbf{X}, \quad (36)$$

are necessarily gauge-independent of the choice of phase of χ_0 , as they are defined independently of the decomposition $\mathbf{X} = \hat{\chi} \psi$. The evolution of these coordinates can be obtained from the ones of the scalar wavepacket by the mean of the relations

$$\langle z \rangle_{\mathbf{X}} = \langle z \rangle_\psi + i\epsilon \chi_0^\dagger \cdot \partial_{k_z} \chi_0, \quad (37)$$

$$\langle k_z \rangle_{\mathbf{X}} = \langle k_z \rangle_\psi - i\epsilon \chi_0^\dagger \cdot \partial_z \chi_0. \quad (38)$$

One observes that the last terms of the right-hand side of Eqs. (37)-(38) are not gauge-independent as they would change under $\chi_0 \mapsto e^{ig(z, k_z)} \chi_0$, implying that the coordinates of the scalar wavepacket are also not gauge-independent. Hence the necessity to formulate ray-tracing equations on the vectorial wavepacket coordinates.

Eqs. (33)-(34) then yield

$$\langle \dot{z} \rangle_{\mathbf{X}} = +\partial_{k_z} \tilde{\Omega} + \epsilon F \langle \dot{z} \rangle, \quad (39)$$

$$\langle \dot{k}_z \rangle_{\mathbf{X}} = -\partial_z \tilde{\Omega} + \epsilon F \langle \dot{k}_z \rangle, \quad (40)$$

where

$$\tilde{\Omega} \equiv \Omega - \frac{i\epsilon}{2} \mathbf{X}_0^\dagger \{ \Omega_0 \mathbf{I}_4, \chi_0 \} = \Omega_0 + \frac{i\epsilon}{2} \chi_0^\dagger \{ \mathbf{H}_0 - \Omega_0 \mathbf{I}_4, \chi_0 \}, \quad (41)$$

$$F = i \{ \chi_0^\dagger, \chi_0 \}. \quad (42)$$

$\{a, b\}$ are the Poisson brackets of a and b defined as $\{a, b\} \equiv \partial_z a \partial_{k_z} b - \partial_{k_z} a \partial_z b$. The full expression of F is given in Appendix A for both acoustic and internal gravity waves.

These are the ray-tracing equations of asteroseismology at order ϵ^1 in finite horizontal size. Working with gauge-invariant coordinates in phase space, the system becomes non-canonically Hamiltonian, due to the term F in the right-hand side (Littlejohn and Flynn 1991). Non-canonical Hamiltonian systems are occasionally encountered in fluid mechanics (e.g. (Morrison 1998)). These systems remain Hamiltonian, and the paths of standing waves remain closed.

This demonstrates that the spatial variations of the polarization relations χ affects the ray trajectories in addition to the dispersion relation Ω . This effect is captured in the Berry curvature F , which is directly given by the derivatives of χ .

3. BERRY PHASE IN NORMAL MODES

Equations (39)-(40) describe the trajectory of a wavepacket for any given initial condition. The trajectories include those of standing waves in the star, which are the specific solutions that are periodic in time. The trajectory represents the radial oscillatory motion of the perturbation inside the star, bouncing between two turning points. These solutions correspond to closed trajectories $(z(\tau), k_z(\tau))$ in the phase space, traveled in a time $T = 2\pi/\omega$ satisfying the condition

$$\omega = \tilde{\Omega}(z, k_z), \quad (43)$$

such that the total phase of the wavepacket over one period is an integer multiple of 2π , i.e.

$$\Delta\phi = 2\pi(n + 1) = \frac{1}{\epsilon} \oint_{\Gamma_\omega} (k_z dz + \epsilon i \chi_0^\dagger \cdot d\chi_0) + \pi. \quad (44)$$

The last term π accounts for the two reflections at the turning points of the wave. Γ_ω represents the periodic trajectory in phase space that satisfies $\omega = \Omega(z, k_z)|_{(z, k_z) \in \Gamma_\omega}$ oriented clockwise. The integer n is chosen to correspond to the conventional radial order n used in asteroseismology.

Applying Stokes' theorem to the second term within the integral, one obtains

$$\oint_{\Gamma_\omega} k dz = \epsilon \left(2\pi \left(n + \frac{1}{2} \right) + \phi_B \right), \quad (45)$$

with

$$\phi_B \equiv \iint_{\Sigma_\omega} F dz dk_z, \quad (46)$$

where Σ_ω denotes the area of the phase space enclosed by Γ_ω . This procedure, which derives the normal modes from ray dynamics, is known as Bohr-Sommerfeld quantization in quantum physics. It introduces here ϕ_B referred to as the *geometric phase* or the *Berry phase* (Berry 1984). This term arises from the vectorial nature of the wave, which perturbs multiple fields simultaneously, with relative phases determined by χ_0 . In an inhomogeneous medium, the gradual change of this vector along the propagation causes the ray trajectory to bend, in addition to the variation of the dispersion relation Ω_0 (Perez et al. 2021). This phenomenon is captured by the terms proportional to the Berry curvature F in the ray-tracing equations (39)-(40) or equivalently, as the Berry phase

in the frequencies of the normal modes. We provide an explicit expression for F for acoustic and gravity waves in Appendix A.

Figure 1 shows that the Berry phase can play a significant role in determining low-order p -modes in the Sun. We numerically calculate the frequencies of the normal modes of oscillation for the standard model of the Sun (Christensen-Dalsgaard et al. 1996) directly from Eq. (6), and compare these results with those obtained using Duvall’s law, usual scalar theories, and the vectorial Bohr-Sommerfeld quantization that includes ϕ_B . Additionally, we compare the results with the available observational helioseismic data from GONG (Hill et al. 1996), which includes modes from $n = 4$ to $n = 22$ that have been observed at $\ell = 25$.

At high radial orders ($n \gtrsim 20$), all methods converge and agree within a relative error of approximately $\sim 1\%$. For low n instead, the prediction accounting for ϕ_B is the only method that achieves a comparable level of accuracy. Notably, Berry’s phase contributes significantly to the total frequency, accounting for 9% of the frequency of the $n = 0$ mode, and 7% of the frequency of the $n = 1$ mode. For these modes, it is found to be $\phi_B \simeq -0.71$ and $\phi_B \simeq -1.17$ respectively. The values of Berry curvature F for acoustic waves in the Sun are shown on Fig 2, as well as the $n = 0..10$ standing waves in phase space. We stress that a quantitative evaluation of the Berry phase should not assume the Cowling approximation in order to match the high level of modern observational precision.

Equation (45) is therefore satisfied by the pulsations ω of the standing waves for small ϵ , i.e for large degrees ℓ . In this limit, it gives the frequencies of the pulsations for any order n . The ray-tracing equations were derived for wavepackets with small spatial extensions, leaving the possibility that these equations are not guaranteed to hold for waves of low radial order n . However, the Bohr-Sommerfeld quantization holds for all n , as evidenced by numerical values obtained on Fig. 1. This effect has been identified in the past. For low n , the trajectories in phase space are close to the extremum of $\tilde{\Omega}(z, k_z)$, and as such are following the dynamics of a harmonic oscillator. Since Bohr-Sommerfeld quantization is exact for harmonic oscillators (Argyres 1965), the law appears valid in both the high- n and low- n limits, albeit for different reasons. The correction term should then still be Berry’s phase and is still accurate, even though it is not a slow change of the Hamiltonian anymore. We suspect a deeper underlying principle explains why the Bohr-Sommerfeld law applies universally, but this remains unclear at present.

4. DISCUSSION AND CONCLUSION

The Berry phase should not be confused with the so-called *phase function* $\alpha(\omega)$, which modifies Duvall’s law by accounting for corrections due to non-zero values of S in the dispersion relation Ω_0 , i.e at order ϵ^0 . The Berry phase is a first-order term in ϵ that arises from the polarization relations. Neglecting ϕ_B is equivalent to considering a scalar ray-tracing theory that propagates using the full dispersion relation in accounting for $\alpha(\omega)$.

Historically, the Berry phase was studied in system that slowly vary in time. Here, it manifests as the background quantities vary in space crossed by a propagating ray. Our results show that vectorial ray-tracing accounts for this phase, also sometimes called the holonomy (Simon 1983), as

well as a corrected dispersion relation $\omega = \tilde{\Omega}$.

The analytical expressions derived in this study enable the prediction of when and to what extent effects of geometric phase will be significant in stellar objects. We find here that the Berry curvature is significant at the surface as is shown on Fig. 2, a region where the pressure scale height is very short and where several phenomena are poorly modeled such as temperature gradients, significant non-adiabaticity and rapid convection (Gough 1990; Ball and Gizon 2014).

Other stellar situations are known to cause difficulties in normal modes computation, among which are found the problem of glitches in red giants (Cunha et al. 2015), rapidly rotating stars (Lignières and Georgeot 2009; Mirouh 2022) and magnetized stars (Loi 2020), where complex geometries and anisotropy complicate the study of normal modes, but ray-tracing equations remain directly applicable (Gough 1993). Two extensions should be performed to apply this study on these problems. Firstly, to adapt the formalism to low degrees $\ell \lesssim 3$ in the spirit of Roxburgh and Vorontsov (2000). Secondly, to extend the theory for ray-tracing of mixed modes, where frequencies of g -modes and p -modes take similar values, implying for the bands to be not well separated as occurs in red giants (Mosser et al. 2014).

Ray-tracing equations are successfully employed by local helioseismology, which examines point sources and time travels of waves at the solar surface (e.g. Gizon et al. 2010). Our findings suggest that these studies may be extended to cases where the ϵ^0 order lacks sufficient accuracy, such as for large-scale excitations.

We finally highlight that in this problem, the Berry curvature arises from two Berry-Chern monopoles with topological charges $\mathcal{C} = \pm 1$ situated at low ℓ values (Perrot et al. 2019; Leclerc et al. 2022). These sources of the Berry curvature impose that ϕ_B tends to $-|\mathcal{C}|\pi = -\pi$ for trajectories that encompass the entire phase space, which corresponds to large n . This amounts to subtracting $-1/2$ to $n + 1/2$ in the quantization law for high n .

Acknowledgments: The authors thank the anonymous referee for a thorough review, and Isabelle Baraffe for discussions on applications. AL is funded by Contrat Doctoral Spécifique Normaliens. GL acknowledges funding from ERC CoG project PODCAST No 864965. The scripts written to support our conclusions are available in the Zenodo dataset [10.5281/zenodo.14944308](https://doi.org/10.5281/zenodo.14944308).

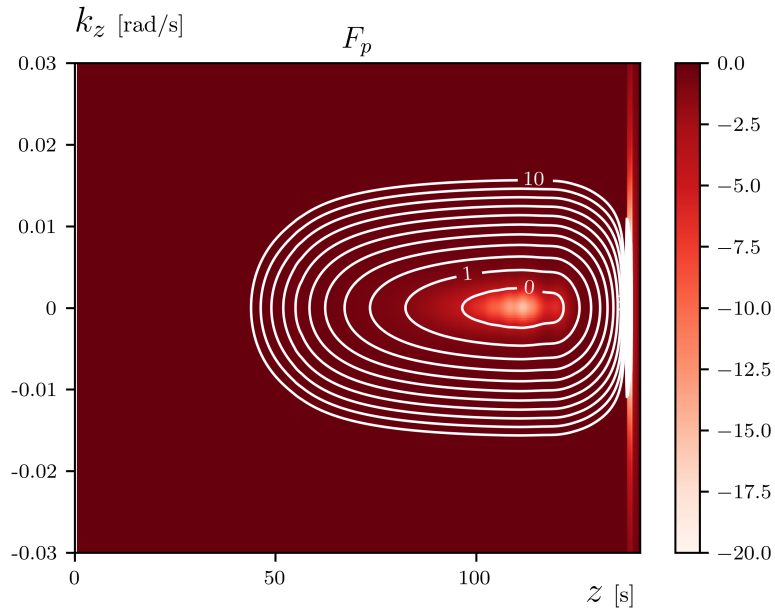


Figure 2. The phase-space trajectories of solar standing acoustic waves enclose a specific amount of Berry curvature F_p , which gives rise to the Berry phase. A sharp feature appears close to the surface ($z \sim 140$). Radial orders shown vary from $n = 0$ to $n = 10$ for $\ell = 25$.

REFERENCES

- Sarbani Basu. Global seismology of the Sun. *Living Reviews in Solar Physics*, 13(1):2, December 2016.
<https://doi.org/10.1007/s41116-016-0003-4>.
- Jørgen Christensen-Dalsgaard. Solar structure and evolution. *Living Reviews in Solar Physics*, 18(1):2, December 2021.
<https://doi.org/10.1007/s41116-020-00028-3>.
- Thomas L Duvall Jr. A dispersion law for solar oscillations. *nature*, 300(5889):242–243, 1982.
- Hiromoto Shibahashi. Modal analysis of stellar nonradial oscillations by an asymptotic method. *Publications of the Astronomical Society of Japan*, Vol. 31, p. 87-104 (1979), 31:87–104, 1979.
- Monique Tassoul. Asymptotic approximations for stellar nonradial pulsations. *Astrophysical Journal Supplement Series*, vol. 43, Aug. 1980, p. 469-490., 43:469–490, 1980.
- Franz-Ludwig Deubner and Douglas Gough. Helioseismology: Oscillations as a diagnostic of the solar interior. IN: *Annual review of astronomy and astrophysics*. Volume 22. Palo Alto, CA, Annual Reviews, Inc., 1984, p. 593-619., 22:593–619, 1984.
- J Christensen-Dalsgaard and F Pérez Hernández. The phase function for stellar acoustic oscillations-i. theory. *Monthly Notices of the Royal Astronomical Society*, 257(1):62–88, 1992.
- DO Gough. Ebk quantization of stellar waves. *Hydrodynamic and magnetodynamic problems in the Sun and stars*, page 117, 1986.
- D. O. Gough. Linear adiabatic stellar pulsation. In J. P. Zahn and J. Zinn-Justin, editors, *Astrophysical Fluid Dynamics - Les Houches 1987*, pages 399–560, January 1993.
- Shyeh Tjing Loi. Magneto-gravity wave packet dynamics in strongly magnetized cores of evolved stars. *Monthly Notices of the Royal Astronomical Society*, 493(4):5726–5742, 2020.
- F Hill, PB Stark, RT Stebbins, ER Anderson, HM Antia, TMea Brown, TL Duvall Jr, DA Haber, JW Harvey, DH Hathaway, et al. The solar acoustic spectrum and eigenmode parameters. *Science*, 272(5266):1292–1295, 1996.
- Armand Leclerc, Guillaume Laibe, Pierre Delplace, Antoine Venaille, and Nicolas Perez. Topological modes in stellar oscillations. *The Astrophysical Journal*, 940(1):84, 2022.

- Armand Leclerc, Lucien Jezequel, Nicolas Perez, Asmita Bhandare, Guillaume Laibe, and Pierre Delplace. Exceptional ring of the buoyancy instability in stars. *Physical Review Research*, 6(1):L012055, 2024.
- Nicolas Perez, Pierre Delplace, and Antoine Venaille. Manifestation of the berry curvature in geophysical ray tracing. *Proceedings of the Royal Society A*, 477(2248):20200844, 2021.
- Antoine Venaille, Yohei Onuki, Nicolas Perez, and Armand Leclerc. From ray tracing to waves of topological origin in continuous media. *SciPost Physics*, 14(4):062, 2023.
- Yohei Onuki. Quasi-local method of wave decomposition in a slowly varying medium. *Journal of Fluid Mechanics*, 883:A56, 2020.
- Robert G. Littlejohn and William G. Flynn. Geometric phases in the asymptotic theory of coupled wave equations. *Phys. Rev. A*, 44:5239–5256, Oct 1991.
<https://doi.org/10.1103/PhysRevA.44.5239>.
 URL <https://link.aps.org/doi/10.1103/PhysRevA.44.5239>.
- Philip J Morrison. Hamiltonian description of the ideal fluid. *Reviews of modern physics*, 70(2):467, 1998.
- Michael Victor Berry. Quantal phase factors accompanying adiabatic changes. *Proceedings of the Royal Society of London. A. Mathematical and Physical Sciences*, 392(1802):45–57, 1984.
- Jørgen Christensen-Dalsgaard, W Däppen, SV Ajukov, ER Anderson, HM Antia, Sea Basu, VA Baturin, G Berthomieu, B Chaboyer, SM Chitre, et al. The current state of solar modeling. *Science*, 272(5266):1286–1292, 1996.
- PN Argyres. The bohr-sommerfeld quantization rule and the weyl correspondence. *Physics Physique Fizika*, 2(3):131, 1965.
- Barry Simon. Holonomy, the quantum adiabatic theorem, and berry’s phase. *Physical Review Letters*, 51(24):2167, 1983.
- Douglas Gough. Comments on helioseismic inference. In Y. Osaki and H. Shibahashi, editors, *Progress of Seismology of the Sun and Stars*, pages 281–318, Berlin, Heidelberg, 1990. Springer Berlin Heidelberg. ISBN 978-3-540-46645-1.
- Warrick H Ball and Laurent Gizon. A new correction of stellar oscillation frequencies for near-surface effects. *Astronomy & Astrophysics*, 568:A123, 2014.
- MS Cunha, D Stello, PP Avelino, J Christensen-Dalsgaard, and RHD Townsend. Structural glitches near the cores of red giants revealed by oscillations in g-mode period spacings from stellar models. *The Astrophysical Journal*, 805(2):127, 2015.
- F Lignières and Bertrand Georgeot. Asymptotic analysis of high-frequency acoustic modes in rapidly rotating stars. *Astronomy & Astrophysics*, 500(3):1173–1192, 2009.
- Giovanni M Mirouh. Forward modelling and the quest for mode identification in rapidly rotating stars. *Frontiers in Astronomy and Space Sciences*, 9:952296, 2022.
- IW Roxburgh and SV Vorontsov. Semiclassical approximation for low-degree stellar p modes—ii. classical ray tracing. *Monthly Notices of the Royal Astronomical Society*, 317(1):151–157, 2000.
- Benoît Mosser, O Benomar, K Belkacem, MJ Goupil, N Lagarde, Etienne Michel, Yveline Lebreton, Dennis Stello, M Vrard, C Barban, et al. Mixed modes in red giants: a window on stellar evolution. *Astronomy & Astrophysics*, 572:L5, 2014.
- Laurent Gizon, Aaron C Birch, and Henk C Spruit. Local helioseismology: three-dimensional imaging of the solar interior. *Annual Review of Astronomy and Astrophysics*, 48(1):289–338, 2010.
- Manolis Perrot, Pierre Delplace, and Antoine Venaille. Topological transition in stratified fluids. *Nature Physics*, 15(8):781–784, 2019.

APPENDIX

A. EXPRESSIONS OF DISPERSION RELATIONS, POLARIZATIONS, AND BERRY CURVATURE

For acoustic waves, the dispersion relation at order ϵ^0 reads

$$\omega = \Omega_{0,p}(z, k_z) = \frac{1}{\sqrt{2}} \sqrt{k_z^2 + L_\ell^2 + N^2 + S^2 + \sqrt{(k_z^2 + L_\ell^2 + N^2 + S^2)^2 - 4N^2L_\ell^2}}. \quad (\text{A1})$$

Their normed polarization relations at order ϵ^0 are

$$\begin{pmatrix} v_h \\ v_r \\ \Theta \\ p \end{pmatrix} = \chi_{0,p} = \begin{pmatrix} \frac{1}{\Omega_{0,p}} L_\ell \\ \frac{\Omega_{0,p}}{\Omega_{0,p}^2 - N^2} (k_z + iS) \\ \frac{iN}{\Omega_{0,p}^2 - N^2} (k_z + iS) \\ 1 \end{pmatrix} \Bigg/ \left\| \begin{pmatrix} \frac{1}{\Omega_{0,p}} L_\ell \\ \frac{\Omega_{0,p}}{\Omega_{0,p}^2 - N^2} (k_z + iS) \\ \frac{iN}{\Omega_{0,p}^2 - N^2} (k_z + iS) \\ 1 \end{pmatrix} \right\|. \quad (\text{A2})$$

The expression of the Berry curvature for acoustic waves is

$$F_p(z, k_z) = \frac{1}{\left((k_z^2 + (L_\ell - N)^2 + S^2)(k_z^2 + (L_\ell + N)^2 + S^2) \right)^{3/2}} \left[\begin{aligned} & (k_z^2 + S^2 + L_\ell^2 + 3N^2)SL_\ell L'_\ell \\ & - (k_z^2 + S^2 + 3L_\ell^2 + N^2)SNN' \\ & - (k_z^2 + S^2 + L_\ell^2 + N^2)(L_\ell^2 - N^2)S' \end{aligned} \right]. \quad (\text{A3})$$

The three external parameters N, L_ℓ and S are functions of z and describe the stratified background. ' $'$ ' denotes the derivative with respect to z .

For internal gravity waves, the dispersion relation at order ϵ^0 reads

$$\omega = \Omega_{0,g}(z, k_z) = \frac{1}{\sqrt{2}} \sqrt{k_z^2 + L_\ell^2 + N^2 + S^2 - \sqrt{(k_z^2 + L_\ell^2 + N^2 + S^2)^2 - 4N^2L_\ell^2}}. \quad (\text{A4})$$

Their polarization relations at order ϵ^0 are

$$\begin{pmatrix} v_h \\ v_r \\ \Theta \\ p \end{pmatrix} = \chi_{0,g} = \begin{pmatrix} \frac{1}{\Omega_{0,g}} L_\ell \\ \frac{\Omega_{0,g}}{\Omega_{0,g}^2 - N^2} (k_z + iS) \\ \frac{iN}{\Omega_{0,g}^2 - N^2} (k_z + iS) \\ 1 \end{pmatrix} \Bigg/ \left\| \begin{pmatrix} \frac{1}{\Omega_{0,g}} L_\ell \\ \frac{\Omega_{0,g}}{\Omega_{0,g}^2 - N^2} (k_z + iS) \\ \frac{iN}{\Omega_{0,g}^2 - N^2} (k_z + iS) \\ 1 \end{pmatrix} \right\|. \quad (\text{A5})$$

The Berry curvature of internal gravity waves is given by

$$F_g = -F_p. \quad (\text{A6})$$

Mathematically, there are two additional wavebands: the acoustic and internal gravity waves with negative frequencies, making a total of four. The only differences are that their dispersion relations have the opposite sign of their positive counterparts, while their Berry curvatures remain unchanged.

Part IV

\mathcal{PT} symmetry and instabilities

\mathcal{PT} symmetry in waves and instabilities

Résumé

Tous les chapitres précédents discutent de topologie des ondes dans des situations *Hermitiennes*, c'est-à-dire dans des cas où elles conservent leur énergie : elles ne sont ni dissipées, ni instables. L'opérateur d'intérêt $\hat{\mathbf{H}}$ décrivant l'évolution à travers l'équation $i\partial_t \mathbf{X} = \hat{\mathbf{H}}\mathbf{X}$ est effectivement Hermitien, de sorte que l'énergie $\mathbf{X}^\dagger \cdot \mathbf{X}$ est une constante du mouvement. Le cadre est alors de topologie Hermitienne, qui est bien établi et bien compris. L'hypothèse d'hermiticité est cruciale pour le théorème d'index et donc de la correspondance bord-volume, et il ne tient pas pour les opérateurs non-Hermitiens. C'est le point de départ du domaine de recherche actuel qu'est la *topologie non Hermitienne*. Les opérateurs non Hermitiens ont des spectres riches et variés, et les liens éventuels entre des nombres topologiques et des propriétés spectrales ne sont pas encore tous évidents ni clairs. Une classe spéciale d'opérateurs obéit à une structure spectrale particulière : les opérateurs \mathcal{PT} -symétriques, qui ne changent pas lorsqu'on renverse simultanément le temps et l'espace.

Puisque la dissipation et les instabilités sont des phénomènes cruciaux en astrophysique, il est apparu important d'étudier si la topologie des ondes pouvait s'appliquer aussi à ces problèmes. Mais étant intrinsèquement non Hermitiens puisqu'ils affectent l'amplitude des perturbations, cela implique d'étudier de la topologie non Hermitienne. Ce chapitre présente des problèmes d'ondes et d'instabilités astrophysiques, qui se révèlent être \mathcal{PT} -symétriques, ou symétriques selon une symétrie analogue. Il se trouve que beaucoup d'instabilités et processus dissipatifs classiques sont symétriques selon de telles symétries. Il est montré que ces symétries structurent les répartitions d'énergie des modes instables / dissipés de manière particulière.

All of the chapters above discuss wave topology in *Hermitian* situations. That is, for waves which conserve their energy: they are not damped, nor are they unstable. In these situations, the operator of interest $\hat{\mathbf{H}}$ involved in the evolution equation $i\partial_t \mathbf{X} = \hat{\mathbf{H}}\mathbf{X}$ is indeed self-adjoint, in order to have the energy $\mathbf{X}^\dagger \cdot \mathbf{X}$ which is a constant of motion. The framework is then the one of *Hermitian topology*, which is well-understood and known. Indeed, it is a crucial assumption of the index theorem, which does not hold for non-Hermitian operators. This is the entry to a modern active field of research: *non-Hermitian topology*.

Non-Hermitian operators exhibit a wide variety of spectra, and the links between topological numbers and spectral features are not yet clear. However, a special class of non-Hermitian operators have special constraints which structure their spectrum: \mathcal{PT} -symmetric operators, which are invariant under a reflection in both time and space, hence the name.

As dissipation and instabilities are both crucially important phenomena in astrophysics, it was important to investigate if wave topology could apply to these situations as well. But being intrinsically non-Hermitian processes as they change the energy of perturbations, this implies dealing with non-Hermitian topology. This chapter presents astrophysical waves problems and instabilities which are \mathcal{PT} -symmetric - or symmetric under a similar symmetry. It just so happens that a lot of famous instabilities and dissipative processes are symmetric under one or several of these symmetries.

The results presented in this chapter have been published in *PT and anti-PT symmetry for astrophysical waves*, Leclerc, Laibe, Perez, Astronomy and Astrophysics 2024 [345]. The article is shown here, truncated of its appendices.

\mathcal{PT} and anti- \mathcal{PT} symmetries for astrophysical waves

Armand Leclerc^{1,*}, Guillaume Laibe¹, and Nicolas Perez¹

Univ Lyon, Univ Lyon1, Ens de Lyon
 CNRS, Centre de Recherche Astrophysique de Lyon UMR5574
 F-69230, Saint-Genis-Laval, France

Received September 15, 1996; accepted March 16, 1997

ABSTRACT

Context. Discrete symmetries have found numerous applications in photonics and quantum mechanics, but remain little studied in fluid mechanics, particularly in astrophysics.

Aims. We aim to show how \mathcal{PT} and anti- \mathcal{PT} symmetries determine the behaviour of linear perturbations in a wide class of astrophysical problems. They set the location of Exceptional Points in the parameter space and the associated transitions to instability, and are associated to the conservation of quadratic quantities that can be determined explicitly.

Methods. We study several classical local problems: the gravitational instability of isothermal spheres and thin discs, the Schwarzschild instability, the Rayleigh-Bénard instability and acoustic waves in dust-gas mixtures. We calculate the locations and the order of the Exceptional Points with a method of resultant, as well as the conserved quantities in the different regions of the parameter space using Krein theory.

Results. All problems studied here exhibit discrete symmetries, even though Hermiticity is broken by different physical processes (self-gravity, buoyancy, diffusion, drag). This analysis provides genuine explanations for certain instabilities, and for the existence of regions in the parameter space where waves do not propagate. Those correspond to breaking of \mathcal{PT} and anti- \mathcal{PT} symmetries respectively. Not all instabilities are associated to symmetry breaking (e.g. the Rayleigh-Benard instability).

Key words. Waves – Instabilities – Methods: analytical

1. Introduction

A large class of astrophysical systems, such as stars or discs, are often treated as fluids (e.g. Pringle and King 2007; Armitage 2010). The properties and the stability of the corresponding linear modes are usually analysed with methods that, to our knowledge, do not fully exploit the symmetries of the perturbed system with respect to parity \mathcal{P} and time \mathcal{T} .

Some of the most striking properties of \mathcal{PT} -symmetric systems emerged in the quantum physics community since the seminal paper by Bender and Boettcher (1998), the first non-Hermitian quantum Hamiltonian situation with a real spectrum, which paved the way to open quantum systems. This framework has been extended to situations exhibiting a spontaneous \mathcal{PT} symmetry breaking phase transition (Bender et al. 1999, 2002). Generalisations to quantum field theory have been developed in Bender et al. (2004) and considerations on the observables of such systems is found in Mostafazadeh and Batal (2004). \mathcal{PT} symmetry have been a particularly powerful tool in optics and photonics, where it has led to the development of novel designs with special properties. The analogy with quantum mechanics comes from the fact that beam dynamics is governed by a Schrödinger equation, where the optical index behaves as a complex potential, which can be designed to satisfy \mathcal{PT} symmetry (El-Ganainy et al. 2007; Makris et al. 2008). Klaiman et al. (2008) identified a spontaneous breaking of \mathcal{PT} symmetry in a waveguide. Musslimani et al. (2008) investigated the nonlinear propagation of optical solitons in \mathcal{PT} -symmetric refraction indexes. Guo et al. (2009); Rüter et al. (2010) made the first ob-

servations of \mathcal{PT} symmetry in optics with a complex index. A decade of developments of \mathcal{PT} symmetry in photonics lead to a multitude of applications (e.g. Feng et al. 2017; El-Ganainy et al. 2018; Özdemir et al. 2019). Feng et al. (2014) use spontaneous breaking of \mathcal{PT} symmetry to design a pure single-mode laser. Peng et al. (2014) propose a design for a low-power optical diode, where the nonlinear regime of the \mathcal{PT} symmetry induces non-reciprocal propagation. Lin et al. (2011); Regensburger et al. (2012); Feng et al. (2013) use \mathcal{PT} symmetry in periodic systems (through gratings, periodic crystals, or lattices) to design unidirectional invisibility. \mathcal{PT} -symmetric degeneracies are now used for their high resonant sensitivity in optical cavities (Hodaei et al. 2017). Similar interest has been aroused by the use of anti- \mathcal{PT} symmetry for novel optical designs (e.g. Ge and Türeci 2013; Zhang et al. 2020a,b). The topological properties of \mathcal{PT} -symmetric systems have recently been investigated in the context of fluid dynamics (Fu and Qin 2023). \mathcal{PT} and anti- \mathcal{PT} symmetries have only recently been taken into account in fluid systems, to directly constrain fluid flows and instabilities by spontaneous symmetry breaking (Qin et al. 2019; Fu and Qin 2020b; David et al. 2022). The \mathcal{PT} symmetry framework has been demonstrated to be particularly adapted to tackle high-dimensional parameter space (e.g. the drift wave instabilities in tokamaks, Qin et al. 2021). The richness underlying \mathcal{PT} -symmetric systems has thus been demonstrated unequivocally.

In this study, we aim to show that \mathcal{PT} and anti- \mathcal{PT} symmetries also control some of the properties of linear modes of astrophysical systems, such as instabilities or absence of propagation, stability exchange, conservation of quadratic quantities and this, for physical processes of different origins. We first define \mathcal{PT} and anti- \mathcal{PT} symmetries in Sect. 2. We then study how

* armand.leclerc@ens-lyon.fr

they condition the outcome of the linear analysis of four canonical astrophysical systems, namely the self-gravity instability in discs (Sect. 3), wave propagation in gas-dust mixtures (Sect. 6), and buoyancy instability in stellar (Sect. 4) and planetary interiors (Sect. 5). We then discuss these analyses in a broader perspective for symmetric systems in Sect. 7.

2. Definitions

2.1. \mathcal{PT} symmetry

The evolution of a monochromatic linear perturbation to the steady state of a fluid can be written under the form of an eigenvalue problem $H(a)X = \omega X$, where the operator H that describes the evolution of the perturbation depends continuously on some real parameter a . The complex eigenvalues are generically denoted by the frequency ω , which can be a complex number *a priori*. This problem is said to be \mathcal{PT} -symmetric if there exists a unitary operator U such that

$$UHU^{-1} = H^*, \quad (1)$$

where $*$ stands for complex conjugation. In this case, the eigenvalues go in pairs: if ω is an eigenvalue of the problem, so is ω^* . Indeed, $HX = \omega X$ implies $H(U^{-1}X^*) = \omega^*(U^{-1}X^*)$. In \mathcal{PT} -symmetric systems, unstable modes are therefore accompanied by damped modes (imaginary parts of opposite sign). When $\omega \neq \omega^*$, \mathcal{PT} symmetry is said to be *spontaneously broken* by H . By defining the symmetry operator $\mathcal{PT} \equiv U\Theta$ where Θ denotes complex conjugation, one has $[\mathcal{PT}, H] = 0$. The two operators commute, but do not share X as an eigenvector for non-real eigenvalues.

Mostafazadeh (2002a,b); Zhang et al. (2020c) showed that \mathcal{PT} symmetry is equivalent to another symmetry, pseudo-Hermiticity, for finite-dimensional problems. A problem described by the operator H is pseudo-Hermitian if there exists an Hermitian operator V such that

$$VHV^{-1} = H^\dagger, \quad (2)$$

where † denotes the Hermitian conjugate with respect to the appropriate Hermitian scalar product of the problem, which we will write \cdot in the following such that $Y_1 \cdot Y_2 \equiv Y_1^\top Y_2$.

Let X_1 and X_2 be two eigenvectors of H satisfying Eq.(2). The eigenvalues ω_1 and ω_2 may take the same value: they degenerate. When the eigenvectors also become identical, the degeneracy is called an Exceptional Point (noted EP in the following). The linear stability of these systems is described by Krein theory (Krein 1950; Kirillov 2013): in such systems, the transition between stability and instability necessarily involves the exceptional degeneracy of stable eigenvalues. This phenomenon is known as a Krein collision. Before the collision, the system is stable, ω_1 and ω_2 are real, \mathcal{PT} symmetry is said to be unbroken and the Krein quantities defined as $X_{1,2} \cdot VX_{1,2}$ are non-zero and of opposite signs. After the collision, the system is unstable, the complex frequencies $\omega_1 = \omega_2^*$ are complex conjugates of each other, and the two Krein quantities are necessarily zero. The Krein quantity $Y \cdot VY$ is a constant of motion of a general solution $Y(t, a)$ of the evolution equation $i\partial_t Y = H(a)Y$. Indeed,

$$i\partial_t(Y \cdot VY) = Y \cdot (-H^\dagger V)Y + Y \cdot VHY \quad (3)$$

$$= Y \cdot (VH - H^\dagger V)Y \quad (4)$$

$$= 0. \quad (5)$$

Hence,

$$Y \cdot VY = \text{cst}. \quad (6)$$

Moreover, for a Fourier mode $Y = e^{-i\omega t}X$, this conserved quantity is exactly zero for unstable and damped modes, and non-zero for propagative modes. This is shown by expressing

$$X \cdot VHX = X \cdot H^\dagger VX = \omega^* X \cdot VX \quad (7)$$

$$= \omega X \cdot VX. \quad (8)$$

According to the identity above, a situation where $\omega \neq \omega^*$ implies that $X \cdot VX = 0$.

2.2. Anti- \mathcal{PT} symmetry

The eigenvalue problem $H(a)X = \omega X$ is said to be anti- \mathcal{PT} -symmetric, or alternatively \mathcal{CP} -symmetric, if there exists a unitary operator \tilde{U} such that

$$\tilde{U}H\tilde{U}^{-1} = -H^*. \quad (9)$$

In this case, the eigenvalues come in pairs: ω and $-\omega^*$. They have equal imaginary parts, and opposite real parts and describe counter-propagating waves. In particular, H being anti- \mathcal{PT} -symmetric is equivalent for iH to be \mathcal{PT} -symmetric. The same equivalence between \mathcal{PT} symmetry and pseudo-Hermiticity then applies, and guarantees that an anti- \mathcal{PT} -symmetric operator H is also pseudo-chiral: there exist an Hermitian operator \tilde{V} such that

$$\tilde{V}H\tilde{V}^{-1} = -H^\dagger. \quad (10)$$

The quantity $X \cdot \tilde{V}X$ is not strictly a Krein quantity, and is not in general a constant of motion of a solution of $i\partial_t X = HX$. However, for a Fourier mode $Y = e^{-i\omega t}X$, it satisfies

$$Y \cdot \tilde{V}Y = e^{2i\text{Im}(\omega)t} X \cdot \tilde{V}X, \quad (11)$$

and is constant to zero for modes with $\text{Re}(\omega) \neq 0$, i.e for modes that spontaneously break the anti- \mathcal{PT} symmetry. Indeed,

$$X \cdot \tilde{V}HX = X \cdot (-H^\dagger \tilde{V})X = -\omega^* X \cdot \tilde{V}X \quad (12)$$

$$= \omega X \cdot \tilde{V}X. \quad (13)$$

One concludes that whenever $\omega \neq -\omega^*$, $X \cdot \tilde{V}X = 0$: the Krein quantity is zero at all times. An analogue of a Krein collision may occur. When the anti- \mathcal{PT} symmetry is unbroken, their exist a pair of eigenvalues of H denoted ω_1 and ω_2 which are purely imaginary.

Consider the situation in which the parameter a passes through an Exceptional Point, so that after the degeneracy we have $\omega_1 = -\omega_2^*$ with non-zero real parts. Then, the anti- \mathcal{PT} symmetry is spontaneously broken. This phenomenon corresponds to a Krein collision for the operator iH . It follows that the quantity $X \cdot \tilde{V}X$ is non-zero and not conserved for non-propagative modes, and strictly zero for propagating modes for all times. Systems that are both \mathcal{PT} and anti- \mathcal{PT} symmetric are called *bi-symmetric*.

The eigenvalues of bi-symmetric systems take the form of $(\omega, -\omega)$ pairs of real or purely imaginary frequencies. When ω is real, the associated eigenvector spontaneously breaks the anti- \mathcal{PT} symmetry. Conversely, when ω is imaginary, the associated eigenvector spontaneously breaks \mathcal{PT} symmetry. Thus, one of those two symmetries is necessarily broken for any value of the parameters a , and either $X \cdot VX = 0$ (broken \mathcal{PT}) or $X \cdot \tilde{V}X = 0$ (broken anti- \mathcal{PT}). In bi-symmetric systems, $X \cdot VX$ is always a constant of motion, while $X \cdot \tilde{V}X$ is constant only when it is zero, in the spontaneously broken anti- \mathcal{PT} symmetry phase.

3. Gravitational instabilities

3.1. Jeans instability

The stability of self-gravitating objects plays a central role in the formation of structures throughout the Universe. The simplest problem to study would be the Jeans instability of a collapsing sphere (Jeans 1902). We consider local radial adiabatic perturbations of a 3D homogeneous self-gravitating, non-rotating, inviscid sphere of constant density ρ_0 and sound speed c_s . Linear perturbations of mass and momentum conservation as well as Poisson equation form a 4×4 system that can be written after Fourier transforms in time and space

$$\omega \begin{pmatrix} \rho'/\rho_0 \\ v'/c_s \end{pmatrix} = H_J \begin{pmatrix} \rho'/\rho_0 \\ v'/c_s \end{pmatrix} \equiv \begin{pmatrix} 0 & c_s \mathbf{k}^\top \\ \left(1 - \frac{4\pi G \rho_0}{c_s^2 |k|^2}\right) c_s \mathbf{k} & 0 \end{pmatrix} \begin{pmatrix} \rho'/\rho_0 \\ v'/c_s \end{pmatrix}. \quad (14)$$

This problem is invariant under both parity and time reversal. It is therefore trivially \mathcal{PT} -symmetric, as can be proved by the statement $H_J = H_J^*$. As such, H_J is pseudo-Hermitian, with the symmetry operator $V = \text{diag}\left(\left(1 - \frac{4\pi G \rho_0}{c_s^2 |k|^2}\right), 1, 1, 1\right)$. The Krein quantity associated to the Krein collision of the Jeans instability is then $X \cdot V X = \left(1 - \frac{4\pi G \rho_0}{c_s^2 |k|^2}\right) |\rho'|^2 + |v'|^2$. This quantity is non-zero for propagating waves, and zero for the unstable modes. Complementarily, H_J is anti- \mathcal{PT} symmetric and pseudo-chiral. Indeed, it satisfies Eq. 10 for $\tilde{V} = \text{diag}\left(-\left(1 - \frac{4\pi G \rho_0}{c_s^2 |k|^2}\right), 1, 1, 1\right)$.

The quantity $X \cdot \tilde{V} X = -\left(1 - \frac{4\pi G \rho_0}{c_s^2 |k|^2}\right) |\rho'|^2 + |v'|^2$ is then zero for propagative modes and non-constant and non-zero for unstable modes. The Krein collision occurs at an Exceptional Point for which H cannot be diagonalised. This EP corresponds to marginal stability, which is reached at the Jeans wavenumber $|k| = k_J \equiv \sqrt{4\pi G \rho_0 / c_s}$. Longer wavelengths are unstable, and shorter wavelengths are propagating.

3.2. Toomre instability

More interesting is the case of a self-gravitating disc (Goodman and Narayan 1988; Goodman 2003; Bertin and Lodato 1999). In this system, \mathcal{P} and \mathcal{T} are broken individually, but the overall system of linear perturbations is still \mathcal{PT} -symmetric. Stabilization of large and small scales by rotation and pressure can be sufficient to stabilize astrophysical discs against gravitational collapse (Toomre 1964). We discuss here the simplest case of axisymmetric perturbations of short radial wavelengths evolving in a razor-thin Keplerian disc. The stability of linear perturbations is given by the celebrated Toomre criterion: $Q \equiv \frac{c_{s,k}}{\pi G \Sigma_0} > 1$, where κ denotes the epicyclic frequency of the disc and Σ_0 its surface density. The razor-thin disc is integrated vertically (Armitage 2010), to give the following set of radial linear perturbation

$$H_{\text{sgd}} \begin{pmatrix} h' \\ v'_r \\ v'_\phi \end{pmatrix} = \begin{pmatrix} 0 & c_s k & 0 \\ -\frac{k}{c_s} \left(\frac{2}{Q|k|} - 1\right) & 0 & 2i \\ 0 & -\frac{i}{2} & 0 \end{pmatrix} \begin{pmatrix} h' \\ v'_r \\ v'_\phi \end{pmatrix} = \omega \begin{pmatrix} h' \\ v'_r \\ v'_\phi \end{pmatrix}, \quad (15)$$

where we used perturbations of the enthalpy h' and the two horizontal velocities v'_r and v'_ϕ as variables, and the orbital time Ω^{-1} and the pressure length $c_s \Omega^{-1}$ as units of time and length.

With $U = \text{diag}(1, 1, -1)$, this problem satisfies Eq. (1) and is therefore \mathcal{PT} -symmetric. Rotation breaks the reflection symmetry in the azimuthal direction and the time reversal symmetry, but not the combination of both. It is expected that the system is pseudo-Hermitian, which can be shown explicitly. With

$$V = \begin{pmatrix} \frac{1}{c_s^2} & 0 & -\frac{4ik}{c_s Q|k|} \\ 0 & 1 & 0 \\ \frac{4ik}{c_s Q|k|} & 0 & 4\left(\frac{2|k|}{Q} + 1\right) \end{pmatrix}, \quad (16)$$

the system satisfies Eq. (2). The Krein quantity associated with this \mathcal{PT} symmetry provides the following energy partition, which applies to the unstable mode

$$X \cdot V X = 0 = \frac{|h'|^2}{c_s^2} + |v'_r|^2 + 4|v'_\phi|^2 \left(1 + \frac{2\pi G \Sigma_0}{\Omega^2} |k|\right) - \frac{8\pi G \Sigma_0}{c_s^2 \Omega} \text{sgn}(k) \text{Im}(hv_\phi^*), \quad (17)$$

where k denotes the wavenumber in dimensional form. We illustrate this result by computing numerically the value of this quantity through a Krein collision, since H_{sgd} has degenerated eigenvalues when $Q = \frac{2|k|}{1+k^2}$. These are the positions of Exceptional Points for H_{sgd} , which corresponds to positions of a Krein collision. The curve of Exceptional Points separates two regions in (Q, k) -space: one is the stable region, the other is the unstable region. Figure 1 shows the EPs curve and the Krein collision that occurs when crossing this curve.

In addition to being \mathcal{PT} -symmetric, H_{sgd} is also anti- \mathcal{PT} -symmetric since

$$\tilde{U} H_{\text{sgd}} \tilde{U}^{-1} = -H_{\text{sgd}}^*, \quad (18)$$

with $\tilde{U} = \text{diag}(1, -1, -1)$. The anti- \mathcal{PT} symmetry is complementary to the \mathcal{PT} symmetry, and the combination of the two symmetries implies that the eigenvalues always come in pairs: they are always opposite $(\omega, -\omega)$, either real or purely imaginary. They are never general complex numbers, a generic property for bi-symmetric systems, since one of the two symmetries is necessarily spontaneously broken.

One has

$$\tilde{V} H_{\text{sgd}} \tilde{V}^{-1} = -H_{\text{sgd}}^\dagger, \quad (19)$$

$$\tilde{V} \equiv \begin{pmatrix} \frac{1}{c_s^2} & 0 & -\frac{4ik(Q|k|-1)}{c_s Q|k|} \\ 0 & 1 & 0 \\ \frac{4ik(Q|k|-1)}{c_s Q|k|} & 0 & -\frac{8k^2}{Q|k|} + 8k^2 - 4 \end{pmatrix}. \quad (20)$$

Equation (20) explicitly shows that H_{sgd} is pseudo-chiral as expected, and Krein theory then applies. When iH_{sgd} has real eigenvalues, anti- \mathcal{PT} symmetry is unbroken, and the Krein quantities $X \cdot \tilde{V} X$ are non-zero. This holds when \mathcal{PT} -symmetry is spontaneously broken, i.e. in the unstable region of parameters, where the first Krein quantity $X \cdot V X$ is zero. Conversely, in the stable range, anti- \mathcal{PT} symmetry is broken and \mathcal{PT} symmetry is unbroken. In this case, $X \cdot \tilde{V} X$ is zero and $X \cdot V X$ is not equal to zero. The Krein quantity $X \cdot \tilde{V} X$ associated to the anti- \mathcal{PT} -symmetry gives the following energy distribution for propagating waves in dimensional form

$$X \cdot \tilde{V} X = \frac{|h'|^2}{c_s^2} + |v'_r|^2 + |v'_\phi|^2 \left(-4 + 8\left(\frac{c_s^2 k^2}{\Omega^2} - \frac{\pi G \Sigma_0}{\Omega^2} |k|\right)\right) - \frac{8\pi G \Sigma_0}{c_s^2 \Omega} \text{sgn}(k) \left(\frac{c_s^2}{\pi G \Sigma_0} |k| - 1\right) \text{Im}(hv_\phi^*). \quad (21)$$

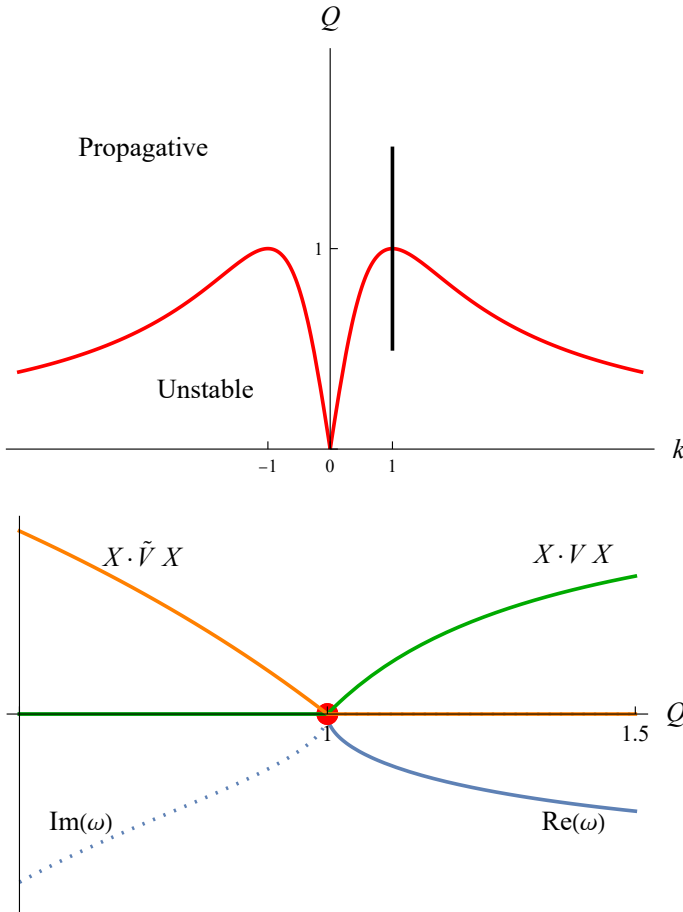


Fig. 1. Top panel : curve of Exceptional Points corresponding to marginal stability. Maximum is reached for $Q = 1$ as expected. Bottom panel : Krein collision of the stability of the Toomre problem when varying the parameters along the black line of the top panel. Depending on the value of Q , exactly one of the two Krein quantities identified is zero, depending on which symmetry is broken by the perturbation. The curve in green is $X \cdot VX$, orange is $X \cdot \tilde{V}X$, solid blue is $\text{Re}(\omega)$ and dotted blue is $\text{Im}(\omega)$, for a destabilizing mode.

Hence, for each mode, either $X \cdot VX$ or $X \cdot \tilde{V}X$ is necessarily zero: the former is zero for unstable modes and the latter is zero for propagating waves. Both are exactly zero at the degeneracy, i.e. for $\omega = 0$, which is true for $Q = \frac{2|k|}{1+k^2}$. Figure 1 shows this exchange in non-zero quantities when crossing the Krein collision. Krein quantities simply provide energy partitions of the system in both regimes.

The matrices V and \tilde{V} identified above are particular cases of more general families of matrices

$$V = \begin{pmatrix} \frac{2c_s(-2k^2 + (-1+k^2)Q|k|)a + k(-2+Q|k|)c}{4c_s^2kQ|k|} & b\frac{(kQ-2\text{sgn}k)}{2c_sQ} & ia \\ b\frac{(kQ-2\text{sgn}k)}{2c_sQ} & \frac{1}{4}(2c_ska + c) & ib \\ -ia & -ib & c \end{pmatrix}, \quad (22)$$

with a, b, c any real numbers such that $\det W \neq 0$. The matrix of Eq. (16) is recovered with $a = -\frac{4k}{c_sQ|k|}$, $b = 0$ and $c = \frac{8|k|}{Q} + 2$. Similarly,

$$\tilde{V} = \begin{pmatrix} \frac{2c_s(-2k^2 + (-1+k^2)Q|k|)a + k(-2+Q|k|)c}{4c_s^2kQ|k|} & b\frac{i(kQ-2\text{sgn}k)}{2c_sQ} & ia \\ -b\frac{i(kQ-2\text{sgn}k)}{2c_sQ} & -\frac{1}{4}(2c_ska + c) & b \\ -ia & b & c \end{pmatrix}$$

The matrix of Eq. (20) is recovered with $a = -\frac{4k(Q|k|-1)}{c_sQk}$, $b = 0$ and $c = -\frac{8}{Q}|k| + 8k^2 - 4$. The same remark holds for the different problems adressed in this study.

4. Buoyancy instability in stars

Consider a non-rotating star in static equilibrium, balanced by thermal pressure and self-gravity. The steady state is spherically symmetric, the density is stratified and decreases towards the surface. This equilibrium can be unstable, since a perturbation can be amplified by buoyancy if the square of the buoyancy frequency N^2 is negative, as given by the Schwarzschild criterion (Schwarzschild 1906).

This problem has been revisited by Leclerc et al. (2023) in inhomogeneous media, where the system proved to be pseudo-Hermitian and pseudo-chiral. Pseudo-Hermiticity was used to determine the Krein quantity. We will now complete the picture by determining the Krein quantity associated to pseudo-chirality, and show the Krein collision in this bi-symmetric problem. Neglecting the self-gravity of the perturbations (Cowling's approximation Cowling 1941), we start from Eq.5 of Leclerc et al. (2023), which is the eigenvalue equation

$$\omega X = H_b X, \quad (24)$$

$$H_b = \begin{pmatrix} 0 & 0 & 0 & L_\ell \\ 0 & 0 & |N| & K_r - iS \\ 0 & -|N| & 0 & 0 \\ L_\ell & K_r + iS & 0 & 0 \end{pmatrix} \quad (25)$$

where ω is the complex eigenfrequency of the perturbation, and $X \equiv (v \ w \ \Theta \ p)^\top$ contains the perturbation's horizontal velocity, radial velocity, entropy and pressure after appropriate rescaling. $N^2 \equiv -g \frac{d\ln\rho_0}{dr} - \frac{g^2}{c_s^2}$ is the square of the buoyancy frequency which is negative here, $S \equiv \frac{c_s}{2g} \left(N^2 - \frac{g^2}{c_s^2} \right) - \frac{1}{2} \frac{dc_s}{dr} + \frac{c_s}{r}$ is another characteristic frequency called the buoyant-acoustic frequency, which quantifies the coupling between g -modes and p -modes in asteroseismic problems, $L_\ell = \frac{c_s}{r} \sqrt{\ell(\ell+1)}$ is the Lamb frequency, K_r represents the local radial wavenumber of the wave (see Appendix E of Leclerc et al. (2023) for details). This problem is both pseudo-Hermitian and pseudo-chiral, and is associated with the two matrices

$$V = \text{diag}(1, 1, -1, 1), \quad (26)$$

$$\tilde{V} = \text{diag}(1, 1, 1, -1). \quad (27)$$

Krein theory can therefore be applied to determine how discrete symmetries constrain the partition of energy. $X \cdot X$ is generally not a conserved quantity, since H_b is not Hermitian. It grows exponentially for unstable modes and is conserved only for stable modes. However, $X \cdot VX$ is a constant of motion for any solution of $\partial_t X = H_b X$, as it has been shown in Sect.2.1. Moreover, this constant is exactly zero only for unstable modes. In contrast, $X \cdot \tilde{V}X$ also grows exponentially for unstable modes, but is constantly equal to zero for stable modes. As such,

$$X \cdot X = |v|^2 + |w|^2 + |\Theta|^2 + |p|^2 \propto e^{2\text{Im}(\omega)t}, \quad (28)$$

$$X \cdot VX = |v|^2 + |w|^2 - |\Theta|^2 + |p|^2 = \text{cst } \delta_{\text{Im}(\omega),0}, \quad (29)$$

$$X \cdot \tilde{V}X = |v|^2 + |w|^2 + |\Theta|^2 - |p|^2 \propto e^{2\text{Im}(\omega)t} \delta_{\text{Re}(\omega),0}, \quad (30)$$

where δ is the Kronecker delta.

For the radial modes $L_\ell = 0$, the modes degenerate over the ring

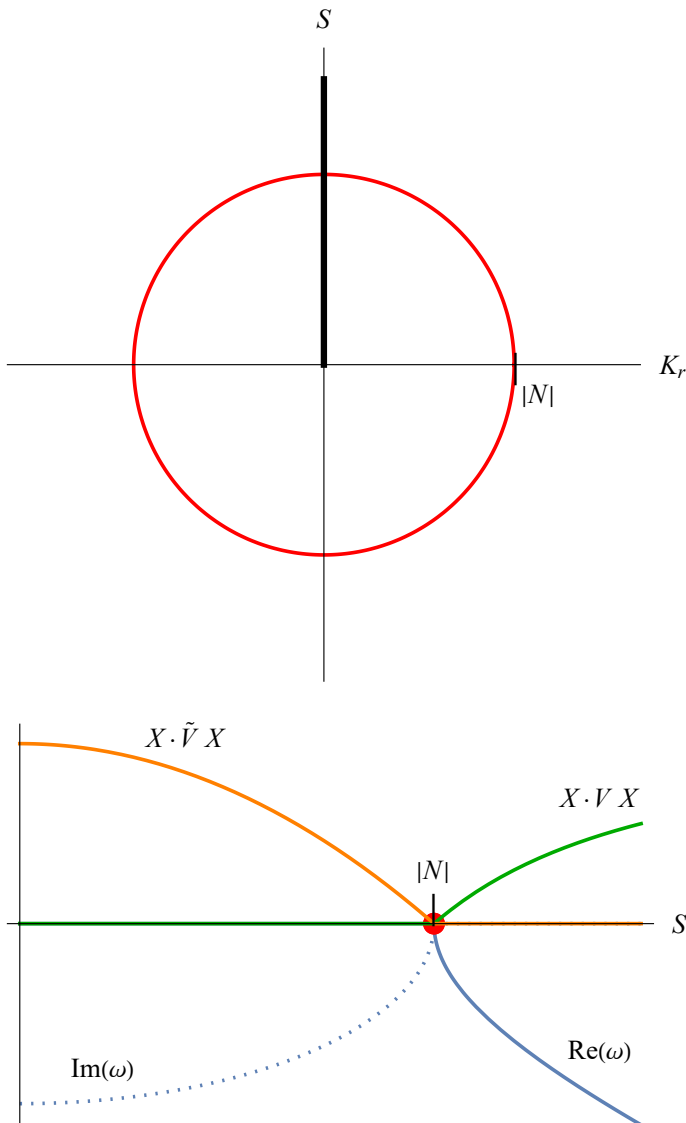


Fig. 2. Same as Fig. 1 for the Schwarzschild instability. Non-hermiticity is broken in this case by buoyancy instead of self-gravity.

parameterised by $K_r^2 + S^2 = -N^2 > 0$. These parameter values are Exceptional Points, as H_b can no longer be diagonalized there. The ring separates two ranges of parameters, the stable and the unstable part. Figure 2 shows the Krein quantities, over the ring of EPs in which the collision takes place. The Krein collision behaves as expected: inside the ring, the system is unstable, and $X \cdot V X$ is zero and $X \cdot \tilde{V} X$ is non-zero. Outside the ring, the modes are stable and propagate as sound waves, and $X \cdot V X$ is non-zero and $X \cdot \tilde{V} X$ is zero.

This structure is equivalent to the bi-symmetric problem of self-gravitating discs discussed in Sect. 3, and shown on Fig. 1, even if the physical situation is very different. The approach followed in this problem is the reverse of that followed in section 3 for the Toomre problem: it is easier to first establish that the system is pseudo-Hermitian and pseudo-chiral, since the matrices V and \tilde{V} have ± 1 on the diagonal.

5. Rayleigh-Bénard instability

Not all instabilities correspond to spontaneous symmetry breakings. The Rayleigh-Bénard instability (Bénard 1900; Rayleigh 1916) is such a case. Interiors of rocky planets are often treated as incompressible with both significant viscous and thermal diffusion (e.g. Bergé and Dubois 1984; Bodenschatz et al. 2000; Brandenburg 2021). This results in a regime of buoyancy instability that is controlled by diffusion effects and differs fundamentally from that discussed in Sect. 4 for adiabatic perturbations in compressible stars or planetary atmospheres. In the Rayleigh-Bénard regime, the instability criterion is given by the value of the Rayleigh number $Ra = g\alpha\beta L^4/\nu\kappa$, which needs to be greater than some critical value of order $10^2 - 10^3$ which depends on the boundary conditions. This famous problem admits analytical solutions for an homogeneous background configuration with rigid-lids isothermal boundary conditions, which provides an illustrative example in this study for discussing the symmetries involving diffusive effects.

The basic set of equations consists of the incompressibility condition, a Navier-Stokes equation, and thermal heat diffusion for a 2D (x, z) fluid (see Appendix A). The x -direction is invariant by translation and infinite, the z -direction is of length L , along which a constant temperature gradient $\partial_z T_0 = -\beta$ is directed. With dimensionless variables, the problem for Fourier modes $\exp(-i\omega t + ik_z z + ik_x x)$ can be converted into the symmetrical form

$$\omega \begin{pmatrix} \tilde{v}_z \\ \tilde{T} \end{pmatrix} = H_{RB} \begin{pmatrix} \tilde{v}_z \\ \tilde{T} \end{pmatrix}, \quad (31)$$

$$H_{RB} = -i \begin{pmatrix} k^2 & -\frac{k_x}{k} \left(\frac{Ra}{Pr}\right)^{1/2} \\ -\frac{k_x}{k} \left(\frac{Ra}{Pr}\right)^{1/2} & k^2/Pr \end{pmatrix}, \quad (32)$$

where $Pr = \nu/\kappa$ is the Prandtl number and $k = \sqrt{k_x^2 + k_z^2}$. This problem is anti- \mathcal{PT} -symmetric and pseudo-chiral, since one reads that

$$H_{RB} = -H_{RB}^* = -H_{RB}^\dagger, \quad (33)$$

for $Ra \geq 0$. In this case, the anti- \mathcal{PT} symmetry is protected and cannot be spontaneously broken since H_{RB} is anti-Hermitian (i.e. iH_{RB} is Hermitian). Indeed, the spectral theorem guarantees that the eigenvalues are purely imaginary and the eigenvectors are orthogonal to each other.

The location of EPs is given by

$$Ra = \left(1 - \frac{(1+Pr)^2}{4Pr}\right) \frac{(k_x^2 + k_z^2)^3}{k_x^2}, \quad (34)$$

which requires Ra to be negative. This condition can only be fulfilled for an inverted temperature gradient, which corresponds to a stably stratified liquid. In this case, the anti- \mathcal{PT} symmetry is no longer protected and can be broken spontaneously, which would lead to propagating, damped internal waves.

Anti-Hermiticity ensures that the eigenvalues $\omega = i\eta$ are purely imaginary for all k_x, k_z, Ra, Pr . The transition to instability is given by the change of sign $\eta < 0$ to $\eta > 0$. This necessarily occurs for $\omega = 0$, providing the marginal stability criterion for the Rayleigh-Bénard instability. This condition is satisfied when

$$Ra = \frac{(k_x^2 + k_z^2)^3}{k_x^2}, \quad (35)$$

whose minimum for each k_x, k_z compatible with the boundary conditions gives the critical value of the Rayleigh number (e.g. $Ra_c = \frac{27}{4}\pi^4$ for stress-free, impenetrable and isothermal boundaries). Figure 3 shows the regions of this problem.

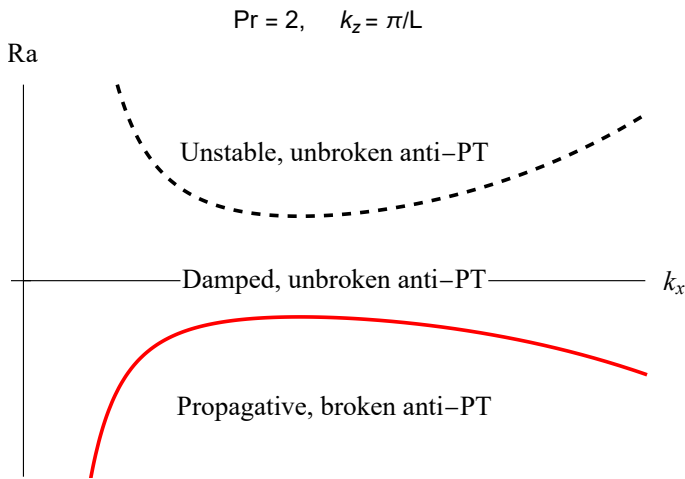


Fig. 3. Different regions of the Rayleigh-Bénard problem in the parameter space. In the upper part $\text{Ra} > 0$, anti- \mathcal{PT} symmetry is protected, frequencies are purely imaginary, the system exhibits an instability (black dashed) and no EPs. In the lower part $\text{Ra} < 0$, anti- \mathcal{PT} is no longer protected by anti-Hermiticity, and the system exhibits a curve of EP2s (red), delimiting a region where perturbations propagate. It is a region where anti- \mathcal{PT} symmetry is spontaneously broken.

6. Waves in dusty mixtures

Mixtures of pressureless dust and inviscid non-magnetised gas are generically used to model basic hydrodynamical properties of the dusty interstellar medium (e.g. Saffman 1962; Baines et al. 1965; Ahuja 1973; Gumerov et al. 1988). Exchange of momentum between gas and dust is modeled as a drag force proportional to the difference in their velocities. The DUSTYWAVE problem consist of studying the propagation of a 1D acoustic wave in an homogeneous dusty medium. The question is whether small disturbances propagate or are simply attenuated, since both regimes are possible (e.g. Laibe and Price 2011; David-Cléris and Laibe 2021). The mixture is initially homogeneous and at rest. Looking for small perturbative solutions as Fourier modes $\exp(i(\omega t - kx))$, one obtains the eigenvalue equation

$$H_{\text{dw}}X = \omega X, \quad (36)$$

$$H_{\text{dw}} \equiv \begin{pmatrix} 0 & 0 & k & 0 \\ 0 & 0 & 0 & k \\ k & 0 & i\epsilon & -i(1-\epsilon) \\ 0 & 0 & -i\epsilon & i(1-\epsilon) \end{pmatrix}, \quad (37)$$

after appropriate rescaling and choice of dimensionless parameters given in App. B. The operator H_{dw} formally depends on two parameters: the wavenumber k and the dust density fraction of the mixture ϵ . H_{dw} satisfies Eq. (9) with $\tilde{U} = \text{diag}(1, 1, -1, -1)$, meaning that H_{dw} is anti- \mathcal{PT} -symmetric. This property stems from the reflection symmetry $x \mapsto -x$ of the fluid in physical space, as it has been shown generically by David et al. (2022). Hence, the eigenvalues of H_{dw} are either imaginary or consist of pairs of complex numbers with opposite real parts. In parameter space, the transition between propagating and non-propagating regions must then be an Exceptional Points at which the solution of two counter-propagating waves degenerates.

The characterization of these EPs is carried out according to the procedure described in Delplace et al. (2021) (see App. C for details). Exceptional Points of order 2 (or EP2s) are located on a manifold of dimension 1 in the parameter space (k, ϵ) , which is a curve in a plane. Values of (k, ϵ) for which an eigenvalue has a multiplicity of two are characterized by the fact that the

characteristic polynomial $P(X)$ of H_{dw} has a root of multiplicity two. Such a root is therefore also a root of its derivative $P'(X)$, which means that the resultant $R_1 \equiv \mathcal{R}(P, P')$ between the two polynomials is 0. The resultant between two polynomials only cancels out if they have a common root. Since H_{dw} is anti- \mathcal{PT} -symmetric, R_1 is a real quantity. The values of (k, ϵ) , for which $R_1 = 0$, therefore define a curve. We calculate

$$R_1 = -4k^6(\epsilon - 1)^2 \left(1 + k^4 - \epsilon + k^2(2 + 9\epsilon(-1 + \frac{3}{4}\epsilon)) \right), \quad (38)$$

and show on Fig. 4 the curve $R_1 = 0$ (top panel, red). This curves provide a simple alternative derivation of the result of David-Cléris and Laibe (2021). Non-propagating waves exist for $\epsilon > 8/9$, which is indeed the minimum of the curve of EPs.

Interestingly, in addition to the EP2s, the above method reveals the existence of Exceptional Points of order 3 for which three eigenvectors merge. These EP3s form a fold of dimension 0, which are two points in (k, ϵ) space. These two points are located at

$$k = \pm \frac{1}{\sqrt{3}}, \quad \epsilon = \frac{8}{9}, \quad (39)$$

which are the points at which the curve of the EP2s loses its regularity. At these EP3s, H_{dw} has only two eigenvectors corresponding to the two eigenvalues 0 and $\frac{-i}{3}$. We note that these EP3s carry topological charges, also called winding numbers W_3 ,

$$W_3|_{\text{EP3}_1} = +1, \quad W_3|_{\text{EP3}_2} = -1, \quad (40)$$

where EP3₁ is the point $(k, \epsilon) = (+\frac{1}{\sqrt{3}}, \frac{8}{9})$ and EP3₂ is the point $(k, \epsilon) = (-\frac{1}{\sqrt{3}}, \frac{8}{9})$ (see App. D). The question of connecting these topological charges to edge modes or particular global modes remains open (e.g. Leclerc et al. 2023).

According to the discussion in Sect. 2.2, H_{dw} must be pseudo-chiral. The operator \tilde{V} can be found explicitly

$$\tilde{V} = \begin{pmatrix} \epsilon & \epsilon - 1 & ik & 0 \\ \epsilon - 1 & \frac{(\epsilon-1)^2}{\epsilon} & 0 & -\frac{ik(\epsilon-1)}{\epsilon} \\ -ik & 0 & 0 & 0 \\ 0 & \frac{ik(\epsilon-1)}{\epsilon} & 0 & 0 \end{pmatrix}. \quad (41)$$

$$(42)$$

As has been shown, pseudo-chirality implies that if $\omega \neq -\omega^*$, the quantity $X \cdot \tilde{V}X$ must be zero. This condition is fulfilled when sound propagates. Although the system is not conservative, it still possesses an associated Krein quantity $X \cdot \tilde{V}X$

$$X \cdot \tilde{V}X = \frac{1-\epsilon}{\epsilon} |\rho_d|^2 + \frac{\epsilon}{1-\epsilon} |\rho_g|^2 - 2 \left(\text{Re}(\rho_g \rho_d) - k \frac{\rho_0}{c_s} \text{Im}(\rho_g v_g^* + \rho_d v_d^*) \right), \quad (43)$$

where $\rho_0 = \rho_{g,0} + \rho_{d,0}$ is the total background density. $X \cdot \tilde{V}X$ must be zero for propagating waves and non-zero for non-propagating waves. Figure 4 shows the numerical confirmation of this result. $X \cdot \tilde{V}X$ is only a constant of motion if it is zero, i.e. only for sound waves. Another technique, where the anti- \mathcal{PT} operator is diagonalized, can be used to extract constants of motions in the unbroken phase, as it is done on the Kelvin-Helmholtz instability by Qin et al. (2019) (see App. E for details).

Finally, it should be noted that in a monofluid description of the mixture, the variables are $\rho = \rho_g + \rho_d$, $v = \rho_g v_g + \rho_d v_d$, $\frac{\rho_d}{\rho_g}$

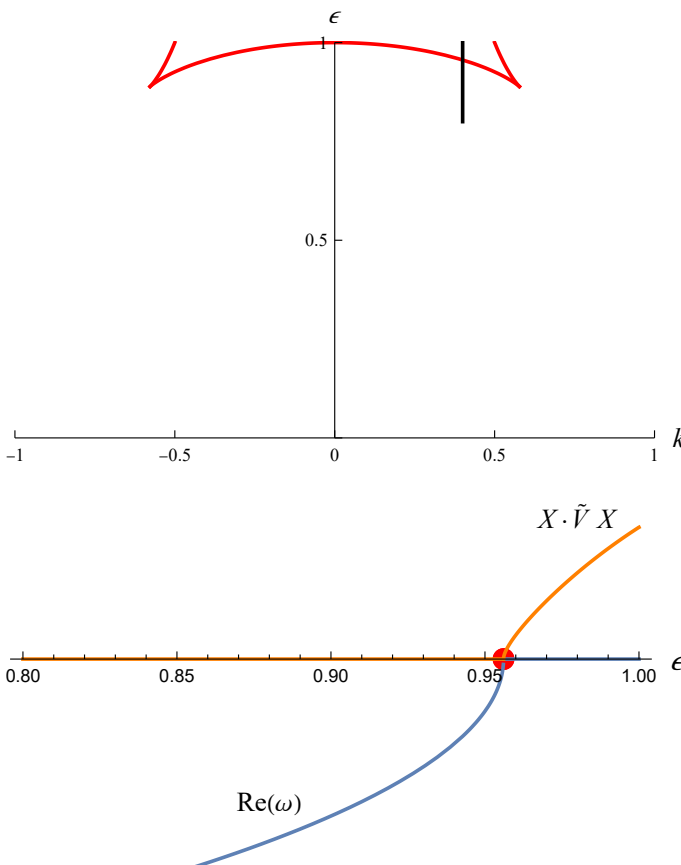


Fig. 4. Same as Fig. 1 for the DUSTYWAVE problem. For $k = 0.4$, the Krein quantity $X \cdot \tilde{V} X$ is represented as a function of ϵ . This Krein quantity provides a quadratic constant of motion for dusty sound waves in the propagating phase (low ϵ).

$\Delta v = v_d - v_g$ (Laibe and Price 2014). If the perturbed quantities are denoted by $'$, the Krein quantity that cancels out for propagating perturbations is

$$X \cdot \tilde{V}_{\text{mono}} X = \frac{(1-\epsilon)^3}{\epsilon} \left| \left(\frac{\rho_d}{\rho_g} \right)' \right|^2 + 2k \text{Im} \left((1-\epsilon)^2 \left(\frac{\rho_d}{\rho_g} \right)' \Delta v^* + \frac{\rho'}{\rho_0} v'^* \right).$$

It is associated with the symmetry operator

$$\tilde{V}_{\text{mono}} = \begin{pmatrix} 0 & 0 & -ik & 0 \\ 0 & \frac{(\epsilon-1)^3}{\epsilon} & 0 & -ik(\epsilon-1)^2 \\ ik & 0 & 0 & 0 \\ 0 & ik(\epsilon-1)^2 & 0 & 0 \end{pmatrix}. \quad (44)$$

Squire and Hopkins (2018) have shown that when grains are additionally streaming through the gas, a generic resonant drag instability develops in the mixture. The system is neither \mathcal{PT} nor anti- \mathcal{PT} symmetric and Krein theory can not be applied directly. The instability comes from a more complex mechanism where a resonance occurs between an anti- \mathcal{PT} symmetric correction due to drag to a leading \mathcal{PT} symmetric perturbation that arises from the streaming (e.g. Zhuravlev 2019; Magnan et al. 2024). Analysis of these problems from the point of view of discrete symmetries requires further specific studies.

7. Gravitational instability of a dusty disc

To our knowledge, there are still no theoretical predictions about what happens when systems with different discrete symmetries

are combined. To illustrate this, we consider a final example, drawing on the analysis of Longarini et al. (2022), which deals with the gravitational instability of a dusty razor-thin disc. In the context of planet formation, the aim is to quantify the ways in which dust can favor the local collapse of gas or even clump itself into planetary embryos. This problem is a combination of the two problems presented in Sect. 3 and Sect. 6 and as such, is of order 6. With the notations used above, the matrix of linear perturbation in the local shearing box is

$$H_{\text{sgd}} = \begin{pmatrix} 0 & ik\Sigma_g & 0 & 0 & 0 & 0 \\ -ik \left(\frac{2\pi G}{|k|} - \frac{c_g^2}{\Sigma_g} \right) & \frac{\epsilon}{t_s} & -2\Omega & -\frac{2i\pi Gk}{|k|} & -\frac{\epsilon}{t_s} & 0 \\ 0 & -2B & \frac{\epsilon}{t_s} & 0 & 0 & -\frac{\epsilon}{t_s} \\ 0 & 0 & 0 & 0 & ik\Sigma_d & 0 \\ -\frac{2i\pi Gk}{|k|} & -\frac{1}{t_s} & 0 & -ik \left(\frac{2\pi G}{|k|} - \frac{c_d^2}{\Sigma_d} \right) & \frac{1}{t_s} & -2\Omega \\ 0 & 0 & -\frac{1}{t_s} & 0 & -2B & \frac{1}{t_s} \end{pmatrix}, \quad (45)$$

where Ω is the orbital frequency and B is the local Oort parameter. c_g and c_d denote the sound speeds of the gas and dust respectively. Time and lengths are rescaled to the stopping time t_s and the stopping length $c_g t_s$. The characteristic polynomial of the system is of order 5, so that the roots $\omega(k)$ cannot be determined analytically. In the regime of weak drag, Longarini et al. (2022) determines the marginal stability numerically.

On the other hand, this problem is \mathcal{PT} -symmetric, with the operator $U = \text{diag}(-1, 1, 1, -1, 1, 1)$. The marginal stability curve is therefore a curve of EPs that corresponds to the spontaneous breaking of \mathcal{PT} symmetry. From the analysis above, its exact expression is

$$\mathcal{R}_{\text{sgd}}(P, P') = 0, \quad (46)$$

a polynomial of high order with respect to the parameters of the problem. The explicit expression of Eq. (46) extends over two pages and is given in the worksheet in the Acknowledgements. Hence, from a general perspective, the \mathcal{PT} -symmetric characterization of a marginal stability criterion allows to derive directly its analytical expression, albeit cumbersomely, without approximations relying on asymptotically strong or weak drag regimes. Following Qin et al. (2021), this astrophysical example shows that the analysis of discrete symmetries therefore provides a powerful way to make analytical predictions about the marginal stability of symmetric systems with high dimensionalities.

8. Conclusion

For several astrophysical objects, the properties of the small perturbations around the equilibrium are controlled by discrete symmetries, such as the \mathcal{PT} symmetry or the anti- \mathcal{PT} symmetry. For example, we show that such symmetries are relevant for

- The stability of isothermal spheres and thin self-gravitating disc: the Jeans and the Toomre problem are bi-symmetric due to self-gravity.
- The propagation of waves and the onset of convection in stratified fluids for compressible and adiabatic perturbations: the Schwarzschild problem is bi-symmetric due to buoyancy.
- The propagation of waves and the onset of convection in stratified fluids for incompressible and diffusive perturbations: the Rayleigh-Bénard problem is anti- \mathcal{PT} -symmetric due to diffusion, as well as anti-Hermitian.

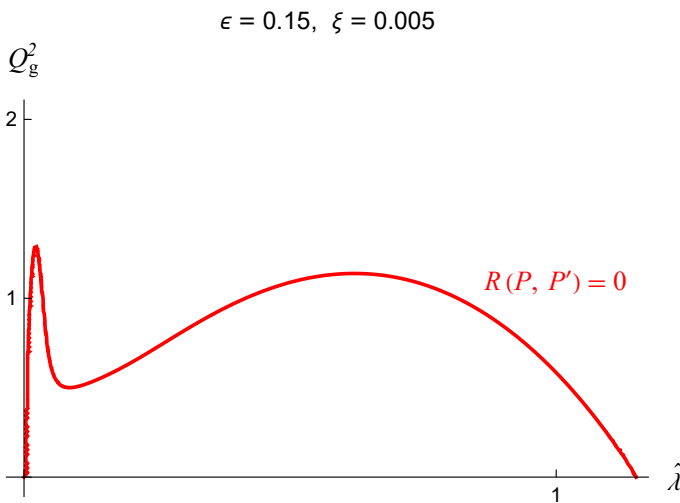


Fig. 5. Exceptional Points of the dusty self-gravitating disk are a consequence of the spontaneous breaking of \mathcal{PT} symmetry. The equation $R(P, P') = 0$ is obtained analytically with a resultant method, reproducing the results of Longarini et al. (2022).

- The propagation of a wave in a dust-gas mixture: the DUSTYWAVE problem is anti- \mathcal{PT} symmetric due to drag.

In these systems, the parameter space can be divided into different regions, in which the discrete symmetries are either broken or not. These regions are separated by Exceptional Points (EPs) for which the system of linear perturbation can no longer be diagonalised.

From a methodology perspective, the analysis of discrete symmetries allows when relevant to determine directly physical quantities that may be harder to obtain alternatively:

- The location of the EPs in the parameter space can be determined analytically from the symmetries without knowing the dispersion relation. This method is particularly effective for systems with high dimensions, where the dispersion relations may be untractable for analytical techniques, as in the case of the dusty self-gravitating disc.
- Krein theory then makes it possible to directly determine the exchange of stability when EPs are crossed, as well as the partition of energy enforced by Krein invariants associated with the discrete symmetries, even for dissipative systems.

Some of these EPs can be of high order and carry topological charges, as this is the case for the DUSTYWAVE problem. Note that not all physical systems allow such discrete symmetries. In particular, their spontaneous breaking is not a necessary condition for the system to be linearly unstable, as the Rayleigh-Bénard problem shows. We have focused here on the analysis of local stability, which applies to homogeneous systems. The study of global modes for inhomogeneous systems requires an extension of the Wigner-Weyl framework to non-Hermitian systems (e.g. Onuki 2020; Perez et al. 2021, 2022; Perez 2022; Leclerc et al. 2023).

Acknowledgements

We thank T. David-Cléris, E. Lynch, C. Longarini, P. Delplace, S. Labrosse and Y. Ricard for stimulating discussions and comments. We thank the conference STAR@LYON for stimulation of this study. GL, AL and NP acknowledge the support of the European Research Council (ERC) CoG project PODCAST No.

864965. AL is funded by Contrat Doctoral Spécifique Normalien. We have used MATHEMATICA (Wolfram Research Inc. 2021), worksheets can be found at <https://github.com/ArmandLeclerc/PTsymInAstroWaves>.

References

- Avtar S Ahuja. Wave equation and propagation parameters for sound propagation in suspensions. *Journal of Applied Physics*, 44(11):4863–4868, 1973.
- Philip J. Armitage. *Astrophysics of Planet Formation*. Cambridge University Press, 2010.
- MJ Baines, IP Williams, AS Asebiomo, and RL Agacy. Resistance to the motion of a small sphere moving through a gas. *Monthly Notices of the Royal Astronomical Society*, 130(1):63–74, 1965.
- Henri Bénard. Les tourbillons cellulaires dans une nappe liquide. *Revue Gen. Sci. Pure Appl.*, 11:1261–1271, 1900.
- Carl M. Bender and Stefan Boettcher. Real spectra in non-hermitian hamiltonians having pt symmetry. *Phys. Rev. Lett.*, 80:5243–5246, Jun 1998. URL <https://link.aps.org/doi/10.1103/PhysRevLett.80.5243>.
- Carl M. Bender, Stefan Boettcher, and Peter N. Meisinger. PT-symmetric quantum mechanics. *Journal of Mathematical Physics*, 40(5):2201–2229, May 1999. ISSN 0022-2488.
- Carl M. Bender, Dorje C. Brody, and Hugh F. Jones. Complex Extension of Quantum Mechanics. *Physical Review Letters*, 89(27):270401, December 2002.
- Carl M. Bender, Dorje C. Brody, and Hugh F. Jones. Extension of \mathcal{PT} -symmetric quantum mechanics to quantum field theory with cubic interaction. *Physical Review D*, 70(2):025001, July 2004.
- P Bergé and M Dubois. Rayleigh-bénard convection. *Contemporary Physics*, 25(6):535–582, 1984.
- G. Bertin and G. Lodato. A class of self-gravitating accretion disks. *A&A*, 350:694–704, October 1999.
- Eberhard Bodenschatz, Werner Pesch, and Guenter Ahlers. Recent developments in rayleigh-bénard convection. *Annual review of fluid mechanics*, 32(1):709–778, 2000.
- Axel Brandenburg. Lecture 4: Rayleigh-bénard problem. http://norlx51.nordita.org/~brandenb/teach/AdvAstroFluids/4_Convection/notes.pdf, 2021.
- Thomas G Cowling. The non-radial oscillations of polytropic stars. *Monthly Notices of the Royal Astronomical Society*, Vol. 101, p. 367, 101:367, 1941.
- Tomos W. David, Pierre Delplace, and Antoine Venaille. How do discrete symmetries shape the stability of geophysical flows? *Physics of Fluids*, 34(5):056605, May 2022. ISSN 1070-6631.
- Timothée David-Cléris and Guillaume Laibe. Large dust fractions can prevent the propagation of soundwaves. *Monthly Notices of the Royal Astronomical Society*, 504(2):2889–2894, 2021.
- Pierre Delplace, Tsuneya Yoshida, and Yasuhiro Hatsugai. Symmetry-protected multifold exceptional points and their topological characterization. *Physical Review Letters*, 127(18):186602, 2021.
- R. El-Ganainy, K. G. Makris, D. N. Christodoulides, and Ziad H. Musslimani. Theory of coupled optical PT-symmetric structures. *Optics Letters*, 32(17):2632–2634, September 2007. ISSN 1539-4794.
- Ramy El-Ganainy, Konstantinos G. Makris, Mercedeh Khajavikhan, Ziad H. Musslimani, Stefan Rotter, and Demetrios N. Christodoulides. Non-Hermitian physics and PT symmetry. *Nature Physics*, 14(1):11–19, January 2018. ISSN 1745-2481.
- Liang Feng, Ye-Long Xu, William S. Fegadolli, Ming-Hui Lu, José E. B. Oliveira, Vilson R. Almeida, Yan-Feng Chen, and Axel Scherer. Experimental demonstration of a unidirectional reflectionless parity-time metamaterial at optical frequencies. *Nature Materials*, 12(2):108–113, February 2013. ISSN 1476-4660.
- Liang Feng, Zi Jing Wong, Ren-Min Ma, Yuan Wang, and Xiang Zhang. Single-mode laser by parity-time symmetry breaking. *Science*, 346(6212):972–975, November 2014.
- Liang Feng, Ramy El-Ganainy, and Li Ge. Non-Hermitian photonics based on parity-time symmetry. *Nature Photonics*, 11(12):752–762, December 2017. ISSN 1749-4893.
- Yichen Fu and Hong Qin. The physics of spontaneous parity-time symmetry breaking in the kelvin-helmholtz instability. *New Journal of Physics*, 22(8):083040, 2020a.
- Yichen Fu and Hong Qin. The physics of spontaneous parity-time symmetry breaking in the Kelvin-Helmholtz instability. *New Journal of Physics*, 22(8):083040, August 2020b. ISSN 1367-2630.
- Yichen Fu and Hong Qin. Topological modes and spectral flows in inhomogeneous PT-symmetric continuous media, September 2023.
- Li Ge and Hakan E Türeci. Antisymmetric pt-photonic structures with balanced positive-and negative-index materials. *Physical Review A*, 88(5):053810, 2013.

- Jeremy Goodman. Self-gravity and quasi-stellar object discs. *Monthly Notices of the Royal Astronomical Society*, 339(4):937–948, 2003.
- Jeremy Goodman and Ramesh Narayan. The stability of accretion tori—iii. the effect of self-gravity. *Monthly Notices of the Royal Astronomical Society*, 231(1):97–114, 1988.
- NA Gumerov, AI Ivandaev, and RI Nigmatulin. Sound waves in monodisperse gas-particle or vapour-droplet mixtures. *Journal of Fluid Mechanics*, 193:53–74, 1988.
- A. Guo, G. J. Salamo, D. Duchesne, R. Morandotti, M. Volatier-Ravat, V. Aimez, G. A. Siviloglou, and D. N. Christodoulides. Observation of $\mathcal{P}\mathcal{T}$ -Symmetry Breaking in Complex Optical Potentials. *Physical Review Letters*, 103(9):093902, August 2009.
- Hossein Hodaei, Absar U Hassan, Steffen Wittek, Hipolito Garcia-Gracia, Ramy El-Ganainy, Demetrios N Christodoulides, and Mercedeh Khajavikhan. Enhanced sensitivity at higher-order exceptional points. *Nature*, 548(7666):187–191, 2017.
- James Hopwood Jeans. I. the stability of a spherical nebula. *Philosophical Transactions of the Royal Society of London. Series A, Containing Papers of a Mathematical or Physical Character*, 199(312-320):1–53, 1902.
- Oleg N Kirillov. Nonconservative stability problems of modern physics. In *Nonconservative Stability Problems of Modern Physics*. de Gruyter, 2013.
- Shachar Klaiman, Uwe Günther, and Nimrod Moiseyev. Visualization of Branch Points in $\mathcal{P}\mathcal{T}$ -Symmetric Waveguides. *Physical Review Letters*, 101(8):080402, August 2008.
- MG Krein. A generalization of some investigations on linear differential equations with periodic coefficients. In *Dokl. Akad. Nauk SSSR A*, volume 73, page 445, 1950.
- Guillaume Laibe and Daniel J. Price. dustybox and dustywave: two test problems for numerical simulations of two-fluid astrophysical dust–gas mixtures. *Monthly Notices of the Royal Astronomical Society*, 418(3):1491–1497, 12 2011. ISSN 0035-8711. URL <https://doi.org/10.1111/j.1365-2966.2011.19291.x>.
- Guillaume Laibe and Daniel J Price. Dusty gas with one fluid. *Monthly Notices of the Royal Astronomical Society*, 440(3):2136–2146, 2014.
- Armand Leclerc, Lucien Jezequel, Nicolas Perez, Asmita Bhandare, Guillaume Laibe, and Pierre Delplace. The exceptional ring of buoyancy instability in stars, 2023.
- Zin Lin, Hamidreza Ramezani, Toni Eichelkraut, Tsampikos Kottos, Hui Cao, and Demetrios N. Christodoulides. Unidirectional Invisibility Induced by $\mathcal{P}\mathcal{T}$ -Symmetric Periodic Structures. *Physical Review Letters*, 106(21):213901, May 2011.
- Cristiano Longarini, Giuseppe Lodato, Giuseppe Bertin, and Philip J Armitage. The role of the drag force in the gravitational stability of dusty planet forming disc – i. analytical theory. *Monthly Notices of the Royal Astronomical Society*, 519(2):2017–2029, dec 2022. URL <https://doi.org/10.1093/mnras%2Fstac3653>.
- Nathan Magnan, Tobias Heinemann, and Henrik N Latter. A physical picture for the acoustic resonant drag instability. *Monthly Notices of the Royal Astronomical Society*, page stae052, 2024.
- K. G. Makris, R. El-Ganainy, D. N. Christodoulides, and Z. H. Musslimani. Beam Dynamics in $\mathcal{P}\mathcal{T}$ -Symmetric Optical Lattices. *Physical Review Letters*, 100(10):103904, March 2008.
- Ali Mostafazadeh. Pseudo-hermiticity versus pt symmetry: the necessary condition for the reality of the spectrum of a non-hermitian hamiltonian. *Journal of Mathematical Physics*, 43(1):205–214, 2002a.
- Ali Mostafazadeh. Pseudo-hermiticity versus pt-symmetry iii: Equivalence of pseudo-hermiticity and the presence of antilinear symmetries. *Journal of Mathematical Physics*, 43(8):3944–3951, 2002b.
- Ali Mostafazadeh and Ahmet Batal. Physical aspects of pseudo-Hermitian and PT-symmetric quantum mechanics. *Journal of Physics A: Mathematical and General*, 37(48):11645, November 2004. ISSN 0305-4470.
- Ziad H Musslimani, Konstantinos G Makris, Ramy El-Ganainy, and Demetrios N Christodoulides. Optical solitons in p t periodic potentials. *Physical Review Letters*, 100(3):030402, 2008.
- Yohei Onuki. Quasi-local method of wave decomposition in a slowly varying medium. *Journal of Fluid Mechanics*, 883:A56, 2020.
- Şahin Kaya Özdemir, Stefan Rotter, Franco Nori, and L Yang. Parity-time symmetry and exceptional points in photonics. *Nature materials*, 18(8):783–798, 2019.
- Bo Peng, Şahin Kaya Özdemir, Fuchuan Lei, Faraz Monifi, Mariagiovanna Gianfreda, Gui Lu Long, Shanhui Fan, Franco Nori, Carl M. Bender, and Lan Yang. Parity-time-symmetric whispering-gallery microcavities. *Nature Physics*, 10(5):394–398, May 2014. ISSN 1745-2481.
- Nicolas Perez. *Topological waves in geophysical and astrophysical fluids*. PhD thesis, Ecole normale supérieure de Lyon-ENS LYON, 2022.
- Nicolas Perez, Pierre Delplace, and Antoine Venaille. Manifestation of the berry curvature in geophysical ray tracing. *Proceedings of the Royal Society A*, 477(2248):20200844, 2021.
- Nicolas Perez, Pierre Delplace, and Antoine Venaille. Unidirectional modes induced by nontraditional coriolis force in stratified fluids. *Physical Review Letters*, 128(18):184501, 2022.
- James E Pringle and Andrew King. *Astrophysical flows*. Cambridge University Press, 2007.
- Hong Qin, Ruili Zhang, Alexander S. Glasser, and Jianyuan Xiao. Kelvin-Helmholtz instability is the result of parity-time symmetry breaking. *Physics of Plasmas*, 26(3):032102, March 2019. ISSN 1070-664X.
- Hong Qin, Yichen Fu, Alexander S. Glasser, and Asher Yahalom. Spontaneous and explicit parity-time-symmetry breaking in drift-wave instabilities. *Physical Review E*, 104(1):015215, July 2021.
- Lord Rayleigh. Lix. on convection currents in a horizontal layer of fluid, when the higher temperature is on the under side. *The London, Edinburgh, and Dublin Philosophical Magazine and Journal of Science*, 32(192):529–546, 1916.
- Alois Regensburger, Christoph Bersch, Mohammad-Ali Miri, Georgy Onishchukov, Demetrios N. Christodoulides, and Ulf Peschel. Parity-time synthetic photonic lattices. *Nature*, 488(7410):167–171, August 2012. ISSN 1476-4687.
- Christian E. Rüter, Konstantinos G. Makris, Ramy El-Ganainy, Demetrios N. Christodoulides, Mordechai Segev, and Detlef Kip. Observation of parity-time symmetry in optics. *Nature Physics*, 6(3):192–195, March 2010. ISSN 1745-2481.
- PG Saffman. On the stability of laminar flow of a dusty gas. *Journal of fluid mechanics*, 13(1):120–128, 1962.
- K. Schwarzschild. On the equilibrium of the Sun's atmosphere. *Nachrichten von der Königlichen Gesellschaft der Wissenschaften zu Göttingen. Math.-phys. Klasse*, 195:41–53, January 1906.
- Jonathan Squire and Philip F Hopkins. Resonant drag instability of grains streaming in fluids. *The Astrophysical Journal Letters*, 856(1):L15, 2018.
- Alar Toomre. On the gravitational stability of a disk of stars. *Astrophysical Journal*, vol. 139, p. 1217–1238 (1964), 139:1217–1238, 1964.
- Wolfram Research Inc. Mathematica, Version 13.0.0, 2021. URL <https://www.wolfram.com/mathematica>. Champaign, IL.
- Fangxing Zhang, Yaming Feng, Xianfeng Chen, Li Ge, and Wenjie Wan. Synthetic anti-pt symmetry in a single microcavity. *Physical review letters*, 124(5):053901, 2020a.
- Huilai Zhang, Ran Huang, Sheng-Dian Zhang, Ying Li, Cheng-Wei Qiu, Franco Nori, and Hui Jing. Breaking anti-pt symmetry by spinning a resonator. *Nano Letters*, 20(10):7594–7599, 2020b.
- Ruili Zhang, Hong Qin, and Jianyuan Xiao. Pt-symmetry entails pseudo-hermiticity regardless of diagonalizability. *Journal of Mathematical Physics*, 61(1):012101, 2020c.
- VV Zhuravlev. On the nature of the resonant drag instability of dust streaming in protoplanetary disc. *Monthly Notices of the Royal Astronomical Society*, 489(3):3850–3869, 2019.

Exceptional modes of convective instability

Résumé

La plupart des étoiles ont une zone convective. Puisque les arguments de topologie utilisés pour prédire l'onde topologique dans le Chapitre V proviennent de topologie Hermitienne, on peut se demander si cette onde se propage à travers une zone convective. En effet, une zone convective est linéairement instable à la convection, et la situation est alors non Hermitienne. Ce chapitre présente l'étude de ce problème, motivée à la fois par la question de savoir si cette onde traverse les zones convectives et l'analyse d'un problème de topologie non Hermitienne. Ces questions avaient des conséquences importante pour l'observabilité de cette onde, puisqu'elle doit traverser de telles zones dans les étoiles de type solaire pour arriver à la surface.

De manière intéressante, les deux monopoles de charge $\mathcal{C} = \pm 1$ trouvés dans la situation de stratification stable collisionnent et disparaissent dans une stratification instable, laissant une autre structure de courbure de Berry avec aucun nombre de Chern : un anneau de Points Exceptionnels, définis au Chapitre VIII. Sans le théorème d'index pour garantir une correspondance bord-volume, il fallait vérifier directement dans le spectre si l'onde topologique était encore présente dans le spectre. Elle est effectivement présente, ce qui garantit qu'elle traverse les zones convectives. De plus, il est trouvé que quelques modes instables sont différents des autres de manière inattendue qui est détaillée plus bas, et il est montré comment ces modes sont liés à cet anneau. Ce problème présente donc des preuves indirectes de modes topologiques non Hermitiens, pour lequel il semble n'y avoir aujourd'hui aucune théorie les expliquant.

Most stars have a convective zone. As the topological wave predicted in Chapter V rests on arguments of Hermitian topology, one could wonder if it still propagates in a convective zone. Indeed, a convective zone is linearly unstable to convective motion, and the situation is then of non-Hermitian topology. This chapter presents the investigation of this problem, both motivated by the question of knowing if this wave propagated through convective zones and the analysis of new topological structures. This had important implications for observability, as this wave would have to cross the convective zone of solar-like stars to reach the surface and be observed.

Interestingly, the Berry-Chern monopoles found in the stable case collide and disappear for unstable stratification, leaving a different structure of the Berry curvature with no Chern number to it: a ring of Exceptional Points, defined in Chapter VIII. Without the index theorem guaranteeing a bulk-boundary correspondence, it was needed to verify if the topological wave still propagated in this situation. It does, which ensures that this wave propagates through convective zones. It is also found that a few unstable modes are different from the others, and are linked to this ring. It provides a situation with circumstantial evidence of topological modes in a non-Hermitian problem, which to our knowledge are still unexplained by known non-Hermitian topology theories.

My interest in this work was focused on the behavior of the Lamb-like in convective zones, and the exceptional unstable modes connected to the ring we found were remarkable. However, the results were not directly applicable for my collaborators interested in convection development in protostars.

The results presented in this chapter have been published in *The Exceptional ring of buoyancy instability*, Leclerc, Jezequel, Perez, Laibe, Delplace, **Physical Review Research** 2024 [346]. The article is shown here, truncated of its appendices.

The Exceptional Ring of buoyancy instability in stars

Armand Leclerc^{1,*} Lucien Jezequel², Nicolas Perez¹, Asmita Bhandare¹, Guillaume Laibe^{1,3,†} and Pierre Delplace²

¹ Univ Lyon, Univ Lyon1, Ens de Lyon, CNRS,

Centre de Recherche Astrophysique de Lyon UMR5574,

F-69230, Saint-Genis-Laval, France.

² Ens de Lyon, CNRS,

Laboratoire de physique, F-69342 Lyon, France.

³ Institut Universitaire de France.

We reveal properties of global modes of linear buoyancy instability in stars, characterised by the celebrated Schwarzschild criterion, using non-Hermitian topology. We identify a ring of Exceptional Points of order 4 that originates from the pseudo-Hermitian and pseudo-chiral symmetries of the system. The ring results from the merging of a dipole of degeneracy points in the Hermitian stably-stratified counterpart of the problem. Its existence is related to spherically symmetric unstable modes. We obtain the conditions for which convection grows over such radial modes. Those are met at early stages of low-mass stars formation. We finally show that a topological wave is robust to the presence of convective regions by reporting the presence of a mode transiting between the wavebands in the non-Hermitian problem, strengthening their relevance for asteroseismology.

A fluid in a gravity field is stratified in density, and results in a stable or an unstable equilibrium. Gravity waves propagate when the stratification is stable, whereas convection develops when the equilibrium is unstable. To develop a convective layer, Sun-like stars must have reached an unstable state where the square of the buoyancy frequency is negative (Schwarzschild criterion $N^2 < 0$, [1]). Then, through the saturation of a linear instability, the star develops a quasi-adiabatic convective region consisting of large-scale flows that excite waves and transport energy. In these regions, N^2 takes small negative values for convection to remain sustained, depending on its efficiency ($N^2 \simeq -0.25\mu\text{Hz}^2$ in the Sun [2, 3]). Recently, Hermitian topology has shed new light on waves propagating in stably stratified fluids [4–6], but the topology of the unstable case, which involves a non-Hermitian formalism, has not yet been studied. The topological study of waves consists of deducing simple conditions constraining the existence of particular linear modes of physical systems from topological arguments. These arguments can be expressed in a simple way, even for a complicated system of equations. Hermitian systems benefit from general topological index theorems from which one can predict the existence of modes transiting between different wavebands and quantized by a topological integer called the Chern number [7–11]. As such, Hermitian wave topology has become ubiquitous in physical fields as diverse as condensed matter [12], plasma physics [13–15], optics [16, 17], materials science [18–20], or oceanography [6, 21, 22]. Recently, topological arguments have been used to reveal the existence of a Lamb-like wave that behaves as a gravity wave at large wavelengths but as a pressure wave at small wavelengths in stably stratified stars [4, 5], raising further questions. Does this wave also

propagate in convective regions, which are ubiquitous in stellar objects (e.g. Jupiter or high-mass stars, Fig. 1 of [5])? Moreover, seeds of convection in protostars have been observed recently in numerical simulations [23, 24]. Performing a linear stability analysis relative to the background reveals a few unstable radial modes whose origin have not been discussed thus far (see Fig. 1). Does topology allows for additional predictions on buoyancy instabilities in stars, to further characterize the physics of the birth of convective layers? To address these questions, we study the non-Hermitian counterpart of the model derived for stellar pulsations. The search for topological properties in non-Hermitian systems has recently stimulated tremendous efforts in condensed matter [25–27], photonics [28–30], electric circuits [31] and geofluids [32], by investigating for instance the existence of topological edge states in non-Hermitian setups, or the appearance of peculiar degeneracy points where the wave operator becomes non-diagonalizable, called exceptional points (EPs). Here, we show that the linear perturbations of a stellar fluid with $N^2 < 0$ are described by a pseudo-Hermitian and pseudo-chiral symmetric theory. These symmetries constrain the eigenfrequencies, and imply the presence of a ring of EPs of order 4, which is associated with unusual spherically symmetric unstable modes. Furthermore, we report the presence of modes transiting between the complex wavebands of the dispersion relation, one of which is the Lamb-like wave whose topological origin was revealed in [4], which we find to be robust to non-Hermitian $N^2 < 0$ regions.

Wave operator, wave symbol

We consider a non-magnetic, non-rotating stellar fluid at rest in a spherically symmetric steady state. Perturbations of this equilibrium involve velocity, pressure, and density. Perturbations are adiabatic, modeling stars where the diffusion time is much longer than the dynamical time [1, 34]. Perturbations of the gravitational po-

* armand.leclerc@ens-lyon.fr

† guillaume.laibe@ens-lyon.fr

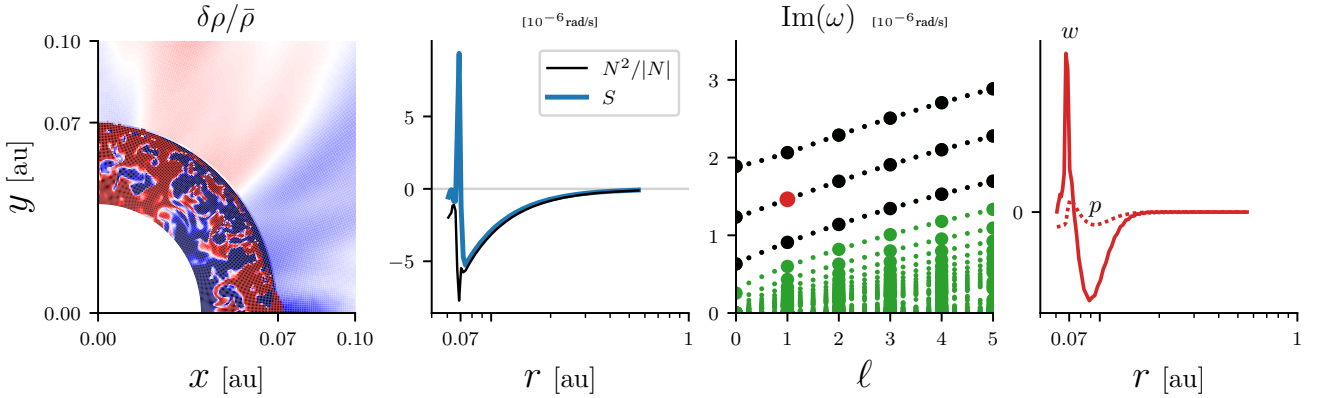


FIG. 1. First panel: density fluctuations with respect to azimuthal average, showing convective-like motion. Data from [23] (2D simulation of an hydrodynamical stellar collapse), zoomed in near the surface of the protostar. Second panel: average azimuthal profiles of N^2 and S , parameters involved in the linear stability analysis Eq.(2). Third and fourth panels: growth rates of a linear stability analysis of this stratification, and profiles of pressure p and radial velocity w of one unstable mode (red), computed numerically with an eigenmodes analysis (see [33]). The instability develops both inside and outside the surface of the protostar. Three modes (black) differ from the others (green): they have non-zero growth rates on radial perturbations ($\ell = 0$).

tential are neglected (Cowling approximation [35]). The equilibrium is still static: no convection has developed yet. We discuss the superadiabatic situation at $N^2 < 0$. We define the perturbation vector $X \equiv (\tilde{v} \ \tilde{w} \ \tilde{\Theta} \ \tilde{p})^\top$ based on re-scaled perturbed quantities (respectively horizontal velocity, radial velocity, entropy and pressure), after projection onto vector spherical harmonics of angular number ℓ (see SM [33]). The set of equations for perturbations of the form $e^{-i\omega t}X(r)$ is

$$\omega X = \mathcal{H}X, \quad (1)$$

where the *wave operator* \mathcal{H} is defined as

$$\mathcal{H} \equiv \begin{pmatrix} 0 & 0 & 0 & L_\ell(r) \\ 0 & 0 & i(N^2)^{1/2} & -iS + \frac{i}{2}c_s' + ic_s\partial_r \\ 0 & -i(N^2)^{1/2} & 0 & 0 \\ L_\ell(r) & iS + \frac{i}{2}c_s' + ic_s\partial_r & 0 & 0 \end{pmatrix} \quad (2)$$

This model involves three characteristic frequencies: the squared Brunt-Väisälä frequency

$$N^2 \equiv -g \frac{d \ln \rho_0}{dr} - \frac{g^2}{c_s^2}, \quad (3)$$

which characterizes buoyancy, the buoyant-acoustic frequency

$$S \equiv \frac{c_s}{2g} \left(N^2 - \frac{g^2}{c_s^2} \right) - \frac{1}{2} \frac{dc_s}{dr} + \frac{c_s}{r}, \quad (4)$$

which gives the rate at which buoyant and acoustic oscillations exchange momentum [5], and the squared Lamb frequency $L_\ell^2 \equiv c_s^2 \ell(\ell+1)/r^2$, which is the momentum in the angular directions. ρ_0 is the steady background

density, c_s is the speed of sound and g is the gravity field, which are all functions of the radius r . Whenever N^2 is negative, the fluid is unstable, and the operator \mathcal{H} is non-Hermitian with respect to the standard scalar product.

The spectrum of the model is obtained by solving the system of ordinary differential Eqs. (1,2), with appropriate boundary conditions (see SM [33]). This system implies parameters varying in space, and an analytical solution is in general out of reach. However, the existence of eigenmodes of \mathcal{H} such as Lamb-like modes, whose frequency transits between other modes when varying a parameter (here ℓ), can be easily accessed without explicitly solving the differential system, but through topological properties of a dual *wave symbol*, a matrix H with scalar coefficients obtained by a Wigner transform of the wave operator \mathcal{H} that maps the differential problem onto phase space [11], as suggested by [36]. H represents physically the local action of the medium on a plane wave, without requiring that the medium varies slowly with respect to the wavelength (see SM [33]). This symbol matrix H reads

$$H \equiv \begin{pmatrix} 0 & 0 & 0 & L_\ell \\ 0 & 0 & iN & K_r - iS \\ 0 & -iN & 0 & 0 \\ L_\ell & K_r + iS & 0 & 0 \end{pmatrix}, \quad (5)$$

and depends on the 3 parameters K_r , L_ℓ and S for fixed N^2 . $K_r = c_s k_r$ with k_r the Wigner symbol of $-i\partial_r$ is the radial wavenumber of a wave locally plane. We denote ω and Ω the eigenvalues of \mathcal{H} and H respectively. When $N^2 > 0$, the matrix H is Hermitian and always diagonalizable with real eigenvalues. When $N^2 < 0$, N is purely imaginary and $H \neq \bar{H}^\top$.

Symmetries and Exceptional Points

For a subset of the parameter space (K_r, S, L_ℓ) , H is non-diagonalizable. These particular points are EPs. At these points, the eigenvalues are degenerate and the eigenvectors coalesce, in the sense that the number of independent eigenvectors is less than the number of eigenvalues that merge. The occurrence of EPs is constrained by the presence of certain symmetries. In our case, one notices that H benefits from a pseudo-Hermitian symmetry

$$UHU^{-1} = \bar{H}^\top, \quad (6)$$

with the unitary transform $U = \text{diag}(1, 1, -1, 1)$. Eigenvalues of pseudo-Hermitian matrices are either real or complex conjugate pairs. Pseudo-Hermiticity also increases the order of EPs in the parameter space [25]. H also has a chiral symmetry $\Gamma H \Gamma^{-1} = -H$, with the unitary transform $\Gamma = \text{diag}(1, 1, -1, -1)$, which can be traced back from the time-reversal symmetry of the fluid lagrangian. Equivalently, this chiral symmetry combined with the pseudo-Hermitian symmetry (Eq. 6) can be taken into account as a pseudo-chiral symmetry

$$(\Gamma U)H(\Gamma U)^{-1} = -\bar{H}^\top, \quad (7)$$

that was also shown to constrain the existence of EPs [25]. We show that the combined effect of both pseudo-chirality and pseudo-Hermiticity leads to a codimension 2 for 4-fold EPs (see SM [33]). This means that, for $N^2 < 0$, the 4 complex-valued eigenbands of H are expected to cross on a curve in the (K_r, S, L_ℓ) space. A direct derivation shows that those EPs satisfy

$$L_\ell = 0, \quad (8)$$

$$K_r^2 + S^2 = -N^2, \quad (9)$$

meaning that they form a circle of radius $|N|$ around the origin in the (K_r, S) plane at $L_\ell = 0$. H is diagonalizable everywhere apart from this circle, where only two eigenvectors exist, $(1 \ 0 \ 0 \ 0)^\top$ and $(0 \ 0 \ (iK_r + S)/N \ 1)^\top$. This *exceptional ring* thus consists of 4-fold EPs (algebraic multiplicity of 4) with a geometric multiplicity of 2.

This ring where modes degenerate separates radial modes ($\ell = 0$) into two regions of distinct spectral properties. Figure 2 shows the real and imaginary parts of the eigenvalues of H . Outside the ring ($K_r^2 + S^2 > |N^2|$), the radial modes behave classically [37]: radial pressure waves have finite real frequencies and radial buoyancy modes have zero growth rates. Inside ($K_r^2 + S^2 < |N^2|$), they behave differently: the acoustic bands degenerate at $\Omega = 0$, and gravity modes have non-zero growth rates, the maximum value $\sqrt{-N^2}$ being reached for $K_r = S = 0$. When crossing the ring, two eigenvalues of H transit from real to pure imaginary values. Since H is pseudo-Hermitian, this can be interpreted as a Krein collision in the framework of Krein signature theory [38]. Unstable (imaginary) eigenvalues with zero Krein signature unfold from the encounter of stable (real) eigenvalues with opposite Krein quantities $\kappa(X) = \bar{X}^\top UX$, X being the

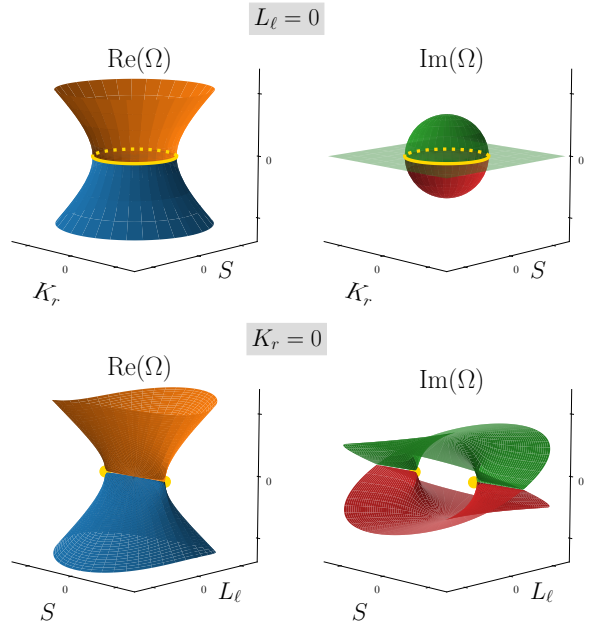


FIG. 2. Eigenvalues Ω of H around the EPs. There are two acoustic bands (orange and blue) with real eigenvalues, and two gravity bands (green and red) with purely imaginary eigenvalues. The yellow rings and points highlight the positions of the Exceptional Points. At large wavelengths $K_r \lesssim N$, pulsations and onset of convection behave very differently from what is expected in the short wavelength limit or in a Boussinesq approximation. Top right: “bubble of instability” [39]. Bottom left: “double-coffee-filter” [38]. Bottom-right: “viaduct” [38].

corresponding eigenvector of H , colliding at the EP ring. A Krein quantity $\tilde{\kappa} = \int d\mathbf{r} d\Phi (|\tilde{v}|^2 + |\tilde{w}|^2 + |\tilde{p}|^2 - |\tilde{\Theta}|^2)$, with Φ the solid angle, can also be defined for any solution $X(\mathbf{r}, t)$ of Eq.(1) and is a conserved quantity of the flow. In particular, $\tilde{\kappa} = 0$ for an unstable mode (see SM [33]).

To date, no theorem connects the EPs of the symbol matrix H to a possible manifestation in the spectrum of \mathcal{H} . If such a connection exists, one expects to find the footprint of EPs in radial modes ($\ell = 0$) as this is where the EP ring is found in the Wigner matrix, when the radial wavelength is large enough and the profiles of N^2 and S are such that the parameters cross the ring shown in Fig. 2 as r varies. Furthermore, the above analysis suggests that the relevant unstable modes are those of wavelengths typically longer than $\sim c_s/|N|$ ($N^2 \neq 0$ since convection has not started nor saturated to a quasi-adiabatic state yet). This condition also requires S to be smaller than $|N|$, at least locally. Figure 3 shows the spectrum of a model where the aforementioned condition is satisfied. The unstable region is wide enough so that low-order radial modes have a sufficiently large radial wavelength, enough for the corresponding K_r to be located inside the ring. The spectrum exhibits three

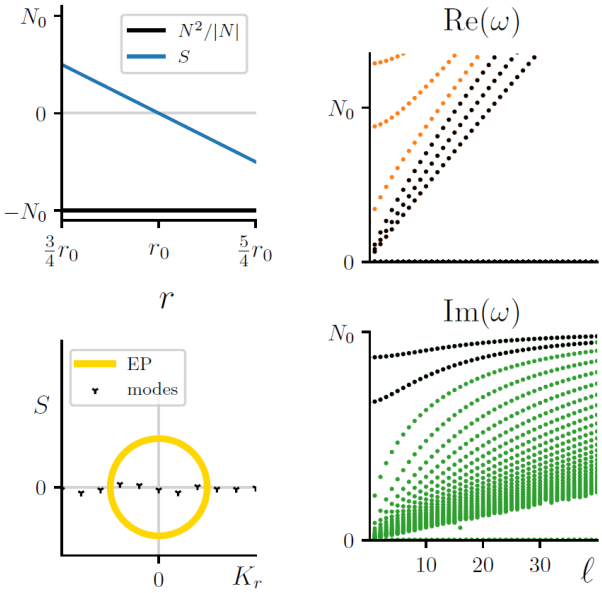


FIG. 3. Spectrum of a model with the stratification profile shown in the top left panel, corresponding to a layer $N^2 < 0$ such that S goes to zero at a given radius r_0 and remains smaller than $|N|$. Right panels: i) three acoustic modes with $\omega(\ell = 0) = 0$ and ii) two gravity modes have non-zero growth rates in the $\ell = 0$ limit. The other modes have a classical behavior. Bottom left: schematic of the location of the modes in parameter space: 5 modes behave differently because they are inside the EP ring. Orange points are acoustic modes, green points are unstable buoyancy modes, black points are Exceptional modes. See SM for details on numerics [33].

acoustic waves with zero frequency for $\ell \rightarrow 0$ and two unstable buoyancy modes with non-zero growth rates for $\ell \rightarrow 0$. Various profiles of pre-convective unstable equilibria have been tested (Fig.4 of SM [33]). They all have such exceptional modes since they are continuous deformations of the model of Fig. 3. Additional modes enter the EP ring by pairs when increasing the length of the layer. These properties are a physical footprint of the existence of EPs. These results are consistent with recent reports of experiments on compressible fluids, in which convection develops via axisymmetric modes [40–42].

Fundamental mode

In the stably stratified problem ($N^2 > 0$), H has degenerated eigenvalues for $(K_r, S, L_\ell) = (0, 0, \pm N)$ for which both the gravity and acoustic waves have frequencies N . Such degeneracies act as monopoles of Berry curvature in the parameter space (K_r, S, L_ℓ) , and carry topological charges given by Chern numbers ± 1 . Those Chern numbers are in direct correspondence with the existence of the Lamb-like waves in the spectrum of the operator \mathcal{H} , and explain the transit of the fundamental mode between the bands [4–6].

In the present study, H is no longer Hermitian, and

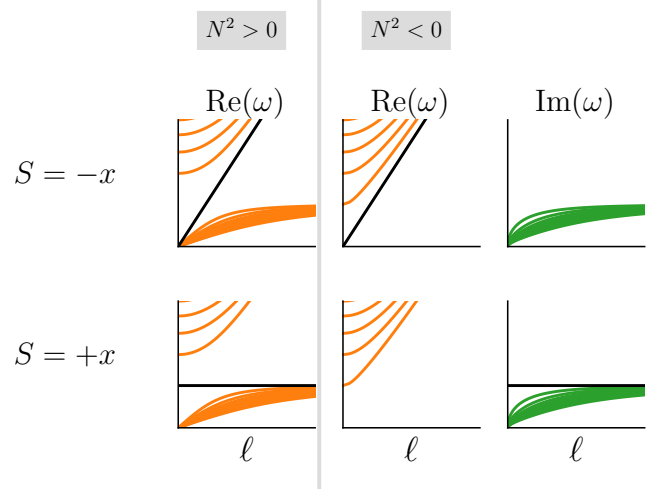


FIG. 4. Frequencies of models with S varying linearly in space (on some appropriately rescaled spatial variable x). Left: Stable stratification. The transiting mode depends on the sign of dS/dx . Right: Unstable stratification. Apart from the buoyancy modes being transposed to imaginary values, the transiting mode behaves as it does in the stable case. When $S = -x$, it arises as a propagating Lamb-like wave. When $S = +x$, it is an unstable mode of growth rate $|N|$, independently of ℓ . Only the first 10 modes of each band are represented.

the correspondence between the Lamb-like wave and the Chern numbers is not guaranteed. Several approaches have recently been developed to address the topological properties of non-Hermitian operators [27, 29–31, 43–50]. In particular, non-Hermitian formulations of the Chern numbers as monopoles of Berry curvature have been proposed, and a non-Hermitian generalization of the correspondence with the transit of the fundamental mode has been developed [26, 51]. However, such a generalization cannot apply here, as the Hermitian degeneracy point is turned into a EP curve when the sign of N^2 is swapped, with zero net Chern number. Other works have introduced winding numbers associated to such circles of EPs [29, 30, 51], which we also find to vanish here. Nevertheless, we confirm below the existence of the the Lamb-like wave in regions with $N^2 < 0$. To do so, we study the normal form, setting linear spatial dependency for S , that is $S(r) = \alpha(r - r_0)$, and $N^2 < 0$, sound speed c_s and Lamb frequency L_ℓ constant [5, 52]. The spectral properties of this problem capture the essential topology that will be reflected in the spectra of real objects. Within these assumptions, Eq. (1) is found to admit a fundamental mode with zero node trapped around the radius r_0 where $S(r_0) = 0$. However, its behaviour depends strongly on the slope of S at r_0 , as shown in Fig. 4 (derivation in SM [33]). For a negative slope ($\alpha < 0$) this mode verifies $\omega^2 = L_\ell^2$ and its eigenfunctions are $\tilde{v}, \tilde{p} \propto \exp\left(-\frac{\alpha}{2c_s}(r - r_0)^2\right)$, $\tilde{w} = \tilde{\Theta} = 0$, which have the peculiar property of having

no radial velocity nor entropy perturbation. This is the Lamb-like wave, and we thus conclude that it still propagates for $N^2 < 0$. In contrast, for a positive slope ($\alpha > 0$), the fundamental mode verifies $\omega^2 = -|N^2|$ and corresponds to a growing perturbation. Its eigenfunctions are $\tilde{v} = \tilde{p} = 0$, $\tilde{w}, \tilde{\Theta} \propto \exp\left(-\frac{\alpha}{2c_s}(r - r_0)^2\right)$, which have no angular velocity or pressure perturbation. We verified numerically that this mode is independent of the boundary conditions (see SM [33]). The importance of polarization relations is key for wave topology [36, 53, 54]. Equation (1) admits non-zero solutions even if some of the component fields are equal to zero. Preserving the vector structure of the problem prevents the filtration of such solutions, as it may happen when decoupling the initial system of equations into a single high-order ordinary differential equation. The general problem is expected to have the same properties, since it is a continuous deformation of this model, as long as no new location where S goes to zero is introduced (Fig.4 of SM [33]). When $N^2(r)$ takes positive and negative values in different regions of the star, the Lamb wave still exists and coexists with an unstable buoyancy band. This is true whether $S(r)$ goes to zero inside the stable or unstable region. In sharp contrast, when the profile of $S(r)$ goes to zero with a positive slope in a region of negative N^2 , we observe an unstable mode with a growth rate $\sim \sqrt{|N^2|}$, independently of ℓ .

Asteroseismology

The topological study of pulsating modes in stars has so far been restrained to radiative regions ($N^2 > 0$), the problem being Hermitian [5]. The question of whether the Lamb-type topological wave could propagate in convective regions (small $N^2 < 0$) remained unanswered. We show in this study that these waves can indeed propagate within them. They are therefore relevant even for objects such as high mass stars or Jupiter (see Fig. 1 of [5]). On top of this, convective regions can also generate multiple exceptional modes that behave like acoustic

waves with zero frequency at $\ell = 0$. The existence or not of such modes in observational data constrains the internal structure of objects with convective interiors.

Birth of convection in protostars

Unstable exceptional modes of low radial order, low ℓ and high growth rates develop when the conditions $N^2 < 0$ and $N^2 + S^2 < 0$ are satisfied. These conditions are met during the formation of a low-mass protostar, as shown in Fig. 1 from 2D simulations [23] (see SM [33] for physical interpretation). This clarifies the origin of radial unstable modes developing around the surface of the protostar. Hence, topological modes provide a possible explanation for the long-lasting problem of how and when convection starts in young stars. Further high-resolution 3D numerical simulations are however required to prove that the kinematic signature observed correspond indeed to convective motion, and to study how these modes will develop in the non-linear regime (e.g. convective eddies or fully developed turbulence).

Future studies are needed to quantify the role of rotation and self-gravity on these modes. Additional symmetries are expected to be broken in some regions of the extended parameter space. Exceptional Points and Krein signature will be key tools to diagnose properties of global modes in such complex objects. The topological invariant associated with exceptional modes remains to be found.

ACKNOWLEDGMENTS

We acknowledge funding from the ERC CoG project PODCAST No 864965. PD is supported by the national grant ANR-18-CE30-0002-01. AL and LJ are funded by a Contrat Doctoral Spécifique Normaliens. We thank A. Marie, G. Chabrier, E. Lynch, M. Rieutord, F. Lignières, B. Commerçon, I. Baraffe and A. Le Saux for useful comments and discussions.

-
- [1] K. Schwarzschild. On the equilibrium of the Sun's atmosphere. *Nachrichten von der Königlichen Gesellschaft der Wissenschaften zu Göttingen. Math.-phys. Klasse*, 195: 41–53, January 1906.
 - [2] Rudolf Kippenhahn, Alfred Weigert, and Achim Weiss. *Stellar structure and evolution*, volume 192. Springer, 1990.
 - [3] Daniel Lecoanet and Eliot Quataert. Internal gravity wave excitation by turbulent convection. *Monthly Notices of the Royal Astronomical Society*, 430(3):2363–2376, 2013.
 - [4] Manolis Perrot, Pierre Delplace, and Antoine Venaille. Topological transition in stratified fluids. *Nature Physics*, 15(8):781–784, 2019.
 - [5] Armand Leclerc, Guillaume Laibe, Pierre Delplace, Antoine Venaille, and Nicolas Perez. Topological modes in stellar oscillations. *The Astrophysical Journal*, 940(1):84, nov 2022. doi:10.3847/1538-4357/ac99d9. URL <https://dx.doi.org/10.3847/1538-4357/ac99d9>.
 - [6] Nicolas Perez, Pierre Delplace, and Antoine Venaille. Unidirectional modes induced by nontraditional coriolis force in stratified fluids. *Physical Review Letters*, 128(18):184501, 2022.
 - [7] Jean Bellisard. Change of the chern number at band crossings. *arXiv:cond-mat/9504030v1*, 1995.
 - [8] Yasuhiro Hatsugai. Chern number and edge states in the integer quantum hall effect. *Phys. Rev. Lett.*, 71:3697–3700, Nov 1993. doi:10.1103/PhysRevLett.71.3697. URL <https://dx.doi.org/10.1103/PhysRevLett.71.3697>.

- <https://link.aps.org/doi/10.1103/PhysRevLett.71.3697>.
- [9] F. Faure and B. Zhilinskii. Topological chern indices in molecular spectra. *Phys. Rev. Lett.*, 85:960–963, Jul 2000. doi:10.1103/PhysRevLett.85.960. URL <https://link.aps.org/doi/10.1103/PhysRevLett.85.960>.
- [10] Gian Michele Graf and Marcello Porta. Bulk-edge correspondence for two-dimensional topological insulators. *Communications in Mathematical Physics*, 324(3):851–895, 2013.
- [11] Pierre Delplace. Berry-Chern monopoles and spectral flows. *SciPost Phys. Lect. Notes*, page 39, 2022. doi:10.21468/SciPostPhysLectNotes.39. URL <https://scipost.org/10.21468/SciPostPhysLectNotes.39>.
- [12] M Zahid Hasan and Charles L Kane. Colloquium: topological insulators. *Reviews of modern physics*, 82(4):3045, 2010.
- [13] Jeffrey B. Parker, J. B. Marston, Steven M. Tobias, and Ziyan Zhu. Topological gaseous plasmon polariton in realistic plasma. *Phys. Rev. Lett.*, 124:195001, May 2020. doi:10.1103/PhysRevLett.124.195001. URL <https://link.aps.org/doi/10.1103/PhysRevLett.124.195001>.
- [14] Jeffrey B Parker. Topological phase in plasma physics. *Journal of Plasma Physics*, 87(2), 2021.
- [15] Hong Qin and Yichen Fu. Topological langmuir-cyclotron wave, 2022. URL <https://arxiv.org/abs/2205.02381>.
- [16] Tomoki Ozawa, Hannah M Price, Alberto Amo, Nathan Goldman, Mohammad Hafezi, Ling Lu, Mikael C Rechtsman, David Schuster, Jonathan Simon, Oded Zilberberg, et al. Topological photonics. *Reviews of Modern Physics*, 91(1):015006, 2019.
- [17] Ling Lu, John D. Joannopoulos, and Marin Soljačić. Topological photonics. *Nature Photonics*, 8(11):821–829, November 2014. ISSN 1749-4893. doi:10.1038/nphoton.2014.248. URL <https://doi.org/10.1038/nphoton.2014.248>.
- [18] Di Xiao, Ming-Che Chang, and Qian Niu. Berry phase effects on electronic properties. *Reviews of modern physics*, 82(3):1959, 2010.
- [19] Sebastian Huber. Topological mechanics. *Nature Physics*, 12:621–623, 06 2016. doi:10.1038/nphys3801.
- [20] Lisa M. Nash, Dustin Kleckner, Alismari Read, Vincenzo Vitelli, Ari M. Turner, and William T. M. Irvine. Topological mechanics of gyroscopic metamaterials. *Proceedings of the National Academy of Sciences*, 112(47):14495–14500, 2015. ISSN 0027-8424. doi:10.1073/pnas.1507413112. URL <https://www.pnas.org/content/112/47/14495>.
- [21] Pierre Delplace, JB Marston, and Antoine Venaille. Topological origin of equatorial waves. *Science*, 358 (6366):1075–1077, 2017.
- [22] A. Venaille and P. Delplace. Wave topology brought to the coast. *Phys. Rev. Res.*, 3:043002, Oct 2021. doi:10.1103/PhysRevResearch.3.043002. URL <https://link.aps.org/doi/10.1103/PhysRevResearch.3.043002>.
- [23] Asmita Bhandare, Rolf Kuiper, Thomas Henning, Christian Fendt, Mario Flock, and Gabriel-Dominique Marleau. Birth of convective low-mass to high-mass second larson cores. *A&A*, 638:A86, 2020. doi:10.1051/0004-6361/201937029. URL <https://doi.org/10.1051/0004-6361/201937029>.
- [24] Adnan Ali Ahmad, Matthias González, Patrick Hennebelle, and Benoît Commerçon. The birth and early evolution of a low mass protostar, 2023.
- [25] Pierre Delplace, Tsuneya Yoshida, and Yasuhiro Hatsugai. Symmetry-protected multifold exceptional points and their topological characterization. *Phys. Rev. Lett.*, 127:186602, Oct 2021. doi:10.1103/PhysRevLett.127.186602. URL <https://link.aps.org/doi/10.1103/PhysRevLett.127.186602>.
- [26] Lucien Jezequel and Pierre Delplace. Non-Hermitian spectral flows and Berry-Chern monopoles, September 2022.
- [27] Ananya Ghatak and Tanmoy Das. New topological invariants in non-hermitian systems. *Journal of Physics: Condensed Matter*, 31(26):263001, Apr 2019. ISSN 1361-648X. doi:10.1088/1361-648x/ab11b3. URL <http://dx.doi.org/10.1088/1361-648x/ab11b3>.
- [28] Bo Zhen, Chia Wei Hsu, Yuichi Igarashi, Ling Lu, Ido Kaminer, Adi Pick, Song-Liang Chua, John D Joannopoulos, and Marin Soljačić. Spawning rings of exceptional points out of dirac cones. *Nature*, 525(7569):354–358, 2015.
- [29] Yong Xu and Chuanwei Zhang. Dirac and weyl rings in three-dimensional cold-atom optical lattices. *Phys. Rev. A*, 93:063606, Jun 2016. doi:10.1103/PhysRevA.93.063606. URL <https://link.aps.org/doi/10.1103/PhysRevA.93.063606>.
- [30] Dan-Wei Zhang, Y. X. Zhao, Rui-Bin Liu, Zheng-Yuan Xue, Shi-Liang Zhu, and Z. D. Wang. Quantum simulation of exotic \mathcal{PT} -invariant topological nodal loop bands with ultracold atoms in an optical lattice. *Phys. Rev. A*, 93:043617, Apr 2016. doi:10.1103/PhysRevA.93.043617. URL <https://link.aps.org/doi/10.1103/PhysRevA.93.043617>.
- [31] Flore K. Kunst, Elisabet Edvardsson, Jan Carl Budich, and Emil J. Bergholtz. Biorthogonal bulk-boundary correspondence in non-hermitian systems. *Phys. Rev. Lett.*, 121:026808, Jul 2018. doi:10.1103/PhysRevLett.121.026808. URL <https://link.aps.org/doi/10.1103/PhysRevLett.121.026808>.
- [32] Ziyan Zhu, Christopher Li, and J. B. Marston. Topology of rotating stratified fluids with and without background shear flow, 2021. URL <https://arxiv.org/abs/2112.04691>.
- [33] See Appendices below for details on derivations, calculations, and numerical tests. They additionally cite [55–65].
- [34] Paul Ledoux. Stellar models with convection and with discontinuity of the mean molecular weight. *Astrophysical Journal*, 105, 1947. ISSN 0004-637X. doi:10.1086/144905.
- [35] T. G. Cowling. The non-radial oscillations of polytropic stars. *Monthly Notices of the Royal Astronomical Society*, 101:367, January 1941. ISSN 0035-8711. doi:10.1093/mnras/101.8.367.
- [36] Yohei Onuki. Quasi-local method of wave decomposition in a slowly varying medium. *Journal of Fluid Mechanics*, 883:A56, 2020. doi:10.1017/jfm.2019.825.
- [37] JL Tassoul. Sur l’instabilité convective d’une masse gazeuse inhomogène. In *Annales d’Astrophysique*, volume 30, page 363, 1967.
- [38] Oleg N Kirillov. *Nonconservative stability problems of modern physics*, volume 14. Walter de Gruyter GmbH & Co KG, 2021.
- [39] RS MacKay. Stability of equilibria of hamiltonian systems. In *Hamiltonian Dynamical Systems*, pages 137–153. CRC Press, 2020.

- [40] Rémi Menaut, Yoann Corre, Ludovic Huguet, Thomas Le Reun, Thierry Alboussière, Michael Bergman, Renaud Deguen, Stéphane Labrosse, and Marc Moulin. Experimental study of convection in the compressible regime. *Phys. Rev. Fluids*, 4:033502, Mar 2019. doi: 10.1103/PhysRevFluids.4.033502. URL <https://link.aps.org/doi/10.1103/PhysRevFluids.4.033502>.
- [41] John P. Koulakis and S. Puttermann. Convective instability in a stratified ideal gas containing an acoustic field. *Journal of Fluid Mechanics*, 915:A25, 2021. doi: 10.1017/jfm.2021.83.
- [42] John P. Koulakis, Yotam Ofek, Seth Pree, and Seth Puttermann. Thermal convection in a central force field mediated by sound. *Phys. Rev. Lett.*, 130:034002, Jan 2023. doi:10.1103/PhysRevLett.130.034002. URL <https://link.aps.org/doi/10.1103/PhysRevLett.130.034002>.
- [43] Zongping Gong, Yuto Ashida, Kohei Kawabata, Kazuaki Takasan, Sho Higashikawa, and Masahito Ueda. Topological phases of non-hermitian systems. *Phys. Rev. X*, 8:031079, Sep 2018. doi: 10.1103/PhysRevX.8.031079. URL <https://link.aps.org/doi/10.1103/PhysRevX.8.031079>.
- [44] Tian-Shu Deng and Wei Yi. Non-bloch topological invariants in a non-hermitian domain wall system. *Phys. Rev. B*, 100:035102, Jul 2019. doi: 10.1103/PhysRevB.100.035102. URL <https://link.aps.org/doi/10.1103/PhysRevB.100.035102>.
- [45] Shunyu Yao and Zhong Wang. Edge states and topological invariants of non-hermitian systems. *Phys. Rev. Lett.*, 121:086803, Aug 2018. doi: 10.1103/PhysRevLett.121.086803. URL <https://link.aps.org/doi/10.1103/PhysRevLett.121.086803>.
- [46] Dan S. Borgnia, Alex Jura Kruchkov, and Robert-Jan Slager. Non-hermitian boundary modes and topology. *Phys. Rev. Lett.*, 124:056802, Feb 2020. doi: 10.1103/PhysRevLett.124.056802. URL <https://link.aps.org/doi/10.1103/PhysRevLett.124.056802>.
- [47] Yuto Ashida, Zongping Gong, and Masahito Ueda. Non-hermitian physics. *Advances in Physics*, 69(3):249–435, Jul 2020. ISSN 1460-6976. doi: 10.1080/00018732.2021.1876991. URL <http://dx.doi.org/10.1080/00018732.2021.1876991>.
- [48] Emil J. Bergholtz, Jan Carl Budich, and Flore K. Kunst. Exceptional topology of non-hermitian systems. *Rev. Mod. Phys.*, 93:015005, Feb 2021. doi: 10.1103/RevModPhys.93.015005. URL <https://link.aps.org/doi/10.1103/RevModPhys.93.015005>.
- [49] Huitao Shen, Bo Zhen, and Liang Fu. Topological band theory for non-hermitian hamiltonians. *Phys. Rev. Lett.*, 120:146402, Apr 2018. doi: 10.1103/PhysRevLett.120.146402. URL <https://link.aps.org/doi/10.1103/PhysRevLett.120.146402>.
- [50] Tony E. Lee. Anomalous edge state in a non-hermitian lattice. *Phys. Rev. Lett.*, 116:133903, Apr 2016. doi: 10.1103/PhysRevLett.116.133903. URL <https://link.aps.org/doi/10.1103/PhysRevLett.116.133903>.
- [51] Yong Xu, Sheng-Tao Wang, and L.-M. Duan. Weyl exceptional rings in a three-dimensional dissipative cold atomic gas. *Phys. Rev. Lett.*, 118:045701, Jan 2017. doi: 10.1103/PhysRevLett.118.045701. URL <https://link.aps.org/doi/10.1103/PhysRevLett.118.045701>.
- [52] Antoine Venaille, Yohei Onuki, Nicolas Perez, and Armand Leclerc. From ray tracing to waves of topological origin in continuous media, 2022. URL <https://arxiv.org/abs/2207.01479>.
- [53] Nicolas Perez, Pierre Delplace, and Antoine Venaille. Manifestation of the berry curvature in geophysical ray tracing. *Proceedings of the Royal Society A*, 477(2248): 20200844, 2021.
- [54] Antoine Venaille, Yohei Onuki, Nicolas Perez, and Armand Leclerc. From ray tracing to waves of topological origin in continuous media, 2022. URL <https://arxiv.org/abs/2207.01479>.
- [55] Rubén G Barrera, GA Estevez, and J Giraldo. Vector spherical harmonics and their application to magnetostatics. *European Journal of Physics*, 6(4):287, 1985.
- [56] Keaton J. Burns, Geoffrey M. Vasil, Jeffrey S. Oishi, Daniel Lecoanet, and Benjamin P. Brown. Dedalus: A flexible framework for numerical simulations with spectral methods. *Physical Review Research*, 2(2):023068, April 2020. doi:10.1103/PhysRevResearch.2.023068.
- [57] Jeffrey S Oishi, Keaton J Burns, Susan E Clark, Evan H Anders, Benjamin P Brown, Geoffrey M Vasil, and Daniel Lecoanet. eigentools: A python package for studying differential eigenvalue problems with an emphasis on robustness. *Journal of Open Source Software*, 6(62):3079, 2021.
- [58] D. O. Gough. *Linear Adiabatic Stellar Pulsation*. Ecole de physique des Houches, January 1993.
- [59] Neil Vaytet, Gilles Chabrier, Edouard Audit, Benoît Commerçon, Jacques Masson, Jason Ferguson, and Franck Delahaye. Simulations of protostellar collapse using multigroup radiation hydrodynamics-ii. the second collapse. *Astronomy & Astrophysics*, 557:A90, 2013.
- [60] Hermann Weyl. Quantenmechanik und gruppentheorie. *Zeitschrift für Physik*, 46(1-2):1–46, 1927.
- [61] Eugene Wigner. On the quantum correction for thermodynamic equilibrium. *Physical review*, 40(5):749, 1932.
- [62] Robert G Littlejohn and William G Flynn. Geometric phases in the asymptotic theory of coupled wave equations. *Physical Review A*, 44(8):5239, 1991.
- [63] Claudio Emmrich and Alan Weinstein. Geometry of the transport equation in multicomponent wkb approximations. *Communications in mathematical physics*, 176(3): 701–711, 1996.
- [64] Leonid Ryzhik, George Papanicolaou, and Joseph B Keller. Transport equations for elastic and other waves in random media. *Wave motion*, 24(4):327–370, 1996.
- [65] J Vanneste and TG Shepherd. On wave action and phase in the non-canonical hamiltonian formulation. *Proceedings of the Royal Society of London. Series A: Mathematical, Physical and Engineering Sciences*, 455(1981):3–21, 1999.

General conclusion

This thesis is part of the line of research on topological physics, by studying how far it roots in astrophysical problems. As presented in Chapter II, these ideas spread from the condensed matter community to many other disciplines of physics in the last two decades, until a recent work brought them into the realm of waves of geophysical fluids in 2017 [141]. The principal goal of this thesis has been to bring topological physics ideas and apply them on problems of waves in astrophysical bodies. Special focus was given to the interior of stars and planets, the most widely studied objects in the Universe both theoretically and observationally. The first step has been to identify the signatures of the concepts of topological physics on astrophysical waves, in order to assert whether they were at play or not. Are the conditions fulfilled for stars to have some of their properties related to topology? Are the predictions of wave topology relevant for realistic and complex stellar interiors? The interest is that topological modes are known to often come with unique properties, like robustness, unidirectionality, and gap-crossing frequencies. The specific target is large scale waves in stellar bodies. Those are more difficult to study theoretically, as many theoretical analyses rely on a form of local approach (local box, wave locally plane, WKB) which benefit from a scale separation. The reward is that the topological analysis gives complementary information, on wave modes falling out of the scope of these techniques, as it can constrain such large waves. Moreover, topological physics demand a special form of wave equation as a Schrödinger equation, uncommon in the stellar wave community. These two difficulties were the main obstacles to overcome in order to identify the possible presence and effects of some topology-related phenomena in stellar waves.

Astrophysics is driven by observations and instrumental capacities, either as data needing explanation or confirming theories. This is especially true for asteroseismology, which in collaboration with exoplanet detection campaigns benefits from instruments with incredibly high precision. And by the Tychonic principle [106], which may be summarized into "Higher resolution, new phenomena", any new order of magnitude of precision leads to discoveries and a more complex understanding of stellar structures. The fact is that today, the high level of precision of observational data causes the limiting factor to be placed on the theory, especially for helioseismology. For example, the problem of near-surface effects causes frequency shifts of uncertain origin [347]. In this regard, it is needed to develop new theoretical techniques who can match this precision level, to explore the physics happening there. This comes with a series of steps: laying the base of the theory, generalizing until it becomes relevant, validating it on observations and using it for predictions.

This thesis started with the work presented in Chapter V: could the topological analysis of waves in plane-parallel, isothermal atmospheres be extended to stellar interiors? It was needed to account for non-isothermal profiles and spherical geometry, and both were found to affect the results. The topological mode was then predicted to propagate in stars, at least in radiative zones. At the time, the prediction was difficult to put in perspective of the results already well-known in asteroseismology, especially the relation between this mode and the f -modes, which looked very similar but were described drastically differently. The interpretation that the topological mode is a part of the branch of f -modes came later. In order to be observable in stars which have an external convective zone, like the Sun, it was needed to assess whether this wave propagated through it or not. This motivated the non-Hermitian analysis performed in Chapter IX, which confirmed that this wave could indeed propagate in convective zones, comforting the possibility to observe it in most stars. This analysis unveiled the importance of PT-symmetry in the convective linear instability, a concept which is not usually used in astrophysical linear instabilities studies. This suggested that other famous instabilities encountered in astrophysical objects could be structured by this symmetry, or one of its cousin symmetries, which lead to the work presented in Chapter VIII. While the application of Krein theory lead to interesting formula on the energy repartition of unstable modes, the current state of non-

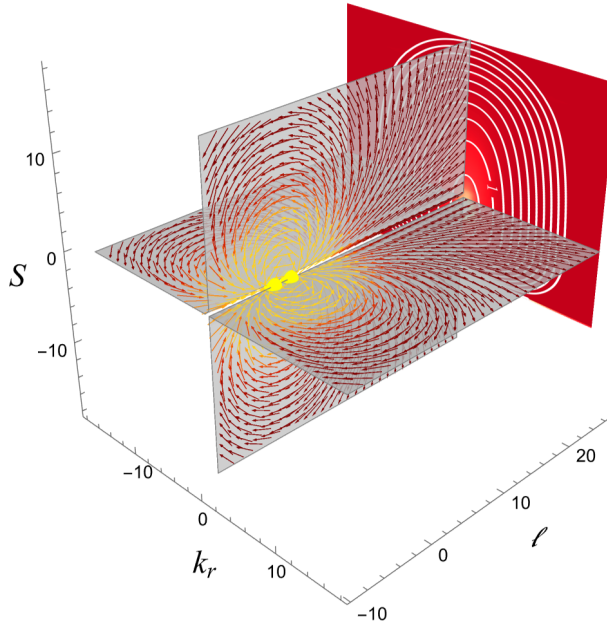


Figure IX.1: Monopoles of Berry curvature in the (k_r, S, ℓ) parameter space of waves in stratified stars generate a net flux of \mathcal{F} in the planes of constant ℓ . It explains why, at a given ℓ , the ray-tracing solutions encircle a non-zero amount of curvature, and thus have a non-zero Berry phase $\phi_B = \iint F_{r,k_r} dr dk_r$.

Hermitian topology is not yet ready to establish strong results on topological unstable linear modes. Thus the following studies turned back to Hermitian topology applied to waves in stable media. This is when Dr. Rekha Jain gave her presentation at AMS80, Mathematical Aspects of Geophysical and Astrophysical Fluid Dynamics in Newcastle, January 2024. Her work on inertial waves in convective zones exhibited what appeared to be a spectral flow of +1, hinting to the possible topology of these waves, which lead to the works of Chapter III. In parallel, it appeared clearly that a topological analysis of waves in rotating stars, accounting for both acoustic and internal waves, was a difficult problem, as it combined inhomogeneous parameters in both the radius and latitude. Such a situation would demand Wigner-Weyl transforms in two curved dimensions simultaneously, which has never been studied before. This technical lock prevents the prediction and study of topological waves in rotating and stratified objects, which is the case of many stars and most planets. As a first step, the effect of spherical geometry with rotation was studied in Chapter IV. The interaction between monopoles in the latitude and in the radial problems remains to be investigated. After that, as the topological wave of asteroseismology was found to propagate through convective zone, it was warranted to study it quantitatively in a hydrodynamical nonlinear simulation, to analyze whether it is excited and propagates as expected. This lead to the collaborative work with Arthur Le Saux, when we could not help but notice that the power spectra he obtained in his solar compressible hydrodynamics simulations showed peaks of power performing a spectral flow. This work is presented in Chapter VI, which confirmed the main predictions and lead to the unveiling of mixed f/g modes in the Sun. It also underscores the importance of full compressibility in hydrodynamical codes, without which numerical experiments on this wave could not be possible. The most recent study is the one presented in Chapter VII, which illustrates the quantitative direct effect of Berry curvature on acoustic modes. While these modes are not topological modes, their frequencies have a trace of the presence of the topological charge through the Berry phase. The manifestation of this trace can be seen by overlaying the phase space of ray-tracing used in Chapter VII with the parameter space where the topological analysis of Chapter V, as shown on Figure IX.1. This phase, present in the constructive interferences of rays constructing a standing wave, is an effect of the polarization relations of acoustic waves varying during the propagation between the turning points. This striking effect asserts that the dispersion relation is not enough to know the phase of the wave.

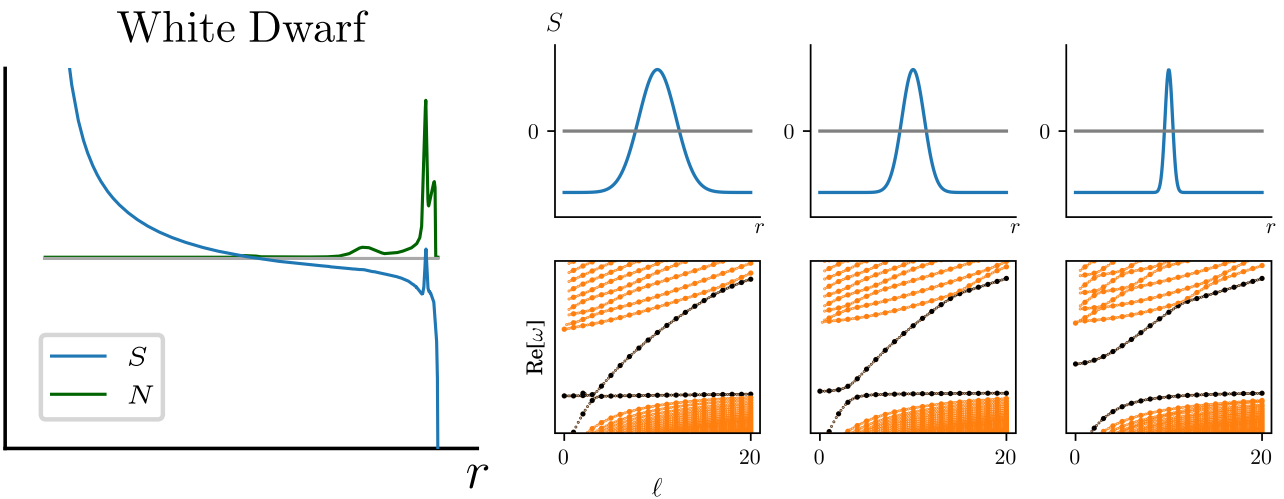


Figure IX.2: **Left:** Two additional cancellations of $S(r)$ are found in a MESA model of White Dwarf, close to the surface, where a peak of $N(r)$ occurs. These two cancellations may cause the existence of two additional topological modes, trapped there. **Right:** A model of double cancellation of $S(r)$. Two topological modes, with opposite spectral flows, are indeed found in the spectra. If their trapping lengths $\sqrt{|\frac{dS}{dr}|/c_s}$ become too large, they overlap and hybridize, leaving a gap in frequency.

One of the main results of this thesis is that the so-called f -mode of asteroseismology is shown to be a topological wave, as its origins are traced back to a topological charge of Chern number $\mathcal{C} = 1$. The branch of f -modes is made of topological modes and free surface modes at low and high degree ℓ respectively. The principle of bulk-boundary correspondence, and the concept of spectral flow, provide the explanation as to why the f -mode frequencies are usually found between p -modes and g -modes: that is because, as the one mode constituting the spectral flow of $\Delta\mathcal{N} = \mathcal{C} = 1$ between the acoustic band and gravity band, its frequency go from g -modes to p -modes as ℓ increases. This analysis also suggests that the low- ℓ part of the f -modes should be a bulk mode, and not a free surface mode as is the case of high ℓ only. In the case of the Sun, the work presented in Chapter VI shows that while this is true, the perturbations' amplitudes do not reflect this fact, because the mode is not strongly localized in the bulk. One actually expects the f -mode to be trapped where $S(r) = 0$, if the length $\sqrt{|\frac{dS}{dr}|/c_s}$ is small compared to R , which is remarkably not found to be the case in the solar interior. However, this is dependent on the stellar structure, and stars of other classes may trap the f -mode more strongly. If this happens, this would impact significantly f -mode propagation and observation, as it would have much more amplitude in the bulk of the star and much less at the surface. This underlines the physical importance of the parameter S , a characteristic frequency of the star which appears to have relevance. Indeed, the full properties of linear adiabatic stellar modes is uniquely given by c_s , N and S . While this frequency S and its expression came as a by-product of the topological analysis, it rather appears to be a fundamentally important frequencies for the waves. Furthermore, the analysis actually states that one topological mode must be expected per region where $S(r) = 0$. Interestingly, this may happen more than once in a stellar structure, and can be seen in the model of White Dwarf shown on Figure IX.2. A peak in the profile of S causes two additional cancellation. This peak is caused by the associated peak in the profile of N , which probably reflects a region of strong composition gradient. This sharp transition in the star's layers may cause strongly trapped, i.e very localized oscillation modes, if the slope $|\frac{dS}{dr}|$ is large enough. This would indicate waves trapped at this transition region, which would constitute probe of the phase transition occurring there. The topological analysis could thus serve here as a guide to waves trapped in phase transition regions. A current project with Laura Caravaglios aims at investigating this idea, in the case of White Dwarfs, as well as Jupiter.

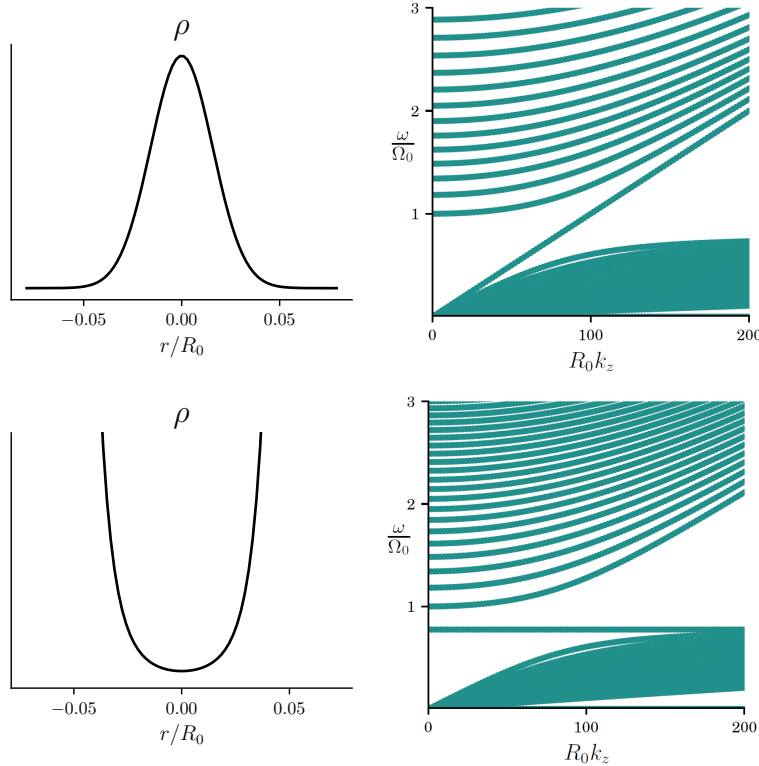


Figure IX.3: The spectral flow in discs occur between the acoustic modes and the inertial modes. There are no internal gravity waves. At pressure (or density) maxima, the topological mode propagates at all frequencies, $\omega = c_s k_z$. At pressure minima, the topological mode has constant frequency $\omega = \kappa \equiv \sqrt{2(2-q)\Omega_0}$, the epicyclic frequency, where $q = \frac{d \ln \Omega}{d \ln r}$.

In addition, while this thesis did focus on waves in stellar interior, there is no intrinsic reason why other astrophysical objects may not host topological waves in their spectra as well. In collaboration with Elliot Lynch, a recent project studied waves in protoplanetary discs, where the medium is mainly supported by rotation rather than thermal pressure like in stars. New difficulties are encountered there, for instance instabilities related to the shear of the flow which is fundamentally keplerian. Discoseismology is less mature than aseismology, but will probably develop in the future, in particular in the fields of black holes and planets formation. In discs are mainly found acoustic waves and inertial waves, in a different geometric configuration from the ones found in convective zones. The analysis of these waves in a simple disc model reveals the presence of topological charges of $C = \pm 1$, in direct analogy with Chapter V. Interestingly, the associated topological modes may be trapped where the density is extremum, i.e in pressure maxima or gaps, as is shown on Figure IX.3. This particular property suggests possible relevance of these modes with planet formation or planet presence in discs, which demands further investigation.

Overall, the works presented in this thesis have investigated whether topological modes are present or not, in stellar spectra of acoustic, internal gravity, or inertial waves. The signature of topological properties of these waves have been looked for in spectra, meaning in the properties of their frequencies. Indeed, this is what is suggested by the concept of spectral flow: a topological mode have frequencies transition between two different wavebands. This is also true in the work regarding ray-tracing and the existence of the Berry phase in solar modes, where topology generates the Berry curvature which affects the eigenfrequencies of standing waves. However, wave topology is also a way of investigating the existence of unidirectional waves. Indeed, the equatorial topological waves of Kelvin and Yanai are purely prograde, and make them able of transporting heat in a preferred direction, here towards the East, while Poincaré and Rossby waves propagate in both directions. This key property of topological modes inspired many studies in meta-materials, as reviewed in Chapter II, for instance for electromagnetic or acoustic waves. Indeed, topology served as a blueprint to

design crystals or sonic crystals which would let light or sound propagate in only one way. This non-reciprocal propagation is particularly efficient, due to its topological origin. While this allows to find many engineering applications, this suggests similar employment in stellar waves. Indeed, an analysis of broken symmetries and calculations of Chern numbers would establish whether some modes propagate in a preferred direction in a given cavity or model. This kind of study could be of importance in the question of radial transport of angular momentum in stars, which is a current open field of research. If some stars host a non-reciprocal propagating wave in the radial direction, it could support a kind of vertical El Niño phenomenon.

A second direction of future research building from the results of this thesis is the general problem of waves in magnetized stars. Topological waves in plasmas and MHD have already received attention, mostly in tokamaks and lab experiments contexts. However, the magnetic field in stars is the subject of many open questions, among which its geometry, configuration and evolution. Thus the spectra of magnetized stars may host topological waves, which could serve as probes of their internal magnetic field which is yet to be fully constrained.

The results obtained in this thesis, as well as the growing body of work on wave topology in fluids, open exciting perspectives on the theory of waves. For astrophysics, the aim is to obtain new results on waves for their seismic probing capabilities or new understanding of their dynamical involvement in transport or instabilities. But conversely, astrophysical fluids are a context of new playground for the development of wave topology in itself, which benefits from this interdisciplinary meeting. Indeed, many questions remain open regarding the theory of topology, among which the role of boundaries, the role of curvature of physical space, the effect of non-Hermitian processes, of nonlinear topology, or the existence of other kinds of topology than with the Chern number – so-called higher-order topological insulators. Waves in astrophysical fluids propose to investigate these questions and ideas in situations different from meta-materials, lattices or crystals. For example, the sphericity of stratification in Chapter V plays a crucial role in the presence and localization of the Berry-Chern monopole in asteroseismology, through the $1/r$ term in $S(r)$. In this instance, spherical geometry helps to manifest the topological degeneracy. But surprisingly, in Chapter IV, it has been found that the sphericity in the shallow-water wave problem generates additional degeneracy points with their own Chern numbers, and they may collide with the original equatorial one and cancel its charge. In that instance, sphericity may instead erase the topological charge of the wave problem. These results, along with the fact that astrophysical fluids propose a variety of geometries, show that it is a natural context to investigate further the interplay between topology and geometry of the physical space.

The results of Chapter IX provide a wave problem in convective zone with modes which were qualified to be exceptional, because of their link to a ring of Exceptional Points. However, no known topological number would explain or characterize their existence. This study thus submits a problem to the development of non-Hermitian topology.

Finally, as advocated by [336], wave topology in fluids has an interesting advantage compared to lattices: the continuous inhomogeneity of the media imposes that the parameter space is a *phase space*. Therefore, a 1D fluid is a situation for waves with a two-dimensional parameter space (x, k_x) . By extension, a 2D fluid is a four-dimensional parameter space for waves, and a 3D fluid is a six-dimensional parameter space. It becomes then clear that waves in fluids may explore structures with high dimensions, which opens the way to investigate higher-order topological physics. For instance, tensor monopoles, a certain generalization of the Berry-Chern monopole, require a parameter space of four dimensions [348]. This object leads to new kinds of topological modes, which has been investigated experimentally very recently in lattices with artificial dimensions [349] or with spin degrees of freedom [350]. Interestingly, a 2D inhomogeneous fluid is sufficient to explore such exotic structures. Even higher-dimensional structures in five or six dimensions may also be explored in fluid wave topology.

Appendices

A Solving for normal modes with DEDALUS

In order to study and explore the properties of topological Lamb-like waves in stellar interiors, it was necessary to have a numerical code with sufficient versatility to input either analytical models or 1D numerical models, change boundary conditions, solve for non-integer values of the harmonic degree ℓ , etc. For this reason, a new script with a solver based on the EVP class of dedalus [139] proved to be more appropriate than existing asteroseismic codes like `gyre` [132]. This appendix gives the Python script solving for the normal oscillations modes of a 1D solar model in the FGONG format. The harmonic degrees for which to solve can be chosen arbitrarily, as well as the inner and outer radii, the outer boundary condition. The equations solved are Eq. (V.31), derived in Chapter V, for adiabatic perturbations in the Cowling approximation. Variations of this script, solving for eigenmodes in other situations, as well as other numerical works used to support the works in this thesis, can be found on my github page <https://github.com/ArmandLeclerc?tab=repositories>. A remark is in order. While the non-integer values of ℓ appeared to be non-physical and were used to obtain continuous branches in the (ν, ℓ) diagram to make spectral flow easily visible, a second usefulness was found later on. The "wedge" geometry used in the MUSIC simulations presented in Chapter VI have the poles removed. As such, actual spherical harmonics Y_ℓ^m are not the eigenfunctions of the angular laplacian. Instead, [91] defined wedge-spherical harmonics, which are generalizations of the spherical harmonics to wedge-shaped domains instead of spheres. In that case, the harmonic degree $\tilde{\ell}$ takes non-integer values, in the eigenvalue equation

$$-\Delta Y_{\tilde{\ell}}^0(\theta) = \tilde{\ell}(\tilde{\ell} + 1)Y_{\tilde{\ell}}^0(\theta). \quad (1)$$

The azimuthal number is $m = 0$ as these simulations are axisymmetric.

Interestingly, the vectorial spherical harmonics and the derivations of Equation (V.31) holds in this generalization, and the linear eigenmodes of such a domain are exactly the solutions of this equation for the corresponding non-integer values of $\tilde{\ell}$.

```
1 from dedalus import public as de
2 from eigentools import Eigenproblem
3 import numpy as np
4 import matplotlib.pyplot as plt
5 from tomso import fgong
6 from scipy import interpolate
7
8 def getEigenMode(nuTarget, ellTarget, ells, nus, etas, modes):
9     idx = (np.abs(nus - nuTarget)/nuTarget + np.abs(ells-ellTarget)/ellTarget).argmin()
10    complexFreq = nus[idx]+j*etas[idx]
11    v,w,theta,p = modes[idx]
12
13    return complexFreq, ells[idx], v, w, theta, p
14
15    ## Load 1D solar model
16 Rsun      = 69.634e9
17 muHzFromPuls = 1e6/2/np.pi
18
19 model_file = 'profile_1D_sun_r15140_Z0p02.data.FGONG'
20 model = fgong.load_fgong(model_file, G=6.67232e-8)
21
22 print("Radius of the model: ",model.r[0]/Rsun)
23
```

```

24 r_model      = np.flip(model.r)
25 N2_model     = np.flip(model.N2)
26 g_model      = np.flip(model.g)
27 cs_model     = np.flip(model.cs)
28 rho_model    = np.flip(model.rho)
29
30 dcdr_model  = np.gradient(cs_model,r_model)
31 S_model      = (cs_model*((N2_model-(g_model/cs_model)**2)/g_model + 2/r_model)-dcdr_model)/2
32 cs_model     = cs_model/Rsun #adim of lengths
33 g_model      = g_model/Rsun #adim of lengths
34 r_model      = r_model/Rsun #adim of lengths
35
36 c   = interpolate.interp1d(r_model,cs_model)
37 dcdr = interpolate.interp1d(r_model,dcdr_model)
38 N2  = interpolate.interp1d(r_model,N2_model)
39 S   = interpolate.interp1d(r_model,S_model)
40 g   = interpolate.interp1d(r_model,g_model)
41 rho = interpolate.interp1d(r_model,rho_model)
42 N   = interpolate.interp1d(r_model,np.sqrt( np.maximum(N2_model,0) ))
43
44 ### Parameters
45 Nr          = 128
46 spaceElls   = np.linspace(0,20,20+1) #angular degrees
47 Rin         = 0.15
48 Rout        = 0.9
49 outer_BC    = "rigid" #"free_surface" or "rigid"
50 driftThresh = 1e4      # threshold of convergence of modes (see Eigentools)
51 ncc_cutoff_waves = 1e-15
52
53 ### Solving for each ell
54 ells, nus, etas, modes = [],[],[],[]
55
56 rbasis = de.Chebyshev('r', Nr, interval = (Rin,Rout))
57 domain = de.Domain([rbasis], mesh=[1])
58 r = rbasis.grid(scale=1) #spatial points for plots
59
60 for ell in spaceElls:
61     #setting up EVP problem
62     problem = de.EVP(domain,
63                         variables=['v','w','T','p'],
64                         eigenvalue='om',
65                         ncc_cutoff=ncc_cutoff_waves)
66     problem.meta[:,['r']]['dirichlet'] = True
67
68     # profiles
69     csound      = domain.new_field(name='cs')
70     csound['g'] = c(r)
71     dcsdr       = domain.new_field(name='dcdr')
72     dcsdr['g'] = dcdr(r)
73     bruntV     = domain.new_field(name='N')
74     bruntV['g'] = N(r)
75     strat       = domain.new_field(name='S')
76     strat['g'] = S(r)
77     lamb        = domain.new_field(name='Ll')
78     lamb['g'] = csound['g'] * np.sqrt(ell*(ell+1))/(r)
79
80     problem.parameters['cs'] = csound
81     problem.parameters['dcdr'] = dcsdr
82     problem.parameters['N'] = bruntV
83     problem.parameters['S'] = strat
84     problem.parameters['Ll'] = lamb

```

```

85 problem.parameters['cout'] = c([Rout])[0]
86 problem.parameters['gout'] = g([Rout])[0]
87 problem.parameters['j'] = complex(0,1)
88
89 # equations
90 problem.add_equation("-om*v + Ll*p = 0")
91 problem.add_equation("-om*w + j*N*T - j*S*p + j*cs*dr(p)+j*dcdr*p/2 = 0")
92 problem.add_equation("-om*T - j*N*w = 0")
93 problem.add_equation("-om*p + Ll*v + j*S*w + j*cs*dr(w)+j*dcdr*w/2 = 0")
94
95 # BCs
96 problem.add_bc("left(w) =0")
97 if outer_BC == "rigid":
98     problem.add_bc("right(w) =0")
99 if outer_BC == "free_surface":
100    problem.add_bc("right(j*om*cout*p - gout*w) =0")
101
102 # solving
103 EP = Eigenproblem(problem,reject=True, drift_threshold=driftThresh, use_ordinal=False)
104 EP.solve(sparse=False)
105 # EP.plot_drift_ratios() #plot selection of "well-converged" modes
106 # plt.show()
107
108 freqs = EP.evalues
109 order = range(len(freqs))
110 print("----- I find {} modes for ell={:.1f} ".format(len(freqs),ell))
111
112 # recording results
113 ells +=[ell for i in order]
114 nus +=[np.real(freqs[i])*muHzFromPuls for i in order]
115 etas +=[np.imag(freqs[i])*muHzFromPuls for i in order]
116 modes +=[ [np.copy(EP.eigenmode(i).fields[0]['g']),
117             np.copy(EP.eigenmode(i).fields[1]['g']),
118             np.copy(EP.eigenmode(i).fields[2]['g']),
119             np.copy(EP.eigenmode(i).fields[3]['g'])] for i in order]
120
121 nus,etas,modes,ells = np.array(nus),np.array(etas),np.array(modes),np.array(ells)
122 print("-----")
123
124 ### Plot 1: frequencies against harmonic degree
125 nuMaxPlot = 4000
126
127 fig,ax = plt.subplots(1,1)
128 img = ax.scatter(ells,nus)
129 ax.set_xlabel(r"$\ell$")
130 ax.set_ylabel(r"$\omega/2\pi[\mu\mathrm{Hz}]$")
131 ax.set_ylim((0,nuMaxPlot))
132
133 plt.grid()
134 plt.tight_layout()
135 plt.show()
136
137 ### Plot 2: displacement perturbations profiles
138 ### Aim for a target mode in the dispersion relation, located at (ellTarget,nuTarget)
139 ### Function getEigenMode shows the eigenfunctions of the closest one
140 ellTarget = 5
141 nuTarget = 400
142
143 complexFreqFound,ellFound,vh,vr,T,p = getEigenMode(nuTarget,ellTarget,ells,nus,etas,modes)
144 nuFound = complexFreqFound.real
145 print("Frequency = ",np.round(complexFreqFound,3),r", ell = ",round(ellFound,3))

```

```

146 phi0 = np.angle(vh[0])
147 vh,vr,T,p = vh*np.exp(-j*phi0),vr*np.exp(-j*phi0),T*np.exp(-j*phi0),p*np.exp(-j*phi0)
148
149 fig,axs = plt.subplots(1,2,figsize=(8,4))
150 axs[0].set_xlabel(r"\ell")
151 axs[0].set_ylabel(r"\omega/2\pi[\mu\mathrm{Hz}]")
152 img = axs[0].scatter(ells,nus)
153 axs[0].scatter([ellFound],[nuFound],s=100,c='red',marker='1')
154 axs[0].set_ylim((0,nuMaxPlot))
155
156 axs[1].set_xlabel(r"r/R")
157 axs[1].set_yticks(())
158 axs[1].plot(r,vh.real/r/np.sqrt(rho(r)),c="tab:blue",label=r"\xi_h.r")
159 axs[1].plot(r,vr.real/r/np.sqrt(rho(r)),c="tab:green",label=r"\xi_r.r")
160 axs[1].plot(r,vh.imag/r/np.sqrt(rho(r)),c="tab:blue",label=r"\xi_h.i",linestyle=':')
161 axs[1].plot(r,vr.imag/r/np.sqrt(rho(r)),c="tab:green",label=r"\xi_r.i",linestyle=':')
162
163 plt.legend(ncol=2)
164 plt.tight_layout()
165 # plt.savefig("fig.pdf")
166 plt.show()

```

As a simple benchmark, two tests proposed recently by Townsend et al. [351] have been performed to estimate the convergence of the calculations. In our variables, their two functions $P_{n,n',\ell}$ and $W_{n,n',\ell}$ read

$$P_{n,n',\ell} = \int \rho r^2 dr (\xi_{r,n}^* \xi_{r,n'} + \ell(\ell+1) \xi_{h,n}^* \xi_{h,n'}) = \omega_n^* \omega_{n'} \int dr (\tilde{v}_{r,n}^* \tilde{v}_{r,n'} + \tilde{v}_{h,n}^* \tilde{v}_{h,n'}), \quad (2)$$

$$W_{n,n',\ell} = \int \rho r^2 dr \left(\frac{1}{\rho^2 c_s^2} P_n^* P_{n'} + N^2 \xi_{r,n}^* \xi_{r,n'} \right) = \int dr (\tilde{p}_n^* \tilde{p}_{n'} + \tilde{\Theta}_n^* \tilde{\Theta}_{n'}). \quad (3)$$

The exact solutions of oscillation modes would satisfy $\omega_{n,\ell}^2 P_{n,n,\ell} = W_{n,n,\ell}$ and $P_{n,n',\ell} = 0$ for $n \neq n'$, and would only be satisfied up to the numerical code's accuracy.

As such, the quantities $\mathcal{E}_{n,\ell}^\omega \equiv (\omega_{n,\ell}^2 - P_{n,n,\ell}/W_{n,n,\ell})/\omega_{n,\ell}^2$ and $\mathcal{E}_{p_1,p_2,\ell=0}^P = P_{p_1,p_2,\ell=0}/\sqrt{P_{p_1,p_1,\ell=0} P_{p_2,p_2,\ell=0}}$ should converge to zero. The results of these two tests, for resolutions $N_r = 16, 32, 64, 128, 256, 512$ are shown on Figure A.1.

B Berry curvature expression for asteroseismology

The presence of Berry curvature and Berry-Chern monopoles for waves in stratified-compressible fluids was first unveiled by [199]. The problem is a 4×4 matrix, and there is no generic formula for the Berry curvature in such dimension, and direct calculation was untractable. They bypassed the issue by squaring the eigenvalue equation as $\omega^2 \mathbf{X} = \mathbf{H}^2 \mathbf{X}$, which reduced the problem to a 2×2 equation for which calculations are well-known in condensed matter. However, the full expression of the Berry curvature was lacking. We show here how to establish its exact expression.

The expression of Berry curvature in the (k_r, S, L_ℓ) space is found by writing $\omega \mathbf{X} = \begin{pmatrix} 0 & h \\ h^\dagger & 0 \end{pmatrix} \mathbf{X}$, and $\mathbf{X} = \begin{pmatrix} \phi \\ \psi \end{pmatrix}$. One has $F_{\mathbf{X}} = i \nabla (\mathbf{X}^\dagger \cdot \nabla \mathbf{X}) = i \nabla (\psi^\dagger \cdot \nabla \psi) + i \nabla (\phi^\dagger \cdot \nabla \phi) = F_\phi + F_\psi$. Demanding $\mathbf{X}^\dagger \cdot \mathbf{X} = \phi^\dagger \cdot \phi + \psi^\dagger \cdot \psi = 1$, and noticing that $\omega \psi = h^\dagger \phi$ and $\omega^2 \phi = h h^\dagger \phi$ and $\omega^2 \psi = h^\dagger h \psi$, one has $\phi^\dagger \cdot \phi = 1/2 = \psi^\dagger \cdot \psi$. From that, ϕ and ψ are determined, and F_ϕ and F_ψ are easily calculated by MATHEMATICA.

One obtains the expression for the Berry curvature for the acoustic waves, which reads

$$F_{\text{sound}} = \frac{1}{((k_x^2 + N^2 + (L_\ell + N)^2)(k_x^2 + N^2 + (L_\ell - N)^2))^{3/2}} \begin{pmatrix} k_x L_\ell (k_x^2 + L_\ell^2 + S^2 + 3N^2) \\ L_\ell S (k_x^2 + L_\ell^2 + S^2 + 3N^2) \\ (L_\ell^2 - N^2)(k_x^2 + L_\ell^2 + S^2 + N^2) \end{pmatrix}. \quad (4)$$

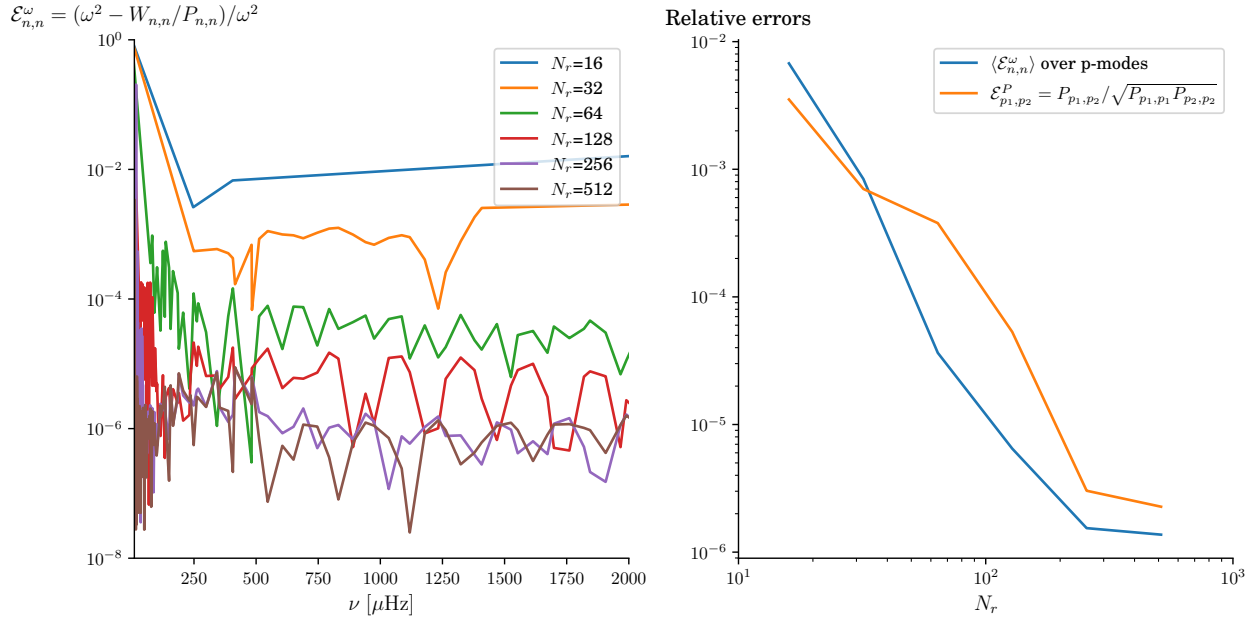


Figure A.1: Convergence of the numerical code, using Dedalus and our set of variables to solve for the oscillation modes of a 1D solar model. $\langle \mathcal{E}^\omega \rangle$ is the average of \mathcal{E}^ω over acoustic modes for $\ell = 0, 1, 2$. The errors seem to decrease as N_r^{-4} .

By symmetry, one has for internal gravity waves

$$F_{\text{igw}} = \frac{-1}{((k_x^2 + N^2 + (L_\ell + N)^2)(k_x^2 + N^2 + (L_\ell - N)^2))^{3/2}} \begin{pmatrix} k_x L_\ell (k_x^2 + L_\ell^2 + S^2 + 3N^2) \\ L_\ell S (k_x^2 + L_\ell^2 + S^2 + 3N^2) \\ (L_\ell^2 - N^2)(k_x^2 + L_\ell^2 + S^2 + N^2) \end{pmatrix}. \quad (5)$$

The denominators show the singularities at the monopoles, located at $k_r = S = 0, L_\ell = \pm N$.

Bibliography

- [1] Jean D'Alembert. *Traité de l'équilibre et du mouvement des fluides*. David l'aîné, 1744.
- [2] Joseph-Louis Lagrange. *Mémoire Sur La Théorie Du Mouvement Des Fluides*. Nouveaux mémoires de l'Académie royale des sciences et belles-lettres de Berlin, 1781.
- [3] Pierre Simon Laplace, Hugh Gordon, John Gordon, and donor DSI Burndy Library. *Traité de mécanique céleste*. A Paris : De L'Imprimerie de Crapelet : Chez J.B.M. Duprat ..., 1798.
- [4] William Thomson. XXVIII. Dynamical problems regarding elastic spheroidal shells and spheroids of incompressible liquid. *Philosophical Transactions of the Royal Society of London*, 153:583–616, January 1863.
- [5] Joseph (1842-1929) Auteur du texte Boussinesq. Théorie des ondes liquides périodiques, par M. J. Boussinesq. <https://catalogue.bnf.fr>, 1872.
- [6] Rayleigh. The Explanation of Certain Acoustical Phenomena 1. *Nature*, 18(455):319–321, July 1878.
- [7] George Gabriel Stokes. Report on Recent Researches on Hydrodynamics. In *Mathematical and Physical Papers*, volume 1 of *Cambridge Library Collection - Mathematics*, pages 157–187. Cambridge University Press, Cambridge, 1880.
- [8] H. Lamb. *Hydrodynamics*. New York: Dover, 1879.
- [9] Sir M. J. Lighthill and James Lighthill. *Waves in Fluids*. Cambridge University Press, November 2001.
- [10] Geoffrey K. Vallis. *Atmospheric and Oceanic Fluid Dynamics*. Cambridge University Press, June 2017.
- [11] Pararas-Carayannis, G. Near and far-field effects of tsunamis generated by the paroxysmal eruptions, explosions, caldera collapses and massive slope failures of the Krakatau volcano in Indonesia on august 26-27, 1883. *Science of Tsunami Hazards*, 2003.
- [12] Horace Lamb. On Atmospheric Oscillations. *Proceedings of the Royal Society of London. Series A, Containing Papers of a Mathematical and Physical Character*, 84(574):551–572, 1911.
- [13] F. P. Bretherton. Lamb waves in a nearly isothermal atmosphere. *Quarterly Journal of the Royal Meteorological Society*, 95(406):754–757, 1969.
- [14] Richard S. Lindzen and Donna Blake. Lamb waves in the presence of realistic distributions of temperature and dissipation. *Journal of Geophysical Research (1896-1977)*, 77(12):2166–2176, 1972.
- [15] Shingo Watada, Yuichi Imanishi, and Kenji Tanaka. Detection of Air Temperature and Wind Changes Synchronized With the Lamb Wave From the 2022 Tonga Volcanic Eruption. *Geophysical Research Letters*, 50(2):e2022GL100884, 2023.

Bibliography

- [16] Walter Munk, Peter Worcester, and Carl Wunsch. *Ocean Acoustic Tomography*. Cambridge Monographs on Mechanics. Cambridge University Press, Cambridge, 1995.
- [17] David B. Enfield. El Niño, past and present. *Reviews of Geophysics*, 27(1):159–187, 1989.
- [18] Chunzai Wang, Clara Deser, Jin-Yi Yu, Pedro DiNezio, and Amy Clement. El Niño and Southern Oscillation (ENSO): A Review. In Peter W. Glynn, Derek P. Manzello, and Ian C. Enochs, editors, *Coral Reefs of the Eastern Tropical Pacific: Persistence and Loss in a Dynamic Environment*, pages 85–106. Springer Netherlands, Dordrecht, 2017.
- [19] David Gubbins. *Seismology and Plate Tectonics*. Cambridge University Press, June 1990.
- [20] Keiiti Aki and Paul G. Richards. Quantitative Seismology, 2nd Ed. *Quantitative Seismology*, 2002.
- [21] Haruo Sato and Michael C. Fehler. *Seismic Wave Propagation and Scattering in the Heterogeneous Earth*. Springer, Berlin, Heidelberg, 2009.
- [22] Graziano Ferrari and Anita Mcconnell. Robert Mallet and the ‘Great Neapolitan earthquake’ of 1857. *Notes and Records of the Royal Society*, 59(1):45–64, January 2005.
- [23] A. Mohorovičić. Earthquake of 8 October 1909. *Geofizika*, 9(2):3–55, 1909.
- [24] Harold Jeffreys. On the Amplitudes of Bodily Seismic Waues. *Geophysical Supplements to the Monthly Notices of the Royal Astronomical Society*, 1(7):334–348, June 1926.
- [25] Claude-Louis Navier. *Mémoire sur les lois du mouvement des fluides*. Académie Royale des Sciences, 1822.
- [26] Siméon-Denis Poisson and Jean Guillaume Garnier. *Traité de mécanique*. Société belge de librairie, 1838.
- [27] S. Rayleigh. XVII. On the maintenance of vibrations by forces of double frequency, and on the propagation of waves through a medium endowed with a periodic structure. *The London, Edinburgh, and Dublin Philosophical Magazine and Journal of Science*, August 1887.
- [28] A. E. H. Love. *A Treatise on the Mathematical Theory of Elasticity*. Cambridge University Press, 1892.
- [29] Horace Lamb. I. On the propagation of tremors over the surface of an elastic solid. *Philosophical Transactions of the Royal Society of London. Series A, Containing Papers of a Mathematical or Physical Character*, 203(359-371):1–42, 1904.
- [30] P. VAROTSOS. Seismic electric currents. *Prakt. Akad. Athenon*, 56:277–286, 1981.
- [31] Hugo Benioff, Frank Press, and Stewart Smith. Excitation of the free oscillations of the Earth by earthquakes. *Journal of Geophysical Research (1896-1977)*, 66(2):605–619, 1961.
- [32] V. Tong and R. García. *Extraterrestrial Seismology*. Cambridge University Press, July 2015.
- [33] G. Latham, M. Ewing, F. Press, and G. Sutton. The Apollo Passive Seismic Experiment. *Science*, 165(3890):241–250, July 1969.
- [34] Don L. Anderson, W. F. Miller, G. V. Latham, Y. Nakamura, M. N. Toksöz, A. M. Dainty, F. K. Duennebier, A. R. Lazarewicz, R. L. Kovach, and T. C. D. Knight. Seismology on Mars. *Journal of Geophysical Research (1896-1977)*, 82(28):4524–4546, 1977.
- [35] L. V. Ksanfomaliti, V. M. Zubkova, N. A. Morozov, and E. V. Petrova. Microseisms at the VENERA-13 and VENERA-14 Landing Sites. *Soviet Astronomy Letters*, 8:241–242, 1982.

Bibliography

- [36] W. Bruce Banerdt, Suzanne E. Smrekar, Don Banfield, Domenico Giardini, Matthew Golombek, Catherine L. Johnson, Philippe Lognonné, Aymeric Spiga, Tilman Spohn, Clément Perrin, Simon C. Stähler, Daniele Antonangeli, Sami Asmar, Caroline Beghein, Neil Bowles, Ebru Bozdag, Peter Chi, Ulrich Christensen, John Clinton, Gareth S. Collins, Ingrid Daubar, Véronique Dehant, Mélanie Drilleau, Matthew Fillingim, William Folkner, Raphaël F. Garcia, Jim Garvin, John Grant, Matthias Grott, Jerzy Grygorczuk, Troy Hudson, Jessica C. E. Irving, Günter Kargl, Taichi Kawamura, Sharon Kedar, Scott King, Brigitte Knapmeyer-Endrun, Martin Knapmeyer, Mark Lemmon, Ralph Lorenz, Justin N. Maki, Ludovic Margerin, Scott M. McLennan, Chloe Michaut, David Mimoun, Anna Mittelholz, Antoine Mocquet, Paul Morgan, Nils T. Mueller, Naomi Murdoch, Seiichi Nagihara, Claire Newman, Francis Nimmo, Mark Panning, W. Thomas Pike, Ana-Catalina Plesa, Sébastien Rodriguez, Jose Antonio Rodriguez-Manfredi, Christopher T. Russell, Nicholas Schmerr, Matt Siegler, Sabine Stanley, Eléanore Stutzmann, Nicholas Teanby, Jeroen Tromp, Martin van Driel, Nicholas Warner, Renee Weber, and Mark Wieczorek. Initial results from the InSight mission on Mars. *Nature Geoscience*, 13(3):183–189, March 2020.
- [37] Mark S. Marley and Carolyn C. Porco. Planetary Acoustic Mode Seismology: Saturn’s Rings. *Icarus*, 106(2):508–524, December 1993.
- [38] M. M. Hedman and P. D. Nicholson. KRONOSEISMOLOGY: USING DENSITY WAVES IN SATURN’S C RING TO PROBE THE PLANET’S INTERIOR. *The Astronomical Journal*, 146(1):12, June 2013.
- [39] P. Gaulme, F.-X. Schmider, J. Gay, T. Guillot, and C. Jacob. Detection of Jovian seismic waves: A new probe of its interior structure. *Astronomy & Astrophysics*, 531:A104, July 2011.
- [40] Robert B. Leighton, Robert W. Noyes, and George W. Simon. Velocity Fields in the Solar Atmosphere. I. Preliminary Report. *The Astrophysical Journal*, 135:474, March 1962.
- [41] Roger K. Ulrich. The Five-Minute Oscillations on the Solar Surface. *The Astrophysical Journal*, 162:993, December 1970.
- [42] P. Ledoux and Th. Walraven. Variable Stars. In Marshal H. Wrubel, H. C. Arp, G. R. Burbridge, E. Margaret Burbidge, Hans E. Suess, Harold C. Urey, Lawrence H. Aller, P. Ledoux, Th. Walraven, Armin J. Deutsch, E. Schatzman, Cecilia Payne-Gaposchkin, and F. Zwicky, editors, *Astrophysics II: Stellar Structure / Astrophysik II: Sternaufbau*, pages 353–604. Springer, Berlin, Heidelberg, 1958.
- [43] W. Unno, Y. Osaki, H. Ando, and H. Shibahashi. *Nonradial Oscillations of Stars*. University of Tokyo Press, January 1979.
- [44] D. O. Gough. Linear adiabatic stellar pulsation. In *Astrophysical Fluid Dynamics - Les Houches 1987*, pages 399–560. Conference Name: Astrophysical Fluid Dynamics - Les Houches 1987, January 1993.
- [45] Svein Rosseland. A Note on Stellar Structure. Mit 1 Abbildung. *Zeitschrift fur Astrophysik*, 4:255, January 1932.
- [46] C. L. Pekeris. Nonradial Oscillations of Stars. *The Astrophysical Journal*, 88:189, September 1938.
- [47] T. G. Cowling. The non-radial oscillations of polytropic stars. *Monthly Notices of the Royal Astronomical Society*, 101:367, January 1941.
- [48] Henrietta S. Leavitt and Edward C. Pickering. Periods of 25 Variable Stars in the Small Magellanic Cloud. *Harvard College Observatory Circular*, 173:1–3, March 1912.
- [49] E. P. Hubble. Cepheids in spiral nebulae. *The Observatory*, 48:139–142, May 1925.
- [50] Edwin Hubble. A Relation between Distance and Radial Velocity among Extra-Galactic Nebulae. *Proceedings of the National Academy of Science*, 15:168–173, March 1929.

Bibliography

- [51] Rachel Howe. Solar Interior Rotation and its Variation. *Living Reviews in Solar Physics*, 6(1):1, December 2009.
- [52] Sarbani Basu. Global seismology of the Sun. *Living Reviews in Solar Physics*, 13(1):2, August 2016.
- [53] Jørgen Christensen-Dalsgaard. Solar structure and evolution. *Living Reviews in Solar Physics*, 18(1):2, April 2021.
- [54] J. Christensen-Dalsgaard, W. Däppen, S. V. Ajukov, E. R. Anderson, H. M. Antia, S. Basu, V. A. Baturin, G. Berthomieu, B. Chaboyer, S. M. Chitre, A. N. Cox, P. Demarque, J. Donatowicz, W. A. Dziembowski, M. Gabriel, D. O. Gough, D. B. Guenther, J. A. Guzik, J. W. Harvey, F. Hill, G. Houdek, C. A. Iglesias, A. G. Kosovichev, J. W. Leibacher, P. Morel, C. R. Proffitt, J. Provost, J. Reiter, E. J. Rhodes, F. J. Rogers, I. W. Roxburgh, M. J. Thompson, and R. K. Ulrich. The Current State of Solar Modeling. *Science*, 272(5266):1286–1292, May 1996.
- [55] Laurent Gizon, Robert H. Cameron, Yuto Bekki, Aaron C. Birch, Richard S. Bogart, Allan Sacha Brun, Cilia Damiani, Damien Fournier, Laura Hyest, Kiran Jain, B. Lekshmi, Zhi-Chao Liang, and Bastian Proxauf. Solar inertial modes: Observations, identification, and diagnostic promise. *Astronomy & Astrophysics*, 652:L6, August 2021.
- [56] Yuto Bekki, Robert H. Cameron, and Laurent Gizon. The Sun’s differential rotation is controlled by high-latitude baroclinically unstable inertial modes. *Science Advances*, 10(13):eadk5643, March 2024.
- [57] M. Agostini, K. Altenmüller, S. Appel, V. Atroshchenko, Z. Bagdasarian, D. Basilico, G. Bellini, J. Benziger, R. Biondi, D. Bravo, B. Caccianiga, F. Calaprice, A. Caminata, P. Cavalcante, A. Chepurnov, D. D’Angelo, S. Davini, A. Derbin, A. Di Giacinto, V. Di Marcello, X. F. Ding, A. Di Ludovico, L. Di Noto, I. Drachnev, A. Formozov, D. Franco, C. Galbiati, C. Ghiano, M. Giammarchi, A. Goretti, A. S. Göttel, M. Gromov, D. Guffanti, Aldo Ianni, Andrea Ianni, A. Jany, D. Jeschke, V. Kobaychev, G. Korga, S. Kumaran, M. Laubenstein, E. Litvinovich, P. Lombardi, I. Lomskaya, L. Ludhova, G. Lukyanchenko, L. Lukyanchenko, I. Machulin, J. Martyn, E. Meroni, M. Meyer, L. Miramonti, M. Misiaszek, V. Muratova, B. Neumair, M. Nieslony, R. Nugmanov, L. Oberauer, V. Orekhov, F. Ortica, M. Pallavicini, L. Papp, L. Pelicci, Ö. Penek, L. Pietrofaccia, N. Pilipenko, A. Pocar, G. Raikov, M. T. Ranalli, G. Ranucci, A. Razeto, A. Re, M. Redchuk, A. Romani, N. Rossi, S. Schönert, D. Semenov, G. Settanta, M. Skorokhvatov, A. Singhal, O. Smirnov, A. Sotnikov, Y. Suvorov, R. Tartaglia, G. Testera, J. Thurn, E. Unzhakov, F. L. Villante, A. Vishneva, R. B. Vogelaar, F. von Feilitzsch, M. Wojcik, M. Wurm, S. Zavatarelli, K. Zuber, G. Zuzel, and The Borexino Collaboration. Experimental evidence of neutrinos produced in the CNO fusion cycle in the Sun. *Nature*, 587(7835):577–582, November 2020.
- [58] P. Goldreich and D. A. Keeley. Solar seismology. II. The stochastic excitation of the solar p-modes by turbulent convection. *The Astrophysical Journal*, 212:243–251, February 1977.
- [59] W. H. Press. Radiative and other effects from internal waves in solar and stellar interiors. *The Astrophysical Journal*, 245:286–303, April 1981.
- [60] Rafael A. García, Sylvaine Turck-Chièze, Sebastian J. Jiménez-Reyes, Jérôme Ballot, Pere L. Pallé, Antonio Eff-Darwich, Savita Mathur, and Janine Provost. Tracking Solar Gravity Modes: The Dynamics of the Solar Core. *Science*, 316(5831):1591–1593, June 2007.
- [61] E. Fossat, P. Boumier, T. Corbard, J. Provost, D. Salabert, F. X. Schmider, A. H. Gabriel, G. Grec, C. Renaud, J. M. Robillot, T. Roca-Cortés, S. Turck-Chièze, R. K. Ulrich, and M. Lazrek. Asymptotic g modes: Evidence for a rapid rotation of the solar core. *Astronomy & Astrophysics*, 604:A40, August 2017.
- [62] T. Appourchaux, K. Belkacem, A.-M. Broomhall, W. J. Chaplin, D. O. Gough, G. Houdek, J. Provost, F. Baudin, P. Boumier, Y. Elsworth, R. A. García, B. N. Andersen, W. Finsterle,

Bibliography

- C. Fröhlich, A. Gabriel, G. Grec, A. Jiménez, A. Kosovichev, T. Sekii, T. Toutain, and S. Turck-Chièze. The quest for the solar g modes. *The Astronomy and Astrophysics Review*, 18(1):197–277, February 2010.
- [63] Hannah Schunker, Jesper Schou, Patrick Gaulme, and Laurent Gizon. Fragile Detection of Solar \$g\$-Modes by Fossat et al. *Solar Physics*, 293(6):95, June 2018.
- [64] K. Belkacem, C. Pinçon, and G. Buldgen. Amplitudes of Solar Gravity Modes: A Review. *Solar Physics*, 297(11):147, November 2022.
- [65] Donald W. Kurtz. Asteroseismology Across the Hertzsprung–Russell Diagram. *Annual Review of Astronomy and Astrophysics*, 60(Volume 60, 2022):31–71, September 2022.
- [66] D. Lecoanet and E. Quataert. Internal gravity wave excitation by turbulent convection. *Monthly Notices of the Royal Astronomical Society*, 430(3):2363–2376, April 2013.
- [67] Arthur N. Cox, Siobahn M. Morgan, Forrest J. Rogers, and Carlos A. Iglesias. An opacity mechanism for the pulsations of OB stars. *The Astrophysical Journal*, 393:272, July 1992.
- [68] W. A. Dziembowski and A. A. Pamyatnykh. The opacity mechanism in B-type stars – I. Unstable modes in β Cephei star models. *Monthly Notices of the Royal Astronomical Society*, 262(1):204–212, May 1993.
- [69] Charly Pinçon. *Du transport de moment cinétique par les ondes internes de gravité à l'heure de la sismologie stellaire*. PhD thesis, Université Paris sciences et lettres, September 2017.
- [70] John Leibacher, Thierry Appourchaux, Gaël Buldgen, Rafael A. García, Laurent Gizon, and Philip Scherrer. Probing the Structure and Dynamics of the Solar Core with Gravity Modes. *Bulletin of the American Astronomical Society*, July 2023.
- [71] D. O. Gough and M. E. McIntyre. Inevitability of a magnetic field in the Sun's radiative interior. *Nature*, 394(6695):755–757, August 1998.
- [72] C. Flores, M. S. Connelley, B. Reipurth, A. Boogert, and G. Doppmann. iSHELL K-band Survey of Class I and Flat Spectrum Sources: Magnetic Field Measurements in the Protostellar Phase. *The Astrophysical Journal*, 972(2):149, September 2024.
- [73] S. Deheuvels, G. Li, J. Ballot, and F. Lignières. Strong magnetic fields detected in the cores of 11 red giant stars using gravity-mode period spacings. *Astronomy & Astrophysics*, 670:L16, February 2023.
- [74] Jim Fuller, Matteo Cantiello, Dennis Stello, Rafael A. Garcia, and Lars Bildsten. Asteroseismology can reveal strong internal magnetic fields in red giant stars. *Science*, 350(6259):423–426, October 2015.
- [75] D. Lecoanet, G. M. Vasil, J. Fuller, M. Cantiello, and K. J. Burns. Conversion of internal gravity waves into magnetic waves. *Monthly Notices of the Royal Astronomical Society*, 466(2):2181–2193, April 2017.
- [76] Daniel Lecoanet, Dominic M Bowman, and Timothy Van Reeth. Asteroseismic inference of the near-core magnetic field strength in the main-sequence B star HD 43317. *Monthly Notices of the Royal Astronomical Society: Letters*, 512(1):L16–L20, May 2022.
- [77] M. Rieutord and J. P. Zahn. Turbulent plumes in stellar convective envelopes. *Astronomy and Astrophysics*, 296:127, April 1995.
- [78] I. Baraffe, J. Pratt, T. Goffrey, T. Constantino, D. Folini, M. V. Popov, R. Walder, and M. Viallet. Lithium Depletion in Solar-like Stars: Effect of Overshooting Based on Realistic Multi-dimensional Simulations. *The Astrophysical Journal Letters*, 845(1):L6, August 2017.

Bibliography

- [79] C. Pinçon, K. Belkacem, and M. J. Goupil. Generation of internal gravity waves by penetrative convection. *Astronomy & Astrophysics*, 588:A122, April 2016.
- [80] P. N. McDermott, H. M. van Horn, and C. J. Hansen. Nonradial Oscillations of Neutron Stars. *The Astrophysical Journal*, 325:725, February 1988.
- [81] Omar Benhar, Emanuele Berti, and Valeria Ferrari. The imprint of the equation of state on the axial w-modes of oscillating neutron stars. *Monthly Notices of the Royal Astronomical Society*, 310:797–803, December 1999.
- [82] K. Hebeler, J. M. Lattimer, C. J. Pethick, and A. Schwenk. EQUATION OF STATE AND NEUTRON STAR PROPERTIES CONSTRAINED BY NUCLEAR PHYSICS AND OBSERVATION. *The Astrophysical Journal*, 773(1):11, July 2013.
- [83] Subrahmanyam Chandrasekhar and S. Detweiler. The quasi-normal modes of the Schwarzschild black hole. *Proceedings of the Royal Society of London. A. Mathematical and Physical Sciences*, 344(1639):441–452, January 1997.
- [84] Kostas D. Kokkotas and Bernd G. Schmidt. Quasi-Normal Modes of Stars and Black Holes. *Living Reviews in Relativity*, 2(1):2, September 1999.
- [85] R. A. Konoplya and Alexander Zhidenko. Quasinormal modes of black holes: From astrophysics to string theory. *Reviews of Modern Physics*, 83(3):793–836, July 2011.
- [86] Nicola Franchini and Sebastian H. Völkel. Testing General Relativity with Black Hole Quasinormal Modes. In Cosimo Bambi and Alejandro Cárdenas-Avendaño, editors, *Recent Progress on Gravity Tests: Challenges and Future Perspectives*, pages 361–416. Springer Nature, Singapore, 2024.
- [87] Dominic M. Bowman and Lisa Bugnet. Asteroseismology, October 2024.
- [88] Evry Schatzman. Do Not Forget Gravity Waves. *Solar Physics*, Volume 169, Issue 2, pp.245–252, 169(2):245, December 1996.
- [89] T. M. Rogers, D. N. C. Lin, J. N. McElwaine, and H. H. B. Lau. INTERNAL GRAVITY WAVES IN MASSIVE STARS: ANGULAR MOMENTUM TRANSPORT. *The Astrophysical Journal*, 772(1):21, July 2013.
- [90] C. Pinçon, K. Belkacem, M. J. Goupil, and J. P. Marques. Can plume-induced internal gravity waves regulate the core rotation of subgiant stars? *Astronomy & Astrophysics*, 605:A31, September 2017.
- [91] Arthur Le Saux. *Understanding Mixing Processes in Stars Using Hydrodynamic Simulations Internal Gravity Waves in Stellar Interiors*. PhD thesis, University of Exeter, January 2023.
- [92] A Le Saux, I Baraffe, T Guillet, D G Vlaykov, A Morison, J Pratt, T Constantino, and T Goffrey. Two-dimensional simulations of internal gravity waves in a 5 M_\odot zero-age-main-sequence model. *Monthly Notices of the Royal Astronomical Society*, 522(2):2835–2849, June 2023.
- [93] Evan H. Anders, Daniel Lecoanet, Matteo Cantiello, Keaton J. Burns, Benjamin A. Hyatt, Emma Kaufman, Richard H. D. Townsend, Benjamin P. Brown, Geoffrey M. Vasil, Jeffrey S. Oishi, and Adam S. Jermyn. The photometric variability of massive stars due to gravity waves excited by core convection. *Nature Astronomy*, 7(10):1228–1234, October 2023.
- [94] Adam S. Jermyn and Jim Fuller. Wave heating during the helium flash and lithium-enhanced clump stars, June 2022.
- [95] J Morton, T Guillet, I Baraffe, A Morison, A Le Saux, D G Vlaykov, T Goffrey, and J Pratt. Mixing by internal gravity waves in stars: Assessing numerical simulations against theory. *Monthly Notices of the Royal Astronomical Society*, 537(1):154–170, February 2025.

Bibliography

- [96] Christopher Garrett and Walter Munk. Oceanic mixing by breaking internal waves. *Deep Sea Research and Oceanographic Abstracts*, 19(12):823–832, December 1972.
- [97] Caitlin B. Whalen, Casimir de Lavergne, Alberto C. Naveira Garabato, Jody M. Klymak, Jennifer A. MacKinnon, and Katy L. Sheen. Internal wave-driven mixing: Governing processes and consequences for climate. *Nature Reviews Earth & Environment*, Volume 1, Issue 11, p.606-621, 1(11):606, October 2020.
- [98] Adrian J. Barker and Gordon I. Ogilvie. On internal wave breaking and tidal dissipation near the centre of a solar-type star. *Monthly Notices of the Royal Astronomical Society*, 404(4):1849–1868, June 2010.
- [99] Yubo Su, Daniel Lecoanet, and Dong Lai. Physics of tidal dissipation in early-type stars and white dwarfs: Hydrodynamical simulations of internal gravity wave breaking in stellar envelopes. *Monthly Notices of the Royal Astronomical Society*, 495(1):1239–1251, June 2020.
- [100] M. Rieutord, B. Georgeot, and L. Valdettaro. Wave Attractors in Rotating Fluids: A Paradigm for Ill-Posed Cauchy Problems. *Physical Review Letters*, 85(20):4277–4280, November 2000.
- [101] M. Rieutord, B. Georgeot, and L. Valdettaro. Inertial waves in a rotating spherical shell: Attractors and asymptotic spectrum. *Journal of Fluid Mechanics*, 435:103–144, May 2001.
- [102] Gordon I. Ogilvie. Wave attractors and the asymptotic dissipation rate of tidal disturbances. *Journal of Fluid Mechanics*, 543:19–44, November 2005.
- [103] M. Rieutord and L. Valdettaro. Viscous dissipation by tidally forced inertial modes in a rotating spherical shell. *Journal of Fluid Mechanics*, 643:363–394, January 2010.
- [104] Laurène Jouve and Gordon I. Ogilvie. Direct numerical simulations of an inertial wave attractor in linear and nonlinear regimes. *Journal of Fluid Mechanics*, 745:223–250, April 2014.
- [105] Jiyang He, Benjamin Favier, Michel Rieutord, and Stéphane Le Dizès. Internal shear layers in librating spherical shells: The case of attractors. *Journal of Fluid Mechanics*, 974:A3, November 2023.
- [106] C. Aerts, J. Christensen-Dalsgaard, and D. W. Kurtz. *Asteroseismology*. Springer Science & Business Media, January 2010.
- [107] Rafael A. García and Jérôme Ballot. Asteroseismology of solar-type stars. *Living Reviews in Solar Physics*, 16(1):4, September 2019.
- [108] Benoit Mosser, Thierry Appourchaux, Claude Catala, Jean-Tristan Buey, and (andthe SIAMOIS team). SIAMOIS: Seismic Interferometer to Measure Oscillations in the Interior of Stars. *Journal of Physics: Conference Series*, 118(1):012042, October 2008.
- [109] J. W. Harvey, F. Hill, R. P. Hubbard, J. R. Kennedy, J. W. Leibacher, J. A. Pintar, P. A. Gilman, R. W. Noyes, A. M. Title, J. Toomre, R. K. Ulrich, A. Bhatnagar, J. A. Kennewell, W. Marquette, J. Patrón, O. Saá, and E. Yasukawa. The Global Oscillation Network Group (GONG) Project. *Science*, 272(5266):1284–1286, May 1996.
- [110] William J. Chaplin, Yvonne Elsworth, Rachel Howe, George R. Isaak, Clive P. McLeod, Brek A. Miller, H. B. Van Der Raay, Sarah J. Wheeler, and Roger New. BiSON performance. *Solar Physics*, 168(1):1–18, September 1996.
- [111] A. H. Gabriel, G. Grec, J. Charra, J.-M. Robillot, T. Roca Cortés, S. Turck-Chièze, R. Bocchia, P. Boumier, M. Cantin, E. Cespedes, B. Cougrand, J. Crétolle, L. Damé, M. Decaudin, P. Delache, N. Denis, R. Duc, H. Dzitko, E. Fossat, J.-J. Fourmond, R. A. García, D. Gough, C. Grivel, J. M. Herreros, H. Lagardère, J.-P. Moalic, P. L. Pallé, N. Pétrout, M. Sanchez, R. Ulrich, and H. B. Van Der Raay. Global Oscillations at Low Frequency from the Soho Mission (GOLF). In B. Fleck, V. Domingo, and A. Poland, editors, *The SOHO Mission*, pages 61–99. Springer Netherlands, Dordrecht, 1995.

Bibliography

- [112] P. H. Scherrer, R. S. Bogart, R. I. Bush, J. T. Hoeksema, A. G. Kosovichev, J. Schou, W. Rosenberg, L. Springer, T. D. Tarbell, A. Title, C. J. Wolfson, and I. Zayer. The Solar Oscillations Investigation—Michelson Doppler Imager. In B. Fleck, V. Domingo, and A. Poland, editors, *The SOHO Mission*, pages 129–188. Springer Netherlands, Dordrecht, 1995.
- [113] Claus Fröhlich, José Romero, Hansjörg Roth, Christoph Wehrli, Bo N. Andersen, Thierry Ap-pourchaux, Vicente Domingo, Udo Telljohann, Gabrielle Berthomieu, Philippe Delache, Janine Provost, Thierry Toutain, Dominique A. Crommelynck, André Chevalier, Alain Fichot, Werner Däppen, Douglas Gough, Todd Hoeksema, Antonio Jiménez, Maria F. Gómez, José M. Her-reros, Teodoro Roca Cortés, Andrew R. Jones, Judit M. Pap, and Richard C. Willson. VIRGO: Experiment for helioseismology and solar irradiance monitoring. *Solar Physics*, 162(1):101–128, December 1995.
- [114] F. Grundahl, T. Arentoft, J. Christensen-Dalsgaard, S. Frandsen, H. Kjeldsen, and P. K. Ras-mussen. Stellar Oscillations Network Group – SONG. *Journal of Physics: Conference Series*, 118(1):012041, October 2008.
- [115] A. Baglin, M. Auvergne, L. Boisnard, T. Lam-Trong, P. Barge, C. Catala, M. Deleuil, E. Michel, and W. Weiss. CoRoT: A high precision photometer for stellar ecolution and exoplanet finding. *36th COSPAR Scientific Assembly*, 36:3749, January 2006.
- [116] William J. Borucki, David Koch, Gibor Basri, Natalie Batalha, Timothy Brown, Douglas Cald-well, John Caldwell, Jørgen Christensen-Dalsgaard, William D. Cochran, Edna DeVore, Ed-ward W. Dunham, Andrea K. Dupree, Thomas N. Gautier, John C. Geary, Ronald Gilliland, Alan Gould, Steve B. Howell, Jon M. Jenkins, Yoji Kondo, David W. Latham, Geoffrey W. Marcy, Søren Meibom, Hans Kjeldsen, Jack J. Lissauer, David G. Monet, David Morrison, Dimitar Sas-selov, Jill Tarter, Alan Boss, Don Brownlee, Toby Owen, Derek Buzasi, David Charbonneau, Laurance Doyle, Jonathan Fortney, Eric B. Ford, Matthew J. Holman, Sara Seager, Jason H. Stef-fen, William F. Welsh, Jason Rowe, Howard Anderson, Lars Buchhave, David Ciardi, Lucianne Walkowicz, William Sherry, Elliott Horch, Howard Isaacson, Mark E. Everett, Debra Fischer, Guillermo Torres, John Asher Johnson, Michael Endl, Phillip MacQueen, Stephen T. Bryson, Jessie Dotson, Michael Haas, Jeffrey Kolodziejczak, Jeffrey Van Cleve, Hema Chandrasekaran, Joseph D. Twicken, Elisa V. Quintana, Bruce D. Clarke, Christopher Allen, Jie Li, Haley Wu, Pe-ter Tenenbaum, Ekaterina Verner, Frederick Bruhwiler, Jason Barnes, and Andrej Prsa. Kepler Planet-Detection Mission: Introduction and First Results. *Science*, 327(5968):977–980, February 2010.
- [117] T. L. Duvall, Jr. Recent Results and Theoretical Advances in Local Helioseismology. In *Structure and Dynamics of the Interior of the Sun and Sun-like Stars*, volume 418, page 581, January 1998.
- [118] Laurent Gizon and Aaron C. Birch. Local Helioseismology. *Living Reviews in Solar Physics*, 2(1):6, December 2005.
- [119] Charles Kittel and Paul McEuen. *Introduction to Solid State Physics*. John Wiley & Sons, 2018.
- [120] John Singleton. *Band Theory and Electronic Properties of Solids*. OUP Oxford, August 2001.
- [121] J. Christensen-Dalsgaard. Lecture Notes on Stellar Oscillations (<https://users-phys.au.dk/jcd/oscilnotes/>), 2019.
- [122] D. O. Gough. Mixing-length theory for pulsating stars. *The Astrophysical Journal*, 214:196–213, May 1977.
- [123] Bill Paxton, Lars Bildsten, Aaron Dotter, Falk Herwig, Pierre Lesaffre, and Frank Timmes. Mod-ules for Experiments in Stellar Astrophysics (MESA). *The Astrophysical Journal Supplement Se-ries*, 192:3, January 2011.
- [124] H. Robe. Les oscillations non radiales des polytropes. *Annales d’Astrophysique*, 31:475, February 1968.

Bibliography

- [125] J. Christensen-Dalsgaard. Some aspects of the theory of solar oscillations. *Geophysical & Astrophysical Fluid Dynamics*, 62(1-4):123–152, December 1991.
- [126] Thomas L. Duvall. A dispersion law for solar oscillations. *Nature*, 300(5889):242–243, November 1982.
- [127] H. Shibahashi. Modal Analysis of Stellar Nonradial Oscillations by an Asymptotic Method. *Publications of the Astronomical Society of Japan*, 31:87–104, January 1979.
- [128] M. Tassoul. Asymptotic approximations for stellar nonradial pulsations. *The Astrophysical Journal Supplement Series*, 43:469–490, August 1980.
- [129] Gordon I. Ogilvie. Lecture notes: Astrophysical fluid dynamics. *Journal of Plasma Physics*, 82(3):205820301, June 2016.
- [130] J. Christensen-Dalsgaard and D.O. Gough. On the dipolar f mode of stellar oscillation. *Monthly Notices of the Royal Astronomical Society*, 326(3):1115–1121, September 2001.
- [131] Chris S. Hanson, Shravan Hanasoge, and Katepalli R. Sreenivasan. Discovery of high-frequency retrograde vorticity waves in the Sun. *Nature Astronomy*, 6(6):708–714, June 2022.
- [132] R. H. D. Townsend and S. A. Teitler. GYRE: An open-source stellar oscillation code based on a new Magnus Multiple Shooting scheme. *Monthly Notices of the Royal Astronomical Society*, 435:3406–3418, November 2013.
- [133] Gaël Buldgen, Jérôme Bétrisey, Ian W. Roxburgh, Sergei V. Vorontsov, and Daniel R. Reese. Inversions of Stellar Structure From Asteroseismic Data. *Frontiers in Astronomy and Space Sciences*, 9, July 2022.
- [134] Earl P. Bellinger, George C. Angelou, Saskia Hekker, Sarbani Basu, Warrick H. Ball, and Elisabeth Guggenberger. FUNDAMENTAL PARAMETERS OF MAIN-SEQUENCE STARS IN AN INSTANT WITH MACHINE LEARNING. *The Astrophysical Journal*, 830(1):31, October 2016.
- [135] Marc Hon, Dennis Stello, and Jie Yu. Deep learning classification in asteroseismology. *Monthly Notices of the Royal Astronomical Society*, 469(4):4578–4583, August 2017.
- [136] A. Le Saux, L. Bugnet, S. Mathur, S. N. Breton, and R. A. Garcia. Automatic classification of K2 pulsating stars using machine learning techniques, June 2019.
- [137] I. Baraffe, J. Pratt, D. G. Vlaykov, T. Guillet, T. Goffrey, A. Le Saux, and T. Constantino. Two-dimensional simulations of solar-like models with artificially enhanced luminosity - I. Impact on convective penetration. *Astronomy & Astrophysics*, 654:A126, October 2021.
- [138] A. Le Saux, T. Guillet, I. Baraffe, D. G. Vlaykov, T. Constantino, J. Pratt, T. Goffrey, M. Sylvain, V. Réville, and A. S. Brun. Two-dimensional simulations of solar-like models with artificially enhanced luminosity - II. Impact on internal gravity waves. *Astronomy & Astrophysics*, 660:A51, April 2022.
- [139] Keaton J. Burns, Geoffrey M. Vasil, Jeffrey S. Oishi, Daniel Lecoanet, and Benjamin P. Brown. Dedalus: A flexible framework for numerical simulations with spectral methods. *Physical Review Research*, 2(2):023068, April 2020.
- [140] L. Horst, P. V. F. Edelmann, R. Andrássey, F. K. Röpke, D. M. Bowman, C. Aerts, and R. P. Ratnasingam. Fully compressible simulations of waves and core convection in main-sequence stars. *Astronomy & Astrophysics*, 641:A18, September 2020.
- [141] Pierre Delplace, J. B. Marston, and Antoine Venaille. Topological origin of equatorial waves. *Science*, 358(6366):1075–1077, 2017.
- [142] Antoine Venaille, Yohei Onuki, Nicolas Perez, and Armand Leclerc. From ray tracing to waves of topological origin in continuous media. *SciPost Physics*, 14(4):062, April 2023.

Bibliography

- [143] S. Pancharatnam. Generalized theory of interference, and its applications. *Proceedings of the Indian Academy of Sciences - Section A*, 44(5):247–262, November 1956.
- [144] Hugh Christopher Longuet-Higgins, U. Öpik, Maurice Henry Lecorney Pryce, and R. A. Sack. Studies of the Jahn-Teller effect .II. The dynamical problem. *Proceedings of the Royal Society of London. Series A. Mathematical and Physical Sciences*, 244(1236):1–16, 1958.
- [145] Michael Victor Berry. Quantal phase factors accompanying adiabatic changes. *Proceedings of the Royal Society of London. A. Mathematical and Physical Sciences*, 392(1802):45–57, 1984.
- [146] Alfred Shapere and Frank Wilczek. *Geometric Phases In Physics*. World Scientific, July 1989.
- [147] Dorje C. Brody and Lane P. Hughston. Geometric quantum mechanics. *Journal of Geometry and Physics*, 38(1):19–53, April 2001.
- [148] Jiang Zhang, Thi Ha Kyaw, Stefan Philipp, Leong-Chuan Kwek, Erik Sjöqvist, and Dianmin Tong. Geometric and holonomic quantum computation. *Physics Reports*, 1027:1–53, July 2023.
- [149] Luciano De Sio, David E. Roberts, Zhi Liao, Sarik Nersisyan, Olena Uskova, Lloyd Wickboldt, Nelson Tabiryan, Diane M. Steeves, and Brian R. Kimball. Digital polarization holography advancing geometrical phase optics. *Optics Express*, 24(16):18297–18306, August 2016.
- [150] Chandroth Pannian Jisha, Stefan Nolte, and Alessandro Alberucci. Geometric Phase in Optics: From Wavefront Manipulation to Waveguiding. *Laser & Photonics Reviews*, 15(10):2100003, 2021.
- [151] C. Alden Mead. The geometric phase in molecular systems. *Reviews of Modern Physics*, 64(1):51–85, January 1992.
- [152] Arno Bohm, Ali Mostafazadeh, Hiroyasu Koizumi, Qian Niu, and Josef Zwanziger. *The Geometric Phase in Quantum Systems: Foundations, Mathematical Concepts, and Applications in Molecular and Condensed Matter Physics*. Springer Science & Business Media, November 2013.
- [153] Giuseppe Falci, Rosario Fazio, G. Massimo Palma, Jens Siewert, and Vlatko Vedral. Detection of geometric phases in superconducting nanocircuits. *Nature*, 407(6802):355–358, September 2000.
- [154] Raffaele Resta. Manifestations of Berry’s phase in molecules and condensed matter. *Journal of Physics: Condensed Matter*, 12(9):R107, March 2000.
- [155] David Vanderbilt. *Berry Phases in Electronic Structure Theory: Electric Polarization, Orbital Magnetization and Topological Insulators*. Cambridge University Press, November 2018.
- [156] M. V. Berry, R. G. Chambers, M. D. Large, C. Upstill, and J. C. Walmsley. Wavefront dislocations in the Aharonov-Bohm effect and its water wave analogue. *European Journal of Physics*, 1(3):154, July 1980.
- [157] Pierre Delplace and Antoine Venaille. From the geometry of Foucault pendulum to the topology of planetary waves. *Comptes Rendus. Physique*, 21(2):165–175, 2020.
- [158] G. B. Whitham. *Linear and Nonlinear Waves*. John Wiley & Sons, 1999.
- [159] D. O. Gough. EBK Quantization of Stellar Waves. In *Proceedings of the Workshop in Honor of Professor Wasaburo Unno’s 60th Birthday*, page 117. Tokyo: University, Department of Astronomy, January 1986.
- [160] Alexei Kitaev. Periodic table for topological insulators and superconductors. *AIP Conference Proceedings*, 1134(1):22–30, May 2009.
- [161] D. J. Thouless, M. Kohmoto, M. P. Nightingale, and M. den Nijs. Quantized Hall Conductance in a Two-Dimensional Periodic Potential. *Physical Review Letters*, 49(6):405–408, August 1982.

Bibliography

- [162] F. D. M. Haldane. Model for a Quantum Hall Effect without Landau Levels: Condensed-Matter Realization of the "Parity Anomaly". *Physical Review Letters*, 61(18):2015–2018, October 1988.
- [163] C. L. Kane and E. J. Mele. $\{Z\}_2$ Topological Order and the Quantum Spin Hall Effect. *Physical Review Letters*, 95(14):146802, September 2005.
- [164] J. E. Moore and L. Balents. Topological invariants of time-reversal-invariant band structures. *Physical Review B*, 75(12):121306, March 2007.
- [165] Nakahara. *Geometry, Topology and Physics*. CRC Press, October 2018.
- [166] Kenneth George Budden and M. S. Smith. Phase memory and additional memory in W. K. B. solutions for wave propagation in stratified media. *Proceedings of the Royal Society of London. A. Mathematical and Physical Sciences*, 350(1660):27–46, January 1997.
- [167] Michael Victor Berry. Budden & Smith's 'additional memory' and the geometric phase. *Proceedings of the Royal Society of London. Series A: Mathematical and Physical Sciences*, 431(1883):531–537, January 1997.
- [168] Robert G. Littlejohn and William G. Flynn. Geometric phases in the asymptotic theory of coupled wave equations. *Physical Review A*, 44(8):5239–5256, October 1991.
- [169] J. Vanneste and T. G. Shepherd. On wave action and phase in the non-canonical Hamiltonian formulation. *Proceedings of the Royal Society of London. Series A: Mathematical, Physical and Engineering Sciences*, 455(1981):3–21, January 1999.
- [170] Oleg A. Godin. Wentzel–Kramers–Brillouin approximation for atmospheric waves. *Journal of Fluid Mechanics*, 777:260–290, August 2015.
- [171] Ming-Che Chang and Qian Niu. Berry Phase, Hyperorbits, and the Hofstadter Spectrum. *Physical Review Letters*, 75(7):1348–1351, August 1995.
- [172] K. Yu. Bliokh and Yu. P. Bliokh. Spin gauge fields: From Berry phase to topological spin transport and Hall effects. *Annals of Physics*, 319(1):13–47, September 2005.
- [173] Hannah M. Price, Tomoki Ozawa, and Iacopo Carusotto. Quantum Mechanics with a Momentum-Space Artificial Magnetic Field. *Physical Review Letters*, 113(19):190403, November 2014.
- [174] Di Xiao, Ming-Che Chang, and Qian Niu. Berry phase effects on electronic properties. *Reviews of Modern Physics*, 82(3):1959–2007, July 2010.
- [175] Ganesh Sundaram and Qian Niu. Wave-packet dynamics in slowly perturbed crystals: Gradient corrections and Berry-phase effects. *Physical Review B*, 59(23):14915–14925, June 1999.
- [176] Shyeh Tjing Loi. Effect of a strong magnetic field on gravity-mode period spacings in red giant stars. *Monthly Notices of the Royal Astronomical Society*, 496(3):3829–3840, August 2020.
- [177] Roland Lehoucq, Jean-Michel Courty, and Edouard Kierlik. *LES LOIS DU MONDE. - NOTRE ENVIRONNEMENT EXPLIQUE PAR LA PHYSIQUE*. Belin, 2003.
- [178] N. Perez, P. Delplace, and A. Venaille. Manifestation of the Berry curvature in geophysical ray tracing. *Proceedings of the Royal Society A: Mathematical, Physical and Engineering Sciences*, 477(2248):20200844, April 2021.
- [179] Brian C. Hall. *Quantum Theory for Mathematicians*, volume 267 of *Graduate Texts in Mathematics*. Springer, New York, NY, 2013.
- [180] Yohei Onuki. Quasi-local method of wave decomposition in a slowly varying medium. *Journal of Fluid Mechanics*, 883:A56, January 2020.

Bibliography

- [181] K. v. Klitzing, G. Dorda, and M. Pepper. New Method for High-Accuracy Determination of the Fine-Structure Constant Based on Quantized Hall Resistance. *Physical Review Letters*, 45(6):494–497, August 1980.
- [182] D. J. Thouless. Quantization of particle transport. *Physical Review B*, 27(10):6083–6087, May 1983.
- [183] R. B. Laughlin. Quantized Hall conductivity in two dimensions. *Physical Review B*, 23(10):5632–5633, May 1981.
- [184] Barry Simon. Holonomy, the Quantum Adiabatic Theorem, and Berry’s Phase. *Physical Review Letters*, 51(24):2167–2170, December 1983.
- [185] Shiing-shen Chern. Characteristic Classes of Hermitian Manifolds. *Annals of Mathematics*, 47(1):85–121, 1946.
- [186] Pierre Delplace. Berry-Chern monopoles and spectral flows. *SciPost Physics Lecture Notes*, page 039, March 2022.
- [187] M. F. Atiyah and I. M. Singer. The index of elliptic operators on compact manifolds. *Bulletin of the American Mathematical Society*, 69(3):422–433, 1963.
- [188] M. F. Atiyah, V. K. Patodi, and I. M. Singer. Spectral asymmetry and Riemannian geometry. III. *Mathematical Proceedings of the Cambridge Philosophical Society*, 79(1):71–99, January 1976.
- [189] Frédéric Faure. Manifestation of the topological index formula in quantum waves and geo-physical waves. *Annales Henri Lebesgue*, 6:449–492, 2023.
- [190] Guillaume Bal and Jiming Yu. Topological equatorial waves and violation (or not) of the Bulk edge correspondence. *Journal of Physics A Mathematical General*, 57:405204, October 2024.
- [191] B. I. Halperin. Quantized Hall conductance, current-carrying edge states, and the existence of extended states in a two-dimensional disordered potential. *Physical Review B*, 25(4):2185–2190, February 1982.
- [192] Yasuhiro Hatsugai. Chern number and edge states in the integer quantum Hall effect. *Physical Review Letters*, 71(22):3697–3700, November 1993.
- [193] Yasuhiro Hatsugai. Edge states in the integer quantum Hall effect and the Riemann surface of the Bloch function. *Physical Review B*, 48(16):11851–11862, October 1993.
- [194] Gian Michele Graf and Marcello Porta. Bulk-Edge Correspondence for Two-Dimensional Topological Insulators. *Communications in Mathematical Physics*, 324(3):851–895, December 2013.
- [195] Taroh Matsuno. Quasi-geostrophic motions in the equatorial area. *Journal of the Meteorological Society of Japan. Ser. II*, 44(1):25–43, 1966.
- [196] William Thomson. 1. On Gravitational Oscillations of Rotating Water. *Proceedings of the Royal Society of Edinburgh*, 10:92–100, January 1880.
- [197] A. Venaille and P. Delplace. Wave topology brought to the coast. *Physical Review Research*, 3(4):043002, 2021.
- [198] Nicolas Perez. *Topological Waves in Geophysical and Astrophysical Fluids*. PhD thesis, Ecole normale supérieure de Lyon - ENS LYON, September 2022.
- [199] Manolis Perrot, Pierre Delplace, and Antoine Venaille. Topological transition in stratified fluids. *Nature Physics*, 15(8):781–784, 2019.
- [200] Nicolas Perez, Pierre Delplace, and Antoine Venaille. Unidirectional Modes Induced by Non-traditional Coriolis Force in Stratified Fluids. *Physical Review Letters*, 128(18):184501, May 2022.

Bibliography

- [201] J. M. Kosterlitz and D. J. Thouless. Ordering, metastability and phase transitions in two-dimensional systems. *Journal of Physics C: Solid State Physics*, 6(7):1181, April 1973.
- [202] V. P. Gusynin and S. G. Sharapov. Unconventional Integer Quantum Hall Effect in Graphene. *Physical Review Letters*, 95(14):146801, September 2005.
- [203] C. L. Kane and E. J. Mele. Quantum Spin Hall Effect in Graphene. *Physical Review Letters*, 95(22):226801, November 2005.
- [204] Yuanbo Zhang, Yan-Wen Tan, Horst L. Stormer, and Philip Kim. Experimental observation of the quantum Hall effect and Berry's phase in graphene. *Nature*, 438(7065):201–204, November 2005.
- [205] Liang Fu, C. L. Kane, and E. J. Mele. Topological Insulators in Three Dimensions. *Physical Review Letters*, 98(10):106803, March 2007.
- [206] M. Zahid Hasan and Joel E. Moore. Three-Dimensional Topological Insulators. *Annual Review of Condensed Matter Physics*, 2(Volume 2, 2011):55–78, March 2011.
- [207] B. Andrei Bernevig, Taylor L. Hughes, and Shou-Cheng Zhang. Quantum Spin Hall Effect and Topological Phase Transition in HgTe Quantum Wells. *Science*, 314(5806):1757–1761, December 2006.
- [208] Markus König, Steffen Wiedmann, Christoph Brüne, Andreas Roth, Hartmut Buhmann, Laurens W. Molenkamp, Xiao-Liang Qi, and Shou-Cheng Zhang. Quantum Spin Hall Insulator State in HgTe Quantum Wells. *Science*, 318(5851):766–770, November 2007.
- [209] D. Hsieh, D. Qian, L. Wray, Y. Xia, Y. S. Hor, R. J. Cava, and M. Z. Hasan. A topological Dirac insulator in a quantum spin Hall phase. *Nature*, 452(7190):970–974, April 2008.
- [210] Haijun Zhang, Chao-Xing Liu, Xiao-Liang Qi, Xi Dai, Zhong Fang, and Shou-Cheng Zhang. Topological insulators in Bi₂Se₃, Bi₂Te₃ and Sb₂Te₃ with a single Dirac cone on the surface. *Nature Physics*, 5(6):438–442, June 2009.
- [211] Y. Xia, D. Qian, D. Hsieh, L. Wray, A. Pal, H. Lin, A. Bansil, D. Grauer, Y. S. Hor, R. J. Cava, and M. Z. Hasan. Observation of a large-gap topological-insulator class with a single Dirac cone on the surface. *Nature Physics*, 5(6):398–402, June 2009.
- [212] D. Hsieh, Y. Xia, D. Qian, L. Wray, F. Meier, J. H. Dil, J. Osterwalder, L. Patthey, A. V. Fedorov, H. Lin, A. Bansil, D. Grauer, Y. S. Hor, R. J. Cava, and M. Z. Hasan. Observation of Time-Reversal-Protected Single-Dirac-Cone Topological-Insulator States in \$\mathrm{Bi}_2\mathrm{Te}_3\$ and \$\mathrm{Sb}_2\mathrm{Te}_3\$. *Physical Review Letters*, 103(14):146401, September 2009.
- [213] Y. L. Chen, J. G. Analytis, J.-H. Chu, Z. K. Liu, S.-K. Mo, X. L. Qi, H. J. Zhang, D. H. Lu, X. Dai, Z. Fang, S. C. Zhang, I. R. Fisher, Z. Hussain, and Z.-X. Shen. Experimental Realization of a Three-Dimensional Topological Insulator, Bi₂Te₃. *Science*, 325(5937):178–181, July 2009.
- [214] D. Hsieh, Y. Xia, D. Qian, L. Wray, J. H. Dil, F. Meier, J. Osterwalder, L. Patthey, J. G. Checkelsky, N. P. Ong, A. V. Fedorov, H. Lin, A. Bansil, D. Grauer, Y. S. Hor, R. J. Cava, and M. Z. Hasan. A tunable topological insulator in the spin helical Dirac transport regime. *Nature*, 460(7259):1101–1105, August 2009.
- [215] Su-Yang Xu, Ilya Belopolski, Nasser Alidoust, Madhab Neupane, Guang Bian, Chenglong Zhang, Raman Sankar, Guoqing Chang, Zhujun Yuan, Chi-Cheng Lee, Shin-Ming Huang, Hao Zheng, Jie Ma, Daniel S. Sanchez, BaoKai Wang, Arun Bansil, Fangcheng Chou, Pavel P. Shibayev, Hsin Lin, Shuang Jia, and M. Zahid Hasan. Discovery of a Weyl fermion semimetal and topological Fermi arcs. *Science*, 349(6248):613–617, August 2015.

Bibliography

- [216] B. Q. Lv, H. M. Weng, B. B. Fu, X. P. Wang, H. Miao, J. Ma, P. Richard, X. C. Huang, L. X. Zhao, G. F. Chen, Z. Fang, X. Dai, T. Qian, and H. Ding. Experimental Discovery of Weyl Semimetal TaAs. *Physical Review X*, 5(3):031013, July 2015.
- [217] Liang Fu and C. L. Kane. Topological insulators with inversion symmetry. *Physical Review B*, 76(4):045302, July 2007.
- [218] B. Andrei Bernevig and Shou-Cheng Zhang. Quantum Spin Hall Effect. *Physical Review Letters*, 96(10):106802, March 2006.
- [219] Netanel H. Lindner, Gil Refael, and Victor Galitski. Floquet topological insulator in semiconductor quantum wells. *Nature Physics*, 7(6):490–495, June 2011.
- [220] Jérôme Cayssol, Balázs Dóra, Ferenc Simon, and Roderich Moessner. Floquet topological insulators. *physica status solidi (RRL) – Rapid Research Letters*, 7(1-2):101–108, 2013.
- [221] M. Z. Hasan and C. L. Kane. Colloquium: Topological insulators. *Reviews of Modern Physics*, 82(4):3045–3067, November 2010.
- [222] F. Duncan M. Haldane. Nobel Lecture: Topological quantum matter. *Reviews of Modern Physics*, 89(4):040502, October 2017.
- [223] Xiao-Gang Wen. Colloquium: Zoo of quantum-topological phases of matter. *Reviews of Modern Physics*, 89(4):041004, December 2017.
- [224] Oskar Vafek and Ashvin Vishwanath. Dirac Fermions in Solids: From High-Tc Cuprates and Graphene to Topological Insulators and Weyl Semimetals. *Annual Review of Condensed Matter Physics*, 5(Volume 5, 2014):83–112, March 2014.
- [225] B. Q. Lv, T. Qian, and H. Ding. Experimental perspective on three-dimensional topological semimetals. *Reviews of Modern Physics*, 93(2):025002, April 2021.
- [226] N. P. Armitage, E. J. Mele, and Ashvin Vishwanath. Weyl and Dirac semimetals in three-dimensional solids. *Reviews of Modern Physics*, 90(1):015001, January 2018.
- [227] Anton Souslov, Kinjal Dasbiswas, Michel Fruchart, Suriyanarayanan Vaikuntanathan, and Vincenzo Vitelli. Topological Waves in Fluids with Odd Viscosity. *Physical Review Letters*, 122(12):128001, March 2019.
- [228] C. Tauber, P. Delplace, and A. Venaille. A bulk-interface correspondence for equatorial waves. *Journal of Fluid Mechanics*, 868:R2, June 2019.
- [229] C. Tauber, P. Delplace, and A. Venaille. Anomalous bulk-edge correspondence in continuous media. *Physical Review Research*, 2(1):013147, February 2020.
- [230] Yohei Onuki, Antoine Venaille, and Pierre Delplace. Bulk-edge correspondence recovered in incompressible geophysical flows. *Physical Review Research*, 6:033161, August 2024.
- [231] Xander M. de Wit, Andrés J. Aguirre Guzmán, Matteo Madonia, Jonathan S. Cheng, Herman J. H. Clercx, and Rudie P. J. Kunnen. Turbulent rotating convection confined in a slender cylinder: The sidewall circulation. *Physical Review Fluids*, 5(2):023502, February 2020.
- [232] Benjamin Favier and Edgar Knobloch. Robust wall states in rapidly rotating Rayleigh–Bénard convection. *Journal of Fluid Mechanics*, 895:R1, July 2020.
- [233] Furu Zhang and Jin-Han Xie. Non-Hermitian Chern number in rotating Rayleigh–Bénard convection. *Journal of Fluid Mechanics*, 999:A65, November 2024.
- [234] Mário G. Silveirinha. Chern invariants for continuous media. *Physical Review B*, 92(12):125153, September 2015.

Bibliography

- [235] Wenlong Gao, Biao Yang, Mark Lawrence, Fengzhou Fang, Benjamin Béri, and Shuang Zhang. Photonic Weyl degeneracies in magnetized plasma. *Nature Communications*, 7(1):12435, August 2016.
- [236] S. Ali Hassani Gangaraj, Mário G. Silveirinha, and George W. Hanson. Berry Phase, Berry Connection, and Chern Number for a Continuum Bianisotropic Material From a Classical Electromagnetics Perspective. *IEEE Journal on Multiscale and Multiphysics Computational Techniques*, 2:3–17, 2017.
- [237] Jeffrey B. Parker, J. B. Marston, Steven M. Tobias, and Ziyan Zhu. Topological Gaseous Plasmon Polariton in Realistic Plasma. *Physical Review Letters*, 124(19):195001, May 2020.
- [238] Jeffrey B. Parker, J. W. Burbry, J. B. Marston, and Steven M. Tobias. Nontrivial topology in the continuous spectrum of a magnetized plasma. *Physical Review Research*, 2(3):033425, September 2020.
- [239] Chen Qian, Yue Jiang, Jicheng Jin, Thomas Christensen, Marin Soljačić, Alexander V. Kildishev, and Bo Zhen. Topological electromagnetic waves in dispersive and lossy plasma crystals. *Scientific Reports*, 13(1):20445, November 2023.
- [240] Yichen Fu and Hong Qin. The dispersion and propagation of topological Langmuir-cyclotron waves in cold magnetized plasmas. *Journal of Plasma Physics*, 88(4):835880401, August 2022.
- [241] Hong Qin and Yichen Fu. Topological Langmuir-cyclotron wave. *Science Advances*, 9(13):eadd8041, March 2023.
- [242] Zhoufei Liu and Jiping Huang. Topological Plasma Transport from a Diffusion View. *Chinese Physics Letters*, 40(11):110305, November 2023.
- [243] Jeffrey B. Parker. Topological phase in plasma physics. *Journal of Plasma Physics*, 87(2):835870202, April 2021.
- [244] Yichen Fu and Hong Qin. Topological phases and bulk-edge correspondence of magnetized cold plasmas. *Nature Communications*, 12(1):3924, June 2021.
- [245] Zhaoju Yang, Fei Gao, Xihang Shi, Xiao Lin, Zhen Gao, Yidong Chong, and Baile Zhang. Topological Acoustics. *Physical Review Letters*, 114(11):114301, March 2015.
- [246] Alexander B. Khanikaev, Romain Fleury, S. Hossein Mousavi, and Andrea Alù. Topologically robust sound propagation in an angular-momentum-biased graphene-like resonator lattice. *Nature Communications*, 6(1):8260, October 2015.
- [247] Xu Ni, Cheng He, Xiao-Chen Sun, Xiao-ping Liu, Ming-Hui Lu, Liang Feng, and Yan-Feng Chen. Topologically protected one-way edge mode in networks of acoustic resonators with circulating air flow. *New Journal of Physics*, 17(5):053016, May 2015.
- [248] Cheng He, Xu Ni, Hao Ge, Xiao-Chen Sun, Yan-Bin Chen, Ming-Hui Lu, Xiao-Ping Liu, and Yan-Feng Chen. Acoustic topological insulator and robust one-way sound transport. *Nature Physics*, 12(12):1124–1129, December 2016.
- [249] Jiuyang Lu, Chunyin Qiu, Liping Ye, Xiying Fan, Manzhu Ke, Fan Zhang, and Zhengyou Liu. Observation of topological valley transport of sound in sonic crystals. *Nature Physics*, 13(4):369–374, April 2017.
- [250] Suraj Shankar, Mark J. Bowick, and M. Cristina Marchetti. Topological Sound and Flocking on Curved Surfaces. *Physical Review X*, 7(3):031039, September 2017.
- [251] Romain Fleury, Alexander B. Khanikaev, and Andrea Alù. Floquet topological insulators for sound. *Nature Communications*, 7(1):11744, June 2016.

Bibliography

- [252] Li Zhang, Yihao Yang, Yong Ge, Yi-Jun Guan, Qiaolu Chen, Qinghui Yan, Fujia Chen, Rui Xi, Yuanzhen Li, Ding Jia, Shou-Qi Yuan, Hong-Xiang Sun, Hongsheng Chen, and Baile Zhang. Acoustic non-Hermitian skin effect from twisted winding topology. *Nature Communications*, 12(1):6297, November 2021.
- [253] Amir Darabi and Michael J. Leamy. Tunable Nonlinear Topological Insulator for Acoustic Waves. *Physical Review Applied*, 12(4):044030, October 2019.
- [254] Xiujuan Zhang, Meng Xiao, Ying Cheng, Ming-Hui Lu, and Johan Christensen. Topological sound. *Communications Physics*, 1(1):1–13, December 2018.
- [255] Haoran Xue, Yihao Yang, and Baile Zhang. Topological acoustics. *Nature Reviews Materials*, 7(12):974–990, December 2022.
- [256] Xiujuan Zhang, Farzad Zangeneh-Nejad, Ze-Guo Chen, Ming-Hui Lu, and Johan Christensen. A second wave of topological phenomena in photonics and acoustics. *Nature*, 618(7966):687–697, June 2023.
- [257] Emil Prodan and Camelia Prodan. Topological Phonon Modes and Their Role in Dynamic Instability of Microtubules. *Physical Review Letters*, 103(24):248101, December 2009.
- [258] Nina Berg, Kira Joel, Miriam Koolyk, and Emil Prodan. Topological phonon modes in filamentary structures. *Physical Review E*, 83(2):021913, February 2011.
- [259] C. L. Kane and T. C. Lubensky. Topological boundary modes in isostatic lattices. *Nature Physics*, 10(1):39–45, January 2014.
- [260] Jayson Paulose, Bryan Gin-ge Chen, and Vincenzo Vitelli. Topological modes bound to dislocations in mechanical metamaterials. *Nature Physics*, 11(2):153–156, February 2015.
- [261] Roman Süsstrunk and Sebastian D. Huber. Observation of phononic helical edge states in a mechanical topological insulator. *Science*, 349(6243):47–50, July 2015.
- [262] Pai Wang, Ling Lu, and Katia Bertoldi. Topological Phononic Crystals with One-Way Elastic Edge Waves. *Physical Review Letters*, 115(10):104302, September 2015.
- [263] Yao-Ting Wang, Pi-Gang Luan, and Shuang Zhang. Coriolis force induced topological order for classical mechanical vibrations. *New Journal of Physics*, 17(7):073031, July 2015.
- [264] V. Peano, C. Brendel, M. Schmidt, and F. Marquardt. Topological Phases of Sound and Light. *Physical Review X*, 5(3):031011, July 2015.
- [265] Toshikaze Kariyado and Yasuhiro Hatsugai. Manipulation of Dirac Cones in Mechanical Graphene. *Scientific Reports*, 5(1):18107, December 2015.
- [266] Roman Süsstrunk and Sebastian D. Huber. Classification of topological phonons in linear mechanical metamaterials. *Proceedings of the National Academy of Sciences*, 113(33):E4767–E4775, August 2016.
- [267] M. Miniaci, R. K. Pal, B. Morvan, and M. Ruzzene. Experimental Observation of Topologically Protected Helical Edge Modes in Patterned Elastic Plates. *Physical Review X*, 8(3):031074, September 2018.
- [268] T C Lubensky, C L Kane, Xiaoming Mao, A Souslov, and Kai Sun. Phonons and elasticity in critically coordinated lattices. *Reports on Progress in Physics*, 78(7):073901, June 2015.
- [269] Guancong Ma, Meng Xiao, and C. T. Chan. Topological phases in acoustic and mechanical systems. *Nature Reviews Physics*, 1(4):281–294, April 2019.

Bibliography

- [270] Hussein Nassar, Behrooz Yousefzadeh, Romain Fleury, Massimo Ruzzene, Andrea Alù, Chiara Daraio, Andrew N. Norris, Guoliang Huang, and Michael R. Haberman. Nonreciprocity in acoustic and elastic materials. *Nature Reviews Materials*, 5(9):667–685, September 2020.
- [271] F. D. M. Haldane and S. Raghu. Possible Realization of Directional Optical Waveguides in Photonic Crystals with Broken Time-Reversal Symmetry. *Physical Review Letters*, 100(1):013904, January 2008.
- [272] S. Raghu and F. D. M. Haldane. Analogs of quantum-Hall-effect edge states in photonic crystals. *Physical Review A*, 78(3):033834, September 2008.
- [273] Zheng Wang, Yidong Chong, J. D. Joannopoulos, and Marin Soljačić. Observation of unidirectional backscattering-immune topological electromagnetic states. *Nature*, 461(7265):772–775, October 2009.
- [274] Yin Poo, Rui-xin Wu, Zhifang Lin, Yan Yang, and C. T. Chan. Experimental Realization of Self-Guiding Unidirectional Electromagnetic Edge States. *Physical Review Letters*, 106(9):093903, March 2011.
- [275] Mohammad Hafezi, Eugene A. Demler, Mikhail D. Lukin, and Jacob M. Taylor. Robust optical delay lines with topological protection. *Nature Physics*, 7(11):907–912, November 2011.
- [276] Kejie Fang, Zongfu Yu, and Shanhui Fan. Realizing effective magnetic field for photons by controlling the phase of dynamic modulation. *Nature Photonics*, 6(11):782–787, November 2012.
- [277] Alexander B. Khanikaev, S. Hossein Mousavi, Wang-Kong Tse, Mehdi Kargarian, Allan H. MacDonald, and Gennady Shvets. Photonic topological insulators. *Nature Materials*, 12(3):233–239, March 2013.
- [278] Maxim A. Gorlach and Alexander N. Poddubny. Topological edge states of bound photon pairs. *Physical Review A*, 95(5):053866, May 2017.
- [279] M. Hafezi, S. Mittal, J. Fan, A. Migdall, and J. M. Taylor. Imaging topological edge states in silicon photonics. *Nature Photonics*, 7(12):1001–1005, December 2013.
- [280] Mikael C. Rechtsman, Julia M. Zeuner, Yonatan Plotnik, Yaakov Lumer, Daniel Podolsky, Felix Dreisow, Stefan Nolte, Mordechai Segev, and Alexander Szameit. Photonic Floquet topological insulators. *Nature*, 496(7444):196–200, April 2013.
- [281] Ling Lu, Chen Fang, Liang Fu, Steven G. Johnson, John D. Joannopoulos, and Marin Soljačić. Symmetry-protected topological photonic crystal in three dimensions. *Nature Physics*, 12(4):337–340, April 2016.
- [282] Tomoki Ozawa, Hannah M. Price, Alberto Amo, Nathan Goldman, Mohammad Hafezi, Ling Lu, Mikael C. Rechtsman, David Schuster, Jonathan Simon, Oded Zilberberg, and Iacopo Carusotto. Topological photonics. *Reviews of Modern Physics*, 91(1):015006, March 2019.
- [283] Jinwoong Cha, Kun Woo Kim, and Chiara Daraio. Experimental realization of on-chip topological nanoelectromechanical metamaterials. *Nature*, 564(7735):229–233, December 2018.
- [284] Gal Harari, Miguel A. Bandres, Yaakov Lumer, Mikael C. Rechtsman, Y. D. Chong, Mercedeh Khajavikhan, Demetrios N. Christodoulides, and Mordechai Segev. Topological insulator laser: Theory. *Science*, 359(6381):eaar4003, March 2018.
- [285] Miguel A. Bandres, Steffen Wittek, Gal Harari, Midya Parto, Jinhan Ren, Mordechai Segev, Demetrios N. Christodoulides, and Mercedeh Khajavikhan. Topological insulator laser: Experiments. *Science*, 359(6381):eaar4005, March 2018.
- [286] Han Zhao, Pei Miao, Mohammad H. Teimourpour, Simon Malzard, Ramy El-Ganainy, Henning Schomerus, and Liang Feng. Topological hybrid silicon microlasers. *Nature Communications*, 9(1):981, March 2018.

Bibliography

- [287] Yongquan Zeng, Udvash Chattopadhyay, Bofeng Zhu, Bo Qiang, Jinghao Li, Yuhao Jin, Lianhe Li, Alexander Giles Davies, Edmund Harold Linfield, Baile Zhang, Yidong Chong, and Qi Jie Wang. Electrically pumped topological laser with valley edge modes. *Nature*, 578(7794):246–250, February 2020.
- [288] Zhe Zhang, Pierre Delplace, and Romain Fleury. Superior robustness of anomalous non-reciprocal topological edge states. *Nature*, 598(7880):293–297, October 2021.
- [289] Ling Lu, John D. Joannopoulos, and Marin Soljačić. Topological photonics. *Nature Photonics*, 8(11):821–829, November 2014.
- [290] Alexander B. Khanikaev and Gennady Shvets. Two-dimensional topological photonics. *Nature Photonics*, 11(12):763–773, December 2017.
- [291] Chenhui Peng, Taras Turiv, Yubing Guo, Qi-Huo Wei, and Oleg D. Lavrentovich. Command of active matter by topological defects and patterns. *Science*, 354(6314):882–885, November 2016.
- [292] Anton Souslov, Benjamin C. van Zuiden, Denis Bartolo, and Vincenzo Vitelli. Topological sound in active-liquid metamaterials. *Nature Physics*, 13(11):1091–1094, November 2017.
- [293] Debarghya Banerjee, Anton Souslov, Alexander G. Abanov, and Vincenzo Vitelli. Odd viscosity in chiral active fluids. *Nature Communications*, 8(1):1573, November 2017.
- [294] Aleksandra Nelson, Dana M. Lobmeyer, Sibani L. Biswal, and Evelyn Tang. Topological edge flows drive macroscopic re-organization in magnetic colloids, January 2025.
- [295] Kinjal Dasbiswas, Kranthi K. Mandadapu, and Suriyanarayanan Vaikuntanathan. Topological localization in out-of-equilibrium dissipative systems. *Proceedings of the National Academy of Sciences*, 115(39):E9031–E9040, September 2018.
- [296] Kazuki Sone, Yuto Ashida, and Takahiro Sagawa. Exceptional non-Hermitian topological edge mode and its application to active matter. *Nature Communications*, 11(1):5745, November 2020.
- [297] Kazuki Sone and Yuto Ashida. Anomalous Topological Active Matter. *Physical Review Letters*, 123(20):205502, November 2019.
- [298] Michel Fruchart, Colin Scheibner, and Vincenzo Vitelli. Odd Viscosity and Odd Elasticity. *Annual Review of Condensed Matter Physics*, 14(Volume 14, 2023):471–510, March 2023.
- [299] He Li, Hugues Chaté, Masaki Sano, Xia-qing Shi, and H. P. Zhang. Robust Edge Flows in Swarming Bacterial Colonies. *Physical Review X*, 14(4):041006, October 2024.
- [300] Mark J. Bowick, Nikta Fakhri, M. Cristina Marchetti, and Sriram Ramaswamy. Symmetry, Thermodynamics, and Topology in Active Matter. *Physical Review X*, 12(1):010501, February 2022.
- [301] Luca Tubiana, Gareth P. Alexander, Agnese Barbensi, Dorothy Buck, Julyan H. E. Cartwright, Mateusz Chwastyk, Marek Cieplak, Ivan Coluzza, Simon Čopar, David J. Craik, Marco Di Stefano, Ralf Everaers, Patrícia F. N. Faísca, Franco Ferrari, Achille Giacometti, Dimos Goundaroulis, Ellinor Haglund, Ya-Ming Hou, Nevena Ilieva, Sophie E. Jackson, Alexandre Japaridze, Noam Kaplan, Alexander R. Klotz, Hongbin Li, Christos N. Likos, Emanuele Locatelli, Teresa López-León, Thomas Machon, Cristian Micheletti, Davide Michieletto, Antti Niemi, Wanda Niemyska, Szymon Niewieczeral, Francesco Nitti, Enzo Orlandini, Samuela Pasquali, Agata P. Perlinska, Rudolf Podgornik, Raffaello Potestio, Nicola M. Pugno, Miha Ravnik, Renzo Ricca, Christian M. Rohwer, Angelo Rosa, Jan Smrek, Anton Souslov, Andrzej Stasiak, Danièle Steer, Joanna Sułkowska, Piotr Sułkowski, De Witt L. Sumners, Carsten Svaneborg, Piotr Szymczak, Thomas Tarenzi, Rui Travasso, Peter Virnau, Dimitris Vlassopoulos, Primož Ziherl, and Slobodan Žumer. Topology in soft and biological matter. *Physics Reports*, 1075:1–137, July 2024.

Bibliography

- [302] Desheng Kong and Yi Cui. Opportunities in chemistry and materials science for topological insulators and their nanostructures. *Nature Chemistry*, 3(11):845–849, November 2011.
- [303] Nitesh Kumar, Satya N. Guin, Kaustuv Manna, Chandra Shekhar, and Claudia Felser. Topological Quantum Materials from the Viewpoint of Chemistry. *Chemical Reviews*, 121(5):2780–2815, March 2021.
- [304] Xiang Ni, Simon Yves, Alex Krasnok, and Andrea Alù. Topological Metamaterials. *Chemical Reviews*, 123(12):7585–7654, June 2023.
- [305] Jianping Xiao, Liangzhi Kou, Chi-Yung Yam, Thomas Frauenheim, and Binghai Yan. Toward Rational Design of Catalysts Supported on a Topological Insulator Substrate. *ACS Catalysis*, 5(12):7063–7067, December 2015.
- [306] Guowei Li and Claudia Felser. Heterogeneous catalysis at the surface of topological materials. *Applied Physics Letters*, 116(7):070501, February 2020.
- [307] Carlos-Andres Palma. Topological Dynamic Matter. *The Journal of Physical Chemistry Letters*, 12(1):454–462, January 2021.
- [308] Xiaoming Zhang, Lirong Wang, Minghang Li, Weizhen Meng, Ying Liu, Xuefang Dai, Guodong Liu, Yuantong Gu, Junxian Liu, and Liangzhi Kou. Topological surface state: Universal catalytic descriptor in topological catalysis. *Materials Today*, 67:23–32, July 2023.
- [309] Barry Bradlyn, L. Elcoro, Jennifer Cano, M. G. Vergniory, Zijun Wang, C. Felser, M. I. Aroyo, and B. Andrei Bernevig. Topological quantum chemistry. *Nature*, 547(7663):298–305, July 2017.
- [310] Luis Elcoro, Benjamin J. Wieder, Zhida Song, Yuanfeng Xu, Barry Bradlyn, and B. Andrei Bernevig. Magnetic topological quantum chemistry. *Nature Communications*, 12(1):5965, October 2021.
- [311] G. E. Volovik. Fermion zero modes on vortices in chiral superconductors. *Journal of Experimental and Theoretical Physics Letters*, 70(9):609–614, November 1999.
- [312] A. Yu Kitaev. Unpaired Majorana fermions in quantum wires. *Physics-Uspekhi*, 44(10S):131, October 2001.
- [313] D. A. Ivanov. Non-Abelian Statistics of Half-Quantum Vortices in \mathbf{p} -Wave Superconductors. *Physical Review Letters*, 86(2):268–271, January 2001.
- [314] P.W. Shor. Fault-tolerant quantum computation. In *Proceedings of 37th Conference on Foundations of Computer Science*, pages 56–65, October 1996.
- [315] A. Yu. Kitaev. Fault-tolerant quantum computation by anyons. *Annals of Physics*, 303(1):2–30, January 2003.
- [316] Liang Fu and C. L. Kane. Superconducting Proximity Effect and Majorana Fermions at the Surface of a Topological Insulator. *Physical Review Letters*, 100(9):096407, March 2008.
- [317] Chetan Nayak, Steven H. Simon, Ady Stern, Michael Freedman, and Sankar Das Sarma. Non-Abelian anyons and topological quantum computation. *Reviews of Modern Physics*, 80(3):1083–1159, September 2008.
- [318] Frank Wilczek. Majorana returns. *Nature Physics*, 5(9):614–618, September 2009.
- [319] C. W. J. Beenakker. Search for Majorana Fermions in Superconductors. *Annual Review of Condensed Matter Physics*, 4(Volume 4, 2013):113–136, April 2013.
- [320] Sankar Das Sarma, Michael Freedman, and Chetan Nayak. Majorana zero modes and topological quantum computation. *npj Quantum Information*, 1(1):1–13, October 2015.

Bibliography

- [321] S. M. Albrecht, A. P. Higginbotham, M. Madsen, F. Kuemmeth, T. S. Jespersen, J. Nygård, P. Krogstrup, and C. M. Marcus. Exponential protection of zero modes in Majorana islands. *Nature*, 531(7593):206–209, March 2016.
- [322] Sangjun Jeon, Yonglong Xie, Jian Li, Zhijun Wang, B. Andrei Bernevig, and Ali Yazdani. Distinguishing a Majorana zero mode using spin-resolved measurements. *Science*, 358(6364):772–776, November 2017.
- [323] Microsoft Azure Quantum, Morteza Aghaee, Alejandro Alcaraz Ramirez, Zulfi Alam, Rizwan Ali, Mariusz Andrzejczuk, Andrey Antipov, Mikhail Astafev, Amin Barzegar, Bela Bauer, Jonathan Becker, Umesh Kumar Bhaskar, Alex Bocharov, Srinivasa Boddapati, David Bohn, Jouri Bommer, Leo Bourdet, Arnaud Bousquet, Samuel Boutin, Lucas Casparis, Benjamin J. Chapman, Sohail Chattoor, Anna Wulff Christensen, Cassandra Chua, Patrick Codd, William Cole, Paul Cooper, Fabiano Corsetti, Ajuan Cui, Paolo Dalpasso, Juan Pablo Dehollain, Gijs de Lange, Michiel de Moor, Andreas Ekefjärd, Tareq El Dandachi, Juan Carlos Estrada Saldaña, Saeed Fallahi, Luca Galletti, Geoff Gardner, Deshan Govender, Flavio Griggio, Ruben Grigoryan, Sebastian Grijalva, Sergei Gronin, Jan Gukelberger, Marzie Hamdast, Firas Hamze, Esben Bork Hansen, Sebastian Heedt, Zahra Heidarnia, Jesús Herranz Zamorano, Samantha Ho, Laurens Holgaard, John Hornibrook, Jinnapat Indrapromkul, Henrik Ingerslev, Lovro Ivancevic, Thomas Jensen, Jaspreet Jhoja, Jeffrey Jones, Konstantin V. Kalashnikov, Ray Kallaher, Rachpon Kalra, Farhad Karimi, Torsten Karzig, Evelyn King, Maren Elisabeth Kloster, Christina Knapp, Dariusz Kocon, Jonne V. Koski, Pasi Kostamo, Mahesh Kumar, Tom Laeven, Thorvald Larsen, Jason Lee, Kyunghoon Lee, Grant Leum, Kongyi Li, Tyler Lindemann, Matthew Looij, Julie Love, Marijn Lucas, Roman Lutchyn, Morten Hannibal Madsen, Nash Madulid, Albert Malmros, Michael Manfra, Devashish Mantri, Signe Brynold Markussen, Esteban Martinez, Marco Mattila, Robert McNeil, Antonio B. Mei, Ryan V. Mishmash, Gopakumar Morthandas, Christian Mollgaard, Trevor Morgan, George Moussa, Chetan Nayak, Jens Hedegaard Nielsen, Jens Munk Nielsen, William Hvilsted Padkar Nielsen, Bas Nijholt, Mike Nystrom, Eoin O’Farrell, Thomas Ohki, Keita Otani, Brian Paquette Wütz, Sebastian Pauka, Karl Petersson, Luca Petit, Dima Pikulin, Guen Prawiroatmodjo, Frank Preiss, Eduardo Puchol Morejon, Mohana Rajpalke, Craig Ranta, Katrine Rasmussen, David Razmadze, Outi Reentila, David J. Reilly, Yuan Ren, Ken Reneris, Richard Rouse, Ivan Sadovskyy, Lauri Sainiemi, Irene Sanlorenzo, Emma Schmidgall, Cristina Sfiligoj, Mustafeez Bashir Shah, Kevin Simoes, Shilpi Singh, Sarat Sinha, Thomas Soerensen, Patrick Sohr, Tomas Stankevic, Lieuwe Stek, Eric Stuppard, Henri Suominen, Judith Suter, Sam Teicher, Nivetha Thiyagarajah, Raj Tholapi, Mason Thomas, Emily Toomey, Josh Tracy, Michelle Turley, Shivendra Upadhyay, Ivan Urban, Kevin Van Hoogdalem, David J. Van Woerkom, Dmitrii V. Viazmitinov, Dominik Vogel, John Watson, Alex Webster, Joseph Weston, Georg W. Winkler, Di Xu, Chung Kai Yang, Emrah Yucelen, Roland Zeisel, Guoji Zheng, and Justin Zilke. Interferometric single-shot parity measurement in InAs-Al hybrid devices. *Nature*, 638(8051):651–655, February 2025.
- [324] Ville Lahtinen and Jiannis Pachos. A Short Introduction to Topological Quantum Computation. *SciPost Physics*, 3(3):021, September 2017.
- [325] Wladimir A. Benalcazar, B. Andrei Bernevig, and Taylor L. Hughes. Quantized electric multipole insulators. *Science*, 357(6346):61–66, July 2017.
- [326] Frank Schindler, Ashley M. Cook, Maia G. Vergniory, Zhijun Wang, Stuart S. P. Parkin, B. Andrei Bernevig, and Titus Neupert. Higher-order topological insulators. *Science Advances*, 4(6):eaat0346, June 2018.
- [327] Ashraf El Hassan, Flore K. Kunst, Alexander Moritz, Guillermo Andler, Emil J. Bergholtz, and Mohamed Bourennane. Corner states of light in photonic waveguides. *Nature Photonics*, 13(10):697–700, October 2019.
- [328] Bi-Ye Xie, Guang-Xu Su, Hong-Fei Wang, Hai Su, Xiao-Peng Shen, Peng Zhan, Ming-Hui Lu, Zhen-Lin Wang, and Yan-Feng Chen. Visualization of Higher-Order Topological In-

Bibliography

- sulating Phases in Two-Dimensional Dielectric Photonic Crystals. *Physical Review Letters*, 122(23):233903, June 2019.
- [329] Haiyan Fan, Baizhan Xia, Liang Tong, Shengjie Zheng, and Dejie Yu. Elastic Higher-Order Topological Insulator with Topologically Protected Corner States. *Physical Review Letters*, 122(20):204301, May 2019.
- [330] Xiujuan Zhang, Zhi-Kang Lin, Hai-Xiao Wang, Zhan Xiong, Yuan Tian, Ming-Hui Lu, Yan-Feng Chen, and Jian-Hua Jiang. Symmetry-protected hierarchy of anomalous multipole topological band gaps in nonsymmorphic metacrystals. *Nature Communications*, 11(1):65, January 2020.
- [331] Zongping Gong, Yuto Ashida, Kohei Kawabata, Kazuaki Takasan, Sho Higashikawa, and Masahito Ueda. Topological Phases of Non-Hermitian Systems. *Physical Review X*, 8(3):031079, September 2018.
- [332] Emil J. Bergholtz, Jan Carl Budich, and Flore K. Kunst. Exceptional topology of non-Hermitian systems. *Reviews of Modern Physics*, 93(1):015005, February 2021.
- [333] Lucien Jezequel and Pierre Delplace. Non-Hermitian Spectral Flows and Berry-Chern Monopoles. *Physical Review Letters*, 130(6):066601, February 2023.
- [334] Daria Smirnova, Daniel Leykam, Yidong Chong, and Yuri Kivshar. Nonlinear topological photonics. *Applied Physics Reviews*, 7(2):021306, June 2020.
- [335] Lucien Jezequel and Pierre Delplace. Nonlinear edge modes from topological one-dimensional lattices. *Physical Review B*, 105(3):035410, January 2022.
- [336] Lucien Jezequel. *Phase Space Approach to Topological Physics : Mode-shell Correspondence and Extentions to Non-Hermitian and Non-Linear Systems*. PhD thesis, Ecole normale supérieure de Lyon - ENS LYON, June 2024.
- [337] Farzad Zangeneh-Nejad, Andrea Alù, and Romain Fleury. Topological wave insulators: a review. *Comptes Rendus. Physique*, 21(4-5):467–499, 2020.
- [338] Sebastian D. Huber. Topological mechanics. *Nature Physics*, 12(7):621–623, July 2016.
- [339] Armand Leclerc, Guillaume Laibe, and Nicolas Perez. Wave topology of stellar inertial oscillations. *Physical Review Research*, 6(4):043299, December 2024.
- [340] Nicolas Perez, Armand Leclerc, Guillaume Laibe, and Pierre Delplace. Topology of shallow-water waves on a rotating sphere. *Journal of Fluid Mechanics*, 1003:A35, January 2025.
- [341] Armand Leclerc, Guillaume Laibe, Pierre Delplace, Antoine Venaille, and Nicolas Perez. Topological Modes in Stellar Oscillations. *The Astrophysical Journal*, 940(1):84, November 2022.
- [342] R. G. Barrera, G. A. Estevez, and J. Giraldo. Vector spherical harmonics and their application to magnetostatics. *European Journal of Physics*, 6(4):287, October 1985.
- [343] Arthur Le Saux, Armand Leclerc, Guillaume Laibe, Pierre Delplace, and Antoine Venaille. A Core-sensitive Mixed f/g-mode of the Sun Predicted by Wave Topology and Hydrodynamical Simulation. *The Astrophysical Journal Letters*, 987(1):L12, June 2025.
- [344] Armand Leclerc and Guillaume Laibe. The Importance of Berry Phase in Solar Acoustic Modes. *The Astrophysical Journal Letters*, 983(1):L17, April 2025.
- [345] Armand Leclerc, Guillaume Laibe, and Nicolas Perez. *PT* and anti-*PT* symmetries for astrophysical waves. *Astronomy & Astrophysics*, 689:A237, September 2024.
- [346] Armand Leclerc, Lucien Jezequel, Nicolas Perez, Asmita Bhandare, Guillaume Laibe, and Pierre Delplace. Exceptional ring of the buoyancy instability in stars. *Physical Review Research*, 6(1):L012055, March 2024.

Bibliography

- [347] W. H. Ball and L. Gizon. A new correction of stellar oscillation frequencies for near-surface effects. *Astronomy & Astrophysics*, 568:A123, August 2014.
- [348] Giandomenico Palumbo and Nathan Goldman. Revealing Tensor Monopoles through Quantum-Metric Measurements. *Physical Review Letters*, 121(17):170401, October 2018.
- [349] You Wang, Hannah M. Price, Baile Zhang, and Y. D. Chong. Circuit implementation of a four-dimensional topological insulator. *Nature Communications*, 11(1):2356, May 2020.
- [350] Mo Chen, Changhao Li, Giandomenico Palumbo, Yan-Qing Zhu, Nathan Goldman, and Paola Cappellaro. A synthetic monopole source of Kalb-Ramond field in diamond. *Science*, 375(6584):1017–1020, March 2022.
- [351] Richard H. D. Townsend, Rianna V. Kuenzi, and Jørgen Christensen-Dalsgaard. Tools for Characterizing the Numerical Error of Stellar Oscillation Codes, May 2025.